THÈSE POUR OBTENIR LE GRADE DE DOCTEUR DE L'UNIVERSITÉ DE MONTPELLIER

En Chimie et Physico-Chimie des Matériaux

École doctorale SCIENCE CHIMIQUES BALARD (SCB)-ED 459

Institut Européen des Membranes (UMR 5635, CNRS, UM, ENSCM)

Contribution de la micro-spectroscopie Raman à l'étude de l'électrolyte pour batteries Li-métal

Contribution of Raman micro-spectroscopy to the study of the electrolyte for Li-metal batteries.

Présentée par Feihong Ren

Le 26 octobre 2022

Sous la direction de Stefano DEABATE

Devant le jury composé de

M. Laurent SERVANT, Professeur, Université de Bordeaux - ISM	Rapporteur
Mme Cristina IOJOIU, DR2, Grenoble INP - LEPMI	Rapporteur
M. Lorenzo STIEVANO, Professeur, Université Montpellier - ICGM	Examinateur
M. François HENN, Professeur, Université Montpellier - L2C	Examinateur

UNIVERSITÉ DE MONTPELLIER

Acknowledgements

Time is like the sea near Montpellier, carrying the ship of my Ph.D. and pushing it with sea waves little by little, of course, I cannot forget those people who are like the winds blowing the sail towards the shore. On this quiet and peaceful afternoon, I would like to thank those who have helped me during these three years with a grateful heart and great respect.

First and foremost, I would like to dedicate my deepest and sincerest gratitude to Prof. Stefano Deabate, my supervisor, for his constant guidance, valuable suggestions, and helpful encouragement both in my study and in my life. Actually, a year before my Ph.D., he had already helped me prepare the materials for applying for the scholarship for my Ph.D. During my Ph.D. study, he instructed me to carry out experiments, gave me the most detailed comments on my manuscripts, and explained me with great patience every time I have difficulties on understanding research problem. I could always get the fastest e-mail reply from him and discussion with him as soon as possible even when he was busy with teaching work. What touched me most is that he sacrificed his vacation time to revise my thesis manuscript. In addition, he helped me with accommodation in France and solved the problem of the two-last-month finance of my Ph.D. study. Even though he has rigorous research attitude, he never puts too much pressure on my shoulders. He is a role model in my life.

I would like to express my great gratitude to Prof. Patrice Huguet, my co-supervisor who gave me supervision, support for setting up experiments, purchasing materials, advice during discussing our research works, and motivation to learn French. His solid professional foundation and rigorous research attitude inspired me.

My heartfelt gratitude goes to my collaborators: Prof. Zhe Peng, Prof. Damien Voiry, Prof. Deyu Wang, Mr. Zhendong Li, Dr. Kun Qi, Mr. Jiefeng Liu, Mr. Yun Zhu, Mr. Jiahe Chen. I would like to appreciate Prof. Zhe Peng for the cooperation which has been 5 years both in my master study and in my Ph.D. study. No matter how difficult the problem I encountered, he always gave me useful guidance and inspiration. I would like to thank Prof. Damien Voiry for the cooperation for the part of CO_2RR in Chapter 5 and the future publication. I would thank Prof. Deyu Wang, my master supervisor for his precious advice for my published article in Nano Energy journal and great encouragement. I am also greatly indebted to Mr. Zhendong Li for the help of battery performance tests, Dr. Kun Qi for the help of CO_2RR tests, the advice for manuscript

and the contact of EXAFS tests with Beijing Synchrotron Radiation Facility (BSRF), Mr. Jiefeng Liu for the help of CO_2RR tests, Mr. Yun Zhu for the help of *in situ* optical microscopy, and Mr. Jiahe Chen for the help of conductivity test.

Many thanks go to those who helped me with material characterizations and equipments: Mr. Eddy Petit (Raman, FTIR, NMR, and sharing fuming cupboard with me), Mr. Didier COT (SEM), Mr. Bertrand Rebiere (SEM and EDS), Ms. Valerie Flaud (XPS), Ms. Karine Parra (NMR), Prof. Umit B. Demirci (glove box) and Mr. Karim Aissou (AFM) though we finally did not put the AFM images into this thesis, they still helped us understand certain points of our research.

I would appreciate my family for giving me love, care and courage, especially my mother for giving me life, raising me up, accompanying me, and trusting me unconditionally, and my grandmother for blessing me in another world. I would like also to thank my friends and colleagues for their selfless help and companionship.

Many gratefulness to the members of the jury for accepting to judge this thesis despite they have a busy schedule: Prof. Laurent Servant, DR. Cristina Iojoiu, Prof. Lorenzo Stievano, and Prof. François Henn.

I would also thank China Scholarship Council (CSC) under the Grant CSC N°201906340005 and French government scholarship (File number: 969949K) who gave me financial support to complete this study.

Last but not least, I would like to thank myself for conquering anxiety, procrastination, depression, pressure, illness…, and never giving up even in the global epidemic. Ph.D. is not the end of study, and I believe there are more things waiting for me to explore…

Table of contents

General introduction 8
Chapter 1. Bibliography and motivation 13
1.1 Introduction and background 13
1.2 Short history of the battery development 13
1.3 Short history of Raman spectroscopy 15
1.4 Li-ion vs. Li-metal batteries 17
1.4.1 Working mechanisms and main features 17
1.4.2 The electrochemical stability window of the electrolyte according to the frontier molecular orbital theory 19
1.4.3 The Solid Electrolyte Interphase (SEI) film 21
1.4.4 The Li-metal anode: main issues and mitigation strategies 24
1.5 Liquid electrolytes for Li-metal batteries 31
1.5.1 Salts, solvents, and additives 32
1.5.2 High-concentration electrolytes (HCE) 35
1.5.3 Localized high-concentration electrolytes 38
1.6 Characterization methods of electrolytes for Li-metal batteries 39
1.6.1 Raman micro-spectroscopy applied to Li-based batteries and electrolytes for Li-metal devices 41
1.6.1.1 Studying the electrolyte solvation structure 42
1.6.1.2 Detecting ion concentration gradients in the electrolyte 44
1.7 Motivation and work plan 46
Chapter 2. Experimental setup and methods 61
2.1 Introduction 61
2.2 Assembly of *in situ* optical cell 61
2.3 Electrochemical measurements 63
2.3.1 Li plating curves 63
2.3.2 Electrochemical impedance spectroscopy 64
2.3.3 Linear sweep voltammetry 67
2.3.4 Cycling performance 68
2.3.5 Average coulombic efficiency 70
2.4 Raman micro-spectroscopy 70
2.4.1 Introduction 70

2.4.2 Principle of Raman micro-spectroscopy and experimental configuration 71
2.4.3 Data processing 74
2.4.3.1 Baseline correction 74
2.4.3.2 Peak fitting 75
2.5 Materials 76
2.6 Complementary measurements (other than μ-Raman) 77
Chapter 3. Raman micro-spectroscopy study of the local composition and structure of low-, high- and localized high-concentration electrolytes: relationships with SEI properties and morphology of the Li deposit 80
3.1 Introduction 80
3.2 Evolution of the local solvation structure as a function of the electrolyte concentration 83
3.3 Effect of the diluent content on the solvation structure of LHCEs 86
3.4 Effect of the diluent content on the electrochemical performances of the Li metal anode 91
3.5 Effect of the diluent content on the SEI composition and Li deposition morphology 93
3.6 Conclusion 96
Supporting information 98
Chapter 4. Probing the local Li^+ concentration in the electrolyte during plating by *in situ* Raman micro-spectroscopy: which relationships with the SEI properties and the morphology of the Li deposit? 107
4.1 Introduction 107
4.2 Preliminary study of the evolution of the local [Li^+] during plating in a low concentration, binary solvent electrolyte: validation of the *in situ* -Raman approach 109
4.3 *In situ* Raman measurements of the Li^+ concentration gradients occurring during plating: comparison between low-, high- and localized high-concentration electrolytes 117
4.4 SEM characterization of the Li deposition morphology 124
4.5 Characterization of the SEI film 126
4.6 Conclusion 130
Supplementary information 133

Chapter 5. Recycling the Li electrolyte into catalyst for CO_2RR applications via laser irradiation 138
5.1 General introduction 138
5.2 Short introduction to the CO_2RR 138
5.3 The photochemical conversion of the electrolyte in contact with Cu into graphitic carbon onto Cu_xO 140
5.3.1 First observations 140
5.3.2 Conditions and mechanism of the photochemical reaction 142
5.3.3 Characterization of the photochemical reaction products 146
5.4 Study of the catalytic properties 150
5.5 Conclusion 153
Supporting Information 155
General conclusion 160
Annex 164

General introduction

Since the first commercial lithium (Li)-ion batteries developed by Sony company in 1990s, this technology has been widely used for the energy storage in various applications involving portable devices, electric vehicles and medical equipment [1]. Today, the use of Li-ion batteries is predominant in the market of portable electronics. Nevertheless, the Li-ion energy density, even if larger than the most of the other batteries currently available, is still inadequate for improving the cruising ability of electric cars as required [2]. This prompts researchers to intensely and urgently work on new electrodes with larger capacity. As far as the anode materials are concerned, one such improved electrode could be the Li metal. Actually, if the practical capacity of graphite, which is the most used anode in current Li-ion batteries, is reaching its theoretical capacity of 372 mAh g^{-1}, that of Li metal is (in principle) 10 times more i.e. 3860 mAh g^{-1} [3]. But several challenges remain to be solved in order to make the Li-metal technology available to the market. Because of the intrinsic properties of Li metal, Li anode has many notorious problems in the process of charging/discharging: protrusive Li deposition (dendrites) leading to the battery short-circuit, high reactivity with electrolyte, whose degradation by side reactions induces poor quality solid electrolyte interphase films at the electrode surface, huge volume change during cycling, dead lithium, etc. [4]. The different strategies currently implemented to overcome these issues focus on the shaping of the electrode surface as well as on the conception of the electrolyte. Improving the Li metal electrode essentially consists in modifying the surface by coatings which act as stable hosts for the Li deposition [5]. But this approach implies to add non-active materials which decrease the mass and the volume energy density of the battery. Electrolytes are improved by working on their composition and concentration [6]. Typically, increasing Li salt concentration delays the appearing of dendritic Li [7] but, at the same time, it also induces excessive viscosity (thus poor wetting ability towards separators), poor ionic conductivity and larger financial burden compared with standard low-concentration electrolytes. A new class of materials, called localized high-concentration electrolytes, has recently been developed, consisting in ternary mixtures obtained by adding a second diluent as “inert” solvent, which cannot dissolve the Li salt but is miscible with the solvent initially used [8]. These new electrolytes, although employing weak global amount of Li salt comparable to those of low-concentration solutions, are made up of highly concentrated salt-solvent clusters

distributed in the non-solvating diluent. This different local structure is expected to maintain the advantages of increasing the Li salt concentration while minimizing disadvantages as cost. Nevertheless, at the state-of-the-art, the electrochemical performances of the metallic Li electrode still remain inadequate.

Current research lacks of detailed and systematic studies comparing the structure and properties of low-, high- and localized high-concentration electrolytes. In order to further progress towards improved Li-metal systems, more work is needed to establish strict relationships between the electrolyte composition, structure, transport properties and reactivity under operation on the one hand, morphology of the Li plated during discharge, properties of the solid electrolyte interphase and electrochemical behavior of the battery on the other. The complexity of the interrelation between these different parameters and phenomena requires the development of new experimental approaches and, namely, the implementation of *in situ* and *operando* measurements.

The work reported in this manuscript deals with the systematic comparison of low-, high- and localized high-concentration electrolytes for Li metal batteries. Their characterization is carried out mainly by *ex* and *in situ* Raman micro-spectroscopy, supplemented case by case by electrochemical and FTIR measurements, scanning electron microscopy, X-ray photoelectron and Extended X-Ray Absorption Fine Structure spectroscopies. Beyond the historical expertise of the research team in Raman spectroscopy, the implementation of this technique was dictated by the following main reasons: the ability to (i) provide local chemical and structural information with high sensitivity, in a non-destructive way (that will have allowed us to obtained some inedited knowledge on the local structure of the localized high-concentration electrolytes, reported in chapter 3); (ii) detect the Li^+ concentration gradients crossing the electrolyte during the battery operation through the signal of the counter-ion and/or solvating molecules. Indeed, the Li deposition morphology is usually considered to results from the [Li^+] gradients occurring more or less heterogeneously along the electrode surface. Excessive local Li^+ consumption leads the Li plating to grow faster toward the bulk electrolyte direction where further Li^+ is available, which induces the protruded Li deposits usually called dendrites [9]. Thus, stronger gradients are generally considered to be associated with a more dendritic-like Li deposition. But, then, it should be note that quite few straightforward experimental data have actually been reported in this regard until today i.e. ion concentration profile mapping has been rarely carried out, and none concerning localized high-concentration electrolytes. The results of our *in situ*

Raman study led us to some unexpected conclusions which will be presented in chapter 4.

Finally, Raman measurements accidentally revealed a phenomenon of photochemical reaction converting the electrolyte in contact with a Cu substrate into a solid layer which is the precursor of an effective catalyst for the electrochemical CO_2 reduction reaction. Considered the actual importance of developing new methods of recycling of the exhausted electrolyte into useful materials, we decided to devote the last part of our work to the characterization of this new catalyst generated *in situ* by the laser irradiation.

This manuscript is composed of five main parts:

The first chapter, bibliographic, is devoted to a reminder of the main features of Li metal batteries, their perspective interest as high energy density systems for portable devices, and discusses main issues still affecting their stability and performances which have to be addressed and solved to attain the large-scale marketing. The reasons of the choice of the electrolyte as the object of our study and of the Raman microscopy as the main characterization technique are illustrated again in more detail.

The second chapter presents the experimental set-up and conditions which were carried out and developed for the *ex* and *in situ* study of low-, high- and localized high-concentration electrolytes.

The third chapter deals with the *ex situ* study of the Li^+ local solvation structure, its evolution with the composition and concentration of the electrolyte and relationships with the electrochemical properties of the Li metal anode.

Chapter 4 is devoted to the *in situ* study of the Li^+ concentration distribution close to the electrode surface during operation and relationships with the morphology of the Li deposited by the electrochemical reduction reaction.

Chapter 5 deals with the photo-catalytic reduction of carbonate-based electrolytes on Cu, phenomenon triggered by the Raman laser irradiation which, in perspective, is of great interest for the recycling of exhausted electrolytes into useful catalyst.

The manuscript ends with a general conclusion summarizing the obtained results and proposing some relevant perspectives.

A part of the results presented in this manuscript gave rise to two publications and four oral communications, listed hereafter.

Publications:

1. F. Ren, Z. Li, J. Chen, P. Huguet, Z. Peng, and S. Deabate, Solvent–Diluent Interaction-Mediated Solvation Structure of Localized High-Concentration Electrolytes, ACS Applied Materials & Interfaces, 2022, 14(3), 4211–4219.
2. F. Ren, Z. Li, Y. Zhu, P. Huguet, S. Deabate, D. Wang, and Z. Peng, Artificial nucleation sites with stable SEI for Li metal anodes by aggressive Al pulverization, Nano Energy, 2020, 73, 104746.

Oral communications:

1. F. Ren, P. Huguet, S. Deabate. The Raman Spectroscopy Study on Carbonate-based Electrolyte for Lithium Metal Batteries. International Congress on Energy Chemistry and Engineering, 18 June 2021, Sichuan University, Chengdu, China.
2. F. Ren, P. Huguet, S. Deabate. Artificial Nucleation Sites and the Study of Solvation Structures in Electrolytes for Lithium Metal Batteries. Balard Chemistry Conference, 17 June 2021, Ecole Nationale Supérieure de Chimie de Montpellier, Montpellier, France.
3. F. Ren, P. Huguet, S. Deabate. Artificial Nucleation Sites with Stable SEI for Li Metal Anodes by Aggressive Al Pulverization. 8th Mediterranean Day of Young Researchers JMJC, 20 November 2020, Université de Toulon, Toulon, France.
4. F. Ren, P. Huguet, S. Deabate. Solvent-Diluent Interaction Mediated Solvation Structure of Localized High Concentration Electrolytes for Li-Metal Batteries. 6th Doctoral Day of IEM, 17 May 2022, Institut Européen des Membranes, Montpellier, France.

References

[1] M. Li, J. Lu, Z. Chen, K. Amine, 30 years of lithium-ion batteries, Advanced materials 30 (2018) 1800561.

[2] M.S. Park, S.B. Ma, D.J. Lee, D. Im, S.-G. Doo, O. Yamamoto, A highly reversible lithium metal anode, Scientific reports 4 (2014) 1–8.

[3] J. Liu, Z. Bao, Y. Cui, E.J. Dufek, J.B. Goodenough, P. Khalifah, Q. Li, B.Y. Liaw, P. Liu, A. Manthiram, Pathways for practical high-energy long-cycling lithium metal batteries, Nature energy 4 (2019) 180–186.

[4] J. Wang, B. Ge, H. Li, M. Yang, J. Wang, Di Liu, C. Fernandez, X. Chen, Q. Peng, Challenges and progresses of lithium-metal batteries, Chemical engineering journal 420 (2021) 129739.

[5] D. Lin, Y. Liu, Y. Cui, Reviving the lithium metal anode for high-energy batteries, Nature nanotechnology 12 (2017) 194–206.

[6] S.S. Zhang, A review on electrolyte additives for lithium-ion batteries, Journal of power sources 162 (2006) 1379–1394.

[7] E.R. Logan, Dahn, JR, Electrolyte design for fast-charging Li-ion batteries, Trends in chemistry 2 (2020) 354–366.

[8] X. Cao, H. Jia, W. Xu, J.-G. Zhang, localized high-concentration electrolytes for lithium batteries, Journal of the electrochemical society 168 (2021) 10522.

[9] J. Xiao, How lithium dendrites form in liquid batteries, Science 366 (2019) 426–427.

Chapter 1. Bibliography and motivation

1.1 Introduction and background

Due to the increasing scarcity and growing pollution of fossil fuels, great efforts are currently devoted to studying and exploiting new energy sources as nuclear, hydrogen, biomass, geothermal, wind energy, etc. [1]. The development of new energies implies improving energy efficiency, which includes in turn the development of effective energy storage technologies. The capture of energy produced at one time for use at a later time, to reduce imbalances between energy demand and energy production, can be carried out in a variety of ways: thermal, mechanical, electrochemical, etc. Common examples of energy storage are the rechargeable batteries, which stores chemical energy readily convertible to electricity. In this field, the Li-ion technology, developed by Sony Corporation in the early 1990s [2], currently stands out as a most useful device for automotive and portable applications, medical science, aerospace, military, etc. However, the actual capacity of graphite anodes used in Li-ion batteries, which is now approaching its theoretic value (372 mAh g^{-1}), does not meet the rising need for high energy density. Thus, in the past decade, the need to developed new, improved anode materials [3], has promoted the revival of a great deal of research on Li-metal batteries, using Li metal anode of the ultrahigh capacity (3860 mAh g^{-1}) and lowest redox potential (-3.04 V vs. Standard Hydrogen Electrode, S.H.E.) [4]. Historically, the Li-metal technology was developed before the Li-ion, at the beginning of the twentieth century, but later abandoned because of safety concerns related to the use of metallic lithium and liquid organic electrolytes [5].

1.2 Short history of the battery development

First observations of the triboelectric effect, the electrostatic phenomenon created by bringing two materials of different natures into contact, are reported in the 6^{th} century BC, in ancient Greece [6]. The first storage device of electric energy was invented much later, in the 18^{th} century: the Leyden jar allowed to store electric charge generated by triboelectrification into a metal inside an insulated bottle [7]. The voltaic pile, the first electrochemistry cell, was invented at the end of the eighteenth century by Alessandro Volta initially doubting the phenomenon of bioelectricity discovered by Luigi Galvani [8]. After that, a series of batteries as zinc||carbon, nickel||iron and others were developed. It is worth mentioning the nickel||iron batteries patented by Thomas Edison

in 1901 and still used nowadays, which can cycle more than 1000 times maintaining a high capacity ratio but has the shortcoming of serious self-discharge and poor rate performance [9].

In the 20th century, Li-based batteries were discovered and continued to be innovated. In 1912, Gilbert N. Lewis assembled firstly a Li-metal cell by using a pure Li metal anode, a lithium amalgam cathode and an electrolyte of propyl amine saturated with lithium iodide under vacuum. The original aim of this experiment was to compare the electrode potential of Li to that of other alkali metals as Na and K [10]. The following research was devoted to the development of non-aqueous electrolytes compatible with the very low redox potential of these alkali metals, particularly Li. In the 1950s, William Harris and his Ph.D. supervisor studied several organic solvents which could be employed stably in Li-metal batteries [11]. In the Electrochemical Society fall meeting held in 1962, Chilton and Cook reported a new battery system, developed for satellites with long lifespan, consisting of a halide compound (e.g. copper chloride or silver chloride) cathode, a Li metal anode and an electrolyte of propylene carbonate with low-melting-point metal salt dissolved [12]. Even if this system ultimately failed, the Chilton and Cook research motivated scientists to turn to the study of intercalation compounds and transition metal oxides to be used as electrodes in primary (non-rechargeable) Li-metal batteries. Thus, in the 1970s, electrochemical cells as Li||carbon fluoride, Li||manganese dioxide (MnO_2) and Li||silver vanadium oxide ($Ag_2V_4O_{11}$) were developed and used in spacecrafts, calculators and medical implants respectively [13]. In 1972, Whittingham designed a rechargeable Li-metal cell composed by a Li metal anode, a titanium disulfide (TiS_2) cathode and an electrolyte of lithium perchlorate in dioxolane. But a great gap between the actual and the theoretical cycling performance was observed [14]. The failure mechanism of the cell was then extensively studied and main issues were found to be related to the development of Li dendrites and of a solid electrolyte interface (SEI) layer at the electrode-electrolyte interface (more details in this specific regard are provided in the following sections, § 1.4.3 and § 1.4.4). In 1980s, major safety hazards were encountered with the Li||MoS_2 battery of Moli Energy corporation [15]. From then on, the study and commercialization of Li-metal batteries were left aside for a period of time and research turned to Li-ion systems. A precursor Li-ion battery was developed by Akira Yoshino in 1985, resulting from a previous research on transition-metal cathode materials carried out by John Goodenough, M. Stanley Whittingham, Rachid Yazami, and Koichi Mizushima

(1970s–1980s) [16]. In 1990s, Sony first commercialized a Li-ion battery composed of a lithium cobalt oxide ($LiCoO_2$) cathode and a carbon anode (coke in 1991 and graphite since 1994) [17]. Later, always at the end of the 20th century, Goodenough developed the $LiFePO_4$ cathode material, which is more commonly used today because of the very high stability and safety [18]. After that, $LiNi_{1/3}Co_{1/3}Mn_{1/3}O_2$ was also proposed, and finally developed into different subtypes of ternary cathode materials [19].

After entering the 21st century, Li-ion batteries have become a popular research frontier. John B. Goodenough, M. Stanley Whittingham, and Akira Yoshino have been awarded the Nobel Prize in Chemistry 2019 for their work in the field [20]. The research and technology of various cathode, anode and electrolyte materials are in full bloom. Nowadays, most of the cathode materials of electric vehicles' batteries are ternary cathode materials, $LiCoO_2$ or lithium iron phosphate ($LiFePO_4$). The anode material can be graphite, lithium titanate, etc. Silicon/carbon composite anode has also been employed tentatively [21,22]. It should be noted that the most recent research shows great interest in pre-lithiation of graphite or silicon anode or even in the addition of inert Li powder directly into the anode active material for boosting the practical energy density [22,23]. This strongly suggests that a transitional period from C/Si to Li-metal anode has begun. Indeed, in 2021, the Pacific Northwest Laboratory (PNNL) of the United States claimed to have developed a pouch cell with an energy density of 350~500 Wh/kg, in which the anode material is Li metal [24]. Other previous research yet led to high-energy-density systems such as Li-S (2600 wh/kg) and Li-Air (using Li_2O_2 as the reaction product, with an energy density of 3505 wh/kg in a non-aqueous electrolyte) [25]. Nowadays, the Li metal system appears the most promising for next-generation Li batteries.

1.3 Short history of Raman spectroscopy

Li batteries and Raman spectroscopy have a parallel development history (Figure 1-1). The discovery of the Raman effect is usually attributed to Chandrasekhara Venkata Raman, who won the Noble Prize in physics in 1930 for his break-through work about the scattering of light [26]. His work originated from his trip to Europe in 1921, during which he asked himself why the Mediterranean ocean is so blue. Then he carried out a series of physical experiments on light scattering by water and transparent ice blocks, thus discovering the phenomenon of inelastic (i.e. Raman) scattering in 1928 [27]. But the use of Raman spectroscopy in research was considerably delayed for decades

because of, on the one hand, the weakness of the exciting radiation obtained from mercury lamps and, on the other, the occurring of fluorescence and stray light disturbing the detection of the Raman signal. According to the literature [28], the first concept of Raman device using dispersive gratings and a laser as exciting radiation was developed by Delhaye and Migeon in 1966, shortly after the laser introduction in the 1960s. In the 1970s, Raman spectrometers was further improved using confocal optics and holographic gratings allowing to limiting fluorescence and stray light. The first precursor of the Raman microscope was presented in 1974 at both the Université des Sciences et Techniques de Lille in France and the National Bureau of Standards in Washington, and finally commercialized in 1976. The introduction of the charge coupled devices (CCD) for detectors in the 1980s further increased the sensitivity of the Raman spectroscopy, simultaneously decreasing the time needed for the spectral acquisition. In the 21st century, Raman spectroscopy has become an indispensable means to study materials science, physics, chemistry and biology [29–31]. More specifically, from 1980s until present, Raman spectroscopy has been widely used to study Li-based batteries, namely to characterize *ex* or *in situ* electrode materials, SEI films and electrolytes. The *in situ* Raman spectroscopy appears all the more interesting as it is non-invasive and now practicable at the laboratory scale [28].

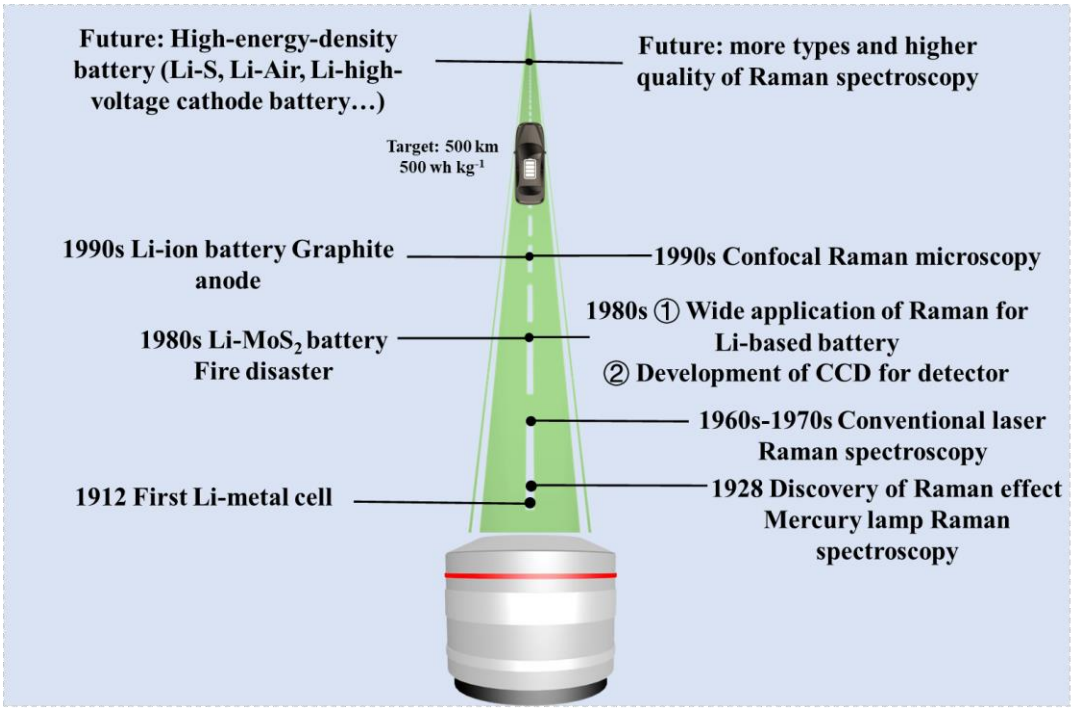


Figure 1-1. The parallel history of the developments of Li-based batteries and Raman spectroscopy.

More details on the Raman spectroscopy principle are given in the annex 1. The topic of the characterization of Li-based secondary batteries by Raman micro-spectrometry is further discussed in the next section 1.6.1.

1.4 Li-ion vs. Li-metal batteries

1.4.1 Working mechanisms and main features

As shown in Figure 1-2a, Li-ion batteries are based on the intercalation and de-intercalation, back and forth between the cathode and anode materials, of Li^+ species (reason why these systems are also known as "rocking chair batteries") [32]. The materials hosting Li^+ at the cathode are generally layer oxides such as $LiCoO_2$, lithium nickelate and manganate, *etc*. The anode material most usually employed is graphite, forming the intercalation compound Li_xC_6 during the battery discharge [33] :

$$xe^- + xLi^+ + 6C \rightarrow Li_xC_6 \text{ (discharge)} \qquad \text{Equation 1-1}$$

$$Li_xC_6 \rightarrow xe^- + xLi^+ + 6C \text{ (charge)} \qquad \text{Equation 1-2}$$

In the specific case of Li-metal batteries, cathode materials other than the intercalation oxide compounds can also be employed like S (Li-S battery) and O_2 (Li-O_2 or Li-air battery). The anode material is Li metal, undergoing stripping (dissolution) and plating (deposition) during the battery charge and discharge [34] :

$$Li \rightarrow Li^+ + e^- \text{ (stripping/discharge)} \qquad \text{Equation 1-3}$$

$$Li^+ + e^- \rightarrow Li \text{ (plating/charge)} \qquad \text{Equation 1-4}$$

During stripping, metallic Li oxidizes and Li^+ cations dissolve in the liquid electrolyte. During plating, Li^+ ions migrate from the electrolyte to the surface of the Li metal where they are reduced back and deposited by electroplating.

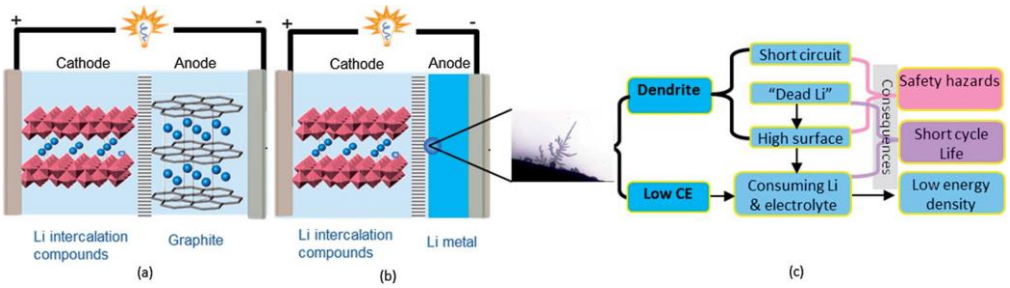


Figure 1-2. Schematic structure of (a) a Li-ion and (b) a Li-metal battery. (c) The weakness of Li-metal batteries [32].

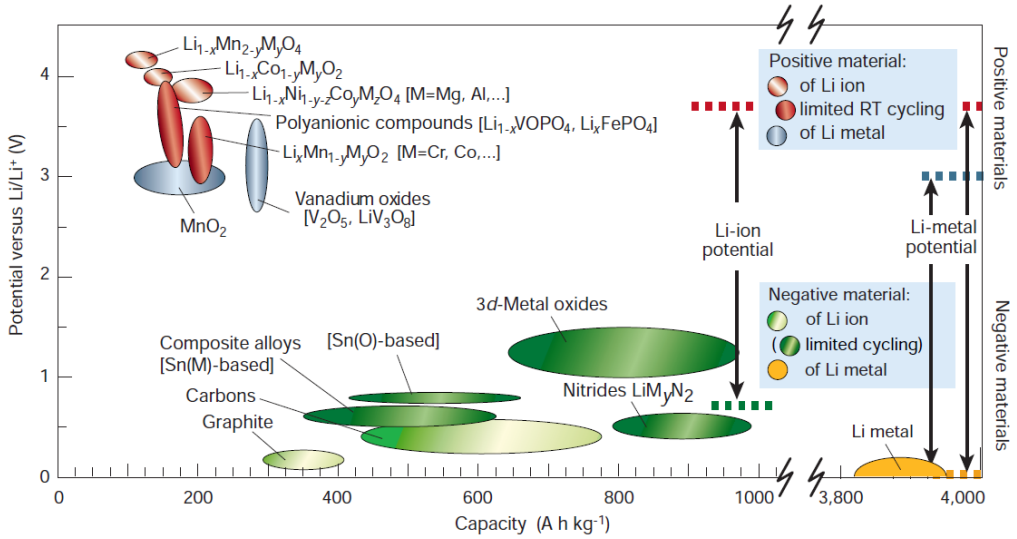


Figure 1-3. Working potential vs. specific capacity of the different cathode and anode materials for Li-based batteries [35].

The theoretical capacity Q_0 of the Li anode can be calculated according to equation 1-5 [36]:

$$Q_0 = F \times \frac{n}{M} \times \frac{1}{3.6} = \frac{26800}{M} \ (\text{mAh g}^{-1}) \qquad \text{Equation 1-5}$$

where F is the Faraday constant, n = 1 the number of electrons exchanged in the electrochemical reaction equation and M the molar mass of the active material. As shown in Figure 1-3, the theoretical mass capacity of the Li metal anode (3860 mAh g^{-1}) is about ten times that of the graphite anode (372 mAh g^{-1}) of Li-ion batteries currently on the market, and also stays significantly higher to most of the other, alternative anode materials, whether carbon- or tin-based, consisting of transition metal oxides (M_xO_y) or transition metal nitrides (M_xN_y) [35]. The only anode having larger theoretical capacity is that consisting of silicon i.e. 4200 mAh g^{-1} (that is the larger capacity value known at present). Nevertheless, the use of silicon as Li^+ intercalation material induces the 400% volume expansion under charging in a battery, which usually correspond to the anode pulverization and consequent shortening of the battery lifetime. Therefore, Si is usually employed just as additive, i.e. added in small amount to the carbon anode material. SiO_x is most often employed, which has a smaller volume expansion coefficient but a lower specific capacity (1500 mAh g^{-1}) [37]. Ultimately, Li metal stays as the best potential anode for the development at the short term of electric vehicles, where the energy storage will be presumably provided either by Li-sulfur (S) or Li-air batteries (Figure 1-4) [38].

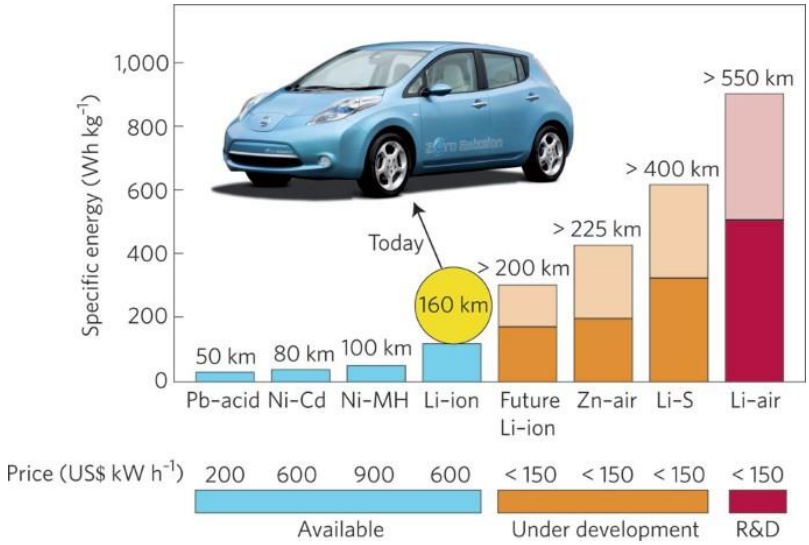


Figure 1-4. The actual energy density of various batteries, the corresponding electric vehicles cruising range and cost [38].

1.4.2 The electrochemical stability window of the electrolyte according to the frontier molecular orbital theory

The electrolyte, the ionic medium ensuring the transfer of ionic charge between the electrodes while blocking electrons, is a key component of electrochemical energy storage devices and its properties as conductivity and electrochemical stability greatly affect the energy capacity, rate performance, cyclability and safety of the battery.

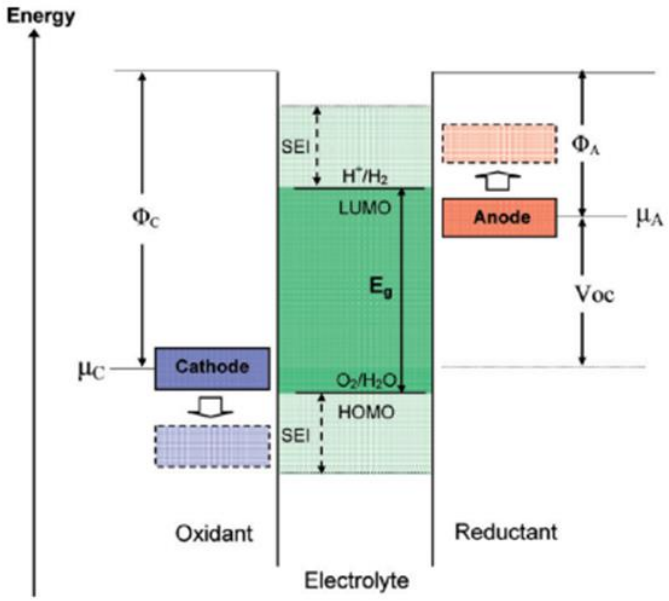


Figure 1-5. Schematic open-circuit energy diagram of an electrolyte: Φ_A and Φ_C are the anode and cathode work functions, E_g is the electrolyte's electrochemical stability window and μ_A and μ_C are the redox potential of the anode and cathode, respectively [39].

The electrochemical stability window of an electrolyte, i.e. the potential range between which it is neither oxidized nor reduced, is usually represented with the energy levels of the highest occupied and the lowest unoccupied molecular orbitals (HOMO and LUMO respectively) of the solvent molecules (Figure 1-5) [39,34]. At anode electrochemical potentials μ_A larger than LUMO, the electrolyte solvent is reduced and, at cathode electrochemical potentials μ_C lower than HOMO, the solvent is oxidized. In other words, the electrolyte is thermodynamically stable if the difference between the LUMO and HOMO energy levels, also noted E_g, is smaller than the open circuit voltage V_{oc} of the battery. This is the reason why the electromotive force of batteries using aqueous electrolytes is (theoretically) limited to 1.2V i.e. the difference between the redox potential of the H^+/H_2 and O_2/O^{2-} couples. It should be noted that, even when thermodynamically stable, sometimes the electrolyte can nevertheless degrade during the battery operation because of the occurring of overpotentials and/or modification of the system ohmic resistance with ageing.

Neglecting overpotentials and polarization resistance occurring under operation, the ability of a battery to store energy can be evaluated as the product between V_{oc} and the theoretical capacity Q_0 (Figure 1-6) [40]. The design of effective, stable electrolytes with large E_g, is then one of the key steps for developing new improved batteries [41,42]. Also, according to the Ohm law, the higher the voltage that the battery can withstand, the higher the current flow that can be applied, which determines the rate performance. Historically, the electrical potential of batteries has been increasing along with time (Figure 1-7) [43].

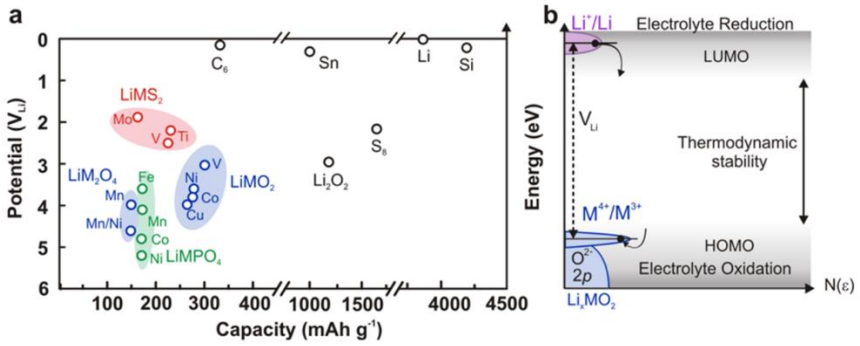


Figure 1-6. (a) Potentials and theoretical specific capacities of common cathode and anode materials and (b) differences between electron energy levels associated with electrode redox and the HOMO/LUMO levels of the electrolyte governing the thermodynamic stability and driving force to form the solid electrolyte interphase film (shaded areas represent the potential ranges for the electrolyte reduction and oxidation) [40].

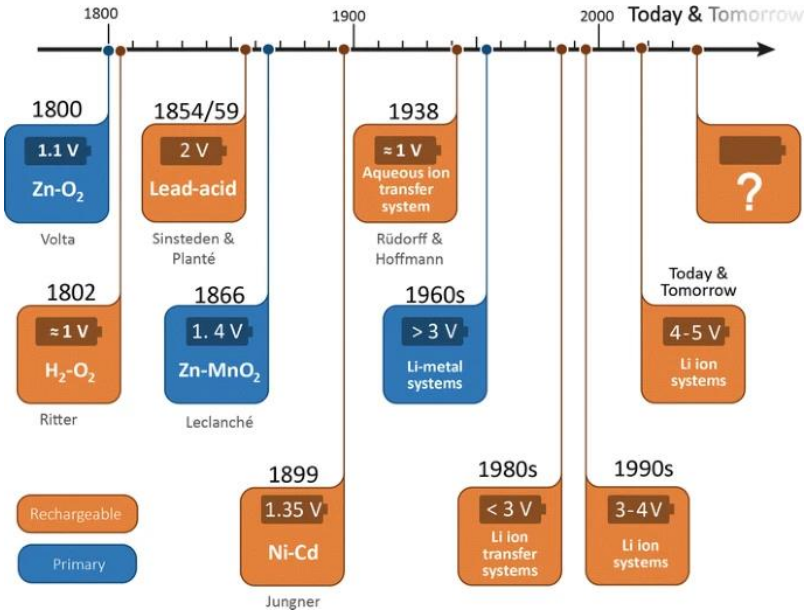


Figure 1-7. The potentials of typical batteries from 1800 until today [43].

Nowadays, Li-ion batteries exhibit the highest voltage. The forthcoming Li-metal system promises to further improve V_{oc} and, overall, the energy storing thanks to the lowest anode electrochemical potential (-3.04 V vs. SHE) and the ultrahigh specific capacity (3860 mAh g^{-1}). These batteries hold almost twice the energy of their widely used Li-ion counterparts and they are also lighter (0.534 g cm^{-3}) [44]. Nevertheless, the Li-metal technology is not yet ready for marketing because of the shorter lifetime compared to Li-ion, the reason for which is related to the way the electrolyte degrades during the electrochemical charge-discharge cycling.

1.4.3 The Solid Electrolyte Interphase (SEI) film

As illustrated in Figure 1-6b, the LUMO energy level of common organic electrolytes for Li based batteries is generally lower than the electrochemical potential of Li metal. This induces electron release from the anode and the consequent, spontaneous reduction of the electrolyte at the interface, forming a nanometer thick passivation film called SEI [45,46]. This phenomenon can occur even when the battery is at rest.

So far, although the SEI chemical composition has not been definitively characterized, it is generally accepted that the film exhibits a double-layer structure including both inorganic and organic compounds (Figure 1-7) [47]. The outer layer mainly consists of high oxidation state organometallic components such as lithium ester ($ROCO_2Li$), alkylide (RLi), ether (ROLi), polyolephines, etc. The inner layer is mainly composed of inorganic salts (LiF and Li_2CO_3), oxide Li_2O, hydroxide LiOH and lithium nitride (Li_3N). Different models have been proposed over time for the formation and structure

of the SEI film (Figure 1-8). The first widely accepted was the Peled model [48], where the film is assumed to form stepwise and, thus, exhibit some growing orientation.

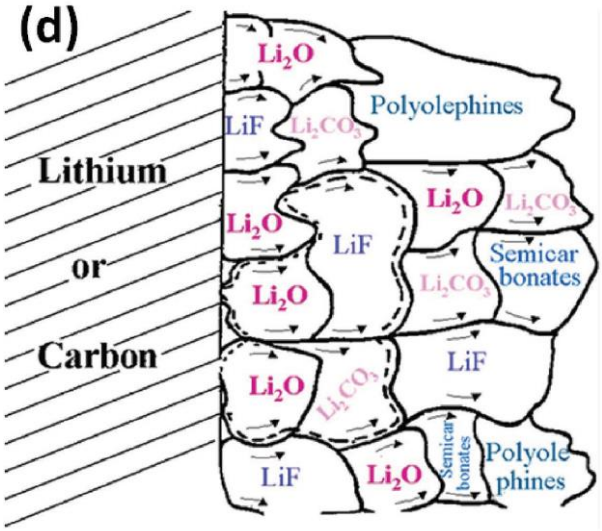


Figure 1-7. The schematic representation of the double layer structure of the SEI film [47].

The film shows an integral structure containing Schottky defects (vacancies) ensuring Li^+ transport. The mosaic model was then proposed in 1997 [49]. In this model, several compounds are formed simultaneously and their precipitation forms a mosaic of microphases. The Li^+ transfer across the film occurs along the boundaries between grains. A last main model is that of the Coulombic interaction mechanism [50], where the decomposition products are lined up with positively charged Li^+ as a "head" and partially positively charged carbons as a "foot", such as the film adhesion is insured, on the one hand, by the tendency of Li^+ to stay closer to the Li metal surface and, on the other, by the larger affinity of the organic moieties to the electrolyte.

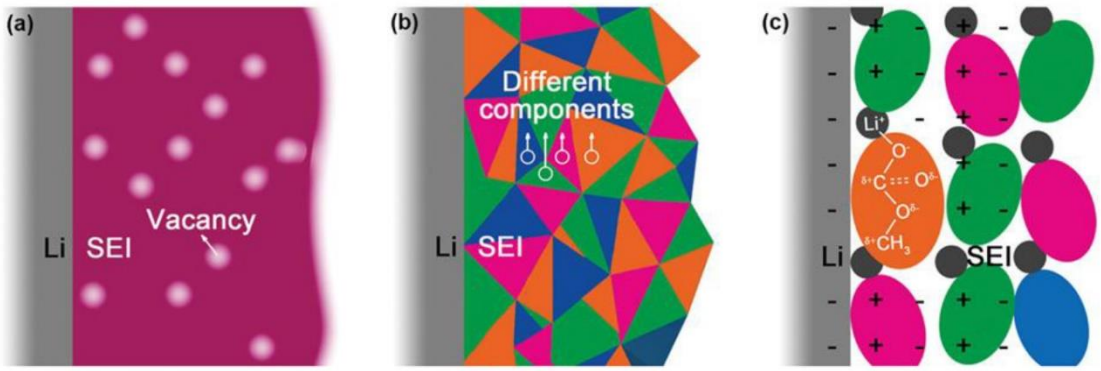


Figure 1-8. Some typical models of the SEI structures: (a) the Peled model, (b) the mosaic model and (c) the Coulombic interaction mechanism [51].

The formation of the SEI film has a crucial impact on the performance of the electrode. Depending on properties such as thickness, chemical and morphological stability, conductivity, etc., SEI can have both positive or negative effects on the battery performances. The SEI film is insoluble in organic solvents and it is ion (Li^+) conductor and electronic insulator. On the one hand, these properties allow to stabilize the electrode/electrolyte interface, limiting the electrolyte consumption by spontaneous degradation and avoiding damage to the electrode material [52]. This can greatly improve the cycling performance and lifetime of the battery.[1] On the other hand, when the thickness of the SEI increases excessively, it may become a passivation layer which hinders the electrochemical reaction at the electrode surface. Also, the irreversible formation of the SEI film implies the consumption of the Li^+ ions and solvent species constituting the electrolyte, what ultimately decreases the Coulombic efficiency (CE) of the battery and the charge/discharge efficiency of the electrode material.[2] A key aspect of the SEI film is the mechanical stability, since it strongly affects both the morphology and the chemical stability of the electrode/electrolyte interface. Over the battery charge and discharge cycles, SEI is submitted to increasing tensile stress due to the volume change of the electroplated Li metal phase (Figure 1-9). Thus, depending on its brittleness and fragility, SEI will response to stress by breaking. Li metal is then exposed again to the electrolyte and the spontaneous consumption of Li salts and solvents restarts with the further growing of the SEI layer [56]. Further, local surface heterogeneities and stresses induce uneven Li electroplating during the battery operation, resulting in the metal surface morphological instability and the deposition of Li protrusions called “dendrites”, whose form (needle-like, mossy or fractal) will depend on the electrolyte composition and the electrochemical conditions [57]. Dendrites, due to their danger for the battery integrity, represent a main issue to solve for the development of the Li-metal system.

[1] For example, LiF, one of the components usually observed in SEIs, has a large energy bandgap of 13.6 eV which confers high electrochemically stability towards both Li metal and high-voltage cathodes. So LiF is currently used as material for artificial SEI films added before the battery assembly or formed *in situ* to protect the anode [53,54].

[2] In industry, this issue is evaded by a preprocessing called formation, in which a very small current is applied to form stable and high qualitied SEI film before the batteries leave the factory [55].

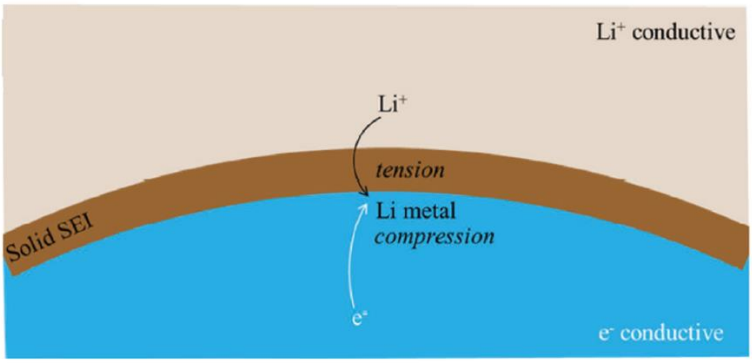


Figure 1-9. Schematic illustration of the SEI film interfacial stress during Li electroplating (as reported by [56]).

Briefly, the SEI is a thin film with a complex and heterogeneous sub-structure. Its formation and properties, essential for both battery performance and durability, largely depend on the electrolyte conception, the last being then a hot topic of research especially for the development of Li-metal systems using the highest potential anode.

1.4.4 The Li-metal anode: main issues and mitigation strategies

Figure 1-10 summarizes, according to Lin *et al.* [58], the relationships existing with main issues related to the Li stripping-plating process, the common point of the different phenomena being the fracture of the SEI film. As previously discussed, the SEI breaking triggers, on the one hand, electrolyte side reactions and, on the other, dendritic deposition. Both phenomena lead concomitantly to the decrease of the CE and, in the extreme case, to the system failing by internal short-circuit [58,54].

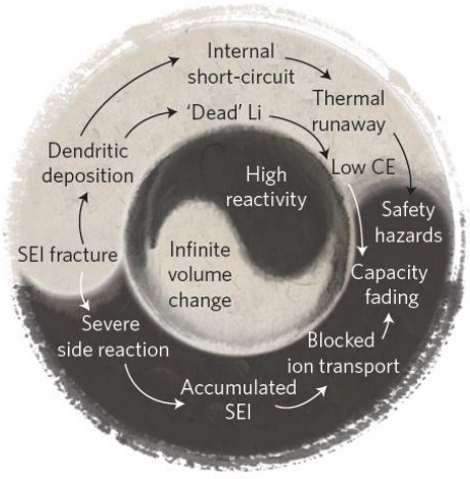


Figure 1-10. Correlations between the Li-metal battery issues [58].

Differently from carbon anode materials, intercalating and de-intercalating Li^+ in their host structure, the Li-metal anode has unpredictable volume expansion during the

electrochemical cycling.[3] This favors the rupture of the SEI film. Consequently, the morphology of electrodeposited Li metal during the continuous deposition-stripping process becomes particularly difficult to control. The growing of Li dendrites (an example is reported in Figure 1-11) is then a main issue since enhanced by the heterogeneity of the deposition substrate (which can be the surfaces of the metal anode, of the current collectors or of the SEI film). Indeed, rough surfaces correspond to uneven charge distribution, inducing Li^+ concentration gradients in the electrolyte i.e. larger ion fluxes towards the substrate locations corresponding to tips or spikes where Li deposits more rapidly with a protruding morphology (Figure 1-11a). The newly formed Li dendrites make the surface of the substrate rougher, which further enhance the accumulation of new dendrites, and so forth. More and more sharp Li dendrites grow, becoming more and more brittle. Under stripping, they can break apart from the substrate and definitively lose the electrical contact (Figure 1-11b). The formation of the so-called "dead Li", since no longer able to participate to the battery charge-discharge cycling, is one of the main phenomena inducing the decreasing of both CE and lifetime of the battery. Concurrently, other Li dendrites continue to grow up until they pierce the separator, causing the battery short-circuit and the consequent safety hazards which led in 1989 to the withdrawal from the market of the first Li-metal batteries [53].

After first commercial Li metal battery caught fire, intensive research has been devoted to the understanding of Li dendrites formation mechanisms. Generally speaking, the dendritic-like growth is a long-range limited diffusion phenomenon (Figure 1-12) [60]. During the electroplating process, Li^+ species are reduced at the electrode surface so that their local concentration results from the rate of their consumption (depending on current) and their diffusion mobility in the electrolyte. When current exceeds diffusion limitation, the Li^+ concentration at the electrode surface decreases to zero at a characteristic time, called "Sand's time" [60], and uniform electroplating becomes

[3] Most of electrode materials undergo volume change during operation. Commercial Li^+ intercalation electrodes such as carbon anodes exhibit a volume change of ~10%. Si-based anodes have a volume change of ~400% for Si. The relative volume change of a Li anode is virtually infinite, owing to its hostless nature. For an electrode whose capacity needs to reach 3 mAh cm^{-2}, as dictated by actual commercial criteria, this corresponds to the deposition under discharge of 14.6 μm of metallic Li. When dealing with future higher energy density battery systems, the anode thickness change could correspond to several tens of μm, which implies a great challenge for the stability of the SEI film.

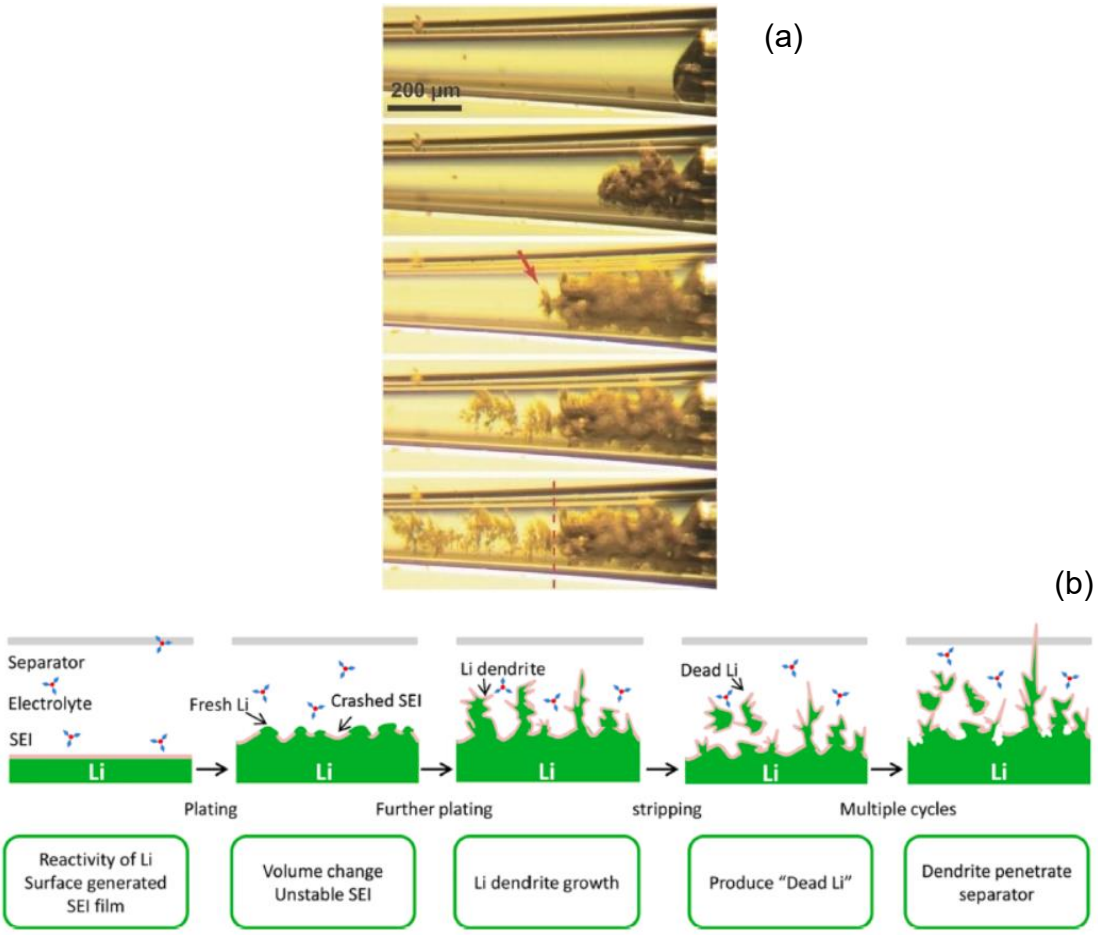


Figure 1-11. (a) *In situ* optical images of Li electrodeposition in a glass capillary filled with an electrolyte solution containing $LiPF_6$ (the chronological order is from top to bottom) [59]: red arrow points to the emergence of dendritic Li from the initial mossy-like deposit. (b) Schematic representation of the chemical and morphological behavior of the electrolyte/Li-metal anode interface under the plating-stripping process [54].

unstable. The scarce supply of cations preferentially deposits onto surface protrusions, leading to a self-amplifying process of dendritic growth.

Pioneering work of Aogak [62], Bruce [63], Chazalviel [64] and their co-workers allowed to establish first relationships between physical parameters like current density, ion concentration, etc. and the morphology of metallic electrodeposits. More recent work of Cui and co-workers approached the problem of Li nucleation and growth using classical nucleation theory as a starting point and exploiting relationships with the overpotential of the reduction reaction [65,61]. The nucleation of a new solid phase has an associated free energy barrier related to the thermodynamic costs of forming a critical cluster of atoms (Figure 1-13a). For electroplating, this nucleation barrier can be adjusted by tuning the overpotential η of the reduction reaction. Main contributions to the driving force for the electro-crystallization process are the nucleation (η_n) and the

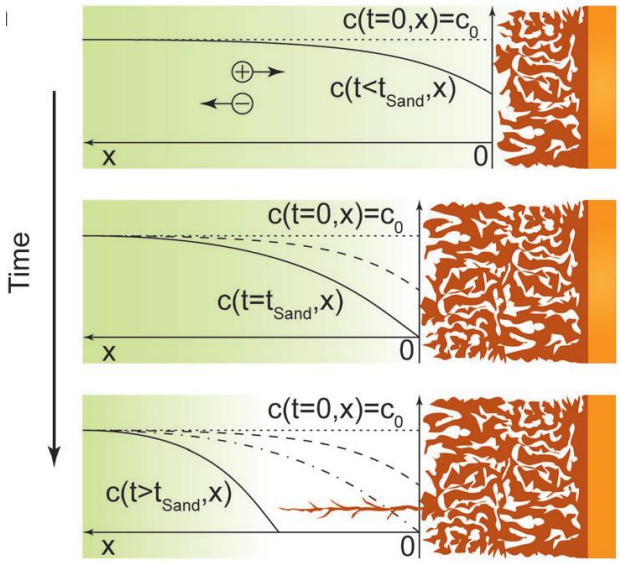


Figure 1-12. Theoretical interpretation of the Li growth mechanism during concentration polarization [60].

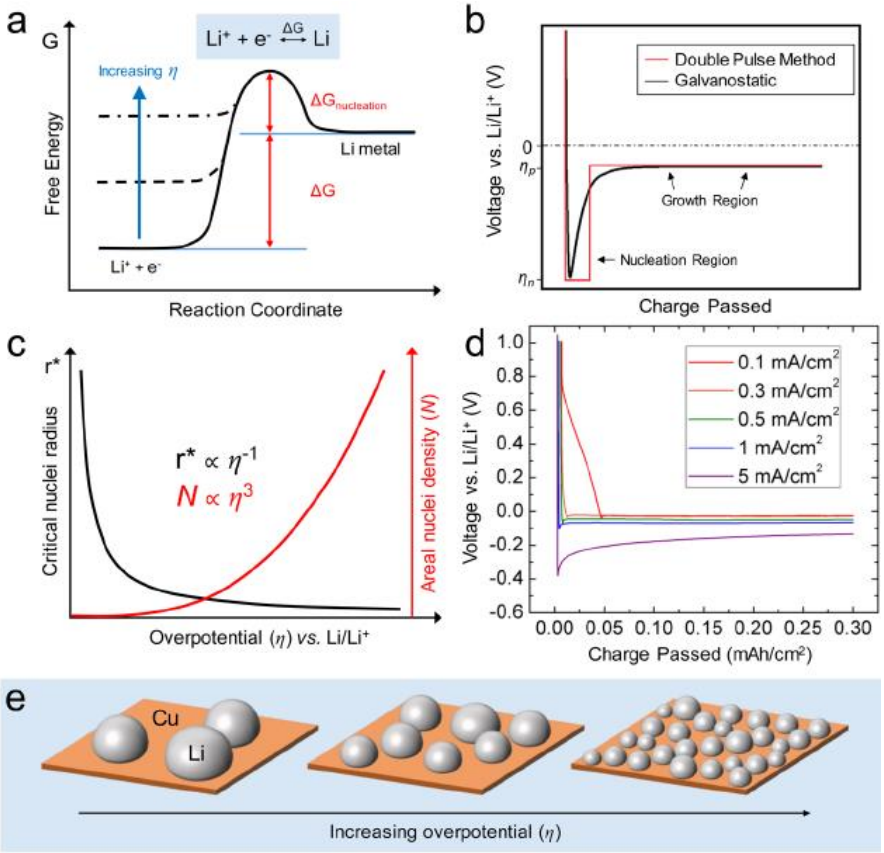


Figure 1-13. Illustration of fundamentals of Li dendrite nucleation and growth: (a) free energy schematic showing the effect of overpotential on the energy barrier for nucleation; (b) Li deposition voltage curves comparing typical galvanostatic (black) and dual voltage pulses (red); (c) schematic evolution of the critical nuclei radius and areal nuclei density with the overpotential of Li deposition; (d) voltage profiles of Li deposition on Cu foil with different current densities; (e) schematic evolution of the size and density of Li nuclei deposited at different overpotentials [61].

plateau (η_p) overpotentials, corresponding respectively to the voltage spike at the onset of Li deposition and the voltage plateau at which Li growth continues (Figure 1-13b). Actually, at the start of the Li deposition process, the potential of the working electrode drops below 0 V vs Li/Li^+ to $-\eta_n$ i.e. the electrochemical overpotential needed for triggering the nucleation of Li embryos. After, since the addition of a Li adatom to an existing Li nucleus needs lower energy, the overpotential rises to $-\eta_p$ during the following Li nuclei growth step. Classical equations for homogeneous nucleation show then that the obtained nuclei size is inversely proportional to overpotential while the areal nuclei density is proportional to η^3 (Figure 1-13c) [61]. When considering that both nucleation barrier and steady Li growth overpotentials increase with current density (Figure 1-13d), it follows that the formation of several small nuclei with high areal density, i.e. dendrites, is favored at the high currents which have to be supplied by improved batteries. Since the work of Cui and his co-workers [66,65,61], a large number of studies has been devoted to the development of methods and materials aiming to decrease the Li nucleation overpotential, so as to promote the lithiophilicity of the deposition substrate and obtain uniform Li plating.

The different strategies developed over the years to deal with the issues affecting the Li deposition can be resumed according to three main approaches (Figure 1-14) [58] : (i) electrolyte engineering, (ii) interface engineering and (iii) use of stable host materials for minimizing Li volume change.

The *electrolyte engineering* (Figure 1-14a) approach usually consists in improving the liquid electrolyte by adjusting or modifying the composition with additives, so as to modify the physico-chemical properties of the SEI and obtain relatively uniform Li-metal deposition/dissolution. The route of developing solid-state electrolytes, forming a physical obstacle to the dendrite propagation and preventing side reactions, has also been explored (since the last century) but with limited results so far. Solid-state electrolyte can be both inorganic (Li-ion conductive ceramics such as sulfides, oxides, nitrides and phosphates) or organic media blending Li salts and polymers. The main issue is that such solid electrolytes exhibit lower Li^+ conductivity and poorer interfacial properties limiting the battery charge/discharge rate performances [67]. As far as the development of improved electrolytes by using reactive additives is concerned, fluorine-containing compounds have been more extensively investigated. The term “reactive” refers to the decomposition, polymerization or adsorption of the additive on the Li surface so that to affect the composition and morphology of the SEI and regulate

the current distribution during the Li plating. Trace amounts (a few ppm) of hydrogen fluoride (HF) and water added to carbonate electrolytes promotes the growth of dense and uniform lithium fluoride (LiF) and lithium oxide (Li_2O) bilayer films on the Li

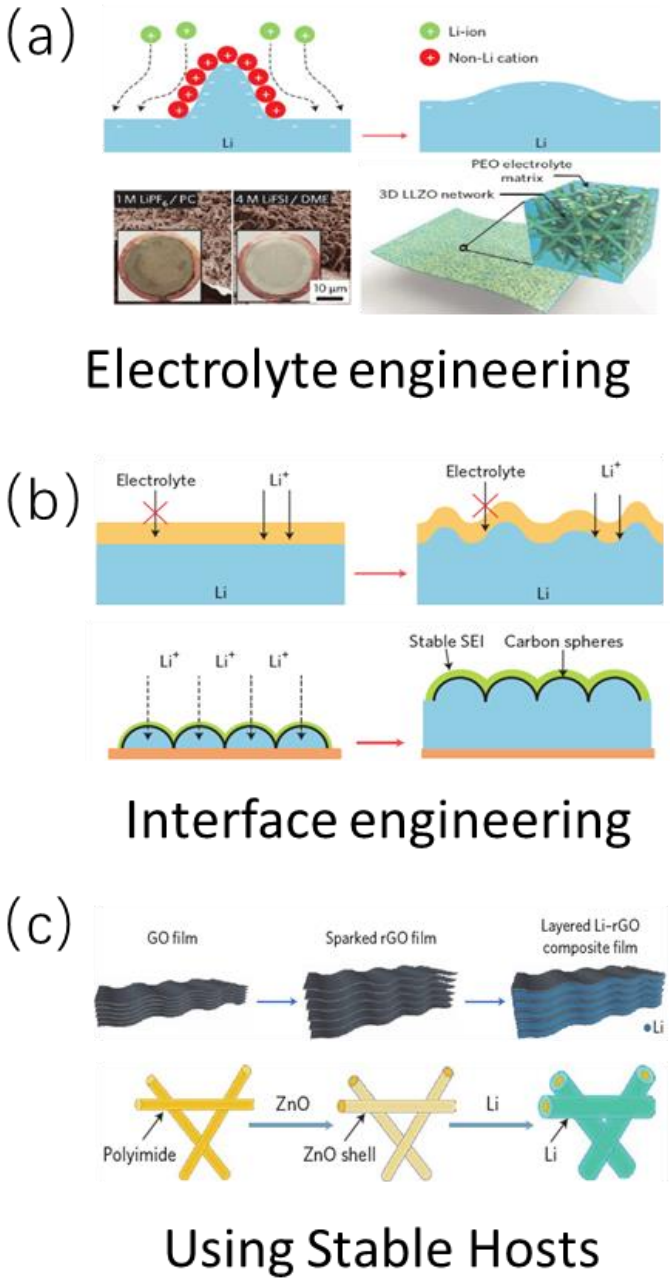


Figure 1-14. Examples of the 3 routes explored to solve the issue of the Li metal deposition morphology: (a) electrolyte engineering, consisting either in adding additives (top), increasing Li salt concentration (left bottom) or developing solid-state Li^+ conductors (right bottom); (b) interface engineering, modifying the electrode surface with artificial SEI (top) or carbon spheres scaffold (bottom); (c) the use of stable hosts for the Li deposition lie reduced graphene oxide films (top) or core–shell PI–ZnO network (down) [58].

surface [68]. Fluoroethylene carbonate (FEC) aids the formation of more homogeneous, softer and thinner SEI films which inhibit the dendrites growth and aid Li^+ transport, so finally improving the Coulombic efficiency [69].

A few non-fluorinated compounds are also used as additives. For example, $LiNO_3$ combined with Li_2S and Li_2S_2 in ether electrolytes allows Li plating with pancake-shaped morphology without dendrites, so improving the Li-metal battery cycling stability at high current density [70]. Xiao and her co-workers [71] developed a self-healing electrostatic shielding mechanism to regulate the Li deposition by adding Rb^+ and Cs^+ (further details about this method are given in section 1.5.1).

A last approach belonging to the framework of the liquid electrolyte engineering consists in developing improved electrodes with larger Li^+ concentration. An elevated concentrations of Li^+ ions mitigates the side reactions consuming the organic solvents and increases the Sand's time i.e. the delay for the appearance of dendrites [72]. A new class of electrolytes called high-concentration electrolytes (HCE) has then been developed, subsequently improved as localized high-concentration electrolytes (LHCE). HCE and LHCE will be presented and discussed more in detail in sections 1.5.2 and 1.5.3 respectively.

The stabilization of the Li anode by *interface engineering* (Figure 1-14b) consists either in the synthesis of artificial, homogeneous and robust SEI films before cycling, acting as protective layers, or in the nano-scale modification of the Li metal surface to stabilize the *in situ* formed SEI film, increase the surface lithiophilicity and homogenize the Li^+ flux. As an example of artificial SEI, we can cite lithium phosphate (Li_3PO_4) which, deposited as thin (~50 nm) film on Li metal, improve the Li^+ conductivity and Young's modulus of the interfacial solid layer so that Li anode still exhibits a smooth and compact surface after 200 plating-stripping cycles [73]. Effective nano-scale modification is reported by Zheng and co-workers [74] by simply chemically polishing the electrode surface with a tetrahydrofuran solution of naphthalene which removes the Li_2O, LiOH and Li_2CO_3 surface species of the original Li foil. This allows the formation of a uniform SEI film at the first discharge process, improving the interfacial chemistry and the electrochemical performances.

Nano-scale modification often relies on using chemically and mechanically stable scaffolds to reinforce the SEI formed during electrochemical cycling. For example, coating the Li-metal anode with a monolayer of flexible, interconnected, hollow amorphous carbon nanospheres helps isolate the Li metal deposit and facilitates the

formation of a stable solid electrolyte interphase [75]. The SEI forms on top of the scaffold and the two move together so as to accommodate the volumetric change of the Li deposition process and to avoid cracks. Simultaneously, Li-ions can pass freely through the scaffold such that deposition can take place underneath without forming dendrites. Another approach of nano-scale modification consists in increasing the effective surface area of the electrode by manipulating the morphology of the metal current collector, so as to dissipate local current densities inducing spatial inhomogeneity of the Li-ion distribution in the electrolyte (see for example the 3D porous current collectors developed by Yang et al. [76]).

Later developed approach, the *use of stable materials hosting Li deposition* also allows to minimize Li volume change and avoid dendrites (Figure 1-14c). Effective lithiophilicity is a prerequisite for such materials. Cui and co-workers first designed a layered host consisting of reduced graphene oxide (rGO) [66]. The corresponding Li–rGO electrode, obtained via molten Li infusion into the pristine rGO, exhibits uniform periodic stacking of nanoscale layered Li and rGO and represents a stable scaffold for Li stripping/plating. The anode has excellent flexibility and a small electrode dimensional change (~20%) during cycling. In the same year, the authors used ZnO coating to enhance lithiophilic ability, thus molten Li can be drawn into the PI-ZnO core-shell to form nano-porous Li electrode. A further example of 3D host materials comes from Ren et al. [77] which have developed vertical graphene nanowall structures conferring uniform Li plating/stripping to the electrode surface even at a 50% depth of discharge together with a CE attaining ~97% even in the corrosive carbonate-based electrolytes.

Concluding, the different strategies presented above, aiming to improve the morphological and chemical stability of the Li metal/electrolyte interface, have all their advantages and weaknesses. It should be noted that the interface engineering approach and that using stable hosts both involve adding non-active materials (sometimes noble metals), which decreases the mass and volume energy density of the battery and increase costs. Thus, the electrolyte engineering way appears to us a more practical and effective approach to address the issues of the Li-metal battery. The following section reviews the state-of-art of liquid electrolytes for high-energy-density Li-metal batteries.

1.5 Liquid electrolytes for Li-metal batteries

The role of the electrolyte is to ensure the transport of ionic species between cathode

and anode, while blocking electrons. Traditional batteries, as for example lead-acid or nickel-metal hydride systems, use aqueous electrolytes consisting of salt, acid or basic solutions whose decomposition voltage is set by water at the theoretical value of 1.23 V [78]. In practice, the overpotential of hydrogen or oxygen can widen the electrochemical stability window up to 2 V, as for the lead-acid batteries [79]. But, as previously mentioned, the operating voltage of Li-based batteries is usually as high as 3 to 4.2 V, so that aprotic solvents have to be used for the electrolyte. Liquid electrolytes for Li-metal batteries usually consist of Li salts dissolved in organic solvents with additives.

The choice of the electrolyte has a great influence on the performance of Li-based batteries. In general, an electrolyte needs to meet several criteria concurrently: chemical stability, especially under high potential and high temperature environment, have wide electrochemical window, high ionic conductivity (>10^{-3} S cm^{-1}), and be inert towards the cathode and anode materials [80].

1.5.1 Salts, solvents, and additives

A suitable Li salt should have good solubility in organic solvents and chemical inertness towards them , high stability in several conditions (e.g. moisture, heat), nontoxicity and low price [81]. Figure 1-15 reports most commonly used Li salts and Table 1-1 qualitatively compares their properties.

In the 1970s and 1980s, early research on Li batteries involved Li-salts consisting of the anions hexafluoroarsenate (AsF_6^-), perchlorate (ClO_4^-), hexafluorophosphate (PF_6^-), tetrafluoroborate (BF_4^-), trifluoromethanesulfonate ($CF_3SO_3^-$) and triflate (Tf). Because of safety and toxicity concerns, $LiAsF_6$ and $LiClO_4$ were ruled out for commercial cells. The low conductivities of LiTf electrolytes made also this salt less popular. Then, with the commercialization of graphite anodes, $LiPF_6$ and $LiBF_4$ became the most common Li-salts, also because they formed stable SEI on graphite when combined with solvents like ethylene carbonate (EC), making rechargeable Li batteries commercially practicable. After, in order to further improve thermal stability and ionic conductivity, other salts inspired by $LiPF_6$ and $LiBF_4$ have been synthesized in recent years. On the one hand, anions made up of ligands arranged around a central atom (e.g. PF_6^-, ClO_4^-) have evolved in large complex anions like bis(trifluoromethanesulfonyl)imide ($TFSI^-$) or organic ligand-based anions like bis(oxalate)borate (BOB^-). On the other hand, inspired to the structure of LiTf, other Li salts such as bis(fluorosulfonyl)imide (FSI^-),

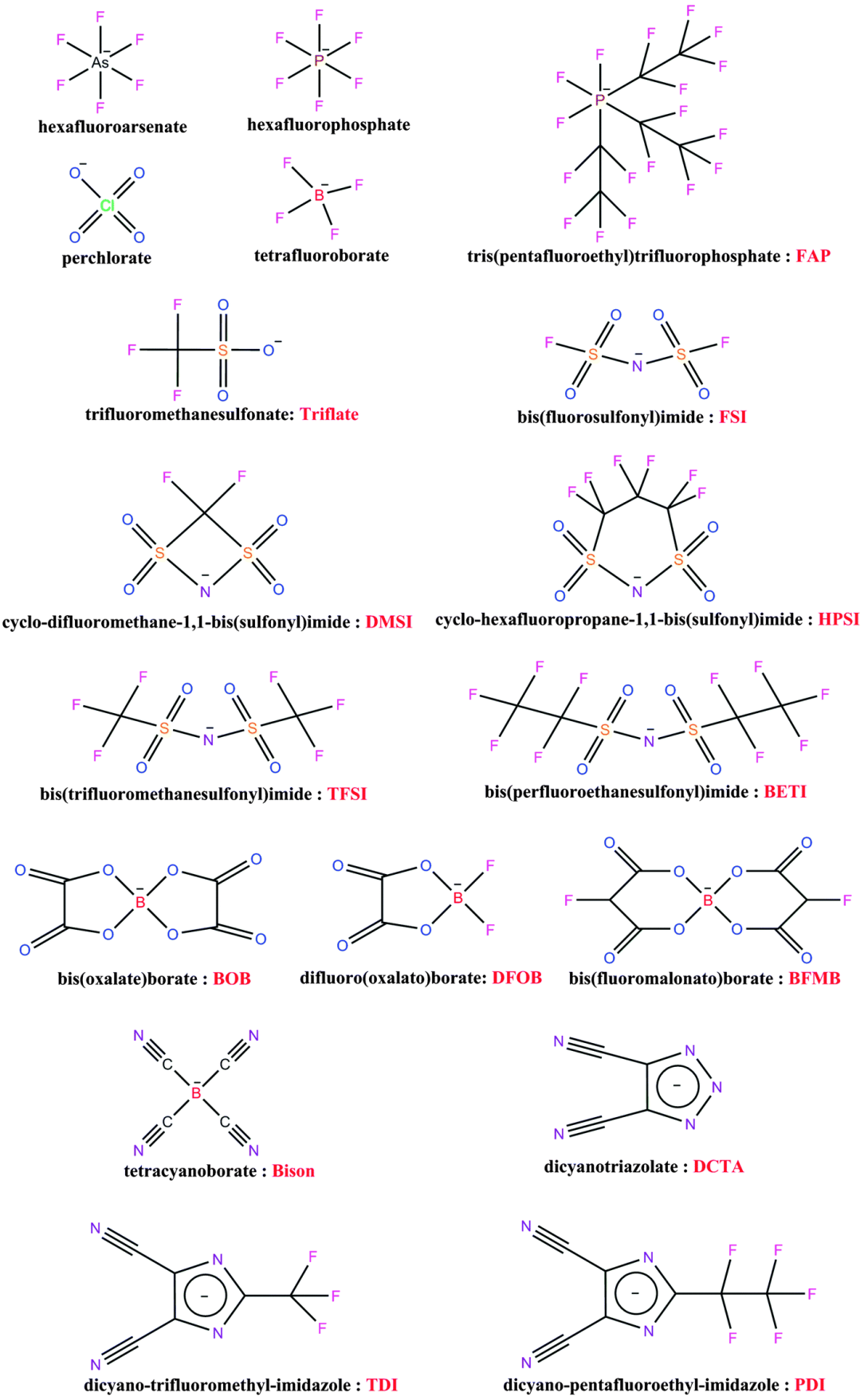


Figure 1-15. Chemical structure of anions of common Li salts [82].

Table 1-1. Properties of common Li salts for Li-based batteries [85,82],

	$LiPF_6$	$LiBF_4$	$LiAsF_6$	$LiClO_4$	LiTFSI
Ionic conductivity	+	o	+	+	+
Electrochemical stability	+	o	+	+	+
Thermal stability	_	o	+	_	+
Humidity stability	_	o	o	o	+
Al passivation	+	+	+	o	_
Nontoxicity	_	_	_	_	_
Safety	_	_	_	_	+
Inexpensiveness	o	_	_	+	_

+ = good/high, o = medium, – = poor/low

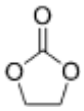
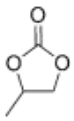
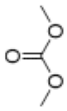
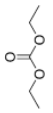
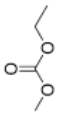
$TFSI^-$, and bis(perfluoroethanesulfonyl)imide ($BETI^-$ or $PFSI^-$) have also been developed.

Nevertheless, $LiPF_6$ still remains the most common salt in commercial batteries [83] since representing the best compromise between the different required properties (Table 1-1), including the ability to form suitable SEI films on the commercial graphite anodes and a protective layer on the aluminum cathode current collector [84].

Table 1-2 reports most commonly used solvents. As for salts, organic solvent for Li-based batteries should have high electrochemical and thermal stability, chemical inertness to all cell components materials, nontoxicity and ability of forming suitable SEI films [86]. Moreover, they should also exhibit good solvation ability towards Li salts and low viscosity, the later to ensure adequate ion diffusion rate. Current electrolyte solvents are typically made up of a binary mixture of cyclic and aliphatic carbonates: ethylene (EC) or propylene carbonate (PC) with high dielectric constants (to allow high concentration of the dissolved Li salt) with linear species such as dimethyl (DMC), diethyl (DEC) and ethyl methyl carbonates (EMC), having low viscosities.

Often, additives are added to improve some properties of the electrolyte as conductivity, viscosity, wettability and others. An additive is, in principle, an organic or inorganic substance which does not directly participate to the battery electrochemical capacity

Table 1-2. Properties of common solvents for Li-based batteries [85].

	EC	PC	DMC	DEC	EMC
Structure					
Dielectric constant	+	+	–	–	–
Viscosity	+	+	–	–	–
Melting temperature	+	–	o	–	–
Boiling temperature	+	+	–	–	–
Flash point	+	+	–	–	–
Volatility	–	–	+	+	+
Contribution to SEI	+	–	–	–	–
Anodic stability	+	+	o	o	o
Safety	+	o	–	–	–

+ = good/high, o = medium, – = poor/low

and is added in a minority amount, i.e. not larger than 10 % in mass or volume content. On the whole, additives are currently used as safety protection agents, i.e. as overcharge protectors and fire retardants, or as SEI forming improvers strengthening the interface layer and promoting more uniform Li deposition [87].

Typically, Zhang et al. [71] developed a self-healing electrostatic shielding method protecting the Li anode from dendrites overgrowth, based on the addition of cesium (Cs^+) and rubidium (Rb^+) ions to the electrolyte. Since these species have an effective reduction potential less than that of Li^+, they are not reduced and thus collect around the nascent Li dendrite inducing a positively charged shield that repel incoming Li^+ and, thus, hinders further Li plating at the tip (Figure 1-16). The self-amplifying process of dendritic growth is then inhibited, the Li deposition carries on at adjacent regions and a smooth plating layer is formed.

1.5.2 High-concentration electrolytes (HCE)

Insofar as the morphology of the Li plating depends on the Li^+ concentration gradients occurring in the liquid phase, a way beyond using additives to prevent dendrites

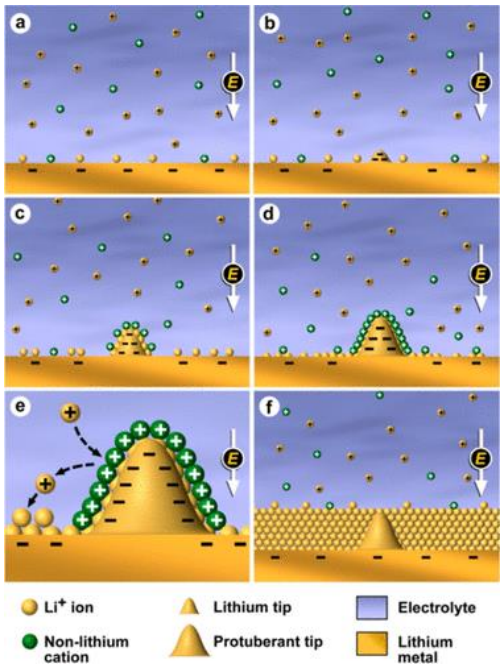


Figure 1-16. Illustration of Li deposition process based on self-healing electrostatic shielding mechanism [71]: (a) initial stage of deposition (both Li and additive cations are adsorbed on the Li metal surface, (b) beginning of the Li dendrite formation, (c) around accumulation of the non-reduced additive cations, (d) formation of the electrostatic shield, (e) repulsion of Li^+ cations and (f) formation of a smooth deposition layer.

generation is to increase the concentration of the Li salt in the electrolyte. According to the Sand's time model, the characteristic time τ (called Sand's time), after which the scarce supply of cations preferentially deposits onto surface protrusions, is proportional to the initial concentration C_0 (mol m^{-3}) of the Li salt solution (Equation 1-6) [64,88]:

$$\tau = \pi D e^2 \left(1 + {}^{\mu_c}/_{\mu_a}\right)^2 C_0{}^2/4J^2 \qquad \text{Equation 1-6}$$

where D (m^2 s^{-1}) is the ambipolar diffusion coefficient,[4] *e* the electronic charge, μ_a and μ_c (m^2 s^{-1} V^{-1}) the mobilities of the Li^+ cation and its counter-anion respectively, and J (A m^{-2}) the electric electrode current density. Thus, the apparition of the dendrite morphology during Li deposition can, in principle, be sensibly delayed by increasing the Li^+ concentration in the organic liquid phase.

The first use of a high-concentration electrolytes (HCEs) is probably reported by Dahn et al. [89] in 1985 (Figure 1-17). In that case, a saturated $LiAsF_6$ solution in PC was

[4] $D = \frac{\mu_a D_c + \mu_c D_a}{\mu_a + \mu_c}$, where D_c and D_a are the diffusion coefficient of the Li^+ cation and its counter-anion respectively.

used to prevent the co-intercalation of PC with Li^+ into the ZrS_2 cathode. Since then, and more particularly in the last 10 years, HCEs have been brought into great focus for protecting Li-metal batteries [90]. Indeed, besides reducing Li dendrites, they bring other several benefits such as wider electrochemical window, excellent rate capability, good anode stability, resistance of Al current collector corrosion, good safety. Nevertheless, HCEs have two main drawbacks: (i) excessive viscosity, resulting in poor ionic conductivity and poor wetting ability towards separators, (ii) their use increase noticeably the final cost of the battery (the cost of the Li salt is higher than that of most other components) [91].

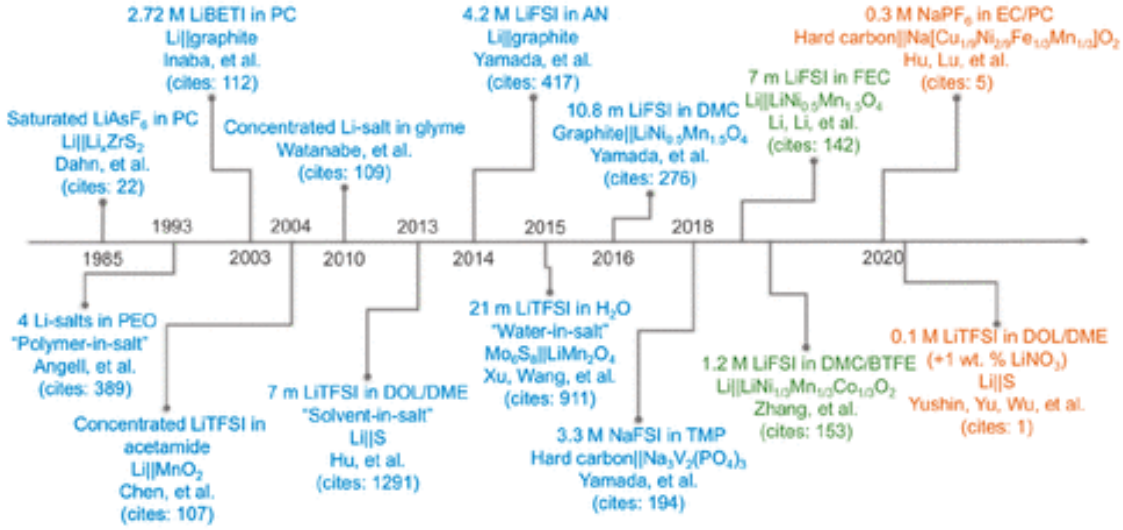


Figure 1-17. Chronology of representative research work on high-concentration electrolytes for Li-based batteries (see [89] and references therein).

The different properties, strengths and drawbacks, of HCEs are related with the solvation structure. As shown in Figure 1-18, in low-concentration electrolyte, Li^+ species are separated from the counter-ion, completely surrounded by solvent molecules (~ 4) and dispersed in the organic medium. They constitute the so-called "solvent-separated ion pair" (SSIP). The electrolyte mainly consists of free solvent molecules screening the coulombic interaction between Li^+ and free anions. Differently, HCEs contain almost no free solvent molecules. Furthermore, due to the strong increase of Li salt, solvent molecules alone cannot fully occupy the solvation structure of Li^+, which induces the salt anion to enter it giving rise to "contact ion pair" (CIP) structures and ionic aggregates (AGGs), where one anion can interact with several Li^+.

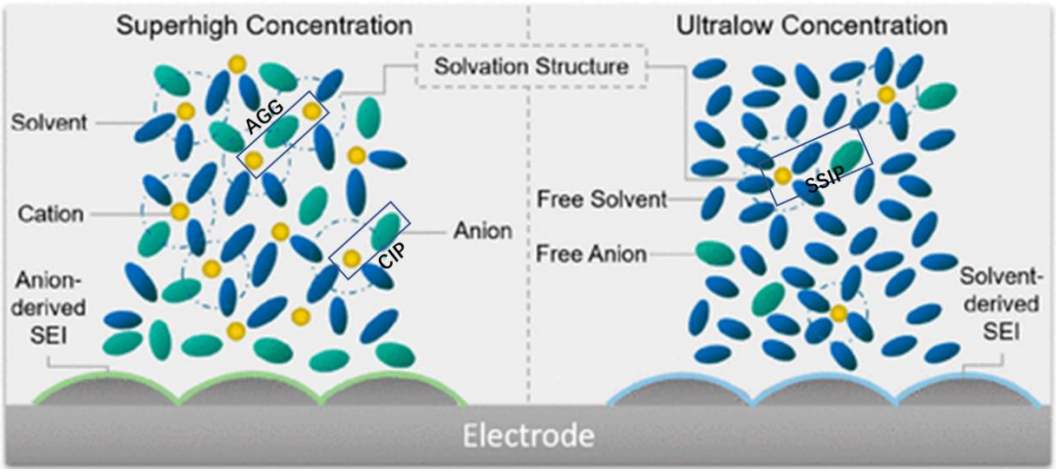


Figure 1-18. Solvation and interfacial structures of high- and low-concentration electrolytes (reported by [89]).

The change of the solvation structure from SSIPs in conventional, diluted electrolytes to CIPs and AGGs in HCEs, corresponds to the change of the relative energies of the HOMO and LUMO molecular orbitals of the solvent and anion species. In a dilute electrolyte, due to the stable solvation structure around the Li^+ ion involving a consistent amount of solvent species, the LUMO is located on the solvent molecules. In highly concentrated electrolytes, Li^+ ions have lower solvent coordination and a significant proportion of anions exist as AGGs or CIPs with strong coulombic interactions with multiple Li^+ cations (Figure 12b). Therefore, the LUMO shifts from the solvent to the anion. As a consequence, while SEI films arising from conventional electrolytes mainly result from the degradation of free solvent molecules, in HCEs the anions of the Li salt decompose first to form inorganic rich SEI, containing for example LiF, generally more stable and robust against cycling. The improved thermodynamic stability of the solvent species is also the reason for the larger electrochemical window and the larger thermal stability of the HCE [92,93]. Furthermore, the stronger coordination of the anions to Li^+ allows to reduce the corrosion of the Al components of the battery by decreasing the availability of reactive for the formation of the $[Al(anion)_x]^{(3-x)+}$ specie [94].

1.5.3 Localized high-concentration electrolytes

Although HCEs have several benefits, their commercial development is still hindered by the main drawbacks of the low viscosity and high cost. To overcome these shortcomings, localized high-concentration electrolyte (LHCEs) has been recently developed [95]. LHCEs are obtained from HCEs by addition of a diluent, generally a

fluorinated ether miscible with the solvent but unable to dissolve the Li salt, which reduces the overall concentration and viscosity but retain the highly concentrated salt-solvent clusters (CIP and AGG structures) of the HCE at the local environment (Figure 1-19a). As for HCE, no free solvent molecules occur in LHCEs, which allow to approach the safety and stability performances of the former (Figure 1-19b). Nevertheless, the 3D network of AGGs is broken by the intrusion of diluent molecules so that ionic conductivity stays lower than that of diluted electrolytes [96,97].

A limited number of work has been reported about LHCEs up to now [95]. In 2019, Zhang and co-workers [98] developed an locally highly concentrated electrolyte consisting of 5.5 M LiFSI/DMC diluted by bis(2,2,2-trifluoroethyl) ether (BTFE). In the same year, Liu and co-workers [99] employed 1,1,1,3,3,3-hexafluoroisopropyl methyl ether (HFPM) as diluent for 3 M $LiPF_6$ in DMC:FEC:HFPM (6/1/3 by vol.). Current research lacks of systemic experimental study addressing relationships between the electrochemical properties and stability of LHCEs and the evolution of the local solvation structure with the nature and relative amount of the different components (salt, solvent and diluent). The chapter 3 of this manuscript is specifically devoted to this subject matter.

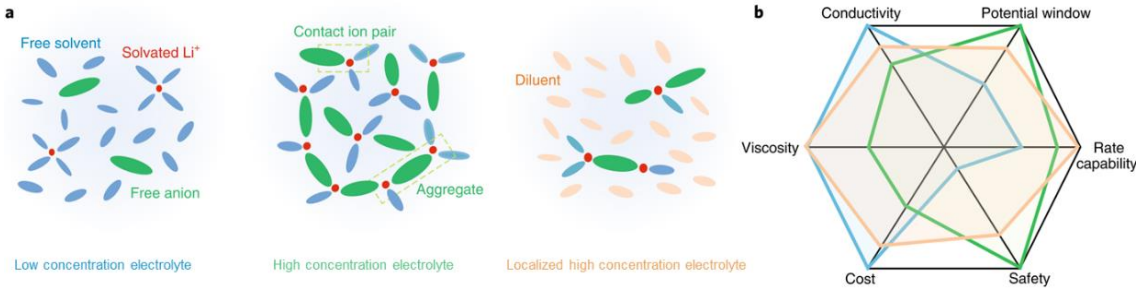


Figure 1-19. (a) Solvation structures and (b) properties of low, high and localized high-concentration electrolytes [95].

1.6 Characterization methods of electrolytes for Li-metal batteries

When dealing with the electrolyte, characterization techniques are mostly devoted to the study of the SEI film resulting from its degradation and the Li deposit, rather than of the electrolyte itself. Basic techniques like atomic force, scanning and transmission electron microscopies (AFM, SEM and TEM) allow to gain information about the Li deposit morphology. Fourier-transform infrared spectroscopy (FTIR), X-ray photoelectron spectroscopy (XPS) and surface-enhanced Raman spectroscopy (SERS) are usually employed to investigate the chemical composition of the SEI film.

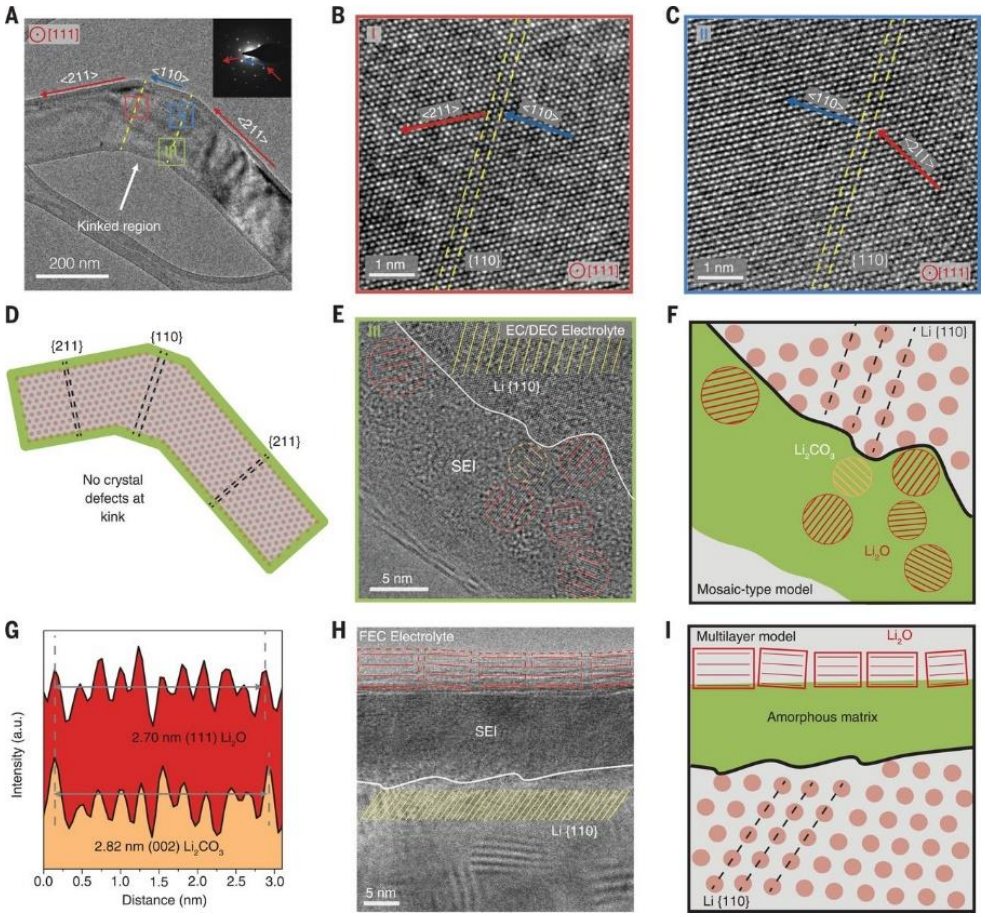


Figure 1-20. Cryo-TEM analysis of Li dendrites and SEI film formed by the electrolyte 1.0 M LiPF6 in 1:1 w/w ethylene carbonate/diethyl carbonate [100]. (a) TEM image of kinked Li metal dendrite that changes from a <211> to <110> and back to <211> growth direction. The dashed yellow lines indicate change in growth direction. (b,c) Magnified images of red and blue regions outlined in (a). (d) Schematic of the single-crystalline nature of the kink. (e) Atomic-resolution image of green region outlined in (a) showing the interface between Li metal and the SEI. The lattice spacings of small crystalline grains of inorganic material dispersed throughout the amorphous film can be matched to Li carbonate (Li_2CO_3, orange circles) and Li oxide (Li_2O, red circles). (f) Schematic of the observed SEI mosaic-type structure formed on Li dendrites. (g) Integrated pixel intensities of Li oxide (red) and Li carbonate (orange) lattice. The peaks and valleys represent rows of atoms and the gaps, respectively. (h) Atomic-resolution image of the SEI formed when 10 vol% fluoroethylene carbonate is added to the electrolyte. (i) Corresponding schematic of the observed multilayered structure formed on Li dendrites.

As far as *ex situ* measurements are concerned, one of the techniques which probably contributed most to the characterization of the SEI film and related Li deposit is the cryogenic transmission electron microscopy. Actually, cryo-TEM allows to studying them at their pristine states i.e. avoiding any degradation due to the electron beam. Cui and co-workers used cryo-TEM to characterize the plating and stripping process of the Li metal anode in carbonate electrolytes (Figure 1-20) [100,101]. It was observed that

Li metal dendrites do not always grow as straight single-crystalline nanowires along a linear direction but, rather, they often change crystallographic growth directions at regions the authors refer to as kinks (Figure 1-20a-d). The preferred crystalline grow directions are the <111> (prevailing), <110> and <211>. The SEI layer recovering the dendrite exhibits a mosaic structure consisting of Li_2CO_3 and Li_2O separated domains (Figure 1-20e-g). After the addition of fluoroethylene carbonate (FEC) to the electrolyte, a common additive used for improving battery performances, the SEI becomes more ordered, with a multilayer structure composed of amorphous and Li_2O stratified films (Figure 1-21h-i). The authors conclude that the more ordered nature of the multilayer structure obtained by adding FEC offers increased mechanical durability, making SEI more robust during battery cycling.

1.6.1 Raman micro-spectroscopy applied to Li-based batteries and electrolytes for Li-metal devices

Raman spectroscopy provides unique information on the chemical composition and structure of inorganic and organic compounds, at the molecular to the atomic scale. Coupled to an optical microscope, this technique becomes a probe with μm resolution allowing spatially and temporally resolved studies of liquid and solid materials [102,28,103]. Then, as optical spectrometry, Raman micro-spectroscopy has several features particularly suitable for the study of active (electrode and electrolyte) materials for electrochemical devices [104]: i) the analysis is nondestructive, at least under careful laser excitation conditions; ii) since Raman spectroscopy is almost unaffected by strong IR absorbers (e.g. CO_2 or silica), no special sample preparation, containers and environmental conditions are needed for analysis, what facilitates the development of experimental devices for *in situ* investigations (see also [105]); iii) the micrometer resolution allows to characterize locally structural and chemical heterogeneities induced by the electrochemical operation and related to the ageing and performance losses of the battery.

Thus, Raman micro-spectroscopy has become the technique of choice to study the intercalation of Li^+ in carbon based materials for Li-ion anodes [106], but is also extensively employed for the characterization of the different transition metal oxides used as positive (or negative) electrode materials, more particularly $LiCoO_2$ [107]. Studies concerning the electrolyte are less common. In this frame, μ-Raman spectroscopy has been used to investigate different properties relevant to the formation

mechanism and morphology of the Li deposit: i) the local solvation structure of Li cations [108], ii) the occurring of Li^+ gradients near the electrode surface during operation [109] and iii) the composition of the SEI layer [110]. It should be noted that the characterization of thin surface layers like the SEI requires Raman signal enhancement techniques (e.g. SERS-Raman spectroscopy) [111,112] that will not be particularly discussed here. In the following sections, we present in more details the few works published so far about the solvation structure of electrolytes of interest to the Li anode and the occurring of ionic concentration gradients.

1.6.1.1 Studying the electrolyte solvation structure

Yamada et al. [113] characterized concentrated solutions of $LiN(SO_2F)_2$ (lithium bis(fluorosulfonyl)amide, LiFSA) in 1,2-dimethoxyethane (DME). The study of the blue-shift of the Raman bands belonging to both the salt anion (Figure 1-21a) and the solvent molecule (Figure 1-21b) with the increasing of the electrolyte concentration attested that both species fully coordinate to Li^+ in the superconcentrated solution at 3.6 M, forming CIPs and AGG clusters. This unique structure, different from conventional organic solutions or ionic liquids, confers high ionic conductivity (despite increased viscosity) and improved de-solvation kinetics. This allows higher Li^+ concentration at the electrode interface and, thus, enhanced Li^+ intercalation rate into the graphite anode.

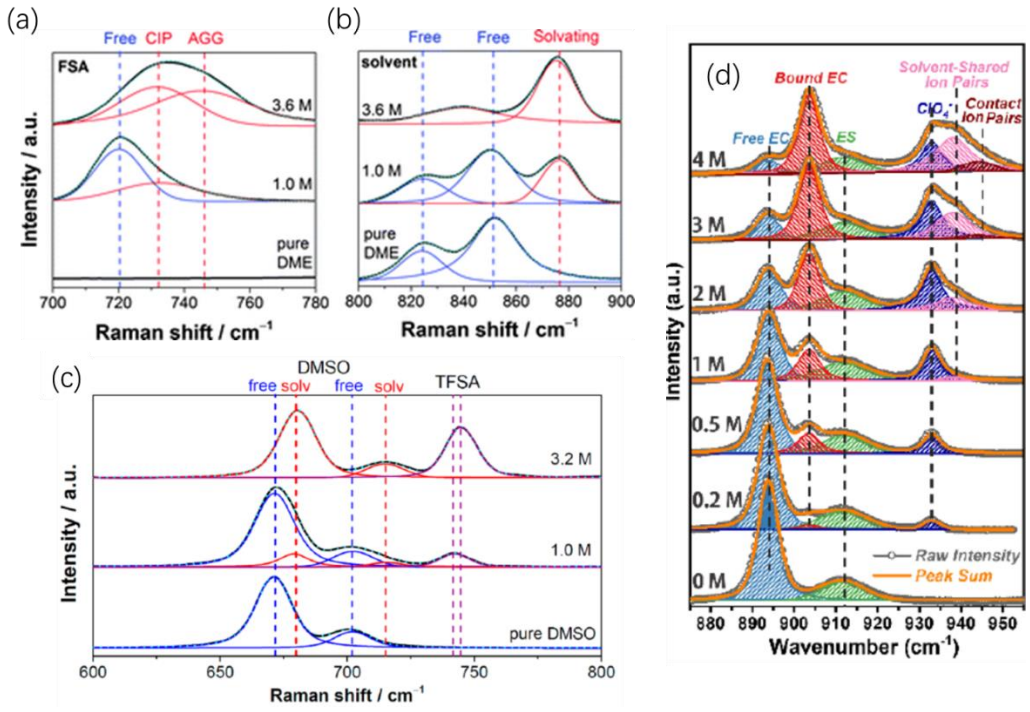


Figure 1-21. Raman spectra of the solutions (a,b) LiFSA-DME [112], (c) LiTFSA-DMSO [113] and (d) $LiClO_4$ in EC/ES [114] at different concentrations of the Li salt.

Yamada et al. [114] also studied solutions of $LiN(SO_2CF_3)_2$ (lithium bis-(trifluoromethanesulfonyl)amide, LiTFSA) in dimethyl sulfoxide (DMSO). The blue shift of solvent and salt anion modes with concentration could be observed also in this case, indicating that all DMSO molecules coordinate to Li^+ at the concentration of 3.2 M (Figure 1-21c). The authors proposed that the change of the species solvating Li^+, which occurs when the electrolyte concentration increases from 1 to 3.2 M, suppresses the solvent co-intercalation into the graphite. The last phenomenon is usually considered to contribute to the progressive anode capacity loss with cycling.

Zhang et al. [115] analyzed solutions of lithium perchlorate ($LiClO_4$) in mixed solvents of ethylene carbonate (EC) and ethylene sulfite (ES) (Figure 1-21d). As [Li^+] increases, the area of the ClO_4^- peak increases and two new components, representing solvent-shared ion pairs and CIPs, become visible as a result of the stronger interaction between ClO_4^- and Li^+. Simultaneously, the EC ring breathing mode at 894 cm^{-1} decreases in intensity, with a new peak appearing and gradually growing at higher wavenumbers. On the contrary, the C-O stretching mode of ES at 912 cm^{-1} neither weakens nor evolves into new peaks, suggesting little effect of Li^+ on this bond in the ES molecule. As a consequence, EC molecules dominate the Li^+ solvation sheath, while ES molecules degrades primarily during the electrochemical operation, producing SEI containing sulfur species like Li_2S and Li_2S_2 which are considered desirable SEI components for Li metal electrode as they extend the electrode cycle life.

Bouteau *et al.* [116] studied the degradation of a 1 M $LiPF_6$ solution in EC/DMC illuminated by a polychromatic light simulating the solar radiation. Even if the authors could not observe any chemical degradation, Raman spectra collected in the spectral range of PF_6^-, C=O and C-O vibrational modes showed the rearrangement of the Li^+ solvation structure (Figure 1-22), which the authors attributed to the increase of the lithium coordination number with ethylene carbonate. This light-induced modification of the Li^+ solvation has the positive impact of improving the electrolyte conductivity.

All the studies resumed here above show clearly how Raman spectroscopy allows to probe the solvation structure of Li^+ and, in this way, to foresee the reactivity of the electrolyte and the mechanisms of the electrochemical reactions occurring at the electrode-electrolyte interface.

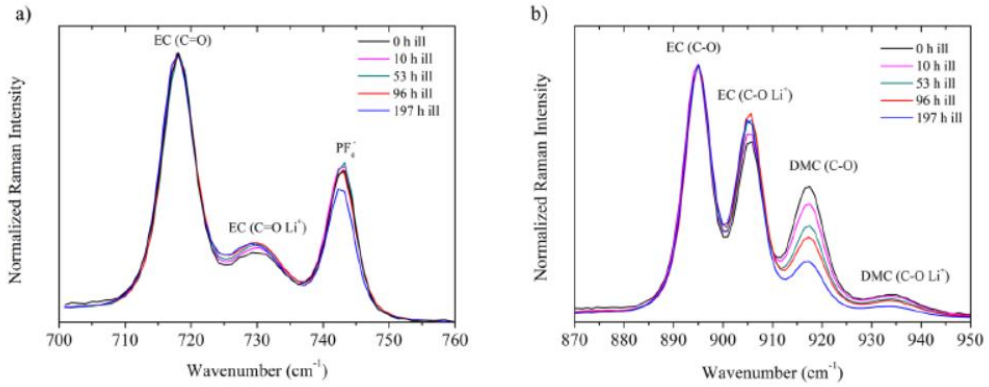


Figure 1-22. Evolution over time of Raman spectra of 1 M $LiPF_6$ in EC/DMC under irradiation from a sun simulator: (a) 700-760 cm^{-1} and (b) 870-950 cm^{-1} regions [116].

1.6.1.2 Detecting ion concentration gradients in the electrolyte

As already mentioned before (§ 1.4.4), the morphology of the electrodeposited Li is related to the occurrence of Li^+ concentration gradients in the electrolyte near the electrode surface (Figure 1-23) [117]. In turn, gradients depend (among others) on the mass transport rate of Li ions by diffusion, convection and migration. Low Li^+ flow towards the electrode, i.e. low Li^+ transfer rate and/or low concentration of the electrolyte, induces the local Li^+ concentration at the surface to drop down to $[Li^+] = 0$ and, hence, the Li metal dendrites to grow towards the bulk electrolyte where more ions are available (Figure 1-23a). On the contrary, large Li^+ flow, i.e. fast ion transfer and/or high electrolyte concentration, provides sufficient cations in all directions and allows a smooth plated surface (Figure 1-23b). On the whole, the surface of the electrodeposited Li is usually uneven because the mass transfer rate varies locally.

In principle, as shown by the studies presented in the previous section (§1.6.1.1), Raman micro-spectroscopy can be used to quantify the distribution of Li^+ species in the electrolyte at the micrometer scale by the measurement of the intensity of Raman peaks belonging to the Li salt anion or to the Li^+-solvating species. An exemplary *in situ* study has been reported by Cheng et al. [118], who used stimulated Raman scattering microscopy to quantitatively capture the fast evolution of the ion concentration at a Li metal surface in a gel electrolyte composed of lithium bis (oxalato)borate (LiBOB) in tetraethylene glycol dimethyl ether (TEGDME) with 22 wt% poly (vinylidene fluoride-cohexa-fluor-opropylene) (PVdf-HFP). The Li^+ concentration could be quantitatively detected by the intensity of the Raman peak of the C=O group belonging to the BOB^- anion (around 1800 cm^{-1}, Figure 1-24). So, the authors observed that the Li deposition occurs in three steps (Figure 1-25): i) slow deposition of mossy Li when surface ions

are not yet depleted, ii) mixed growth of mossy Li and dendrites during partial depletion and iii) dendrite growth after full depletion. Dendritic Li protrusions locally appears at the intermediate step (when most Li surface areas are still at the slow-growing "mossy" step) because of the spatial heterogeneities of Li^+ concentration and flux, with larger depletion at the valleys of the electrode surface. The newly formed Li protrusions grow more rapidly and initiate a positive feedback loop between the Li growth rate and [Li^+] heterogeneity, which leads to dendrite eruption upon full depletion.

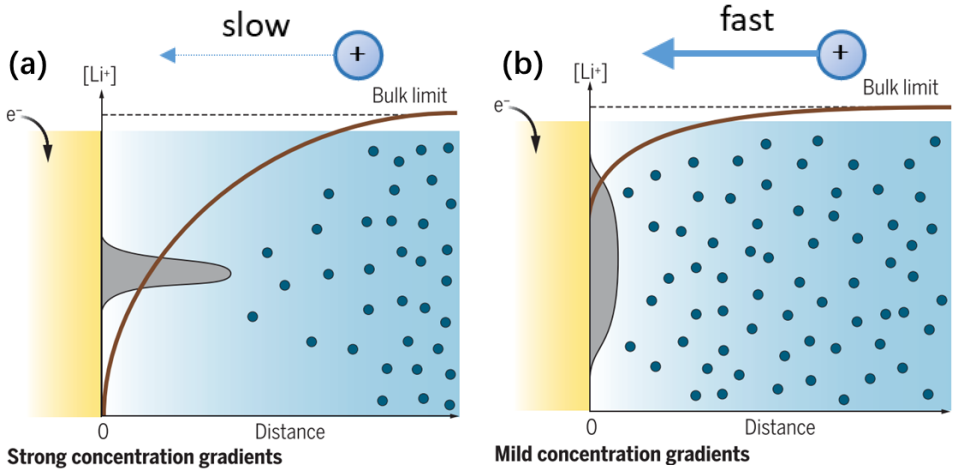


Figure 1-23. Schematic relationship between the local Li^+ concentration gradient near the electrode surface and the Li deposit morphology: (a) strong concentration gradients due to low mobility of Li ions and (b) mild concentration gradients due to fast Li transfer [117].

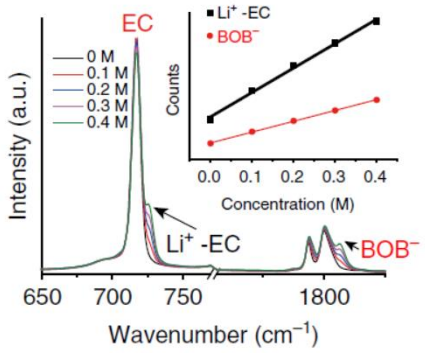


Figure 1-24. Raman spectra of LiBOB in TEGDME/EC at different concentrations ranging from 0 M to 0.4 M [118].

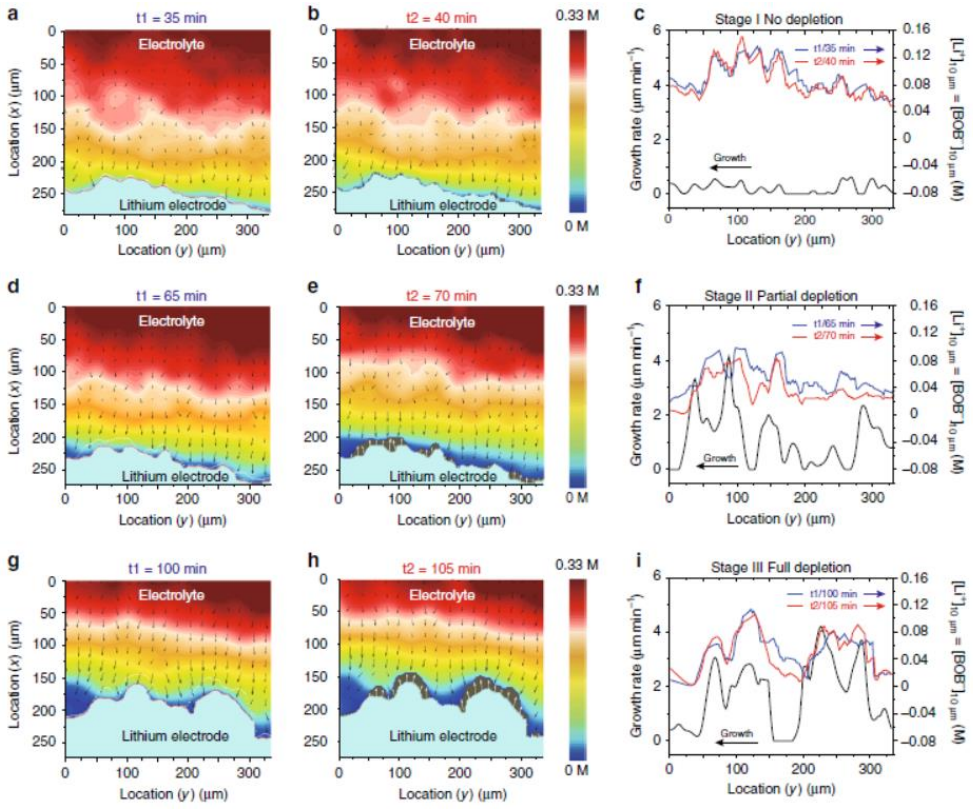


Figure 1-25. Evolution in time of the Li^+ concentration profile at the Li metal electrode as mapped by *in situ* stimulated Raman scattering microscopy (left and middle columns) and corresponding growth rate of the lithium deposition (right column), according to [118]: (a - c) first step (no Li^+ depletion), (d - f) second step (partial depletion) and (g - i) third step (full depletion).

1.7 Motivation and work plan

Li-metal batteries are re-arising as a promising next-generation battery system due to their potential high energy density, but their future use depends on whether the issue of the electrode/electrolyte interface instability can be effectively addressed [4,53]. On the one hand, the use of a metallic Li anode allows the direct exploitation of the Li^+/Li redox couple, having the highest capacity (3860 mAh g^{-1}) and the lowest redox potential (-3.04 vs. S.H.E.) [35]. On the other hand, the Li metal surface is readily active towards usual liquid electrolytes and the resulting interface chemical and morphological instability leads to short cycle lifetime and potential safety problems [119]. More particularly, the uneven Li deposition morphology occurring during the battery cycling, especially the formation of Li dendrites, appears as a main issue hindering the large-scale marketing of Li metal anodes [65]. Studying, understanding and overcoming the Li plating behavior is then a key challenge to develop stable Li metal batteries. In principle, increasing the Li salt concentration in the electrolyte should delay the Li

dendrite appearance by increasing the Sand's time [98]. Besides the improved anode stability, high-concentration electrolytes (HCEs) have other advantages such as large electrochemical potential window, excellent rate capability, high-level safety, improved resistance of the Al current collectors to corrosion. But, at the same time, excessive Li salt not only implies larger economic burden but also increases the electrolyte viscosity, thus inducing poor ionic conductivity and poor separators wetting ability. To maintain the assets and minimize the disadvantage of HCEs, localized high-concentration electrolytes (LHCEs) have been developed by adding a second "inert" solvent (also called diluent) which cannot dissolve the Li salt but is miscible with the solvent initially used [99,96,91]. This allows to decrease the global concentration of the Li salt while locally preserving high salt concentration structures. These local solvation structures (AGG and CIP) affect the relative reactivity of salts and solvents towards the Li metal anode so as to lead to the formation of more stable, inorganic rich SEI films increasing the battery lifetime and stabilizing performances [112,108]. It should then be pointed out that, though a number of studies has yet been carried about the effect of the diluent type and composition of the LHCE on the Li metal battery performances [98,96,97,99], several aspects of the electrolyte local structure still await to be investigated in detail. In order to definitively improve LHCEs, the systematic study of the evolution of the Li^+ solvation sheath with the nature and relative amounts of diluent, solvent and salt has to be carried out. More generally, consistent experimental work is still needed to establish strict relationships between the local structure and composition of the LHCE, the electrochemical and morphological behavior of the electrode-electrolyte interface and the performances of the battery. Furthermore, this investigation has necessarily to be supplemented by the complementary study of the establishment of the Li^+ concentration gradients during the electrode operation, which are usually considered to have a direct relevance (as for the local solvation structure) to the Li deposition morphology.

Since its discovery in 1928, Raman spectroscopy has become an effective way to characterize the structure of materials from their vibrational and rotational features [20]. From 1980s, Raman spectroscopy has been abundantly used for studying Li-based batteries due to its outstanding properties of non-destructive analysis and (relatively) easy operation [104]. As discussed before, both the solvation structure and the ion concentration of the electrolyte can be characterized by this technique through the Raman peaks belonging to the Li salt anions, free solvents and Li^+-solvating species.

This thesis is mainly devoted to the μ-Raman study of the electrolyte solvation structure and of the occurrence of Li^+ concentration gradients across the electrolyte during the battery operation. In order to establish relationships with the electrochemical behavior of the Li metal anode i.e. (capacity and stability), the spectroscopic investigation is implemented by the characterization of the electrode surface (SEI composition and Li deposit morphology) by usual techniques as scanning electron microscopy (SEM) and x-ray photoelectron spectroscopy (XPS). Several low-, high- and localized high-concentration electrolytes are studied and compared. Besides, the last part of this work deals with the photo-catalytic reduction, i.e. promoted by the laser irradiation, of carbonate-based electrolytes on Cu, that is how to recycle the electrolyte into useful catalyst.

Our work begins with the systematic μ-Raman *ex situ* characterization of the solvation structures of low-, high- and localized high-concentration electrolyte constituted of $LiPF_6$ in DMC and in DMC/HFPM (chapter 3). We will show an unexpected effect of the diluent amount on the solvation structures of the LHCE: as the diluent amount increases, the proportions of free solvent molecules and CIPs rise up simultaneously. This observation represents a new criterion for the chemical formulation of improved LHCEs since, accordingly, a moderately diluted LHCE shows the best Coulombic efficiency of the Li metal anodes (99.6%), compared with the precursor HCE (97.4%) or highly diluted LHCE (99.0%). Two possible mechanisms are proposed for the DMC decomposition and the consequent SEI formation at the electrode surface

Afterwards, *in situ* μ-Raman is used to study the Li^+ concentration attenuation in the same low-, high- and localized high-concentration electrolytes during the Li plating (chapter 4). $[Li^+]$ is measured at fixed points, at different distances from the electrode surface (10, 50 and 100 μm), during time. The effect of the Li salt concentration and of the plating current density are investigated. For the first time, the establishment of $[Li^+]$ gradients across LCEs, HCEs and LHCEs consisting of the same Li salt and solvent is compared. Approximate Li^+ diffusion coefficients are obtained. Even if the results of this study represent useful inputs for forthcoming numerical studies, we will show that, under the specific experimental conditions here applied, they do not allow to establish straightforward relationships between $[Li^+]$ gradients and Li deposit morphology. In reverse, the characterization of the electrode surface after the plating process suggests that a main parameter affecting the Li deposit morphology is the Li^+ mobility across the SEI layer.

Finally, we extent the research topic concerning the electrolyte to the issue of its recycling (chapter 5). Recycling of exhausted Li batteries is essential to limit pollution and loss of resources. The importance of the electrolyte recycling is often neglected and, anyway, the traditional methods require to separate Li salts from solvents of the dead battery, which is complex and expensive. During Raman measurements, we accidently observed the photochemical degradation of the Li carbonate-based electrolyte in contact with the Cu foil into a mixed LiF/graphitic carbon layer deposited on Cu_xO. We will show that this material is the precursor of an effective catalyst for the electrochemical CO_2 reduction. Then, being the electrolyte photochemical degradation a useful way to convert exhausted solutions into useful catalyst, we will study the catalytic mechanism in more depth and characterize its efficiency.

References

[1] N. Lior, Sustainable energy development: The present (2009) situation and possible paths to the future, Energy 35 (2010) 3976–3994.

[2] M. Li, J. Lu, Z. Chen, K. Amine, 30 years of lithium-ion batteries, Advanced Materials 30 (2018) 1800561.

[3] J. Liu, Z. Bao, Y. Cui, E.J. Dufek, J.B. Goodenough, P. Khalifah, Q. Li, B.Y. Liaw, P. Liu, A. Manthiram, Pathways for practical high-energy long-cycling lithium metal batteries, Nature Energy 4 (2019) 180–186.

[4] M.S. Park, S.B. Ma, D.J. Lee, D. Im, S.-G. Doo, O. Yamamoto, A highly reversible lithium metal anode, Scientific reports 4 (2014) 1–8.

[5] M. Winter, B. Barnett, K. Xu, Before Li ion batteries, Chemical reviews 118 (2018) 11433–11456.

[6] K.-E. Byun, Y. Cho, M. Seol, S. Kim, S.-W. Kim, H.-J. Shin, S. Park, S. Hwang, Control of triboelectrification by engineering surface dipole and surface electronic state, ACS applied materials & interfaces 8 (2016) 18519–18525.

[7] D.P. Dubal, Y.P. Wu, R. Holze, Supercapacitors: From the Leyden jar to electric busses, ChemTexts 2 (2016) 1–19.

[8] J. Mertens, Shocks and sparks: The voltaic pile as a demonstration device, Isis 89 (1998) 300–311.

[9] B. Scrosati, History of lithium batteries: Journal of solid state electrochemistry 15 (2011) 1623–1630.

[10] G.N. Lewis, F.G. Keyes, The potential of the lithium electrode, Journal of the American chemical society 35 (1913) 340–344.

[11] W.S. Harris, Electrochemical studies in cyclic esters, University of California Radiation Laboratory (1958).

[12] J.E. Chilton, G.M. Cook, New cathode--anode couples using nonaqueous electrolytes. Final report. [Li/LiCl, AlCl/sub 3/, propylene carbonate/Ag or Ni chloride] (1962).

[13] E.S. Takeuchi, R.A. Leising, D.M. Spillman, R. Rubino, H. Gan, K.J. Takeuchi, A.C. Marschilok, Lithium batteries for medical applications, in: Lithium Batteries,

Springer, (2009) 686–700.

[14] M.S. Whittingham, F.R. Gamble Jr, The lithium intercalates of the transition metal dichalcogenides, Materials research bulletin 10 (1975) 363–371.

[15] R.F. Bis, J.A. Barnes, W.V. Zajac, P.B. Davis, R.M. Murphy, Safety characteristics of lithium primary and secondary battery systems, Formulation of a lithium battery safety matrix (1986).

[16] X. Zhao, Y. Wu, Y. Wang, H. Wu, Y. Yang, Z. Wang, L. Dai, Y. Shang, A. Cao, High-performance Li-ion batteries based on graphene quantum dot wrapped carbon nanotube hybrid anodes, Nano research 13 (2020) 1044–1052.

[17] K. Brandt, Historical development of secondary lithium batteries, Solid state ionics 69 (1994) 173–183.

[18] C. Masquelier, A.K. Padhi, K.S. Nanjundaswamy, J.B. Goodenough, New cathode materials for rechargeable lithium batteries: The 3-D framework structures $Li_3Fe_2(XO_4)_3$ (X= P, As), Journal of solid state chemistry 135 (1998) 228–234.

[19] T. Ohzuku, Y. Makimura, Layered lithium insertion material of $LiCo_{1/3}Ni_{1/3}Mn_{1/3}O_2$ for lithium-ion batteries, Chemistry letters 30 (2001) 642–643.

[20] A. Ramanan, Nobel prize in chemistry 2019, Resonance 24 (2019) 1381–1395.

[21] B. Wang, J. Ryu, S. Choi, X. Zhang, D. Pribat, X. Li, L. Zhi, S. Park, R.S. Ruoff, Ultrafast-charging silicon-based coral-like network anodes for lithium-ion batteries with high energy and power densities, ACS nano 13 (2019) 2307–2315.

[22] K.H. Kim, J. Shon, H. Jeong, H. Park, S.-J. Lim, J.S. Heo, Improving the cyclability of silicon anodes for lithium-ion batteries using a simple pre-lithiation method, Journal of power sources 459 (2020) 228066.

[23] P. Bärmann, M. Mohrhardt, J.E. Frerichs, M. Helling, A. Kolesnikov, S. Klabunde, S. Nowak, M.R. Hansen, M. Winter, T. Placke, Mechanistic insights into the pre-lithiation of silicon/graphite negative electrodes in “dry state” and after electrolyte addition using passivated lithium metal powder, Advanced energy materials 11 (2021) 2100925.

[24] C. Niu, D. Liu, J.A. Lochala, C.S. Anderson, X. Cao, M.E. Gross, W. Xu, J.-G. Zhang, M.S. Whittingham, J. Xiao, Balancing interfacial reactions to achieve long

cycle life in high-energy lithium metal batteries, Nature energy 6 (2021) 723–732.

[25] B. Liu, H. Pan, Rechargeable lithium metal batteries, in: Nanostructured materials for next-generation energy storage and conversion, Springer, (2019) 147–203.

[26] B.S. Kademani, V.L. Kalyane, A.B. Kademani, Scientometric portrait of nobel laureate Dr. CV Raman, Indian journal of information, library and society 7 (1994) 215–249.

[27] I.L. Fabelinskiĭ, Seventy years of combination (Raman) scattering, Physics-uspekhi 41 (1998) 1229.

[28] V. Stancovski, S. Badilescu, In situ Raman spectroscopic–electrochemical studies of lithium-ion battery materials: A historical overview, Journal of applied electrochemistry 44 (2014) 23–43.

[29] D.A. Long, Early history of the Raman effect, International reviews in physical chemistry 7 (1988) 317–349.

[30] H.G.M. Edwards, Probing history with Raman spectroscopy, Analyst 129 (2004) 870–879.

[31] H. Mitsutake, R.J. Poppi, M.C. Breitkreitz, Raman imaging spectroscopy: History, fundamentals and current scenario of the technique, Journal of the brazilian chemical society 30 (2019) 2243–2258.

[32] W. Xu, J. Wang, F. Ding, X. Chen, E. Nasybulin, Y. Zhang, J.-G. Zhang, Lithium metal anodes for rechargeable batteries, Energy & environmental science 7 (2014) 513–537.

[33] G.G. Papavasileiou, C.S. Psomopoulos, G.C. Ioannidis, S.D. Kaminaris, Recycling of spent rechargeable batteries: A review for the lithium-ion batteries, Proceedings of the fifth international conference on environmental management, engineering, planning & economics, (2015) 315-320.

[34] D. Ren, K. Smith, D. Guo, X. Han, X. Feng, L. Lu, M. Ouyang, J. Li, Investigation of lithium plating-stripping process in Li-ion batteries at low temperature using an electrochemical model, Journal of the electrochemical society 165 (2018) A2167.

[35] J.-M. Tarascon, M. Armand, Issues and challenges facing rechargeable lithium batteries, in: Materials for sustainable energy: a collection of peer-reviewed

research and review articles from nature publishing group, World scientific, (2011) 171–179.

[36] R. Sivaraman, I. Patra, M.J.C. Opulencia, R. Sagban, H. Sharma, A.T. Jalil, A.G. Ebadi, Evaluating the potential of graphene-like boron nitride as a promising cathode for Mg-ion batteries, Journal of electroanalytical chemistry (2022) 116413.

[37] X. Luo, H. Zhang, W. Pan, J. Gong, B. Khalid, M. Zhong, H. Wu, SiO_x nanodandelion by laser ablation for anode of lithium-ion battery, Small 11 (2015) 6009–6012.

[38] P.G. Bruce, S.A. Freunberger, L.J. Hardwick, J.-M. Tarascon, Li–O_2 and Li–S batteries with high energy storage, Nature materials 11 (2012) 19–29.

[39] J.B. Goodenough, Y. Kim, Challenges for rechargeable Li batteries, Chemistry of materials 22 (2010) 587–603.

[40] M. Gauthier, T.J. Carney, A. Grimaud, L. Giordano, N. Pour, H.-H. Chang, D.P. Fenning, S.F. Lux, O. Paschos, C. Bauer, Electrode–electrolyte interface in Li-ion batteries: Current understanding and new insights, The journal of physical chemistry letters 6 (2015) 4653–4672.

[41] A. Mauger, M. Armand, C.M. Julien, K. Zaghib, Challenges and issues facing lithium metal for solid-state rechargeable batteries, Journal of power sources 353 (2017) 333–342.

[42] W. Zhang, S. Zhang, L. Fan, L. Gao, X. Kong, S. Li, J. Li, X. Hong, Y. Lu, Tuning the LUMO energy of an organic interphase to stabilize lithium metal batteries, ACS energy letters 4 (2019) 644–650.

[43] T. Placke, R. Kloepsch, S. Dühnen, M. Winter, Lithium ion, lithium metal, and alternative rechargeable battery technologies: The odyssey for high energy density, Journal of solid state electrochemistry 21 (2017) 1939–1964.

[44] F. Wang, B. Wang, J. Li, B. Wang, Y. Zhou, D. Wang, H. Liu, S. Dou, Prelithiation. A crucial strategy for boosting the practical application of next-generation lithium ion battery, ACS nano 15 (2021) 2197–2218.

[45] S. Bertolini, P.B. Balbuena, Effect of solid electrolyte interphase on the reactivity of polysulfide over lithium-metal anode, Electrochimica acta 258 (2017) 1320–1328.

[46] J.Y. Kim, D.O. Shin, T. Chang, K.M. Kim, J. Jeong, J. Park, Y.M. Lee, K.Y. Cho, C. Phatak, S. Hong, Effect of the dielectric constant of a liquid electrolyte on lithium metal anodes, Electrochimica acta 300 (2019) 299–305.

[47] J. Ko, Y.S. Yoon, Recent progress in LiF materials for safe lithium metal anode of rechargeable batteries: Is LiF the key to commercializing Li metal batteries?, Ceramics international 45 (2019) 30–49.

[48] E. Peled, The electrochemical behavior of alkali and alkaline earth metals in nonaqueous battery systems—the solid electrolyte interphase model, Journal of the electrochemical society 126 (1979) 2047.

[49] E. Peled, D. Golodnitsky, G. Ardel, Advanced model for solid electrolyte interphase electrodes in liquid and polymer electrolytes, Journal of the electrochemical society 144 (1997) L208.

[50] Y. Ein-Eli, A new perspective on the formation and structure of the solid electrolyte interface at the graphite anode of Li-ion cells, Electrochemical and solid-state letters 2 (1999) 212.

[51] X.-B. Cheng, R. Zhang, C.-Z. Zhao, F. Wei, J.-G. Zhang, Q. Zhang, A review of solid electrolyte interphases on lithium metal anode, Advanced science 3 (2016) 1500213.

[52] C. Yang, K. Fu, Y. Zhang, E. Hitz, L. Hu, Protected lithium-metal anodes in batteries: From liquid to solid, Advanced materials 29 (2017) 1701169.

[53] S.F. Liu, X.L. Wang, D. Xie, X.H. Xia, C.D. Gu, J.B. Wu, J.P. Tu, Recent development in lithium metal anodes of liquid-state rechargeable batteries, Journal of alloys and compounds 730 (2018) 135–149.

[54] J. Wang, B. Ge, H. Li, M. Yang, J. Wang, Di Liu, C. Fernandez, X. Chen, Q. Peng, Challenges and progresses of lithium-metal batteries, Chemical engineering journal 420 (2021) 129739.

[55] S.P.S. Badwal, S.S. Giddey, C. Munnings, A.I. Bhatt, A.F. Hollenkamp, Emerging electrochemical energy conversion and storage technologies, Frontiers in chemistry 2 (2014) 79.

[56] S. Li, M. Jiang, Y. Xie, H. Xu, J. Jia, J. Li, Developing high-performance lithium metal anode in liquid electrolytes: Challenges and progress, Advanced materials

30 (2018) 1706375.

[57] K.N. Wood, M. Noked, N.P. Dasgupta, Lithium metal anodes: Toward an improved understanding of coupled morphological, electrochemical, and mechanical behavior, ACS energy letters 2 (2017) 664–672.

[58] D. Lin, Y. Liu, Y. Cui, Reviving the lithium metal anode for high-energy batteries, Nature nanotechnology 12 (2017) 194–206.

[59] X. Guan, A. Wang, S. Liu, G. Li, F. Liang, Y.-W. Yang, X. Liu, J. Luo, Controlling nucleation in lithium metal anodes, Small 14 (2018) 1801423.

[60] P. Bai, J. Li, F.R. Brushett, M.Z. Bazant, Transition of lithium growth mechanisms in liquid electrolytes, Energy & environmental science 9 (2016) 3221–3229.

[61] A. Pei, G. Zheng, F. Shi, Y. Li, Y. Cui, Nanoscale nucleation and growth of electrodeposited lithium metal, Nano letters 17 (2017) 1132–1139.

[62] R. Aogaki, T. Makino, Theory of powdered metal formation in electrochemistry—morphological instability in galvanostatic crystal growth under diffusion control, Electrochimica acta 26 (1981) 1509–1517.

[63] P.G. Bruce, C.A. Vincent, Steady state current flow in solid binary electrolyte cells, Journal of electroanalytical chemistry and interfacial electrochemistry 225 (1987) 1–17.

[64] J.-N. Chazalviel, Electrochemical aspects of the generation of ramified metallic electrodeposits, Physical review A 42 (1990) 7355.

[65] K. Yan, Z. Lu, H.-W. Lee, F. Xiong, P.-C. Hsu, Y. Li, J. Zhao, S. Chu, Y. Cui, Selective deposition and stable encapsulation of lithium through heterogeneous seeded growth, Nature energy 1 (2016) 1–8.

[66] D. Lin, Y. Liu, Z. Liang, H.-W. Lee, J. Sun, H. Wang, K. Yan, J. Xie, Y. Cui, Layered reduced graphene oxide with nanoscale interlayer gaps as a stable host for lithium metal anodes, Nature nanotechnology 11 (2016) 626–632.

[67] C.-Z. Zhao, H. Duan, J.-Q. Huang, J. Zhang, Q. Zhang, Y.-G. Guo, L.-J. Wan, Designing solid-state interfaces on lithium-metal anodes. A review, Science china chemistry 62 (2019) 1286–1299.

[68] J. Qian, W. Xu, P. Bhattacharya, M. Engelhard, W.A. Henderson, Y. Zhang, J.-G.

Zhang, Dendrite-free Li deposition using trace-amounts of water as an electrolyte additive, Nano energy 15 (2015) 135–144.

[69] J.S. Kim, D. Byun, J.K. Lee, Electrochemical characteristics of amorphous silicon thin film electrode with fluoroethylene carbonate additive, Current applied physics 14 (2014) 596–602.

[70] S.-F. Ng, M.Y.L. Lau, W.-J. Ong, Lithium–sulfur battery cathode design: Tailoring metal-based nanostructures for robust polysulfide adsorption and catalytic conversion, Advanced materials 33 (2021) 2008654.

[71] F. Ding, W. Xu, G.L. Graff, J. Zhang, M.L. Sushko, X. Chen, Y. Shao, M.H. Engelhard, Z. Nie, J. Xiao, Dendrite-free lithium deposition via self-healing electrostatic shield mechanism, Journal of the American chemical society 135 (2013) 4450–4456.

[72] B. Sun, P. Xiong, U. Maitra, D. Langsdorf, K. Yan, C. Wang, J. Janek, D. Schröder, G. Wang, Design strategies to enable the efficient use of sodium metal anodes in high-energy batteries, Advanced materials 32 (2020) 1903891.

[73] J. Niu, M. Wang, T. Cao, X. Cheng, R. Wu, H. Liu, Y. Zhang, X. Liu, Li metal coated with Li_3PO_4 film via atomic layer deposition as battery anode, Ionics 27 (2021) 2445–2454.

[74] W. Tang, X. Yin, Z. Chen, W. Fu, K.P. Loh, G.W. Zheng, Chemically polished lithium metal anode for high energy lithium metal batteries, Energy storage materials 14 (2018) 289–296.

[75] G. Zheng, S.W. Lee, Z. Liang, H.-W. Lee, K. Yan, H. Yao, H. Wang, W. Li, S. Chu, Y. Cui, Interconnected hollow carbon nanospheres for stable lithium metal anodes, Nature nanotechnology 9 (2014) 618–623.

[76] C.-P. Yang, Y.-X. Yin, S.-F. Zhang, N.-W. Li, Y.-G. Guo, Accommodating lithium into 3D current collectors with a submicron skeleton towards long-life lithium metal anodes, Nature communications 6 (2015) 1–9.

[77] F. Ren, Z. Lu, H. Zhang, L. Huai, X. Chen, S. Wu, Z. Peng, D. Wang, J. Ye, Pseudocapacitance induced uniform plating/stripping of Li metal anode in vertical graphene nanowalls, Advanced functional materials 28 (2018) 1805638.

[78] H. Inoue, Y. Namba, E. Higuchi, Preparation and characterization of Ni-based

positive electrodes for use in aqueous electrochemical capacitors, Journal of power sources 195 (2010) 6239–6244.

[79] P.T. Moseley, Consequences of including carbon in the negative plates of Valve-regulated Lead–Acid batteries exposed to high-rate partial-state-of-charge operation, Journal of power sources 191 (2009) 134–138.

[80] Y. Huang, L. Zhao, L. Li, M. Xie, F. Wu, R. Chen, Electrolytes and electrolyte/electrode interfaces in sodium-ion batteries. From scientific research to practical application, Advanced materials 31 (2019) 1808393.

[81] L. Suo, Y.-S. Hu, H. Li, M. Armand, L. Chen, A new class of solvent-in-salt electrolyte for high-energy rechargeable metallic lithium batteries, Nature communications 4 (2013) 1–9.

[82] R. Younesi, G.M. Veith, P. Johansson, K. Edström, T. Vegge, Lithium salts for advanced lithium batteries. Li–metal, Li–O_2, and Li–S, Energy & environmental science 8 (2015) 1905–1922.

[83] M.V. Reddy, A. Mauger, C.M. Julien, A. Paolella, K. Zaghib, Brief history of early lithium-battery development, Materials 13 (2020) 1884.

[84] L.O. Valøen, J.N. Reimers, Transport properties of $LiPF_6$-based Li-ion battery electrolytes, Journal of The electrochemical society 152 (2005) A882.

[85] J. Kalhoff, G.G. Eshetu, D. Bresser, S. Passerini, Safer electrolytes for lithium-ion batteries. State of the art and perspectives, ChemSusChem 8 (2015) 2154–2175.

[86] S.J. An, J. Li, C. Daniel, D. Mohanty, S. Nagpure, D.L. Wood III, The state of understanding of the lithium-ion-battery graphite solid electrolyte interphase (SEI) and its relationship to formation cycling, Carbon 105 (2016) 52–76.

[87] S.S. Zhang, A review on electrolyte additives for lithium-ion batteries, Journal of power sources 162 (2006) 1379–1394.

[88] C. Brissot, M. Rosso, J.-N. Chazalviel, P. Baudry, S. Lascaud, In situ study of dendritic growth inlithium/PEO-salt/lithium cells, Electrochimica acta 43 (1998) 1569–1574.

[89] Y.-S. Hu; Y. Lu, The mystery of electrolyte concentration: From superhigh to ultralow, ACS energy letters, 5 (2020) 3633-3636.

[90] E.R. Logan, Dahn, JR, Electrolyte design for fast-charging Li-ion batteries, Trends in chemistry 2 (2020) 354–366.

[91] G. Jiang, F. Li, H. Wang, M. Wu, S. Qi, X. Liu, S. Yang, J. Ma, Perspective on high-concentration electrolytes for lithium metal batteries, Small structures 2 (2021) 2000122.

[92] K. Matsumoto, K. Inoue, K. Nakahara, R. Yuge, T. Noguchi, K. Utsugi, Suppression of aluminum corrosion by using high concentration LiTFSI electrolyte, Journal of power sources 231 (2013) 234–238.

[93] J. Zheng, P. Yan, D. Mei, M.H. Engelhard, S.S. Cartmell, B.J. Polzin, C. Wang, J.-G. Zhang, W. Xu, Highly stable operation of lithium metal batteries enabled by the formation of a transient high-concentration electrolyte layer, Advanced energy materials 6 (2016) 1502151.

[94] S.S. Zhang, T.R. Jow, Aluminum corrosion in electrolyte of Li-ion battery, Journal of power sources 109 (2002) 458–464.

[95] Y. Yamada, J. Wang, S. Ko, E. Watanabe, A. Yamada, Advances and issues in developing salt-concentrated battery electrolytes, Nature energy 4 (2019) 269–280.

[96] X. Ren, S. Chen, H. Lee, D. Mei, M.H. Engelhard, S.D. Burton, W. Zhao, J. Zheng, Q. Li, M.S. Ding, Localized high-concentration sulfone electrolytes for high-efficiency lithium-metal batteries, Chem 4 (2018) 1877–1892.

[97] L. Yu, S. Chen, H. Lee, L. Zhang, M.H. Engelhard, Q. Li, S. Jiao, J. Liu, W. Xu, J.-G. Zhang, A localized high-concentration electrolyte with optimized solvents and lithium difluoro (oxalate) borate additive for stable lithium metal batteries, ACS energy letters 3 (2018) 2059–2067.

[98] S. Chen, J. Zheng, D. Mei, K.S. Han, M.H. Engelhard, W. Zhao, W. Xu, J. Liu, J.-G. Zhang, High-voltage lithium-metal batteries enabled by localized high-concentration electrolytes, Advanced materials 30 (2018) 1706102.

[99] W. Dai, N. Dong, Y. Xia, S. Chen, H. Luo, Y. Liu, Z. Liu, Localized concentrated high-concentration electrolyte enhanced stability and safety for high voltage Li-ion batteries, Electrochimica acta 320 (2019) 134633.

[100] Y. Li, Y. Li, A. Pei, K. Yan, Y. Sun, C.-L. Wu, L.-M. Joubert, R. Chin, A.L. Koh, Y. Yu, Atomic structure of sensitive battery materials and interfaces revealed by

cryo–electron microscopy, Science 358 (2017) 506–510.

[101] Y. Li, Y. Li, Y. Cui, Catalyst. How cryo-EM shapes the development of next-generation batteries, Chem 4 (2018) 2250–2252.

[102] M. Inaba, H. Yoshida, Z. Ogumi, T. Abe, Y. Mizutani, M. Asano, In situ Raman study on electrochemical Li intercalation into graphite, Journal of the electrochemical society 142 (1995) 20.

[103] X.-q. Cheng, H.-j. Li, Z.-x. Zhao, Y.-z. Wang, X.-m. Wang, The use of in-situ Raman spectroscopy in investigating carbon materials as anodes of alkali metal-ion batteries, New carbon materials 36 (2021) 93–105.

[104] R. Baddour-Hadjean, J.-P. Pereira-Ramos, Raman microspectrometry applied to the study of electrode materials for lithium batteries, Chemical reviews 110 (2010) 1278–1319.

[105] G.J. Puppels, Confocal Raman microspectroscopy (1991).

[106] P.C. Eklund, G. Dresselhaus, M.S. Dresselhaus, J.E. Fischer, Raman scattering in graphite-lithium intercalation compounds, Physical review B 21 (1980) 4705.

[107] M. Inaba, Y. Iriyama, Z. Ogumi, Y. Todzuka, A. Tasaka, Raman study of layered rock-salt LiCoO2 and its electrochemical lithium deintercalation, Journal of Raman spectroscopy 28 (1997) 613–617.

[108] P.C. Shi, M. Lin, H. Zheng, X.D. He, Z.M. Xue, H.F. Xiang, C.H. Chen, Effect of propylene carbonate-Li^+ solvation structures on graphite exfoliation and its application in Li-ion batteries, Electrochimica acta 247 (2017) 12–18.

[109] Z. Wei, A. Salehi, G. Lin, J. Hu, X. Jin, E. Agar, F. Liu, Probing Li-ion concentration in an operating lithium ion battery using in situ Raman spectroscopy, Journal of power sources 449 (2020) 227361.

[110] A. Gajan, C. Lecourt, B.E. Torres Bautista, L. Fillaud, J. Demeaux, I.T. Lucas, Solid electrolyte interphase instability in operating lithium-ion batteries unraveled by enhanced-Raman spectroscopy, ACS energy letters 6 (2021) 1757–1763.

[111] R.M. Jarvis, A. Brooker, R. Goodacre, Surface-enhanced Raman spectroscopy for bacterial discrimination utilizing a scanning electron microscope with a Raman spectroscopy interface, Analytical chemistry 76 (2004) 5198–5202.

[112] M.G. Giorgini, K. Futamatagawa, H. Torii, M. Musso, S. Cerini, Solvation structure around the Li^+ ion in mixed cyclic/linear carbonate solutions unveiled by the Raman noncoincidence effect, The journal of physical chemistry letters 6 (2015) 3296–3302.

[113] Y. Yamada, M. Yaegashi, T. Abe, A. Yamada, A superconcentrated ether electrolyte for fast-charging Li-ion batteries, Chemical communications 49 (2013) 11194–11196.

[114] Y. Yamada, K. Usui, C.H. Chiang, K. Kikuchi, K. Furukawa, A. Yamada, General observation of lithium intercalation into graphite in ethylene-carbonate-free superconcentrated electrolytes, ACS applied materials & interfaces 6 (2014) 10892–10899.

[115] Y. Zhang, Y. Zhong, Z. Wu, B. Wang, S. Liang, H. Wang, Solvent molecule cooperation enhancing lithium metal battery performance at both electrodes, Angewandte chemie international edition 59 (2020) 7797–7802.

[116] G. Bouteau, A.N. Van-Nhien, M. Sliwa, N. Sergent, J.-C. Leprêtre, G. Gachot, I. Sagaidak, F. Sauvage, Effect of standard light illumination on electrolyte's stability of lithium-ion batteries based on ethylene and di-methyl carbonates, Scientific reports 9 (2019) 1–9.

[117] J. Xiao, How lithium dendrites form in liquid batteries, Science 366 (2019) 426–427.

[118] Q. Cheng, L. Wei, Z. Liu, N. Ni, Z. Sang, B. Zhu, W. Xu, M. Chen, Y. Miao, L.-Q. Chen, Operando and three-dimensional visualization of anion depletion and lithium growth by stimulated Raman scattering microscopy, Nature communications 9 (2018) 1–10.

[119] Y.-S. Hong, C.-Z. Zhao, Y. Xiao, R. Xu, J.-J. Xu, J.-Q. Huang, Q. Zhang, X. Yu, H. Li, Safe Lithium-Metal Anodes for Li− O2 Batteries. From fundamental chemistry to advanced characterization and effective protection, Batteries & supercaps 2 (2019) 638–658.

Chapter 2. Experimental setup and methods

2.1 Introduction

We present here the experimental setups and methods pertinent to studies reported in chapter 3 and chapter 4. The current chapter is organized in 3 main parts:

- First, we describe components and assembly of the electrochemical-optical cell used for the *in situ* Raman micro-spectroscopy study of the electrolyte for Li-metal batteries as well as for some independent electrochemical measurements.
- Then, we illustrate the different electrochemical measurements implemented to investigate the electrode/electrolyte interfacial electrochemistry and establish relationships between the electrolyte properties and the electrochemical performances.
- Finally, we report the experimental conditions and data processing concerning *ex* and *in situ* Raman micro-spectroscopy measurements.

2.2 Assembly of *in situ* optical cell

The optical cell used for *in situ* μ-Raman spectroscopy as well as for independent electrochemical measurements has been purchased from MTI Corporation (type: STC-Q) [1]. Components and assembly are reported in Figure 2-1.

Shells are made of polyetheretherketone (PEEK), having mechanical strength, good corrosion resistance (specially to fluorine-containing organic electrolytes), antistatic and insulating properties. Tightness is ensured by fuororubber sealing rings and an optical window. As detailed below, electrodes, separator, electrolyte and current collectors are placed in the groove at the middle of the lower shell.

For our experiments, we chose the widely employed Li‖Cu half-cell configuration (Figure 2-2) [2], since easy to assembly and avoiding all interference phenomena which would be involved by the use of actual cathode materials. In order to prevent Li salts hydrolysis and Li foil oxidation, the electrochemical cell is assembled in an argon-filled glove box (MBraun M200B; O_2 < 0.1 ppm and H_2O < 0.1 ppm). All solvents are previously dehydrated using molecular sieves (4 Å, Sigma-Aldrich Corporation). Electrolytes are fully mixed using a minishker MS2 IKA, then left for 12 h in an argon-filled glovebox before use. Firstly, two Cu foils (10 mm x 100 mm, Goodfellow) are clipped at the two sides of the groove at the middle of the lower shell (Figure 2-2b). Then, a Li foil (10 mm x 10 mm, Sigma-Aldrich Corp.) is placed beside the Cu foil

(Figure 2-2c) and a glass fiber (Whatman) is used to fill the groove and separate the Li and the counter Cu foils (Figure 2-2d). Finally, 140 µL of electrolyte are added dropwise, so as to completely soak the fiber (Figure 2-2e), and the optical window is placed at the upper shell to seal the system (Figure 2-2f). In the so-assembled cell, the Li metal foil is the counter (and reference) electrode, the Cu foil in contact with it is the current collector, the opposite Cu foil is the working electrode and the glass fiber is the separator.

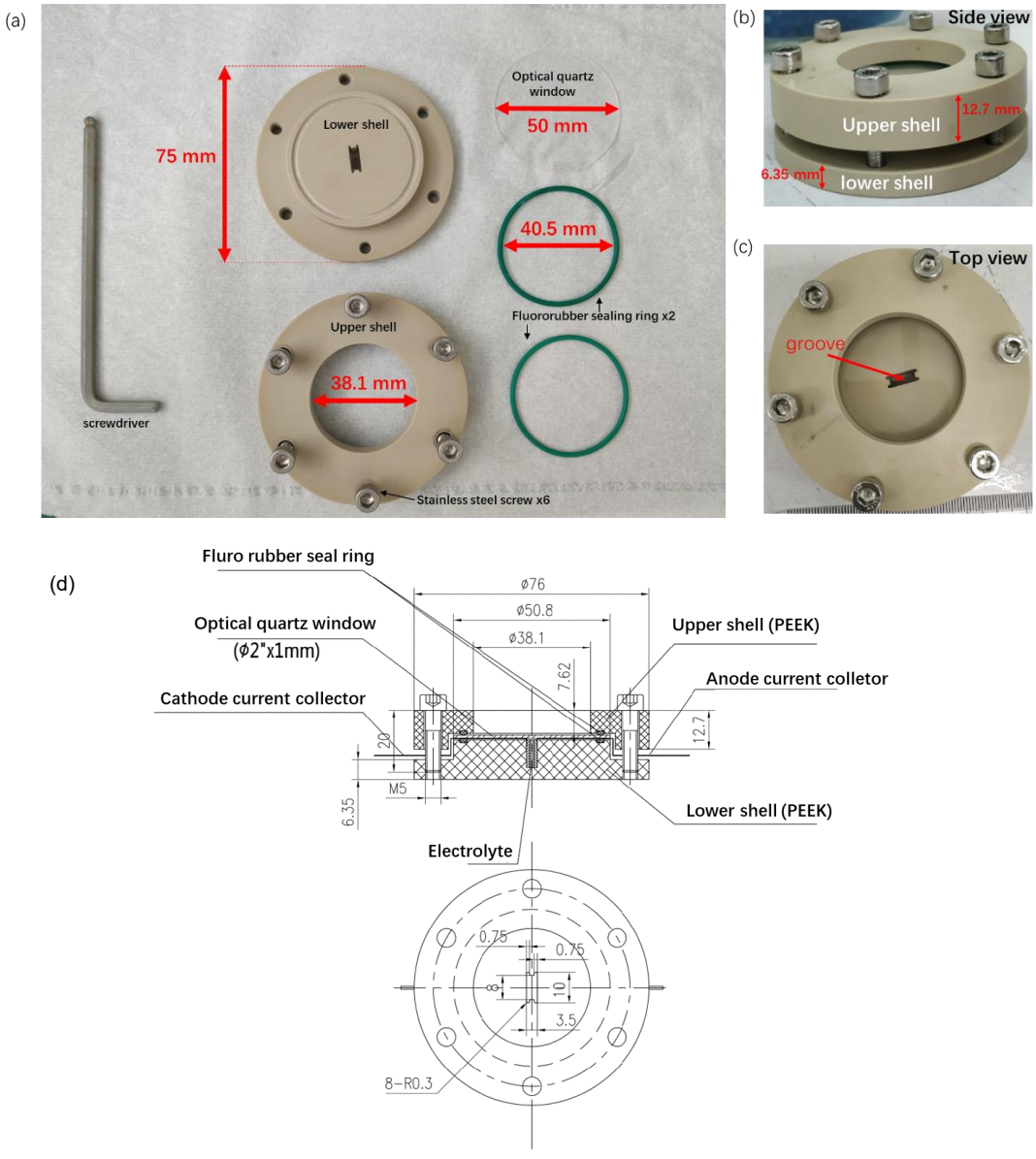


Figure 2-1. (a) Components, (b) side view, (c) top view and (d) schematic of the assembly of the optical cell used for *in situ* µ-Raman spectroscopy [1].

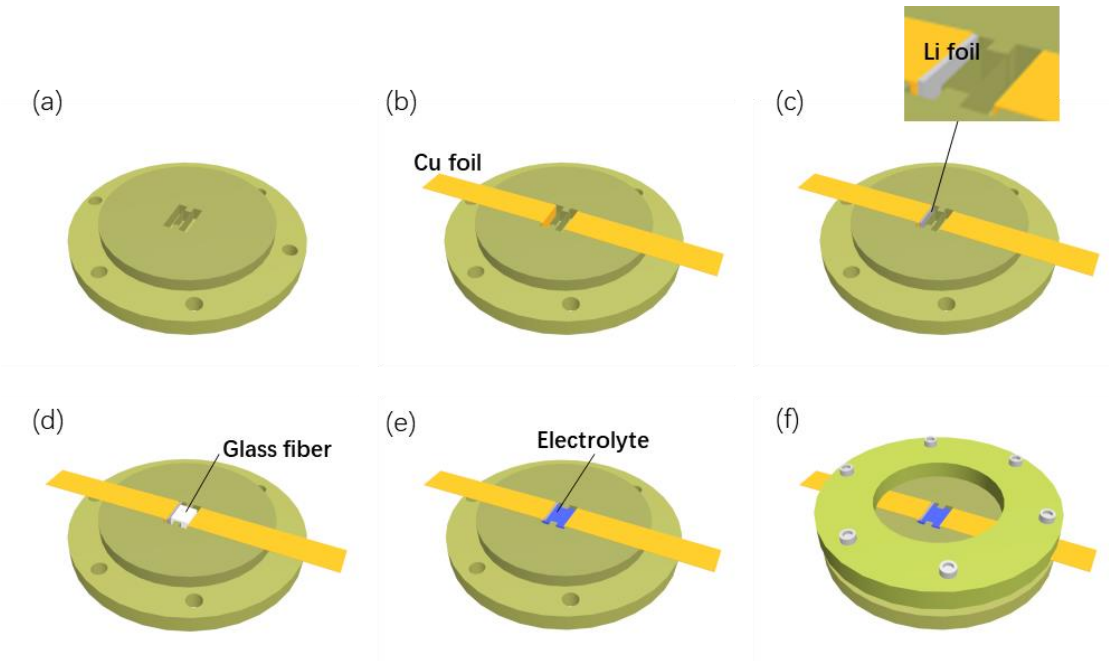


Figure 2-2. The different steps of the assembly of the *in situ* optical cell according to the Li‖Cu half-cell configuration (order: a-f).

2.3 Electrochemical measurements

The electrochemical properties of the Li-metal cell are characterized by Li plating curves, electrochemical impedance spectroscopy (EIS), linear sweep voltammetry (LSV) and the evaluation of both cycling performance and average Coulombic efficiency (CE). In the following paragraphs, we present the principle of these characterizations and the experimental conditions.

Unless indicated otherwise, electrochemical measurements have been carried out with the SP-150 potentiostat/galvanostat from Biologic, including an electrochemical impedance spectroscopy (EIS) module and controlled by the EC-lab software [3].

2.3.1 Li plating curves

The processes of SEI film formation, metallic Li nucleation and growth have been studied under chronopotentiometry conditions i.e. a constant current is applied to the working electrode and the potential is recorded as a function of time. The cell set-up and usual electrochemical conditions are reported in Figure 2-3: a constant current I_s = -1 mA is applied during 1 h so that Li plating capacity is 1 mAh cm^{-2} (the surface area of the Cu current collector is 1 cm^2).

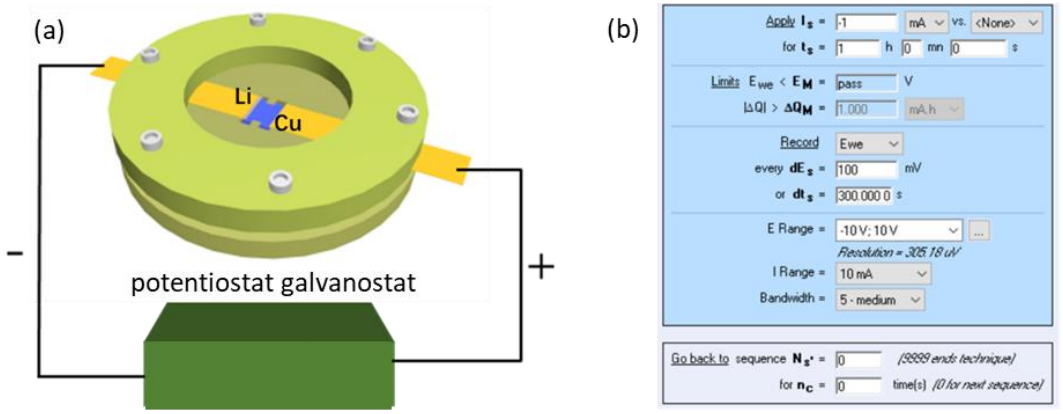


Figure 2-3. (a) Electrochemical set-up and (b) typical chronopotentiometry conditions, as entered in the software interface, for the study of Li plating with the Li‖Cu cell.

The so-obtained discharge, voltage vs. capacity, curves typically show 3 main steps (Figure 2-4): (i) the sudden drop of the cell potential from OCV (~ 3V) to 0 V, corresponding to the SEI film generation by reduction of the electrolyte components, then, at negative potentials, (ii) the Li nucleation and (iii) growth processes. The overpotential related to the starting of the Li deposition process i.e. nucleation (see Figure 1-13), corresponding to -0.104 V in the example reported in Figure 2-4, is evaluated from the difference between the lower voltage attained by the cell during the discharge (-0.547 V) and the potential plateau finally achieved by the system over the longer period (-0,443 V).

2.3.2 Electrochemical impedance spectroscopy

The electrochemical impedance spectroscopy (EIS) technique is widely used for the analysis of interfacial properties of electrochemically active materials as well as to measure their electronic and ionic conductivities [4]. EIS consists to apply a sinusoidal current (or voltage) signal (of low amplitude around a nominal value) to the electrochemical device and to measure the alternating voltage (or current) response, recording phase shift and amplitude changes (Figure 2-5).

Impedance spectra are usually obtained by varying the frequency ω of the exciting signal and recording the system response as a function of ω. The electrochemical impedance, i.e. the opposition to alternating current/voltage presented by the combined effect of the system resistance and reactance[5], is defined as the ratio between the voltage

[5] Where reactance is the opposition presented to alternating current by inductance or capacitance [4]. Greater reactance gives smaller current for the same applied voltage. Reactance is similar to resistance in this respect, but differs in that reactance does not lead to dissipation of electrical energy as heat.

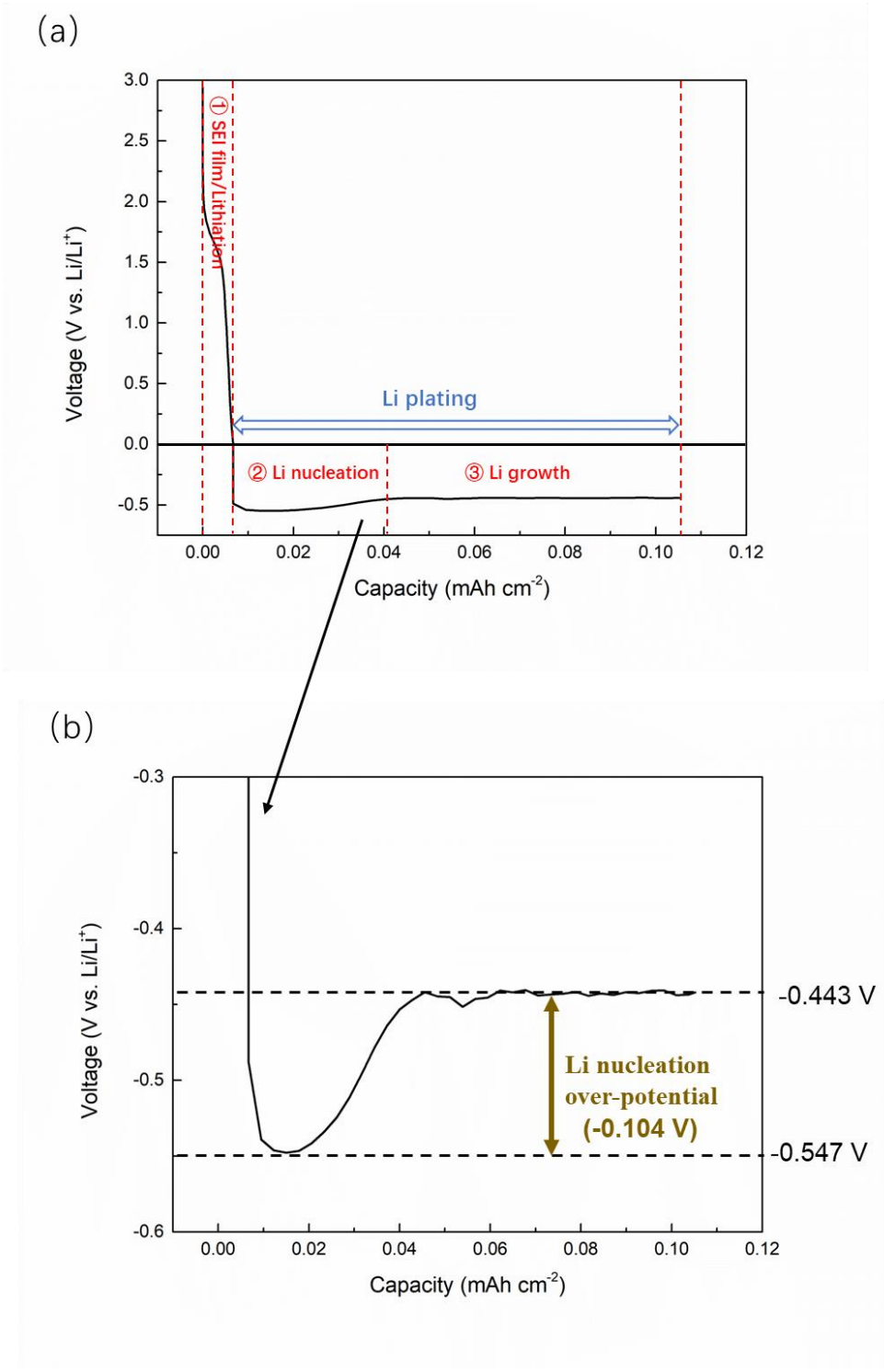


Figure 2-4. (a) Overall discharge curve of the Li‖Cu cell obtained under chronopotentiometry conditions and (b) magnification of Li plating range (steps ② and ③).

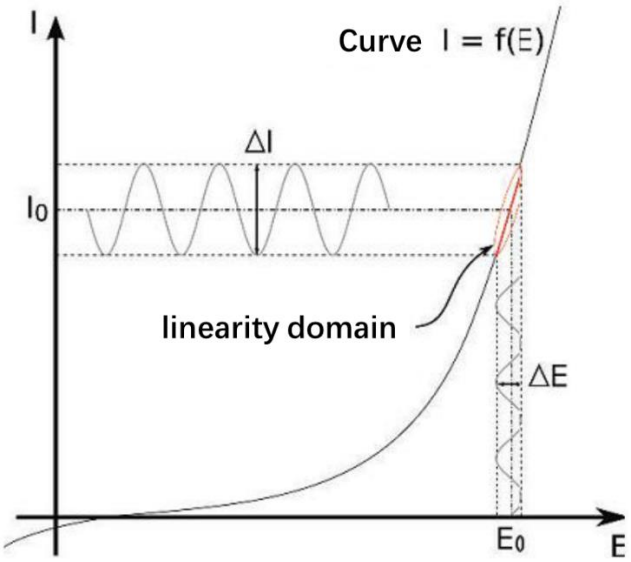


Figure 2-5. Principle of electrochemical impedance spectroscopy (according to [4]).

at the terminals of the system and the current passing through it. This ratio can be expressed as a complex number [4]:

$$Z(\omega)=\left|\frac{\Delta E}{\Delta I}\right|\cdot e^{j\Phi(\omega)}=\mathrm{Re}\big(Z(\omega)\big)+j\mathrm{Im}(Z(\omega)) \qquad \text{Equation 2-1}$$

where $\omega=2\pi f$ with ω the angular velocity in rad s^{-1} and f the frequency in Hz.

Results from EIS are usually represented according to two ways: the Bode and/or the Nyquist plot. In the Bode chart, the magnitude and phase of the impedance are plotted as a function of frequency, whereas in the Nyquist plot the imaginary part of the impedance is plotted as a function of the real part for each frequency. Figure 2-6 presents an example of Nyquist plot obtained in our study. The semicircle-like spectrum exhibits two points of intersection at the real part axis, where the value of the imaginary part is zero: R_{Ohm} and $R_{Ohm}+R_{ct}$. The resistance measured at R_{Ohm} can be attributed to the sum of contributions from the electrolyte, the separator and the current collectors. The other factors usually being negligible, R_{Ohm} can be considered to correspond to the ohmic resistivity of the electrolyte. R_{ct} originates from the charge transfer resistance at the electrode/electrolyte interface. Excessive electrolyte degradation giving rise to thick SEI films or, more generally, bad quality SEI are usually associated to larger R_{ct}.

The EIS measurements reported in this work were carried out by potential perturbation (PEIS) and performed in the frequency range from 1 x 10^{-1} to 1 x 10^{5} Hz with a voltage amplitude of 5 mV (Figure 2-7).

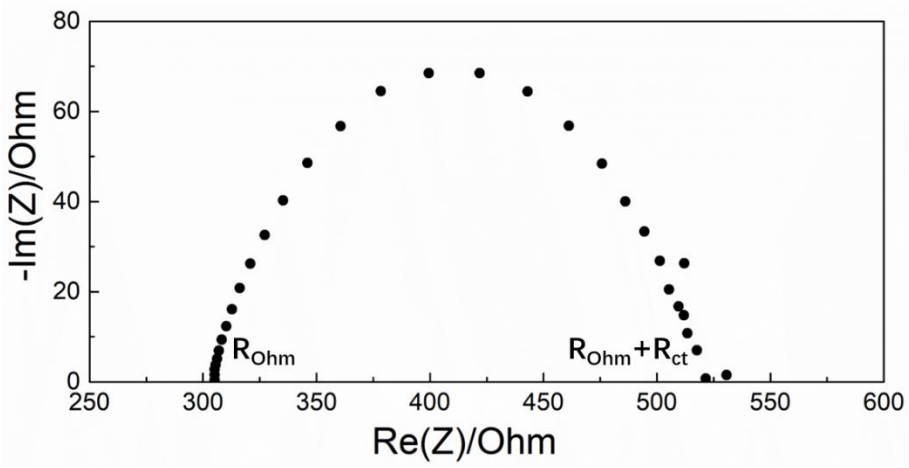


Figure 2-6. An example of Nyquist plot obtained with the Cu‖Li cell filled with 4 M $LiPF_6$ solution in DMC:HFPM (7:3, v/v).

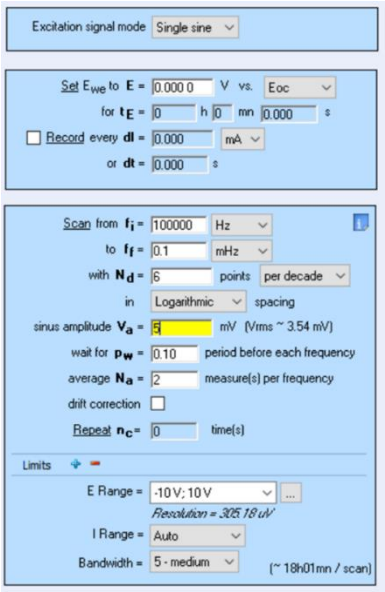


Figure 2-7. Typical conditions for the PEIS characterizations as entered in the software interface.

2.3.3 Linear sweep voltammetry

The reductive (in)stability of the different studied electrolytes has been tested by linear sweep voltammetry (LSV), carried out with a potentiostat/galvanostat 1470E from Solartron. LSV is an electroanalytical method consisting in measuring the current as the potential is varied continuously in time. Here, LSV consisted in a single linear sweep from OCV (~ 3.0 V) towards negative potentials, at the sweep rate of 0.1 mV s^{-1} (Figure 2-8a). A negative current peak is then observed before the potential corresponding to the Li deposition phenomenon i.e. between 3.0 and 0.0 V. Figure 2-8b reports the example of the redox peak appearing at 1.64 V during the LSV test carried

out with the Li‖Cu cell filled with the electrolyte 1 M $LiPF_6$ in EC:DEC (1:1, v/v). The negative peak is due to the reduction reaction of species belonging to the electrolyte, e.g. solvent. The current intensity involved and the potential corresponding to the maximum of the peak provide information on the electrolyte stability and components of the SEI film.

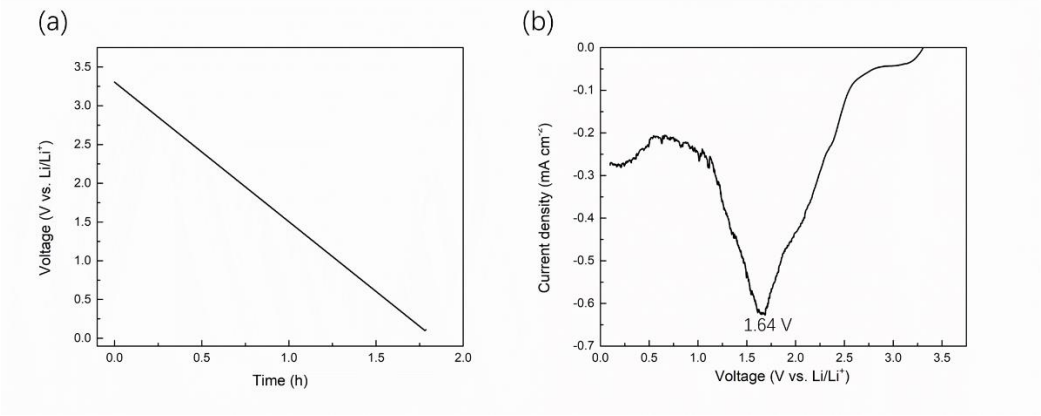


Figure 2-8. (a) Linear potential sweep and (b) the corresponding current vs. voltage LSV curve as obtained with the Li‖Cu cell filled with 1 M LiPF6 in EC:DEC (1:1, v/v) (voltage range from 3.0 V to 0.1 V).

2.3.4 Cycling performance

Cycling performance test is a significant way to evaluate Li-based batteries both in laboratory and industry. As far as Li metal batteries are concerned, CR2032 coin cells are mostly used for this test. The two configurations of coin cell used in this work are reported in Figure 2-9. The working electrode is the Cu foil in the half-cell (Figure 2-9a) while it corresponds to the cathode in the full-cell (Figure 2-9b). In the last case, the active material is $LiFePO_4$ on Al foil as current collector. The amount of electrolyte used is 50 mL. The separator is a Celgard film. Spacers and springs are made by stainless steel.

The cycling performance measurements were carried out on a battery testing system LandCT2001 from LAND electronics Co, Ltd. Measurements consisted in operating several cycles of Li plating and stripping under galvanostatic conditions and reporting the coulombic efficiency CE, i.e. the ratio between the Li stripping and Li plating capacities, or the electrochemical capacity C as a function of the cycle number. For the Li‖Cu half-cell test, each cycle consisted in a first step of Li plating on Cu foil at 1 mA cm^{-2}, up to the amount corresponding to 1 mAh cm^{-2}, followed by Li stripping carried out at the same current density up to the cut-off potential of 1 V vs. Li/Li^+.

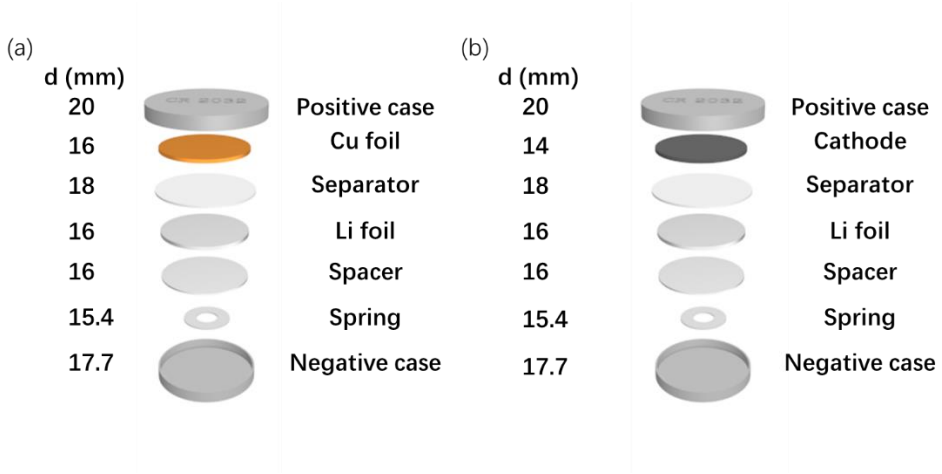


Figure 2-9. The CR2032 coin cell assembly for (a) Li‖Cu half-cell and (b) full cell tests.

An example of half-cell test is shown in Figure 2-10, comparing the CE decrease with the cycle number of bare copper foil to other improved Cu electrodes (see more details in chapter 4, § 4.2).

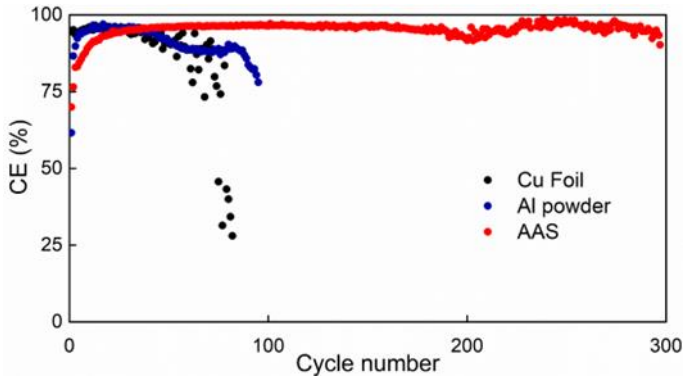


Figure 2-10. Li‖Cu half-cell cycling performance tests comparing different working electrodes consisting of surface modified Cu foils: (●) bare, (●) Al powder coated and (●) coated with Si–Al alloy micro-spheres.

For full-cell tests, the $LiFePO_4$ (LFP) was used as cathode material. The LFP electrode (loading capacity ~2.5 mAh cm^{-2}) was prepared by casting a well-mixed slurry of LFP, Carbon black (Super-P) and polyvinylidene difluoride (PVDF) (8:1:1) in NMP (1-Methyl-2-pyrrolidone) on Al foil, followed by vacuum drying at 120°C for 12h. Before the performance test, the cell was conditioned by 5 cycles at the 0.1 C charge/discharge rate, in the voltage range of 2.5-4.4 V vs. Li/Li^+. Then, electrochemical cycling was carried out at 0.33 C charge/discharge rate.

2.3.5 Average coulombic efficiency

The coulombic efficiency is usually used to describe the released battery capacity. It refers to the ratio of the discharge capacity after the full charge and the charging capacity of the same cycle. In this work, the average CE of the Li‖Cu coin half-cell has been measured according to the modified Aurbach method reported by Adams *et al.* [5]. Typically, this method consists of four main steps as illustrated in the Figure 2-11: (i) a first preliminary cycle, corresponding to Li plating for 1.4 mAh cm^{-2} followed by stripping of all the residual Li at cutoff potential of 1 V vs Li/Li^+; (ii) deposition of 1.4 mAh cm^{-2} of Li; (iii) 10 repeated cycles of Li stripping/plating of 0.35 mAh cm^{-2}; (iv) final stripping of all the residual Li at cutoff potential of 1 V vs Li/Li^+. All steps are carried out at the same current density of 0.2 mA cm^{-2}. The CE is then calculated as follows:

$$CE=\frac{nQ_c+Q_s}{nQ_c+Q_p} \qquad \text{Equation 2-2}$$

where n is the cycle number, Q_p is the initial Li plating amount (1.4 mAh cm^{-2}) at the second step, Q_c is the Li striping/plating amount related to the third step consisting of repeated 10 cycles (0.35 mAh cm^{-2}) and Q_s the final stripped amount of the residual Li at the fourth step.

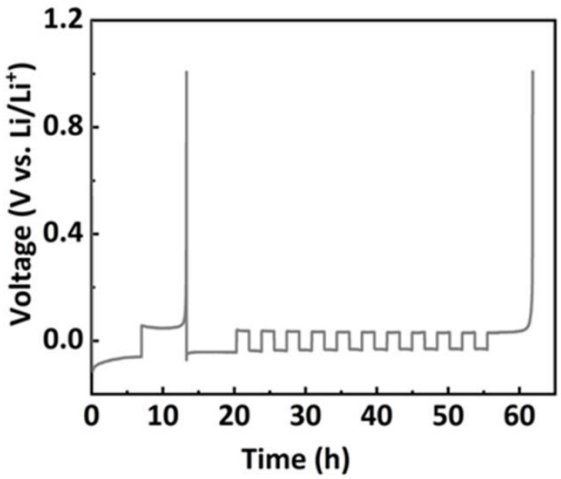


Figure 2-11. Voltage vs. time plot of the Li‖Cu half-cell cycling used to determine the average CE, according to the modified Aurbach method [5]: example of the electrolyte 6 M LiFSI in DMC.

2.4 Raman micro-spectroscopy

2.4.1 Introduction

Raman micro-spectroscopy allows to probe the volume of transparent materials with a

spatial resolution of the order of a few μm and a temporal resolution of the order of a few minutes. Furthermore, Raman micro-spectroscopy is a sensitive, non-invasive and non-destructive technique for the determination of molecular compositions and chemical gradients. All these features make it particularly suitable for the study of the electrolyte for Li-metal batteries, more particularly solvation structures and Li^+ concentration gradients which are key parameters affecting the SEI formation and the Li deposition morphology, thus the electrochemical performances.

The general principle of Raman spectroscopy i.e. the scattering of incident light at an energy shifted by the vibrational energy (hν) of the molecule, is reported in Annex 1. Here below we introduce some aspects of micro-spectroscopy and describe the experimental set-up for *ex* and *in situ* studies as well as the procedure implemented for the treatment of spectroscopic data.

2.4.2 Principle of Raman micro-spectroscopy and experimental configuration

Raman micro-spectroscopy is based on the focusing of an exciting laser beam in a small volume (of the order of a few μm^3) of the sample and on the analysis of the inelastic scattering of light induced by this volume. The Raman scattering resulting from this small volume contains structural, qualitative and quantitative information. The probed volume can be estimated according to:

$$V = \pi\left(\frac{d}{2}\right)^2 \Delta z \qquad \text{Equation 2-3}$$

where d is diameter of the focal point and Δz the axial resolution. Both depend on the wavelength of the exciting radiation and the numerical aperture of the microscope objective used, according to the following equations:

$$d = \frac{1.22\lambda_{ex}}{NO} \qquad \text{Equation 2-4}$$

$$\Delta z = \frac{\pm 4.4 n \lambda_{ex}}{2\pi (NO)^2} \qquad \text{Equation 2-5}$$

where λ_{ex} is the wavelength of the exciting laser, NO the numerical aperture of the objective and n the ratio between the optical indexes of the probed material and of the external environment. These parameters are practically invariant for all measurements reported in chapter 3 and 4, since the exciting laser and the objective used was always the same i.e. Ar-Kr laser with λ = 659.55 nm and 50X Leica objective HCX PL Fluotar with NO = 0.55. Only the composition of the electrolyte changes but, considered that

all the samples investigated appeared transparent to the visible light, the effect on the optical index of the liquid mixture can be considered negligible. Thus, the probed volume is assumed to be constant, resulting from d = 2 μm and Δz = 10 μm.

Raman spectra were recorded with a HORIBA Jobin LabRAM HR800UV confocal spectrometer equipped with a charge coupled device detector (CDD) with a 1800 grooves mm^{-1} grating (spectral resolution around 1 cm^{-1}) and cooled by a double Peltier effect. A Si reference (Raman band at 520.7 cm^{-1}) was employed for spectral axis calibration before the daily experiment.

As far as the *ex situ* study is concerned, Li salts, solvents and their mixture (electrolyte) were analyzed in sealed quartz glass tube (Figure 2-12a). Raman spectra were typically collected with 30 s exposure time and 3 accumulations at a nominal laser power of 50 mW (~20 mW at the sample). An example of raw spectrum (1 M $LiPF_6$ in DMC) is shown in Figure 2-12b. Strong fluorescence could sometimes be observed due to fluorine components such as $LiPF_6$, so that some data processing (e.g. baseline) was needed (see the following).

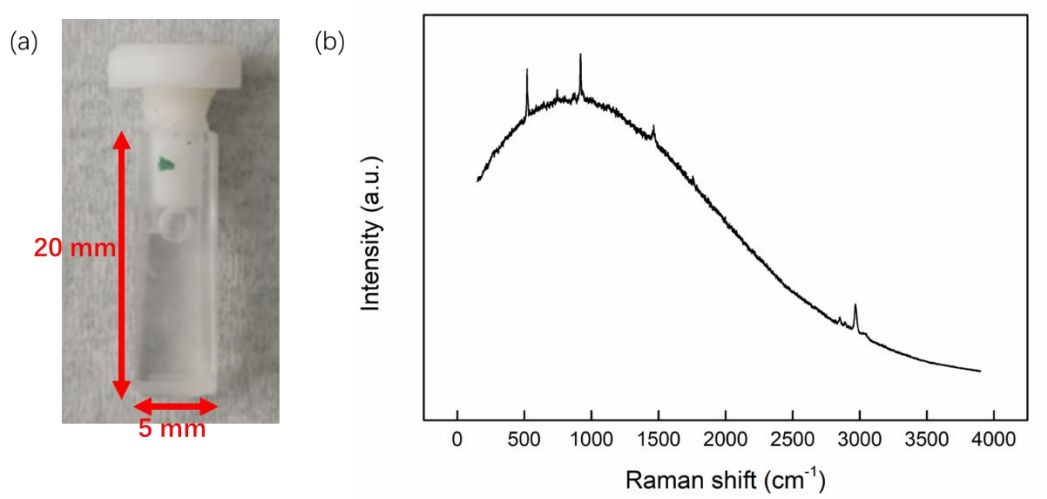


Figure 2-12. (a) the quartz glass tube used as sample holder in *ex situ* Raman analyses and (b) the raw spectrum of 1 M $LiPF_6$ in DMC.

In situ Raman study was carried out with the optical Li‖Cu half-cell whose components and assembly are illustrated in section 2.2. Figure 2-13 reports the schematic of the experimental set-up and coupling with the Raman spectrometer. The cell is placed on an automatic sliding plate allowing micro-displacements, so as to collect spectra at certain fixed positions along the xy-plane during the cell operation, typically at 10, 50 and 100 μm from the Cu electrode (Figure 2-13c). In order to study the occurring and evolution with time of the Li^+ concentration gradients due to Li^+ depletion at the

electrode/electrolyte interface, the spectra acquisition started at the same time as the Li plating process i.e. as soon as the cell potential dropped below 0 V (corresponding to the end of the SEI generation step). Li plating was carried out at the fixed capacity of 1 mAh cm^{-2} but at different current densities: 0.5, 1 and 2 mA cm^{-2}. Raman spectra were collected over time at the 3 different positions for 3 different experiments until the end of the plating process. Each spectrum results from 3 accumulations during 20 s. As for *ex situ* measurements, the laser nominal power was 50 mW (around 20 mW at the sample). An example of *in situ* Raman spectroscopy is shown in Figure 2-14. It can be observed that the intensity of Raman signals belonging to the Li^+ counter-anion PF_6^- and Li^+ interacting solvent molecules (δ O-C-O and ν C-O vibrational modes) change as the Li plating process progresses, attesting the modification of the Li^+ concentration at the probed position.

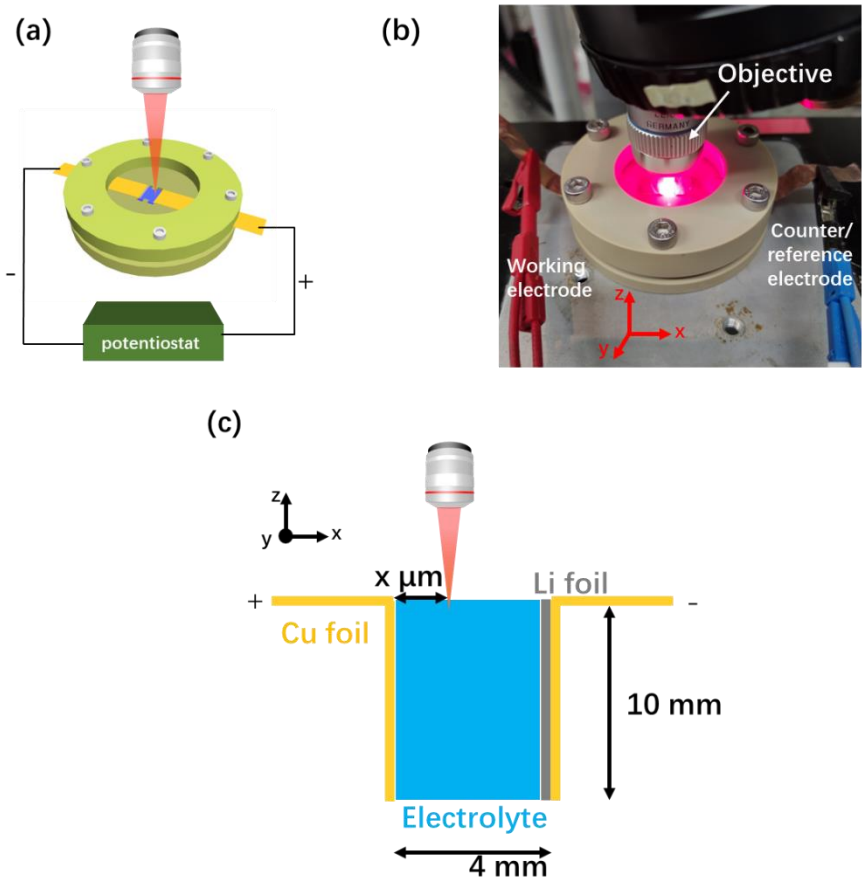


Figure 2-13. (a) Schematic of the experimental set-up for *in situ* Raman micro-spectroscopy, (b) image of the Li‖Cu half-cell during operation at the Raman microscope and (c) illustration of the focusing of the laser beam at the electrolyte allowing the acquisition of Raman spectra at different distances (x = 10, 50, 100 µm) from the Cu electrode.

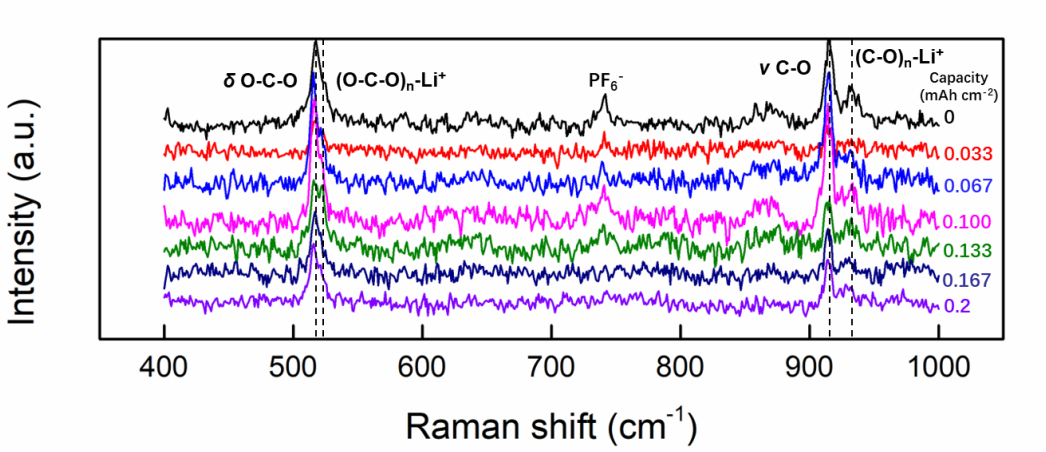


Figure 2-14. Example of *in situ* Raman spectroscopy of the electrolyte 1 M $LiPF_6$ in DMC, in the Li‖Cu half-cell operating at 1 mA cm^{-2}: spectra collected at 10 µm from Cu electrode.

2.4.3 Data processing

In order to carry out the quantitative measurement of the different chemical species composing the sample, raw Raman spectra usually need to be processed. In our case, there are 2 essential steps to be carried out: the correction of the baseline and the measurement of the Raman band surface by integration.

2.4.3.1 Baseline correction

Raman scattering and fluorescence emission are two competing phenomena, which have similar origins [6]. Thus, Raman spectra are often affected by fluorescence which can hides Raman features. In our specific case, the salt $LiPF_6$ exhibits significant fluorescence (see Figure 2-12b and 2-15a) affecting the baseline. The last has then to be corrected to allow the accurate measurement of the Raman peak surfaces. A baseline is calculated using the Labspec 5 software, according to a polynomial function having a degree of 8, then subtracted to the whole spectral range of interest (here between 400 and 1000 cm^{-1}) to finally obtain a Raman spectrum with a linear baseline whose mean intensity is around 0 (Figure 2-15). This is a critical action since the original intensity of the Raman signal must be preserved. The quality of the baseline subtraction strongly depends on the researcher's choice of the background points through which the baseline is constrained to pass (see square points in Figure 2-15b). Their position must avoid any Raman signal.

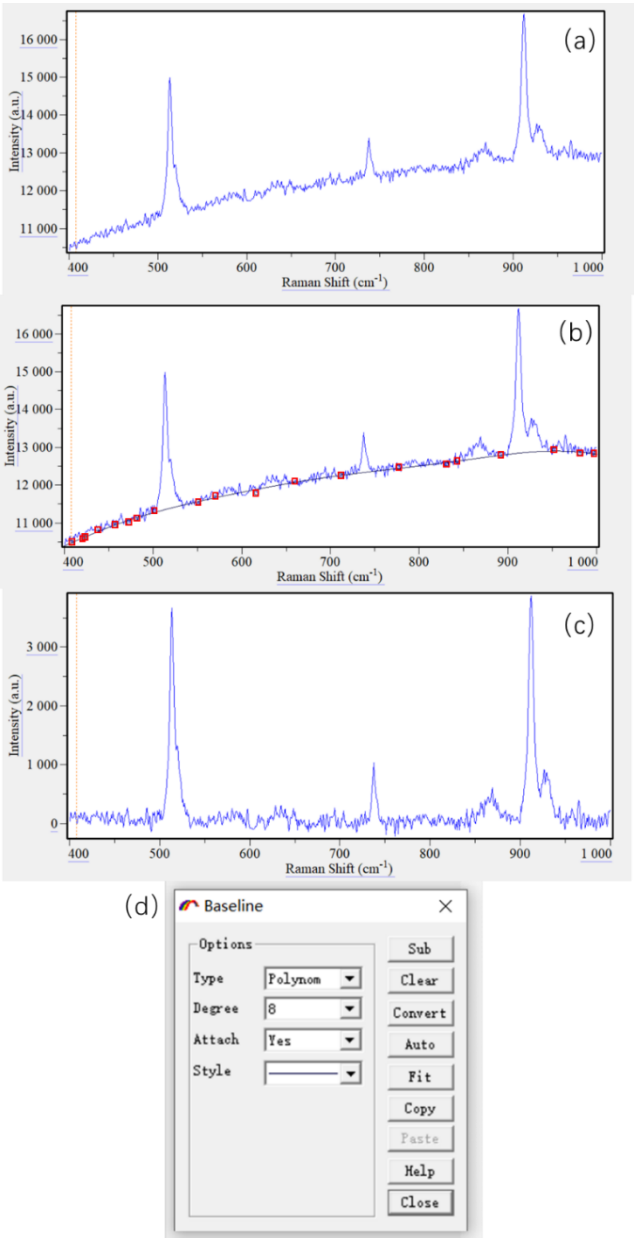


Figure 2-15. (a) Raw Raman spectrum of 1 M $LiPF_6$ in DMC (400 – 1000 cm^{-1} range), (b) corresponding baseline, (c) spectrum after the baseline subtraction and (d) baseline parameters entered in the software interface.

2.4.3.2 Peak fitting

Once the baseline correction carried out, the local concentration of a given molecular species can be calculated from the overall intensity, i.e. surface, of the corresponding Raman peak. Indeed, the Raman signal intensity $S_{\Delta\lambda}$ is related to the number of scattering molecules in the volume probed by the exciting radiation by the following equation:

$$S_{\Delta\lambda}=I_0\sigma_{\lambda_{ex}}N\Omega S_d s_{\Delta\lambda}=f(N) \qquad \text{Equation 2-6}$$

where I_0 (W m^{-2}) is the laser irradiance at the sample, $\sigma_{\lambda_{ex}}$ (m^2 sr^{-1} mol^{-1}) the differential cross-section for the Raman band excited by the monochromatic radiation of wavelenght λ_{ex}, N (mol) the number of molecules of the scattering species in the probed volume, Ω (sr) the solid angle of collection of the Raman light, S_d (m^2) the area of the detector lighted by the scattered light and $s_{\Delta\lambda}$ the average sensitivity of the detector in the wavelength range $\Delta\lambda$.

In this work, in order to determine the Li^+ local concentration in the electrolyte, we applied appropriate calibration procedures using the ratio between the signal area related to Raman active species coordinated to Li^+ (i.e. organic solvent molecules or counter-ion PF_6^-) and those from free, i.e. non solvating, solvent species (details in sections 3.2 and 4.3 of chapter 3 and 4, respectively). The surfaces of the different Raman bands were obtained by peak fitting with Labspec 5 software, using the Gauss function and the least-square method to reproduce the experimental spectral profile (Figure 2-16).

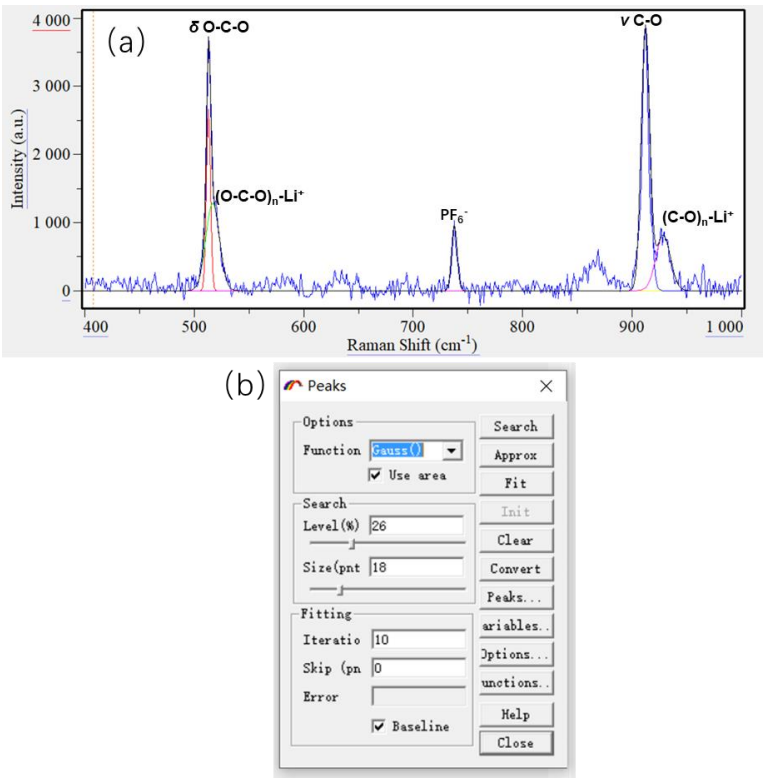


Figure 2-16. (a) Example of peak fitting of the Raman spectrum of 1 M $LiPF_6$ in DMC and (b) related parameters entered in the Labspec 5 software interface.

2.5 Materials

For preparing the electrolytes investigated in our study, we used: $LiPF_6$, LiFSI and KPF_6

as salts; DMC, DME, EC, DEC and Diethyl ether as solvents; HFPM and TTE as diluents. Lithium hexafluorophosphate ($LiPF_6$, 98%), potassium hexafluorophosphate (KPF_6, 99%), dimethyl carbonate (DMC, 99%) and 1,1,1,3,3,3-hexafluoroisopropyl methyl ether (HFPM, 99%) were purchased from Sigma-Aldrich Corporation. 1,2-dimethoxyethane (DME, 99%) was purchased from Alfa Aesar, lithium bis(fluorosulfonyl)imide (LiFSI, 98%) was purchased from Aladdin, ethylene carbonate (EC), diethyl carbonate (DEC) and 1,1,2,2-tetrafluoroethyl-2,2,3,3-tetrafluoropropyl ether (TTE, 98%) was purchased from Macklin Inc. Diethyl ether (99.98%) was purchased from Fisher Scientific. The Cu (99.9 %, thickness: 8 μm) and Al foils (99%, thickness: 0.4 μm) were purchased from Goodfellow. Potassium hydroxide (KOH, 90%) and potassium bicarbonate ($KHCO_3$, 99.7%) were purchased from Sigma Aldrich. Nafion-117 was obtained from Fuel Cell Store. All the solvents and diluents were dehydrated using molecular sieves (4 Å, Sigma-Aldrich Corporation) before use. All the electrolytes were fully mixed using a minishker MS2 IKA, and then left for 12 h in an argon-filled glovebox (MBraun M200B; $O_2 < 0.1$ ppm and $H_2O < 0.1$ ppm) before use.

2.6 Complementary measurements (other than μ-Raman)

Attenuated total reflectance infrared (ATR-FTIR) spectra were recorded in the 600 to 4000 cm^{-1} range with a ThermoFisher NEXUS spectrometer equipped with a diamond ATR "Golden Gate" plate. A vial cap was put above the liquid sample drop to avoid volatilization. The ^7Li Nuclear Magnetic Resonance (NMR) spectra were carried out with a BRUKER Avance III – 500MHz spectrometer with a reference tube of 1 M LiCl in D_2O. Scanning electron microscopy (SEM) was performed on a FEI QUANTA 250 FEG microscope (chapter 3) and a Hitachi S4800 microscope (chapter 4 & 5). Elemental analysis of the same sample was carried out by energy-dispersive X-ray spectroscopy (EDS) on a Zeiss EVO HD15 device coupled with an Oxford Instruments X-Max N SDD detector. X-ray photoelectron spectroscopy (XPS) characterization from chapter 3 was performed on a Kratos Axis Ultra DLD spectrometer, with a Mg Kα exciting radiation source at a constant power of 100 W (15 kV and 6.67 mA). XPS characterization from chapter 4 & 5 was performed on a Thermo Electron ESCALAB 250 spectrometer equipped with a monochromatic radiation source (Al kα = 1486.6 eV) and the charge was compensated by an electron beam (-2eV). The XPS analysed surface had a diameter of 500 μm and the XPS Spectra were calibrated in binding energies

relative to the energy of C 1s at 284.4 eV (C-C bonding). The Li deposits on Cu foil were sealed in a PTFE box filled with Ar gas for SEM and XPS analysis. Ionic conductivities were measured by using a DDS-307A conductivity meter (LEICI, Shanghai INESA Co.) in a glovebox (MBRAUN, $H_2O \leqslant 0.1$ ppm, $O_2 \leqslant 0.1$ ppm).

Extended X-ray absorption fine structures

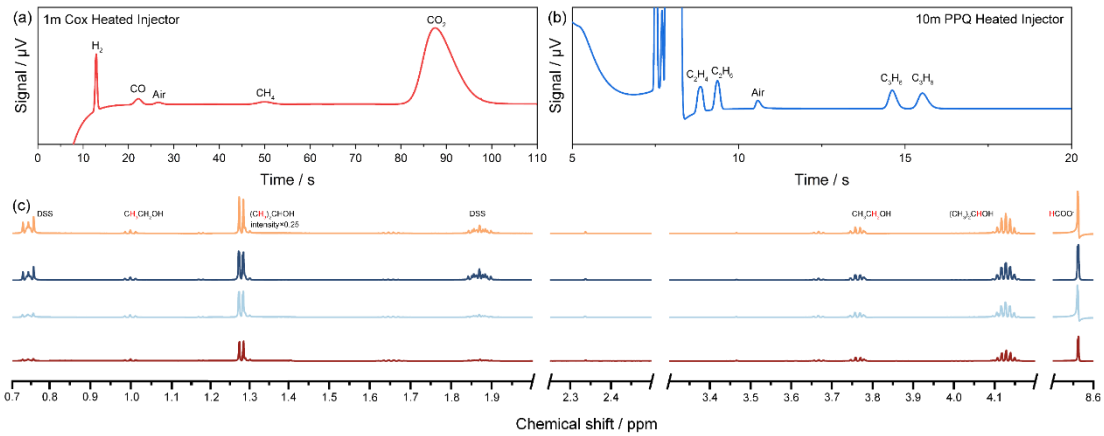
EXAFS spectra were obtained at the Beijing Synchrotron Radiation Facility (BSRF). Curve fitting and data analysis were carried out by the Artemis and IFEFFIT softwares. Each sample of XAS data was aligned and processed using the Athena program. Spectra were baseline corrected using a linear pre-edge function between -200 and -50 eV and normalized using a linear or quadratic function between 150 and 700 eV, including a flattening function in the post-edge region. The XAFS signal was isolated from the adsorption edge background using a fit to a cubic spline with nodes defined by the AUTOBKG function in IFEFFIT, with a *k*-weight of 3 and with the Rbkg parameter set to 1. Fourier transformations of k^3-weighted spectra were using a Kaiser-Bessel window with a 1 $Å^{-1}$ sill width. The magnitude parts of the Fourier transformed spectra are reported with a radial distance scale that is not corrected for phase shift. For EXAFS fitting, theoretical scattering paths were calculated with FEFF6 using Artemis. All EXAFS spectra were fit for distances (ΔR), coordination number (CN), and mean-square displacement of interatomic distance (σ^2) using the Artemis interface with a fixed amplitude reduction factor (S_0^2) of 0.707 to 1.000. The parameters such as interatomic distance (R), CN, the difference in threshold energy (ΔE_0) and Debye-Waller factor (σ^2) were first established with reasonable guesses and then were fitted in R-space. The error in the overall fits was determined using the R-factor = $\Sigma(\chi_{data} - \chi_{fit})^2 / \Sigma(\chi_{data})^2$. Good quality fits correspond to a R-factor < 0.05.

Analysis of gaseous and liquid products from the CO_2RR experiment

The analysis of gaseous products was carried out using an Agilent Micro GC-490 gas chromatograph equipped with a TCD detector, a Molsieve 5A column and using argon as carrier gas.

The liquid products were quantified by ^{1}H nuclear magnetic resonance (NMR) spectroscopy. NMR spectra of freshly acquired samples were collected on a Bruker Avance III 600 MHz spectrometer with a cryoprobe Prodigy TCI with 10 % deuterated water (D_2O) and 0.1 % (w/w) of sodium trimethylsilylpropanesulfonate (DSS) as the

internal standard. A 1D sequence water suppression using excitation sculpting with gradients (zgesgp) was used for the acquisition (32 scans and 30s relaxation delay between pulses were used to allow complete relaxation of the protons).



GC calibration spectra for gas products quantification with (a) 1m Cox Heated Injector and (b) 10m PPQ Heated Injector. (c) NMR calibration spectra for liquid products at different known concentrations.

References

[1] https://www.mtixtl.com/PEEKSplitTestCellwithQuartzObservationWindowforin-situX-RayAnaly.aspx.

[2] C.-J. Huang, B. Thirumalraj, H.-C. Tao, K.N. Shitaw, H. Sutiono, T.T. Hagos, T.T. Beyene, L.-M. Kuo, C.-C. Wang, S.-H. Wu, W.-N. Su, B.J. Hwang, Decoupling the origins of irreversible coulombic efficiency in anode-free lithium metal batteries, Nature communications 12 (2021) 1452.

[3] https://www.biologic.net/support-software/ec-lab-software/.

[4] C. Gabrielli, Méthodes électrochimiques - Mesures d'impédances, dans les techniques de l'ingénieur P 2210 // Méthodes électrochimiques - Mesures d'impédances, Corrosion vieillissement (1994).

[5] B.D. Adams, J. Zheng, X. Ren, W. Xu, J.-G. Zhang, Accurate determination of coulombic efficiency for lithium metal anodes and lithium metal batteries, Advanced energy materials 8 (2018) 1702097.

[6] G. Panczer, D. de Ligny, C. Mendoza, M. Gaft, A.-M. Seydoux-Guillaume, X. Wang, J. Dubessy, M.C. Caumon, Raman and fluorescence, EMU notes in mineralogy 12 (2012) 61–82.

Chapter 3. Raman micro-spectroscopy study of the local composition and structure of low-, high- and localized high-concentration electrolytes: relationships with SEI properties and morphology of the Li deposit

3.1 Introduction

Through the contemporary history of battery research, replacing propylene carbonate (PC) by ethylene carbonate (EC) solvents in the electrolyte was probably one of the most important milestones leading to the commercialization of Li ion batteries. This action definitively tuned the interfacial chemistry between the graphite anode and electrolyte by the formation of the solid electrolyte interphase (SEI) that inhibits the irreversible graphite exfoliation caused by the co-intercalation of Li^+-solvent pairs [1]. Afterwards, designing functional electrolytes has always been a central issue for the development of emergent battery technologies. As already mentioned in chapter 1, for pursuing the ever-increasing demand of high-energy-density energy storage systems, replacing the graphite (339 mAh g^{-1} in form of LiC_6) by silicon (Si, 1970 mAh g^{-1} in form of $Li_{21}Si_5$) or Li metal (3860 mAh g^{-1}) anodes represents the challenge for next-generation Li batteries [2,3]. But the conventional low concentration electrolytes (LCEs, with a typical concentration of ≈1 M) used for the Li-ion batteries with graphite anodes are unable to undergo stable cycling with Si and Li anodes. The inhomogeneity and brittleness of the SEI layers derived from the LCEs are considered as the main cause of the uneven volume expansion and interphase failure of the high capacity Si and Li anodes [4,5]. Furthermore, the poor thermodynamic stability of the LCEs leads to fast reductive decompositions of the free solvents at the electrode/electrolyte interface, thickening the SEI, increasing the internal impedance of the cell and strongly limiting the lifetime [6].

Besides the efforts of using various electrolyte solvents, salts, and additives for improving the performances of the LCEs [7–12], high-concentration electrolytes (HCEs), ones of the most important concepts in recent electrolyte development, have shown great compatibility with the high-energy-density anodes [13–16]. Differently from the LCEs mainly consisting of solvent-separated ion pairs (SSIPs, where one Li^+ coordinates with 4 or more solvent molecules, Figure 3-1a) with a large relative amount

of free solvent molecules, HCEs have much higher salt/solvent ratios, resulting in the structural transition from SSIPs into contact ion pairs (CIPs) and ionic aggregates (AGGs) with much fewer solvent molecules (much more salt anions) in the solvation sheath of the Li^+ cations (Figure 3-1b). During the formation of the SEIs, the decomposition of the salt anions species occurs before that of solvent molecules, because of the lower energy of the lowest unoccupied molecular-orbital (LUMO). This allows the enrichment of the SEIs in inorganic species (such as LiF, Li_2O) with significantly improved stability [13,17]. Kinetically, the increase of the Li^+ transport number due to the anions confinement in the CIPs and AGGs is also a concern for the improved rate ability of HCEs [13]. Furthermore, the thermodynamic stability of the coordinated solvent molecules is much enhanced than that of the free solvent molecules, providing wider operation voltage and temperature range for HCEs compared to LCEs [18,19].

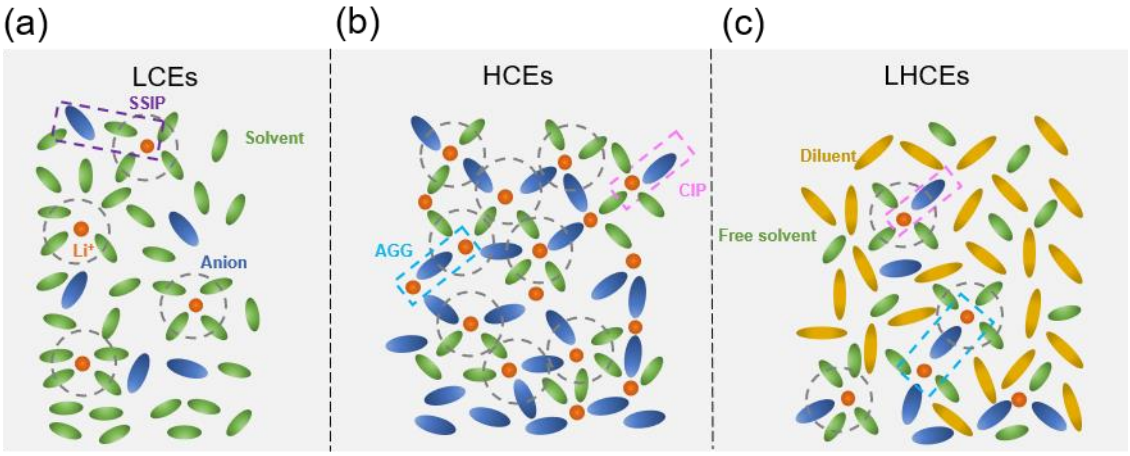


Figure 3-1. Solvation structures of (a) LCEs, (b) HCEs and (c) LHCEs.

Despite the above achievements, the high viscosity, poor wettability and high price of the HCEs still represent main drawbacks for their practical applications. Thus, a new class of localized high-concentration electrolytes (LHCEs) has been developed to further improve HCEs for high-energy-density Li batteries [20–23]. As already explained in chapter 1, the LHCEs are obtained by the addition of appropriate nonsolvating diluent species to the HCEs, *i.e.* molecules that cannot coordinate Li^+ cations but have good miscibility with their solvation complexes through dipole-dipole interactions. Consequently, the overall solvation structure of the HCE, involving CIPs and AGGs, is retained in the inner solvation sheath and the diluent forms an outer nonsolvating medium (Figure 3-1c) [24]. In principle, LHCEs not only exhibit the same

advantages of the HCEs in terms of forming high-quality SEIs and high chemical stability against Li metal anodes, but also have improved physical properties, as lower viscosity and higher wettability, providing their wide application in high-energy-density Li batteries.

The stability of the Li metal anode results from the overall properties of the electrode/electrolyte interface, including the charge transfer kinetic, the thermodynamic stability and the SEI nature, which are in turn all directly related to the chemical composition and concentration of the electrolyte. Consequently, the comprehensive understanding of the inner structure of the advanced electrolytes, especially HCEs and LHCEs, is of great importance. Despite some previous works have addressed the effect of the diluent type and content on the LHCE structure and Li metal battery performances [25,26], more detailed and direct experimental proofs are still needed for the better understanding of the diluent effect on the structure of the solvation sheath of Li^+ cations. The work reported in this chapter lies on the systematic Raman study of the chemical structures of a model HCE and its derivative LHCEs over a wide range of salt and diluent concentrations. The relationships with the Li deposition morphology, the SEI composition and, finally, the cycling performances of the electrochemical cell are investigated. The widely used lithium hexafluorophosphate ($LiPF_6$) and dimethyl carbonate (DMC) are employed as the basic salt and solvent to prepare LCEs and HCEs of different concentrations, while 1,1,1,3,3,3-hexafluoroisopropyl methyl ether (HFPM) is used as the diluent for the preparation of LHCEs. The nonsolvating property of HFPM is attested by the observation of $LiPF_6$ precipitation from $LiPF_6$/HFPM mixtures even at salt concentration as low as 0.1 M (Figure 3-2).

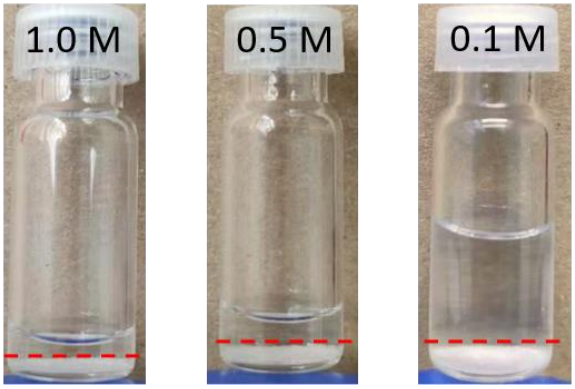


Figure 3-2. Images of 1.0 M, 0.5 M and 0.1 M $LiPF_6$ in HFPM. Consistent sediments can be observed in the bottoms of vials, indicating the nonsolvating property of HFPM.

Although the nonsolvating diluents added to LHCEs are usually considered not to affect the inner solvation structure, results reported below will show the impact of the diluent nature and relative amount on the solvation sheath of the Li^+ cations. By increasing the diluent amount, the number of free solvent molecules and the ratio of CIPs onto AGGs rise up simultaneously, showing that the diluent molecules not only create a nonsolvating medium, but also break the inner solvation structures via the dipole-dipole interactions between the diluent and solvent molecules. This phenomenon, observed for all the different diluents and salts studied here, affect the behavior of the Li‖Cu cell: better electrochemical performances are observed with moderately diluted LHCEs compared to the corresponding HCE and highly diluted LHCE obtained with the same constituents.

3.2 Evolution of the local solvation structure as a function of the electrolyte concentration

The Raman spectra of pure DMC, HFPM and $LiPF_6$ are shown in Figure 3-3. For DMC, different characteristic signals of stretching and bending vibrations (represented by symbols ν and δ, respectively) are observed, including δ O-C-O (518 cm^{-1}), ν C-O (918 cm^{-1}), ν C=O (1755 cm^{-1}), δ CH_3 (1461 cm^{-1}) and ν C-H (2824-3087 cm^{-1}) [27]. Because of the weakness of the ν C=O mode, the δ O-C-O and ν C-O signals are selected to study the Li^+ coordination behavior in the electrolyte (wavenumber range between 500 and 960 cm^{-1}). It should be mentioned that no significant modifications of the bands related to δ CH_3 and ν C-H vibrations were observed, which attests that there is no Li^+ coordination to the alkyl group.

Figure 3-4a reports Raman spectra collected for different concentrations of $LiPF_6$ in DMC, ranging from 0.1 to 6.0 M (the last being the saturation concentration). The corresponding molar ratios are listed in Table S3-1 of the Supporting Information (SI), reported at the end of the chapter. The gradual increase of coordination between DMC

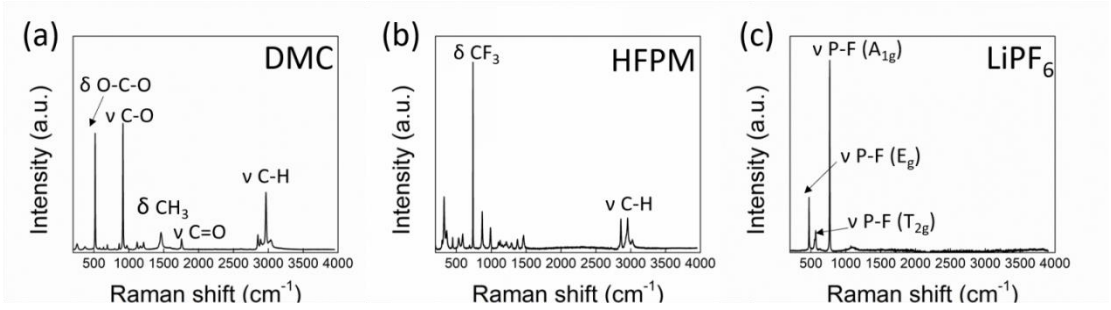


Figure 3-3. Raman spectra of pure (a) DMC, (b) HFPM and (c) $LiPF_6$.

and Li^+ with the increase of the $LiPF_6$ concentration is attested by the upshift of the δ O-C-O and ν C-O modes, from 518 cm^{-1} and 918 cm^{-1} (typical positions for free DMC) in the 0.1 M electrolyte to 525 cm^{-1} and 937 cm^{-1} in the 6.0 M electrolyte, respectively. This well attests the formation of solvated species [27] that will be referred as $(O\text{-}C\text{-}O)_n\text{-}Li^+$ and $(C\text{-}O)_n\text{-}Li^+$ in the following. Notably, signals from free DMC molecules are almost disappeared at $[LiPF_6]$ = 4.0 M. Simultaneously, the progressive upshift of the PF_6^- peak is observed, which thus approaches at the larger concentrations the characteristic peak of at 771 cm^{-1} observed in pure ionic solid $LiPF_6$ [28]. This shift corresponds to the solvate state transition from SSIP (741 cm^{-1}) to CIP (747 cm^{-1}) in the electrolytes from 0.1 to 3 M, and then to the formation of AGG (751 cm^{-1}) beyond 3 M. Different concentrations of $LiPF_6$ in DMC:HFPM (7:3, v/v) are compared in Figure 3-4b (molar ratios are reported in Table S3-2 in SI). Both macroscopic (from 0.1 to 5 M) and local concentrations (in brackets) are reported. Macroscopic concentrations correspond to the usual, macroscopic value obtained from the ratio between the salt

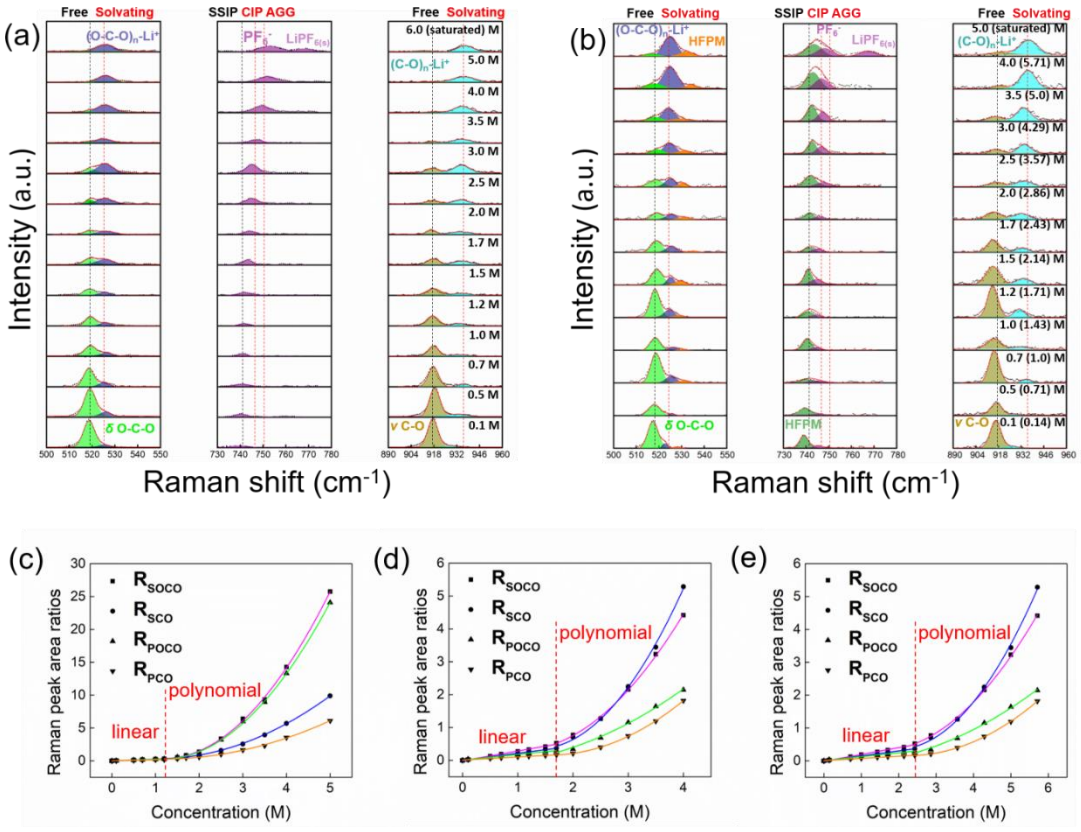


Figure 3-4. Raman spectra of (a) $LiPF_6$ in DMC and (b) $LiPF_6$ in DMC:HFPM (7:3, v/v) at different concentrations. Raman peak intensity ratios versus macroscopic concentration for (c) $LiPF_6$ in DMC and (d) $LiPF_6$ in DMC:HFPM (7:3, v/v). (e) Raman peak area ratios versus local concentration for $LiPF_6$ in DMC:HFPM (7:3, v/v).

amount and the global volume of the electrolyte as resulting from the addition of both solvent and diluent. Local concentrations refer to the concentration of the inner solvation structure i.e. as obtained from the ratio between the quantity of salt and the solvent volume only. Besides the appearance of the characteristic peak of HFPM (compare Figures 3-4b and 3-3b), the peak shift trends of the solvents and PF_6^- anions are quite similar to those observed in the electrolyte without HFPM (Figure 3-4a). Two main differences are observed compared to Figure 3a: i) the signals of free solvent persist up to the concentrations of 4.0 (5.71) M and 5.0 (saturated) M, ii) CIPs and AGGs still coexist in the LHCE at the concentration of 3.5 (5.0) M (Figure 3b), while only AGGs can be observed in the HCE at the concentration of 5.0 M (Figure 3a). This suggests that the diluent molecules inhibit the formation of the highly coordinated AGGs. These results show that the addition of the nonsolvating diluents affects the solvation structure of Li^+ cations in the LHCEs.

To further quantify the above phenomena and detail the coordination environment of the investigated electrolytes, the evolution of the Raman peak area (S) ratios between Li^+ coordinated and free solvent signals or between PF_6^- and free solvent are studied as a function of concentrations. Herein, the Raman peak area ratios $S_{solvating\ O\text{-}C\text{-}O}/S_{free\ O\text{-}C\text{-}O}$, $S_{solvating\ C\text{-}O}/S_{free\ C\text{-}O}$, $S_{PF6^-}/S_{free\ O\text{-}C\text{-}O}$, and $S_{PF6^-}/S_{free\ C\text{-}O}$ are denoted as R_{soco}, R_{sco}, R_{poco}, and R_{pco}, respectively. All the so-obtained curves exhibit a first range of linear increment followed by a polynomial domain (Figures 3-4c to 3-4e). Figure 3-4c reports Raman peak area ratios versus (macroscopic) concentration for the electrolyte consisting of $LiPF_6$ in DMC. Taking into account the peak shifts observed in Figure 3-4a, the linear increase ranging from 0.1 to 1.2 M corresponds to the progressive conversion of SSIPs into CIPs. The following step (below 1.2 M) reflects accelerated coordination reactions, corresponding to the ongoing formation of CIPs and the additional formation of AGGs. Figures 3-4d and 4e report the ratios evolution for $LiPF_6$ in DMC:HFPM (7:3, v/v) as functions of the macroscopic and local concentrations, respectively. In both cases, the inflection points corresponding to the transition from the linear to the polynomial behavior occurs at larger concentration values (1.7 and 2.4 M for the macroscopic and local concentrations, respectively) than for $LiPF_6$ in DMC (Figure 3-4c). This strongly suggests that the diluent inhibits the formations of highly coordinated structures, probably due to the withdrawing effect from the dipole-dipole interaction between diluent and solvent molecules (see next section).

3.3 Effect of the diluent content on the solvation structure of LHCEs

To further assess the impact of the diluent content on the inner solvation structure of LHCEs, three electrolytes with different macroscopic but equal local concentration (4 M) have been specifically prepared and studied: 1 M $LiPF_6$ in DMC:HFPM (1:3, v/v) (named Ely-B), 2 M $LiPF_6$ in DMC:HFPM (1:1, v/v) (Ely-C) and 3 M $LiPF_6$ in DMC:HFPM (3:1, v/v) (Ely-D). These LHCEs has been compared to the LCE of 1 M $LiPF_6$ in DMC (Ely-A) and the HCE of 4 M $LiPF_6$ in DMC (Ely-E) . The molar ratios of all electrolytes are reported in SI, Table S3-3. Corresponding Raman spectra are shown in Figure 3-5a. The signals of free solvents and CIPs are clearly observed for the LHCEs, while they are not present in the spectra of the HCE. Furthermore, the signals of free solvents and CIPs increase with the diluent content. Considering that the local concentrations of these LHCEs are equal to that of the HCE, i.e. 4 M, these results clearly demonstrate that the diluent molecules affect the inner solvation structures of the LHCEs. According to the spectral changes occurring from the HCE (Ely-E) to the LHCE (Ely-D), we can propose that the increase of free solvents and CIPs arise from the split of the AGGs by the withdrawing effect resulting from the interaction between diluents and coordinated solvents species, as schematized in Figure 3-5d.

The release of free solvent molecules by increasing the diluent content is also confirmed by ATR-FTIR spectroscopy (see SI for experimental details). As shown in Figure 3-5b, the signals of free C=O (1750 cm^{-1}) and C-O (1263 cm^{-1}) species increase with the diluent content (the signals of coordinated C=O (1719 cm^{-1}) and C-O (1306 cm^{-1}) decrease) in the LHCE [29–31].

The coordination environments of the investigated electrolytes are further assessed by ^{7}Li nuclear magnetic resonance (NMR) spectroscopy (see SI for experimental details). As shown in Figure 3-5c, the ^{7}Li NMR peaks progressively shift towards lower ppm values from Ely-A to Ely-E. The chemical shift is directly related to the shielding effect of the probed Li^+ environment. The shielding ability of the Li^+-PF_6^- pair is stronger than that of the Li^+-solvent complexes. Thus the upshift of the ^{7}Li NMR peak from Ely-D to Ely-B clearly shows the weakening of the coordination environment by increasing the diluent content.

All these results point out that the medium formed by the diluent is not “ideally inert” in the LHCE, but still able to affect the inner solvation structure: larger the amount of diluents added to the LHCE, more the effect of splitting the highly coordinated AGGs into CIPs and free solvents, as illustrated in Figure 3-5d.

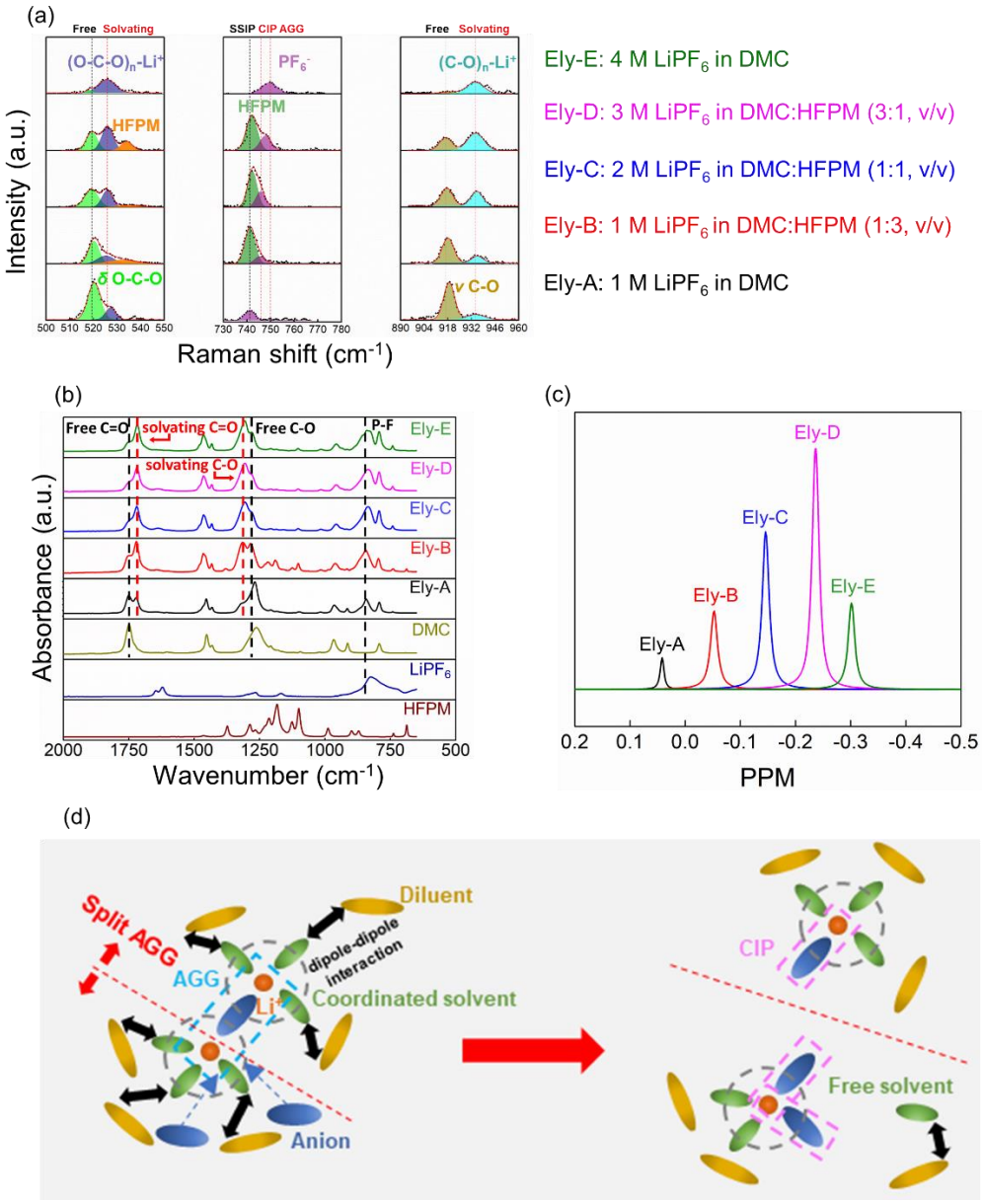


Figure 3-5. (a) Raman, (b) FTIR and (c) ^{7}Li NMR spectra of 1 M $LiPF_6$ in DMC (Ely-A), 1 M $LiPF_6$ in DMC:HFPM (1:3, v/v) (Ely-B), 2 M $LiPF_6$ in DMC:HFPM (1:1, v/v) (Ely-C), 3 M $LiPF_6$ in DMC:HFPM (3:1, v/v) (Ely-D), and 4 M $LiPF_6$ in DMC (Ely-E). (d) Illustration of the AGG split by the dipole-dipole interactions between diluent and solvent molecules.

Worth of noting, the release of free solvents by increasing the diluent content is still observed when solvents with higher dielectric constant than DMC are used. Figure 3-6 reports Raman spectra of the binary solvent electrolytes obtained by mixing DMC with EC, whose dielectric constant is ~95.3 at room temperature, definitively larger than the ~3.1 value of DMC [32]. Considering that the binding between the Li^+ cation and the solvent increases with the dielectric constant of the last, this result suggests the high strength of the dipole-dipole interactions between solvent and diluent to trigger the

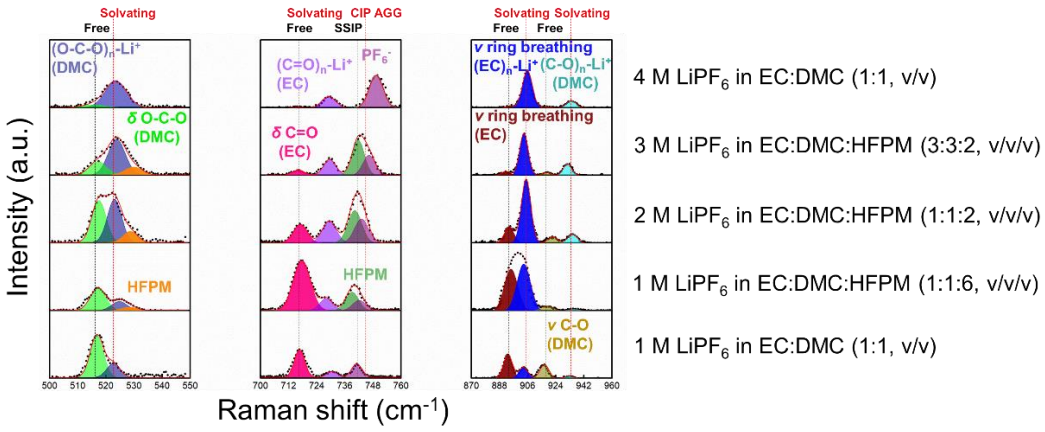


Figure 3-6. Raman spectra of 1 M $LiPF_6$ in EC:DMC (1:1, v/v), 1 M $LiPF_6$ in EC:DMC:HFPM (1:1:6, v/v/v), 2 M $LiPF_6$ in EC:DMC:HFPM (1:1:2, v/v/v), 3 M $LiPF_6$ in EC:DMC:HFPM (3:3:2, v/v/v) and 4 M $LiPF_6$ in EC:DMC (1:1, v/v).

splitting phenomenon of AGGs.

The first measurements of the cycling performances related to the Li metal deposition/dissolution process in the electrolyte composed of 4 M $LiPF_6$ in DMC:HFPM (7:3, v/v) have shown an extremely poor Coulombic efficiency (Figure 3-7). The long-term cycling is still not possible even in such an electrolyte with limited content of free solvent. As a consequence, we decided to extend our investigation to further salts and diluents for LHCEs, namely to lithium bis(fluorosulfonyl)imide (LiFSI) and 1,1,2,2-tetrafluoroethyl-2,2,3,3-tetrafluoropropyl ether (TTE), which have been proven to form an LHCE with the 1,2-dimethoxyethane (DME) solvent that greatly enhances the stability of high voltage Li metal batteries up to a working potential of 4.5 V [33]. The Raman spectra of pure LiFSI and TTE are shown in Figure 3-8.

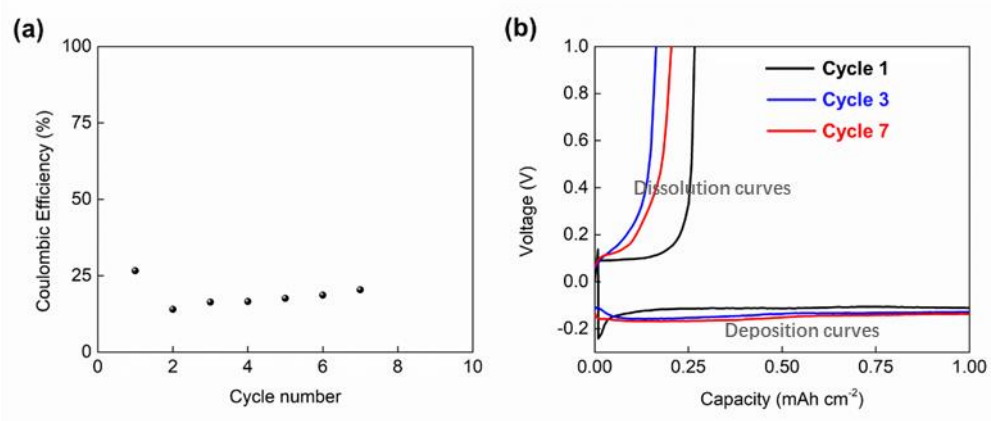


Figure 3-7. (a) Coulombic efficiency and (b) voltage profiles of the Li deposition/dissolution process carried out in the Li||Cu coin cell filled with 4 M $LiPF_6$ in DMC:HFPM (7:3, v/v), at 1 mA cm^{-2} (deposited Li amount: 1 mAh cm^{-2}).

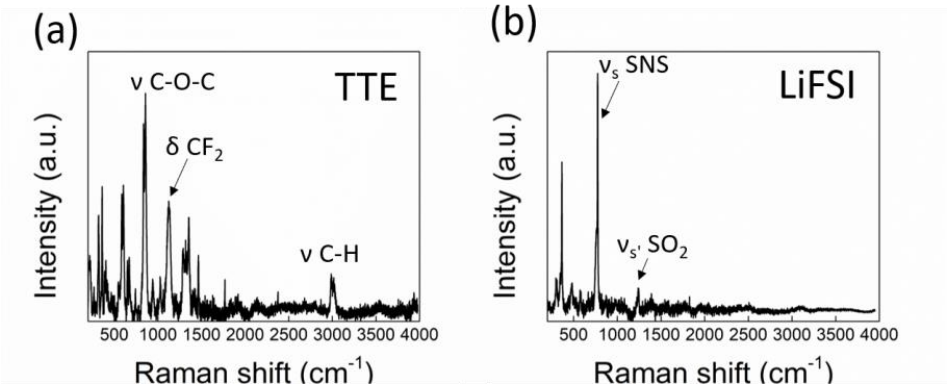


Figure 3-8. Raman spectra of pure (a) TTE and (b) LiFSI.

First, we studied the evolution of the solvation structure by replacing the HFPM in the LHCEs by the diluent TTE while maintaining all the other electrolyte components. As shown in Figure 3-9, the contents of free solvents and CIPs still increase by increasing the TTE content. It's worth noting that the dielectric constant of TTE (~6.21 at room temperature) is even lower than that of HFPM (~14.79 at room temperature), showing that the dipole-dipole interactions between diluent and solvent molecules can take place in a general way [34,35]. Besides, the donor number[6], which is another important parameter reflecting the solvating ability, is lower than 10 for TTE [36], while it is 17.2 for DMC [37]. Hence, DMC and TTE can be separately used as the solvent and diluent for constructing LHCE.

Then, we replaced $LiPF_6$ by LiFSI, so as to obtain a reference HCE of 6 M LiFSI in DMC (Ely-I). The reason for choosing Ely-I as the control HCE is the relatively high CE attained when increasing the salt concentration to 6 M LiFSI, as shown in Figure 3-10 but also reported by others [38]. Finally, various LHCEs with the equal local concentration of 6 M but different solvent/diluent ratios were prepared: 1 M LiFSI in DMC:TTE (1:5, v/v) (Ely-F), 2 M LiFSI in DMC:TTE (1:2, v/v) (Ely-G) and 4 M LiFSI in DMC:TTE (2:1, v/v) (Ely-H). The molar ratios of the different electrolytes are listed in Table S3-4 of SI. The same tendency, i.e. more released free solvents species by

[6] Many empirical parameters have been suggested to measure solvent effects in chemical reactions. Gutmann's donor number (DN) has been a successful parameter to quantify the electron-donating property of the solvent molecule. The DN is then a measure of the ability of a solvent to solvate cations and Lewis acid. It is defined as the enthalpy change of the addition reaction (1:1 adduct formation) of the solvent molecule (Lewis base) to the standard Lewis acid $SbCl_5$ in the noncoordinating solvent 1,2-dichloroethane with a zero DN. Calorimetric measurements are usually applied to determine this quantity.

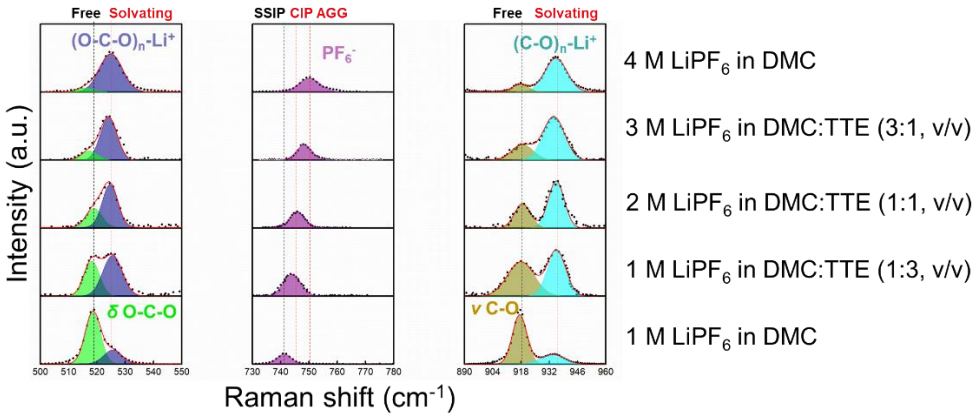


Figure 3-9. Raman spectra of 1 M $LiPF_6$ in DMC, 1 M $LiPF_6$ in DMC:TTE (1:3, v/v), 2 M $LiPF_6$ in DMC:TTE (1:1, v/v), 3 M $LiPF_6$ in DMC:TTE (3:1, v/v) and 4 M $LiPF_6$ in DMC.

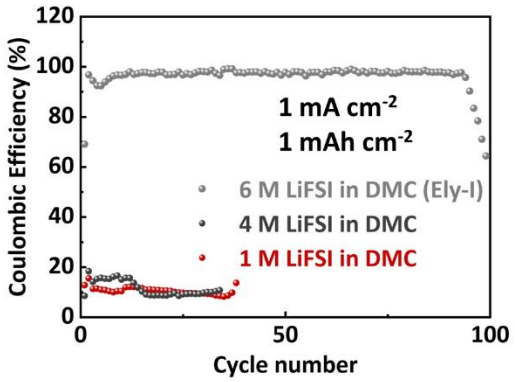


Figure 3-10. Evolution with the cycle number of the CE of Li||Cu coin cells using (○) 1 M, (○) 4 M and (○) 6 M LiFSI in DMC (Ely-I).

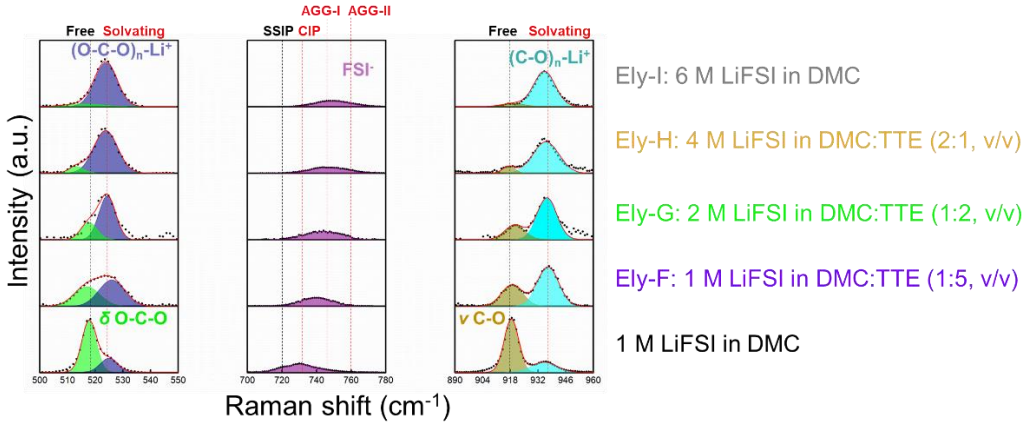


Figure 3-11. Raman spectra of 1 M LiFSI in DMC:TTE (1:5, v/v) (Ely-F), 2 M LiFSI in DMC:TTE (1:2, v/v) (Ely-G), 4 M LiFSI in DMC:TTE (2:1, v/v) (Ely-H), and 6 M LiFSI in DMC (Ely-I).

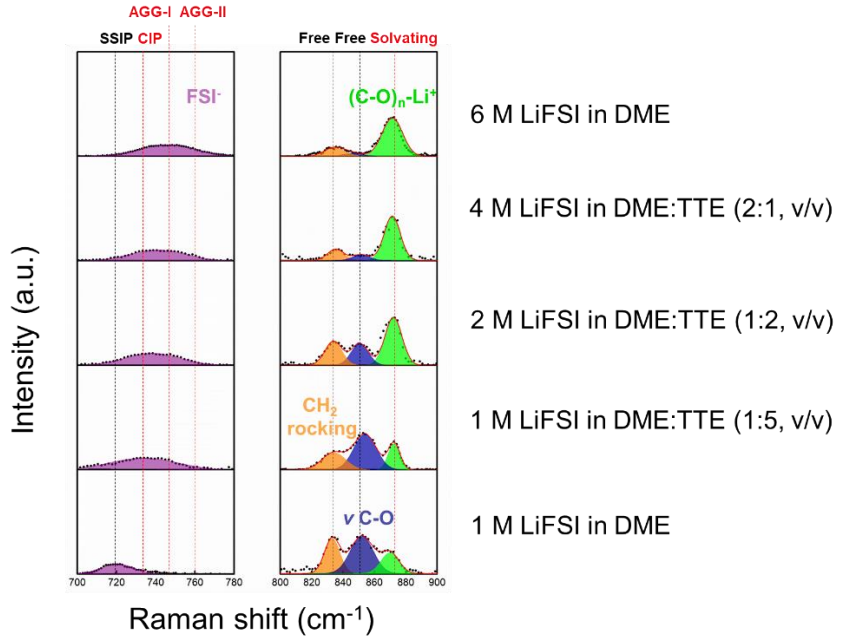


Figure 3-12. Raman spectra of 1 M LiFSI in DME, 1 M LiFSI in DME:TTE (1:5, v/v), 2 M LiFSI in DME:TTE (1:2, v/v), 4 M LiFSI in DME:TTE (2:1, v/v), and 6 M LiFSI in DME.

increasing the diluent content, is obtained when using LiFSI and TTE (Figure 3-11), even in the case that the solvent DMC is replaced by dimethyl ether (DME, Figure 3-12).

3.4 Effect of the diluent content on the electrochemical performances of the Li metal anode

To assess the impact of the solvent-diluent interaction-mediated solvation structure on the Li metal anode properties, electrochemical measurements have been carried out in Li||Cu coin cells (§ 2.3.4, Figure 2-9a). As a preliminary, it can be noted that the separator wettability by the electrolyte is improved by the use of the diluent i.e. the larger the diluent content, the larger the wettability (Figure 3-13a). At the same time, the increasing of the TTE content in the electrolyte decreases the LHCE ionic conductivity (Figure 3-13b). A similar phenomenon was yet observed in a previous study on LHCEs [39]. Supposing that conductivity mechanism is hopping-type (see figure S3-1), the reason is probably the discontinuous Li^+ conducting network due to the separation of solvent molecules by the diluent medium. This shows that a too high content of diluent should be avoided for the preparation of LHCEs.

Figure 3-14a and 14b report results from long-term cycling and average CE determination measurements, respectively (§ 2.3.4 and 2.3.5). Interestingly, both the

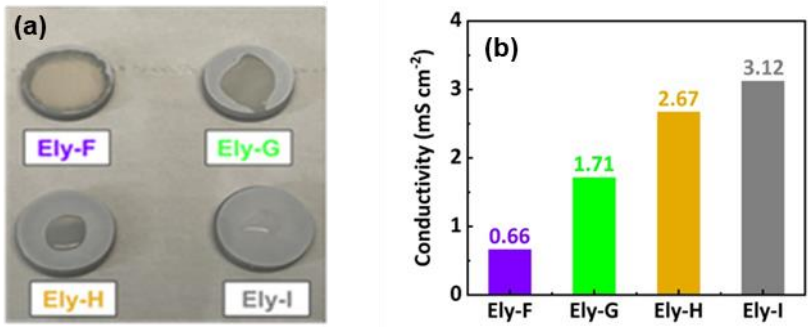


Figure 3-13. (a) Separator wettability by the different electrolytes and (b) ionic conductivities of 1 M LiFSI in DMC:TTE (1:5, v/v) (Ely-F), 2 M LiFSI in DMC:TTE (1:2, v/v) (Ely-G), 4 M LiFSI in DMC:TTE (2:1, v/v) (Ely-H) and 6 M LiFSI in DMC (Ely-I).

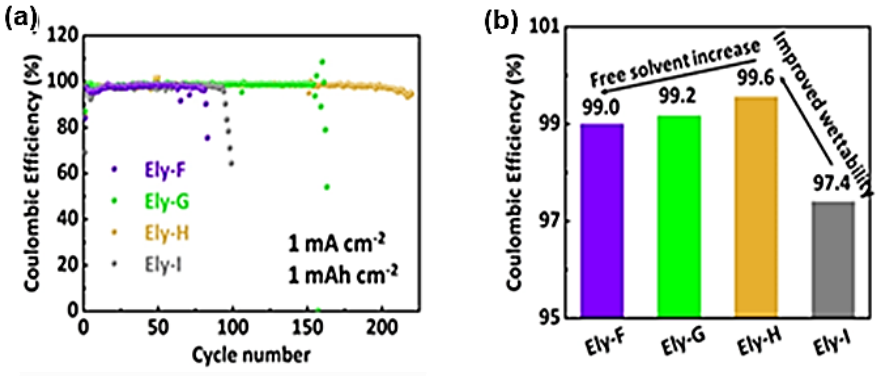


Figure 3-14. (a) Li metal cycling stability (carried out at the current intensity of 1 mA cm^{-2}, capacity of 1 mAh cm^{-2}) and (b) average Li CE of 1 M LiFSI in DMC:TTE (1:5, v/v) (Ely-F), 2 M LiFSI in DMC:TTE (1:2, v/v) (Ely-G), 4 M LiFSI in DMC:TTE (2:1, v/v) (Ely-H) and 6 M LiFSI in DMC (Ely-I).

cycling lifespan and average CE achieve the maximum with Ely-H. The better cycling performance of Li metal in Ely-H than Ely-I should be due to the improved physical properties of the LHCE such as viscosity and wettability, while the reasons for the progressively degraded performances from Ely-H to Ely-F are the concomitantly decrease of conductivity (see Figure 3-13b) and increase of the number of free solvent species undergoing side reactions with Li metal (see next section 3.5). The last reason is supported by linear sweep voltammetry (LSV) measurements showing that the reductive redox peak related to DMC shifts towards higher potentials (vs. Li/Li^+) from Ely-I to -F progressively, which correspond to the decrease of the reductive stability of LHCEs with the increasing of the diluent TTE content.

Cycling performances have also been tested with the Li||$LiFePO_4$ full cell (§ 2.3.4, Figure 2-9b) using LFP cathodes with moderate capacity of ~2.5 mAh cm^{-2}. Consistently with the results obtained in Li||Cu half cells, Ely-H still exhibits the best

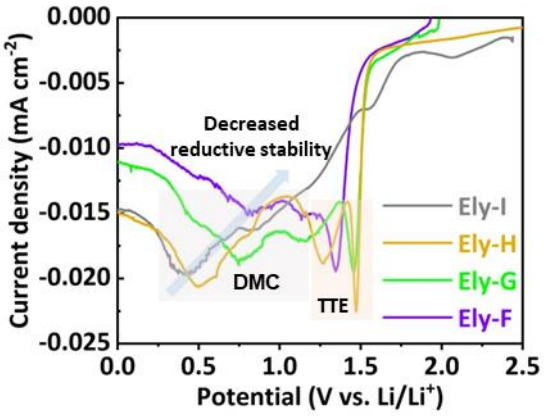


Figure 3-15. LSV curves of 1 M LiFSI in DMC:TTE (1:5, v/v) (Ely-F), 2 M LiFSI in DMC:TTE (1:2, v/v) (Ely-G), 4 M LiFSI in DMC:TTE (2:1, v/v) (Ely-H) and 6 M LiFSI in DMC (Ely-I).

performances (Figure 3-16). As shown in Figure 3-16a, the capacity and CE of the cell using Ely-H are maintained at ~99% and ~2.4 mAh cm^{-2} respectively for 100 cycles, while that of cells using Ely-I (25 cycles), Ely-G (30 cycles) and Ely-F (17 cycles) decrease quickly.

Figure 3-17b reports the voltage profiles of the different cells. The cell using Ely-I shows the largest polarization increase, i.e. the largest increase of the ΔV separating the charge and discharge profiles, upon cycling: changing from ~0.13 V at the 5^{th} cycle to ~0.75V at the 25^{th} cycle. In contrast, the polarization of the cell using Ely-H remains constant at 0.4 V from the 10^{th} cycle to the 100^{th} cycle. The cells filled with Ely-F and Ely-G seem to exhibit less polarization but over a number of electrochemical cycles that remains limited because of the faster capacity failure.

3.5 Effect of the diluent content on the SEI composition and Li deposition morphology

Cu foils of the Li||Cu half cell have been analyzed by X-ray Photoelectron Spectroscopy (XPS) after 5 cycles of Li plating/stripping at 1 mA cm^{-2} (capacity of 1 mAh cm^{-2}). C 1s spectra reported in Figure 3-17a show the highest relative signals of Li_2CO_3 (CO_3^{2-}, C=O and C-O species), which is a typical reductive product of the free DMC solvent [40], when the LCE (1 M LiFSI in DMC) i.e. the electrolyte with the highest free solvent content is used. As well, the relative signals intensity of Li_2CO_3 progressively decreased from Ely-F to Ely-I, according to the decreasing of the amount of free DMC solvent. The F 1s, N 1s and S 2p spectra are shown in Figures 3-17b, 3-17c and 3-17d respectively. Although the cycled electrodes have been rinsed by fresh DMC solvent,

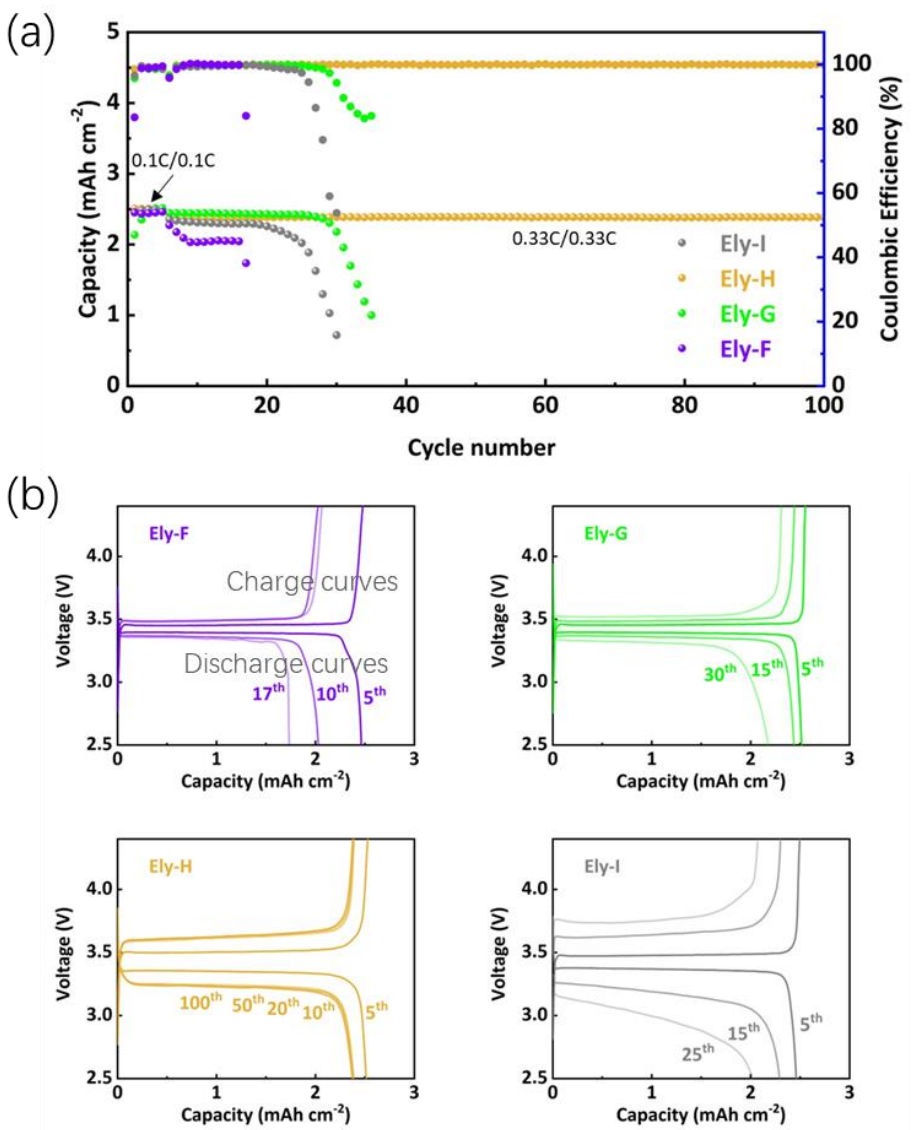


Figure 3-16. (a) Comparison of the cycling performances of the Li|| $LiFePO_4$ full cell using 1 M LiFSI in DMC:TTE (1:5, v/v) (Ely-F), 2 M LiFSI in DMC:TTE (1:2, v/v) (Ely-G), 4 M LiFSI in DMC:TTE (2:1, v/v) (Ely-H) and 6 M LiFSI in DMC (Ely-I). (b) Corresponding voltage profiles.

the signals of the FSI^- anion from residual salt is still observed for all samples, together with its degradation products LiF, Li_3N and Li_2SO_3 [38]. Ely-I exhibits larger LiF, Li_3N and Li_2SO_3 amounts than 1 M LiFSI in DMC, due to the prevailing of the FSI^- anion decomposition in HCEs [41,42,38], instead of the prevailing free solvent decomposition occurring in LCEs. It is worth noting that the relative signals of LiF, Li_3N and Li_2SO_3 decrease brutally from Ely-I to Ely-H, and then restore progressively from Ely-H to Ely-F. This trend is related to the different cycling performances. The highest CE of Ely-H (Figure 3-14b) reflects the largest stability of the FSI^- anion against the electrochemical degradation, which leads to the lowest LiF, Li_3N and Li_2SO_3

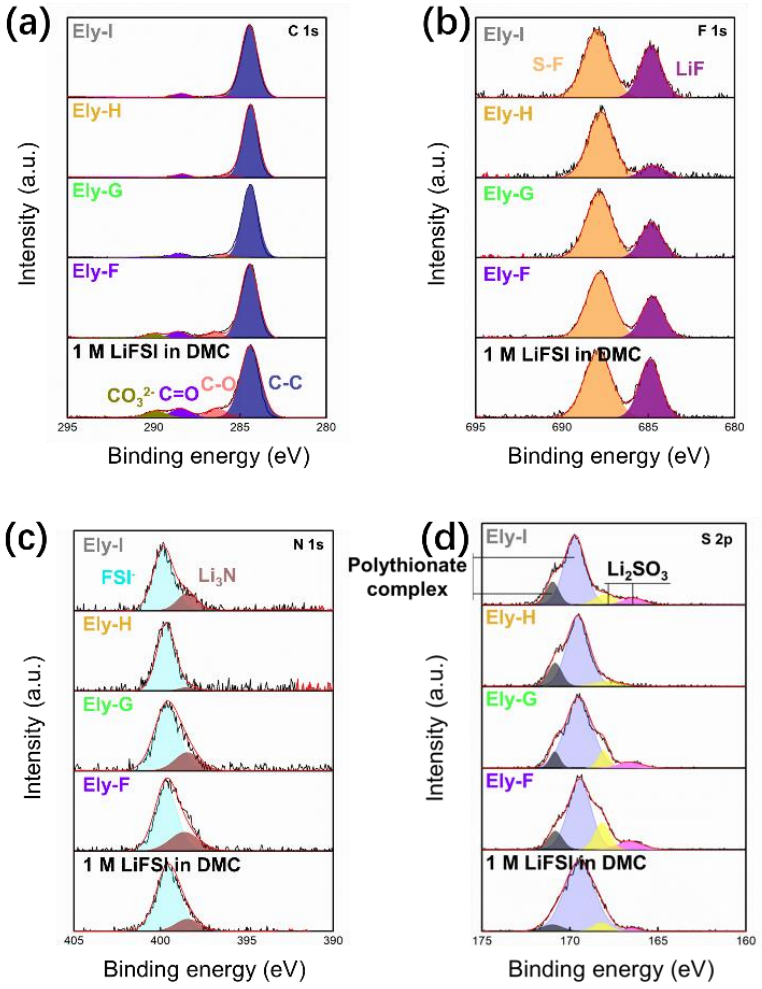


Figure 3-17. XPS analysis of the Cu electrode after 5 cycles (0.5 mA cm^{-2}, 1 mAh cm^{-2}) in the different electrolytes (indicated in the figure): (a) C 1s, (b) F 1s, (c) N 1s and (d) S 2p spectra.

contents at the electrode surface.

The morphologies of the different Li deposits obtained in 1 M LiFSI in DMC, Ely-F, -G, -H and -I have been characterized by Scanning Electron Microscopy (SEM). Sharply different microstructures can be observed (Figure 3-18). Namely, the fine dendritic Li filaments obtained with the LCE (1 M LiFSI in DMC) are progressively replaced by large granular Li deposits increasingly smooth from LHCE Ely-F to H. The smoothest morphology is observed with the HCE Ely-I. These data attest that not only the concentration of the Li salt but also the diluent content in the LHCE affects the morphology of the Li deposit significantly.

The same morphological differences between the investigated electrolytes are maintained when the Li plating capacity is increased from 1 to 2 and 4 mAh cm^{-2} (Figure 3-19a). Interestingly, on the Li deposit surfaces formed in Ely-H and Ely-I,

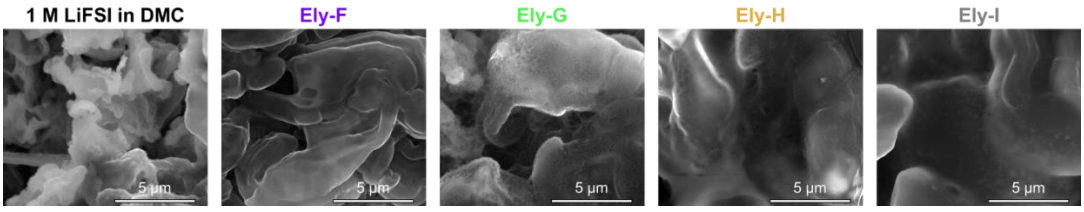


Figure 3-18. SEM images of Li deposits obtained at the 1 mAh cm^{-2} capacity with 1 M LiFSI in DMC, Ely-F, -G, -H and -I.

swelling or bubbling features are also observed (indicated in the figure by yellow arrows). Generally, such swelling phenomena induced under the electron beam in SEM arise from the chemical degradation of organic species. Indeed, the O 1s (Figure 3-19b) and Li 1s (Figure 3-19c) XPS spectra of the cycled Cu electrodes show additional signals of ROLi species for Ely-H and -I [43,44], which are otherwise virtually absent from spectra of 1 M LiFSI-DMC, Ely-F and Ely-G. LiFSI and DMC are the two common substances to Ely-H and -I. Hence, it can be presumed that the ROLi products originate from the DMC decomposition, since the LiFSI salt can only be degraded into inorganic species such as LiF and Li_3N [38].

Two reduction routes can be supposed for the DMC decomposition: route 1 can generate ROOCLi and ROLi, whereas route 2 produces Li_2CO_3 and $LiCH_3$ (Figure 3-19d) [45,40]. Based on the above results, it seems that in addition to the main product Li_2CO_3, ROLi via route 1 is also favored in the electrolytes with limited amount of free DMC molecules i.e. Ely-H and Ely-I. Although further study is needed to understand the reaction mechanism behind, results here reported show that the solvation structure as well as the free solvent amount can have key impact on the SEI composition and Li plating morphology.

3.6 Conclusion

The lastly developed LHCEs exhibit great potentiality to pave the route for high-energy-density batteries. Nevertheless, in order to implement their wide application, more understanding is needed about the relationships between the inner electrolyte structure and the electrochemical behavior. More precisely, the impact of the diluent content on the inner solvation structure of the LHCE, and the consequences on the electrochemical performances, were often neglected so far. In the work presented above, we establish that free solvents and CIPs, nearly not observable in HCEs, appear in LHCEs by addition of diluent molecules, presumably by the partial split of the AGGs via the dipole-dipole interactions between the diluent and the solvent molecules. The

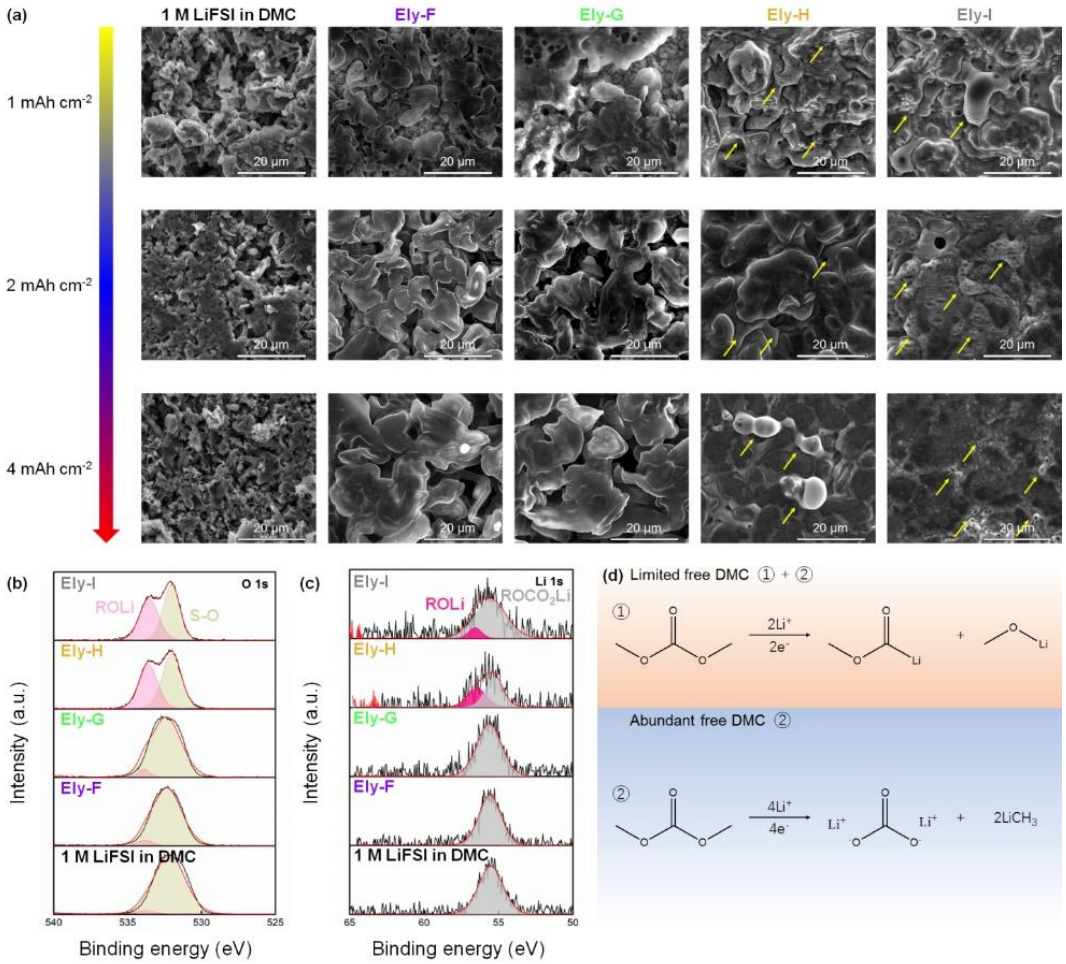


Figure 3-19. (a) SEM images of Li deposits obtained at different plating capacities with 1 M LiFSI in DMC, 1 M LiFSI in DMC:TTE (1:5, v/v) (Ely-F), 2 M LiFSI in DMC:TTE (1:2, v/v) (Ely-G), 4 M LiFSI in DMC:TTE (2:1, v/v) (Ely-H) and 6 M LiFSI in DMC (Ely-I). The yellow arrows indicate the chemical degradation of organic species under the electron beam. The electroplating was carried out at 0.5 mA cm^{-2}. (b) O 1s and (c) Li 1s spectra from the XPS analysis of the Cu electrode after 5 cycles (0.5 mA cm^{-2}, 1 mAh cm^{-2}) in the above electrolytes. (d) Possible DMC decomposition routes in the electrolytes with limited or abundant free DMC.

amount of the released free solvents and CIPs increases with the diluent content. This feature has a significant impact both on the physical properties of the electrolyte (e.g. viscosity and wettability), the electrode interphase composition, the Li metal plating morphology and, finally, the cycling stability of the Li metal cell. Accordingly, when a high-performance HCE (with a Li CE of 97.4%) is used as the precursor of LHCEs, the moderately diluted LHCE shows a further improved Li CE of 99.6% compared with the highly diluted LHCE (99.0%). This clearly attests the importance of the diluent content as key parameter for the designing of improved LHCEs for high-energy-density batteries.

Supporting information

Table S3-1. Molar ratios of components in electrolytes in Figure 3-4a.

Electrolyte component	Concentration /M (mol/L)	Molar ratio of $LiPF_6$:DMC
$LiPF_6$ in DMC	5.0	500:1187
	4.0	400:1187
	3.5	350:1187
	3.0	300:1187
	2.5	250:1187
	2.0	200:1187
	1.7	170:1187
	1.5	150:1187
	1.2	120:1187
	1.0	100:1187
	0.7	70:1187
	0.5	50:1187
	0.1	10:1187

Table S3-2. Molar ratios of components in electrolytes in Figure 3-4b.

Electrolyte component	Macroscopic concentration (local concentration) /M (mol/L)	Molar ratio of $LiPF_6$:DMC:HFPM
$LiPF_6$ in DMC:HFPM (7:3, v/v)	4.0 (5.71)	40:83:23
	3.5 (5.0)	35:83:23
	3.0 (4.29)	30:83:23
	2.5 (3.57)	25:83:23
	2.0 (2.86)	20:83:23
	1.7 (2.43)	17:83:23
	1.5 (2.14)	15:83:23
	1.2 (1.71)	12:83:23
	1.0 (1.43)	10:83:23
	0.7 (1.0)	7:83:23
	0.5 (0.71)	5:83:23
	0.1 (0.14)	1:83:23

Table S3-3. Molar ratios of components in electrolytes in Figure 3-5a.

Electrolyte component	Electrolyte code name	DMC:HFPM (v/v)	Macroscopic concentration (local concentration) /M (mol/L)	Molar ratio of $LiPF_6$:DMC:HFPM or $LiPF_6$:DMC
$LiPF_6$ in DMC:HFPM	Ely-D	3:1	3 (4)	30:89:19
	Ely-C	1:1	2 (4)	400:1187:758
	Ely-B	1:3	1 (4)	400:1187:2274
$LiPF_6$ in DMC	Ely-E	/	4	400:1187
	Ely-A	/	1	100:1187

Table S3-4. Molar ratios of components in electrolytes in Figure 3-11a.

Electrolyte component	Electrolyte code name	DMC:TTE (v/v)	Macroscopic concentration (local concentration) /M (mol/L)	Molar ratio of LiFSI:DMC:TTE or LiFSI:DMC
LiFSI in DMC:TTE	Ely-H	2:1	4 (6)	120:237:66
	Ely-G	1:2	2 (6)	600:1187:1321
	Ely-F	1:5	1 (6)	600:1187:3301
LiFSI in DMC	Ely-I	/	6	600:1187
	/	/	1	100:1187

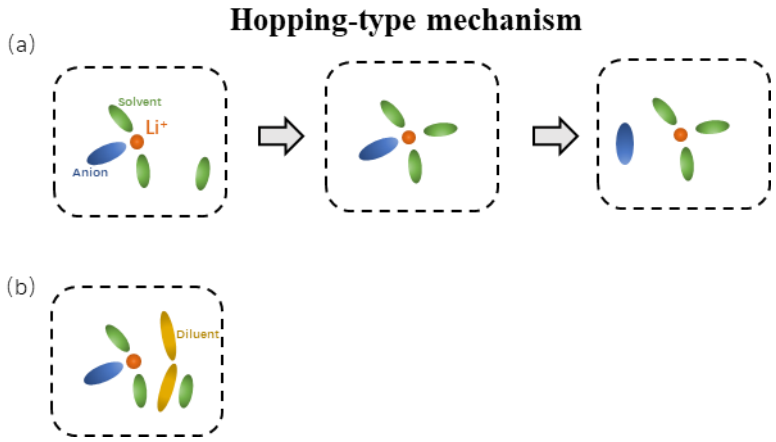


Figure S3-1. (a) Schematic of hopping-type mechanism in HCEs and (b) Li^+ transport hindering by the diluent in LHCEs.

References

[1] W. Cai, Y.-X. Yao, G.-L. Zhu, C. Yan, L.-L. Jiang, C. He, J.-Q. Huang, Q. Zhang, A review on energy chemistry of fast-charging anodes, Chemical society reviews 49 (2020) 3806–3833.

[2] J.B. Goodenough, Y. Kim, Challenges for rechargeable Li batteries, Chemistry of materials 22 (2010) 587–603.

[3] W. Xu, J. Wang, F. Ding, X. Chen, E. Nasybulin, Y. Zhang, J.-G. Zhang, Lithium metal anodes for rechargeable batteries, Energy & environmental science 7 (2014) 513–537.

[4] J.W. Choi, D. Aurbach, Promise and reality of post-lithium-ion batteries with high energy densities, Nature reviews materials 1 (2016) 1–16.

[5] X.-B. Cheng, R. Zhang, C.-Z. Zhao, Q. Zhang, Toward safe lithium metal anode in rechargeable batteries: A review, Chemical reviews 117 (2017) 10403–10473.

[6] O. Borodin, X. Ren, J. Vatamanu, A. von Wald Cresce, J. Knap, K. Xu, Modeling insight into battery electrolyte electrochemical stability and interfacial structure, Accounts of chemical research 50 (2017) 2886–2894.

[7] X. Ren, Y. Zhang, M.H. Engelhard, Q. Li, J.-G. Zhang, W. Xu, Guided lithium metal deposition and improved lithium coulombic efficiency through synergistic effects of $LiAsF_6$ and cyclic carbonate additives, ACS energy letters 3 (2017) 14–19.

[8] J. Zheng, M.H. Engelhard, D. Mei, S. Jiao, B.J. Polzin, J.-G. Zhang, W. Xu, Electrolyte additive enabled fast charging and stable cycling lithium metal batteries, Nature energy 2 (2017) 1–8.

[9] Z. Zhu, Y. Tang, Z. Lv, J. Wei, Y. Zhang, R. Wang, W. Zhang, H. Xia, M. Ge, X. Chen, Fluoroethylene carbonate enabling a robust LiF-rich solid electrolyte interphase to enhance the stability of the MoS_2 anode for lithium-ion storage, Angewandte chemie international edition 57 (2018) 3656–3660.

[10] J. Zhang, L. Zhou, H. Ming, Y. Wu, W. Wahyudi, Z. Cao, L. Cavallo, L. Wang, J. Ming, Lithium dendrite-free plating/stripping. A new synergistic lithium ion solvation structure effect for reliable lithium–sulfur full batteries, Chemical communications 55 (2019) 5713–5716.

[11] Y. Jie, X. Liu, Z. Lei, S. Wang, Y. Chen, F. Huang, R. Cao, G. Zhang, S. Jiao, Enabling high-voltage lithium metal batteries by manipulating solvation structure in ester electrolyte, Angewandte chemie international edition 59 (2020) 3505–

3510.

[12] Q. Li, Z. Cao, W. Wahyudi, G. Liu, G.-T. Park, L. Cavallo, T.D. Anthopoulos, L. Wang, Y.-K. Sun, H.N. Alshareef, Unraveling the new role of an ethylene carbonate solvation shell in rechargeable metal ion batteries, ACS energy letters 6 (2020) 69–78.

[13] L. Suo, Y.-S. Hu, H. Li, M. Armand, L. Chen, A new class of solvent-in-salt electrolyte for high-energy rechargeable metallic lithium batteries, Nature communications 4 (2013) 1–9.

[14] J. Qian, W.A. Henderson, W. Xu, P. Bhattacharya, M. Engelhard, O. Borodin, J.-G. Zhang, High rate and stable cycling of lithium metal anode, Nature communications 6 (2015) 1–9.

[15] X. Ren, L. Zou, S. Jiao, D. Mei, M.H. Engelhard, Q. Li, H. Lee, C. Niu, B.D. Adams, C. Wang, High-concentration ether electrolytes for stable high-voltage lithium metal batteries, ACS energy letters 4 (2019) 896–902.

[16] Z. Peng, X. Cao, P. Gao, H. Jia, X. Ren, S. Roy, Z. Li, Y. Zhu, W. Xie, D. Liu, High-power lithium metal batteries enabled by high-concentration acetonitrile-based electrolytes with vinylene carbonate additive, Advanced functional materials 30 (2020) 2001285.

[17] J. Wang, Y. Yamada, K. Sodeyama, C.H. Chiang, Y. Tateyama, A. Yamada, Superconcentrated electrolytes for a high-voltage lithium-ion battery, Nature communications 7 (2016) 1–9.

[18] L. Suo, O. Borodin, T. Gao, M. Olguin, J. Ho, X. Fan, C. Luo, C. Wang, K. Xu, “Water-in-salt” electrolyte enables high-voltage aqueous lithium-ion chemistries, Science 350 (2015) 938–943.

[19] C. Yang, J. Chen, T. Qing, X. Fan, W. Sun, A. von Cresce, M.S. Ding, O. Borodin, J. Vatamanu, M.A. Schroeder, 4.0 V aqueous Li-ion batteries, Joule 1 (2017) 122–132.

[20] X. Ren, S. Chen, H. Lee, D. Mei, M.H. Engelhard, S.D. Burton, W. Zhao, J. Zheng, Q. Li, M.S. Ding, Localized high-concentration sulfone electrolytes for high-efficiency lithium-metal batteries, Chem 4 (2018) 1877–1892.

[21] S. Chen, J. Zheng, D. Mei, K.S. Han, M.H. Engelhard, W. Zhao, W. Xu, J. Liu, J.-G. Zhang, High-voltage lithium-metal batteries enabled by localized high-concentration electrolytes, Advanced materials 30 (2018) 1706102.

[22] S. Chen, J. Zheng, L. Yu, X. Ren, M.H. Engelhard, C. Niu, H. Lee, W. Xu, J. Xiao,

J. Liu, High-efficiency lithium metal batteries with fire-retardant electrolytes, Joule 2 (2018) 1548–1558.

[23] X. Fan, X. Ji, L. Chen, J. Chen, T. Deng, F. Han, J. Yue, N. Piao, R. Wang, X. Zhou, All-temperature batteries enabled by fluorinated electrolytes with non-polar solvents, Nature energy 4 (2019) 882–890.

[24] X. Ren, P. Gao, L. Zou, S. Jiao, X. Cao, X. Zhang, H. Jia, M.H. Engelhard, B.E. Matthews, H. Wu, Role of inner solvation sheath within salt–solvent complexes in tailoring electrode/electrolyte interphases for lithium metal batteries, Proceedings of the national academy of sciences 117 (2020) 28603–28613.

[25] X. Cao, P. Gao, X. Ren, L. Zou, M.H. Engelhard, B.E. Matthews, J. Hu, C. Niu, D. Liu, B.W. Arey, Effects of fluorinated solvents on electrolyte solvation structures and electrode/electrolyte interphases for lithium metal batteries, Proceedings of the national academy of sciences 118 (2021) e2020357118.

[26] X. Cao, L. Zou, B.E. Matthews, L. Zhang, X. He, X. Ren, M.H. Engelhard, S.D. Burton, P.Z. El-Khoury, H.-S. Lim, Optimization of fluorinated orthoformate based electrolytes for practical high-voltage lithium metal batteries, Energy storage materials 34 (2021) 76–84.

[27] Y. Zhang, Y. Zhong, Z. Wu, B. Wang, S. Liang, H. Wang, Solvent molecule cooperation enhancing lithium metal battery performance at both electrodes, Angewandte chemie international edition 59 (2020) 7797–7802.

[28] S. Hwang, D.-H. Kim, J.H. Shin, J.E. Jang, K.H. Ahn, C. Lee, H. Lee, Ionic conduction and solution structure in $LiPF_6$ and $LiBF_4$ propylene carbonate electrolytes, The journal of physical chemistry C 122 (2018) 19438–19446.

[29] M.D.S. Lekgoathi, B.M. Vilakazi, J.B. Wagener, J.P. Le Roux, D. Moolman, Decomposition kinetics of anhydrous and moisture exposed $LiPF_6$ salts by thermogravimetry, Journal of fluorine chemistry 149 (2013) 53–56.

[30] B.-R. Choi, S.-J. Park, S. Kim, Study on ion-conducting properties of ionic liquid containing carbonate electrolytes against carbon electrode, Journal of nanoscience and nanotechnology 16 (2016) 2765–2768.

[31] W. Li, S. Qin, Q. Zhang, Z. Guo, X. Zhang, Reaction rate constants with OH radicals at 253–328 K and atmospheric implications for $(CF_3)_2CHOC_xH$ (2x+ 1) (x= 1, 2, 3), Chemical physics letters 714 (2019) 125–130.

[32] D.S. Hall, J. Self, Dahn, JR, Dielectric constants for quantum chemistry and Li-ion batteries. Solvent blends of ethylene carbonate and ethyl methyl carbonate,

The Journal of physical chemistry C 119 (2015) 22322–22330.

[33] X. Ren, L. Zou, X. Cao, M.H. Engelhard, W. Liu, S.D. Burton, H. Lee, C. Niu, B.E. Matthews, Z. Zhu, Enabling high-voltage lithium-metal batteries under practical conditions, Joule 3 (2019) 1662–1676.

[34] N. Nakazawa, M. Kawamura, A. Sekiya, K. Ootake, R. Tamai, Y. Kurokawa, J. Murata, Liquid dielectric constants of fluorinated ethers, fluorinated ketone and fluorinated alcohol, Transactions of the Japan society of refrigerating and air conditioning engineers 18 (2011) 263–271.

[35] T. Doi, Y. Shimizu, M. Hashinokuchi, M. Inaba, Dilution of highly concentrated LiBF4/propylene carbonate electrolyte solution with fluoroalkyl ethers for 5-V $LiNi_{0.5}Mn_{1.5}O_4$ positive electrodes, Journal of The electrochemical society 164 (2017) A6412.

[36] K. Dokko, N. Tachikawa, K. Yamauchi, M. Tsuchiya, A. Yamazaki, E. Takashima, J.-W. Park, K. Ueno, S. Seki, N. Serizawa, Solvate ionic liquid electrolyte for Li–S batteries, Journal of the electrochemical society 160 (2013) A1304.

[37] F. Cataldo, A revision of the Gutmann donor numbers of a series of phosphoramides including TEPA, European chemical bulletin 4 (2015) 92–97.

[38] X. Fan, L. Chen, X. Ji, T. Deng, S. Hou, J. Chen, J. Zheng, F. Wang, J. Jiang, K. Xu, Highly fluorinated interphases enable high-voltage Li-metal batteries, Chem 4 (2018) 174–185.

[39] N. Piao, X. Ji, H. Xu, X. Fan, L. Chen, S. Liu, M.N. Garaga, S.G. Greenbaum, L. Wang, C. Wang, X. He, Countersolvent electrolytes for lithium-metal batteries, Advanced energy materials 10 (2020) 1903568.

[40] A.H. Tamboli, A.A. Chaugule, H. Kim, Catalytic developments in the direct dimethyl carbonate synthesis from carbon dioxide and methanol, Chemical engineering journal 323 (2017) 530–544.

[41] C.-Z. Zhao, X.-B. Cheng, R. Zhang, H.-J. Peng, J.-Q. Huang, R. Ran, Z.-H. Huang, F. Wei, Q. Zhang, Li_2S_5-based ternary-salt electrolyte for robust lithium metal anode, Energy storage materials 3 (2016) 77–84.

[42] R. Younesi, F. Bardé, Electrochemical performance and interfacial properties of Li-metal in lithium bis (fluorosulfonyl) imide based electrolytes, Scientific reports 7 (2017) 1–6.

[43] X.-B. Cheng, H.-J. Peng, J.-Q. Huang, R. Zhang, C.-Z. Zhao, Q. Zhang, Dual-phase lithium metal anode containing a polysulfide-induced solid electrolyte

interphase and nanostructured graphene framework for lithium–sulfur batteries, ACS nano 9 (2015) 6373–6382.

[44] X.-B. Cheng, C. Yan, X. Chen, C. Guan, J.-Q. Huang, H.-J. Peng, R. Zhang, S.-T. Yang, Q. Zhang, Implantable solid electrolyte interphase in lithium-metal batteries, Chem 2 (2017) 258–270.

[45] D. Aurbach, A. Zaban, Y. Ein-Eli, I. Weissman, O. Chusid, B. Markovsky, M. Levi, E. Levi, A. Schechter, E. Granot, Recent studies on the correlation between surface chemistry, morphology, three-dimensional structures and performance of Li and Li-C intercalation anodes in several important electrolyte systems, Journal of power sources 68 (1997) 91–98.

Chapter 4. Probing the local Li^+ concentration in the electrolyte during plating by *in situ* Raman micro-spectroscopy: which relationships with the SEI properties and the morphology of the Li deposit?

4.1 Introduction

In chapter 1 & 3, we have introduced that the Li deposition morphology is usually considered to have a strict relation with the Li^+ concentration gradients occurring close to the electrode surface during plating [1]. Results reported in chapter 3 show how the starting concentration of the electrolyte affects the Li deposition morphology. In principle, *in situ* μ-Raman spectroscopy can be used to fill the gap between these two observations i.e. to establish relationships between the starting, global concentration of the electrolyte and the [Li^+] gradients occurring under operation [2–4]. However, as far as we know, no systemic studies have been carried out in this regard on LHCEs or even HCEs so far. Only a few works concerning LCEs in Li-ion batteries have been already reported [5–7]. Particularly, Yamanaka *et al.* [5] studied the ionic concentration changes occurring in the electrolyte 1 M $LiClO_4$ in EC:DEC (1:1, v/v) of a graphite‖$LiFePO_4$ cell by multi-microprobe Raman spectroscopy (Figure 4-1). Six probes were inserted at different positions corresponding to the cathode side, the anode side and the middle of the cell (Figure 4-1a and b). The authors measured the local Li^+ concentration using the intensities of the EC-Li^+ peak at 905 cm^{-1} (Figure 4-1c). The evolution of the concentration gradients was then followed during the cell working (Figure 4-2) and rough Li^+ diffusion coefficient deduced by the Fick's law. It was found that the diffusion coefficient decreased considerably at the anode during cycling ($D_{anode} < 1.93 \times 10^{-12}$ [m^2/s] as calculated from $N = J/zF$ [0.28 mA/cm^2/(1× 96485 C mol^{-1})] = $-dC_{Li+}/dx$ (0.75 M/50 μm) × D_{Anode}; see the anode side at Figure 4-2b), presumably due to the growing and thickening of the SEI film.

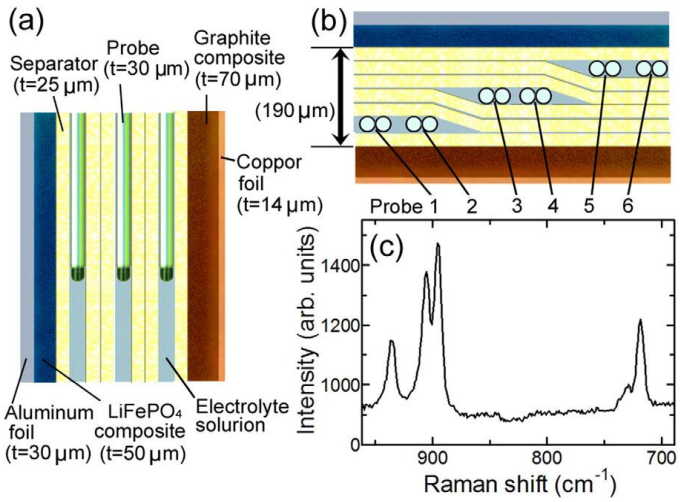


Figure 4-1. (a,b) Multi-microprobe experimental setup used by Yamanaka *et al.* [5] for *in situ* Raman spectroscopy and (c) example of the Raman spectrum of the electrolyte solution 1 M $LiClO_4$ in EC: DEC (1:1, v/v) as collected by the probe 1: symmetric ring deformation modes of free EC and EC solvating Li^+ (EC-Li^+) at 718 and 730 cm-1 respectively, ring breathing modes of free EC and EC-Li^+ at 894 and 905 cm^{-1}, ClO_4^- symmetric stretching mode at 935 cm^{-1}.

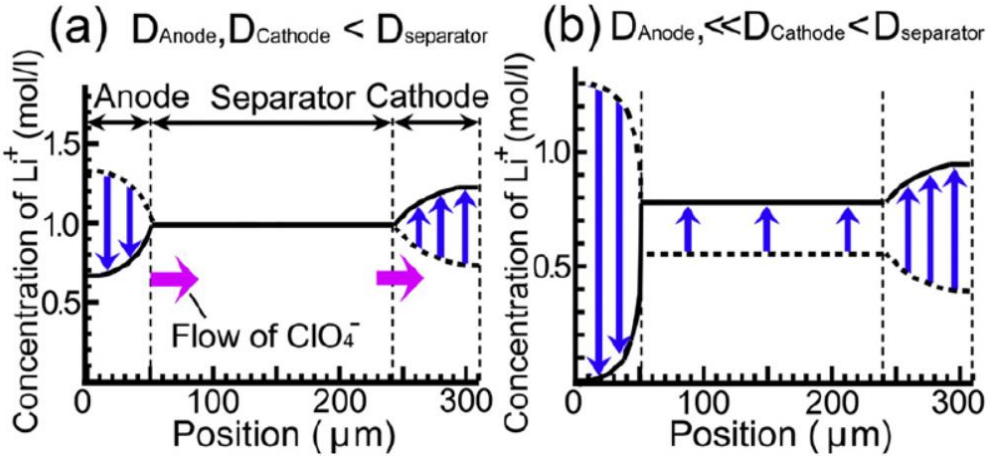


Figure 4-2. Schematic illustrations of the evolution of the ionic concentration gradient inside the electrolyte 1 M $LiClO_4$ in EC:DEC (1:1, v/v) of the graphite‖LiFePO4 cell, according to Yamanaka *et al.* [5]: (a) concentration profile at the early stage of the electrochemical operation and (b) after repeated cycles.

Local Li^+ concentration and diffusion coefficient D_{Li+} are key information for improving our understanding of Li-based batteries operation mechanisms. In this chapter, we compare the evolution of the Li^+ concentration gradients (and of other related parameters as the diffusion coefficient) occurring across low-, high- and localized high-concentration electrolytes during the Li plating process. Relationships

with the SEI composition and the Li deposition morphology are discussed.

4.2 Preliminary study of the evolution of the local [Li^+] during plating in a low concentration, binary solvent electrolyte: validation of the *in situ* μ-Raman approach

The first measurements of *in situ* μ-Raman spectroscopy during Li plating was carried out on Cu foils coated by Al-based particles supposed to operate as protective structures limiting uneven nucleation and fragile solid electrolyte interphase. The initial aim was to obtain and compare first spectroscopic results from electrodes with very different electrochemical performances and Li plating morphologies. We then compared a Cu foil coated with commercial Al powder to another, especially developed by us [8], modified with Si–Al alloy particles having a core-shell structure with Al core and alumina-silica (Al_2O_3-SiO_2) shell (AAS). The electrolyte employed was the widely used 1 M $LiPF_6$ in EC:DEC (1:1, v/v), with 5% vol. of fluoroethylene carbonate (FEC) as additive. Measurements were carried out according to the experimental setup reported in Figure 2-13 (chapter 2). The position probed by the laser beam was at 10 μm from the surface of the Cu electrode.

As more detailed in [8], commercial Al powders, even if increasing the stability of the Cu electrode, cannot avoid SEI crack and Li dendrites formation under prolonged cycling since they convert into big bulks due to the impeded lithiation caused by the insulating Al_2O_3 outer layer (Figure 4-3a and 3b, top side). Differently, AAS allow abundant artificial nucleation sites and robust SEI films, leading to homogeneous Li deposition/stripping and high Li Coulombic efficiency (Figure 4-3a and 3b, bottom side). The active SiO_2 sites not only contribute to form robust SEI layer, but also facility the lithiation of the AAS, accelerating the conversion of reversible Li-Al alloy into inert Li_3Al_2 phase. The as-generated AAS with Li_3Al_2 and $Li_{12}Si_7$ phases possess negligible Li nucleation over-potential (~0.7 mV) (Figure S4-1 in SI), resulting in stable SEI layer and uniform granular Li deposition. The last allows optimal artificial nucleation sites for dendrite-free Li plating/stripping. The result is a prolonged life-span of 6 times longer than that of the unprotected, bare Cu electrode (Figure 4-3c).

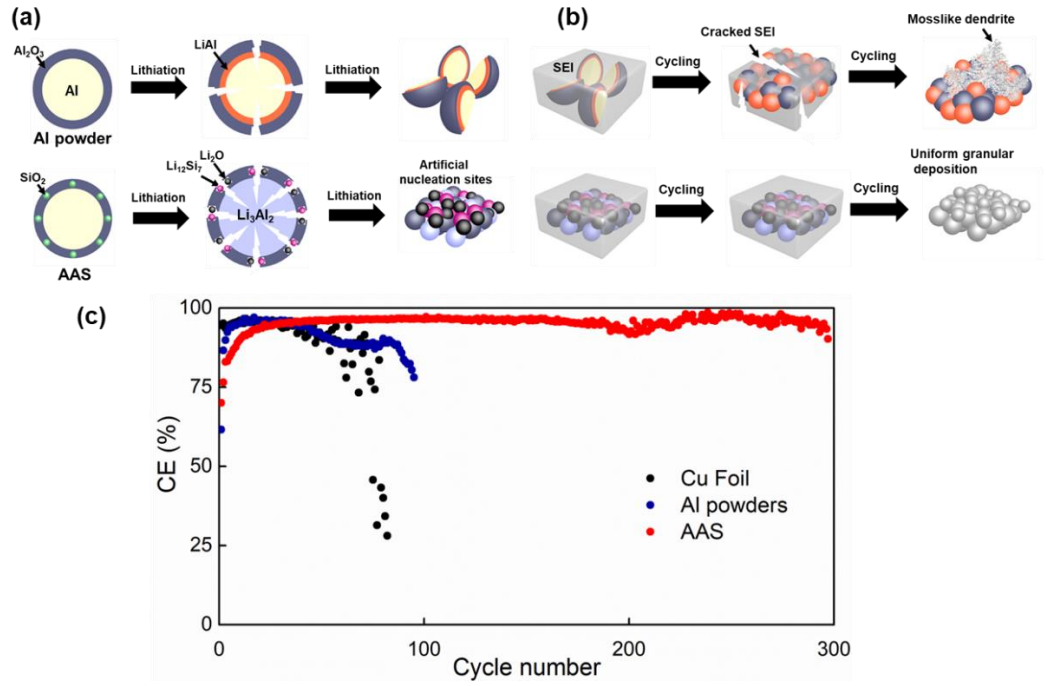


Figure 4-3. Schematic representations of (a) lithiation and (b) Li plating processes occurring with the Al powder coated and AAS modified Cu electrodes. (c) Comparison of the CE evolution with cycling of non-coated, Al powders coated and AAS modified Cu electrodes for Li plating/stripping at a current density of 0.5 mA cm^{-2} (fixed capacity of 1 mAh cm^{-2}). The electrolyte is 1 M $LiPF_6$ in EC:DEC (1:1, v/v) with vol. 5% FEC.

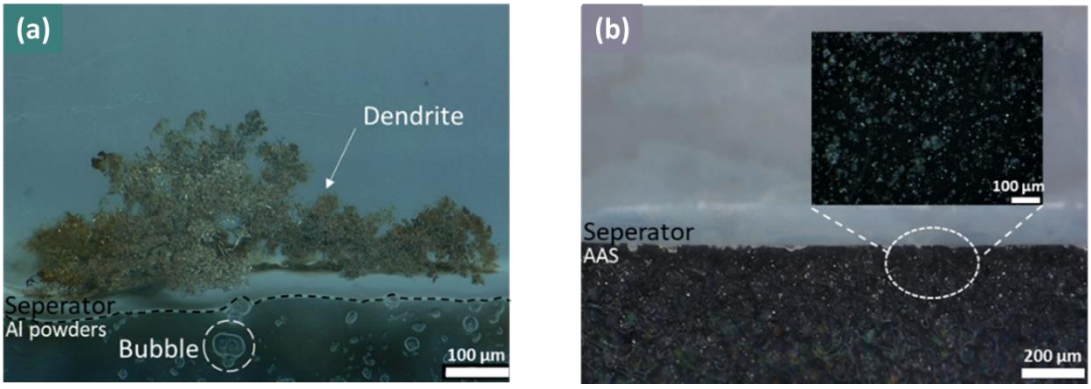


Figure 4-4. Cross-sectional optical images of 5 mAh cm^{-2} Li plating on (a) Al powders coated and (b) AAS modified Cu foils. The electrolyte employed is 1 M $LiPF_6$ in EC:DEC (1:1, v/v) with vol. 5% FEC.

The great difference between the Li plating morphologies obtained with Al powder and AAS coatings is clearly attested by the optical images obtained after 5 mAh cm^{-2} Li plating (Figure 4-4). Large dendritic deposition piercing the separator are observed on the lithiated Al powders (tremendous gas bubbles can be also noticed, Figure 4-4a) whereas granular Li deposits with metallic luster are homogeneously dispersed on AAS

particles (Figure 4-4b).

The different stabilities of the SEI layers obtained with the two different coating particles are well attested by results from the electrochemical impedance and *in situ* Raman spectroscopy measurements. EIS spectra recorded at the 5th, 10th, 15th and 20th plating/stripping cycles show the larger increase of the charge transfer resistance R_{ct} (from ~33 to 122 Ω) of the Al powder coated electrode/electrolyte interface, compared to that of the AAS modified electrode staying in the 20-40 Ω range (Figure 4-5). The faster increase of the Al powder coated electrode R_{ct} is the hint of the larger accumulation of resistive side products at the electrode surface.

Raman measurements have been carried out during the Li plating process (Figure 4-6). Stable voltage profiles and Raman intensities are observed for the AAS protected electrode (Figure 4-6b), the only notable change being the relative gradual decrease of the 741 and 904 cm^{-1} Raman bands (Figure 6c). Differently, large voltage fluctuations and overall Raman signal loss occur for the Al powder coated electrode (compare Figure 4-6a to 6b). It should be pointed out that, since it is unlikely to ascribe the simultaneous and homogeneous loss of intensity of all the different Raman bands to any side reactions degrading the electrolyte, this phenomenon should be rather attributed to the loss of the back-scattered Raman signal due to gas generation e.g. C_2H_4 from the carbonate decomposition (as also supported by the optical images, Figure 4-4a).

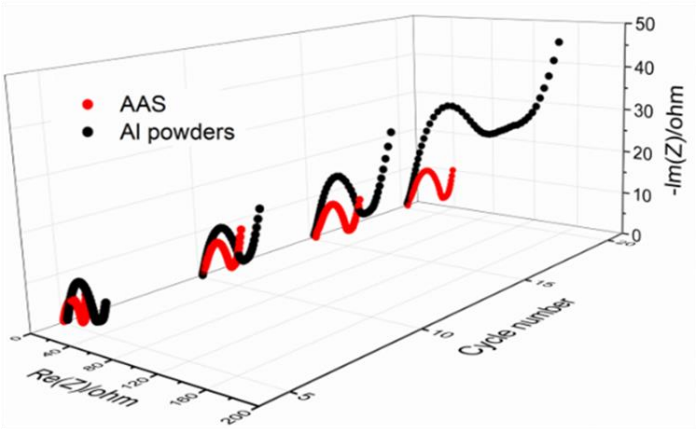


Figure 4-5. Comparison between the evolution of the EIS spectra of the Li‖Cu half cells using the (●) Al powder coated and (●) AAS modified Cu foils as working electrodes, during Li plating/stripping at a current density of 0.5 mA cm^{-2} for a fixed areal capacity of 1 mAh cm^{-2}.

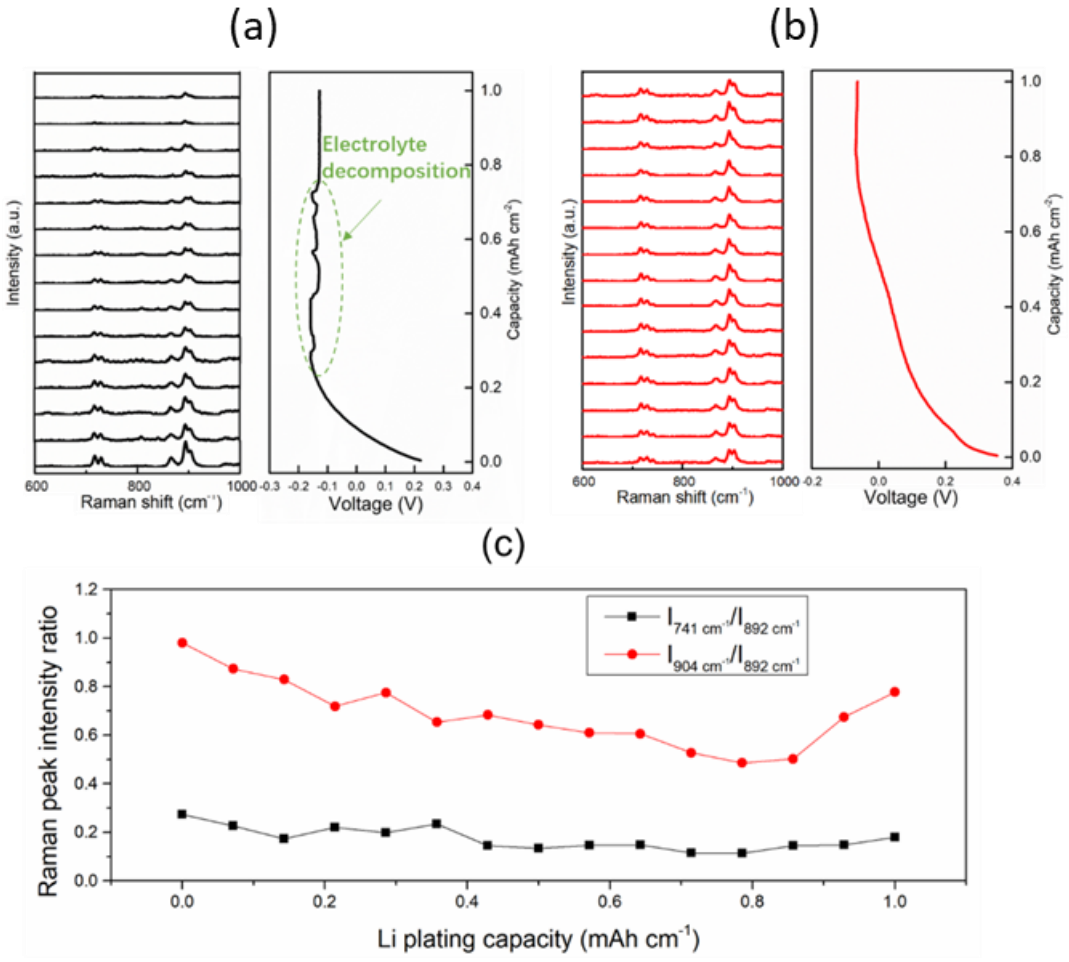


Figure 4-6. Li plating discharge curves and corresponding *in situ* μ-Raman spectra obtained with (a) Al powder coated and (b) AAS modified Cu electrodes at a current density of 0.5 mA cm^{-2} for a fixed areal capacity of 1 mAh cm^{-2}. (c) Raman peak intensity ratios $I_{741cm\text{-}1}/I_{892\ cm\text{-}1}$ and $I_{904\ cm\text{-}1}/I_{892\ cm\text{-}1}$ versus Li plating capacity for (b): the modes at 741 and 904 cm^{-1} are related to the PF_6^- and solvating EC species while that at 892 cm^{-1} belongs to free EC (see below)

The observation of the gradual decrease, as the plating at the AAS protected electrode proceeds, of the intensities of the 741 and 904 cm^{-1} bands (figure 4-6c) related to PF_6^- and Li^+ solvating EC species respectively (see below), attests the capability of *in situ* μ-Raman measurements to characterize the changes affecting the electrolyte composition and structure during the electrochemical reaction. Following this initial finding, we carried out the systemic Raman investigation of the electrolyte $LiPF_6$ in EC:DEC (1:1, v/v),. The Raman spectra of pure $LiPF_6$, EC, DEC as well as of the mixture of EC and DEC (1:1, v/v) are shown in Figure 4-7a. The Raman bands at 2800-3200 cm^{-1}, ascribed to *ν* C-H modes from EC and DEC, are not expected to be affected

by the Li^+ solvation [9]. Similarly, the Raman bands at 1000-1850 cm^{-1}, attributed to vibrations of alkyls groups and carbon-oxygen groups (C-O, C=O, etc.), either do not exhibit any Li^+ solvation behavior or have too weak intensity to be used for our purposes [10]. Differently, the vibrational modes appearing in the 700-925 cm^{-1} range are strong enough and their position presumably affected by solvation interactions with Li^+, so they can in principle be used to probe the local [Li^+]. Indeed, the Raman bands observed at 717, 730, 741, 892 and 904 cm^{-1} are attributed respectively to the vibrational modes δ C=O (EC), δ $(C=O)_n$-Li^+, ν P-F (PF_6^-), o O-C-O (EC) and o $(O\text{-}C\text{-}O)_n$-Li^+ (where o denote the ring breathing mode) [11]. As the concentration of the electrolyte increases from 0.1 to 1 M, the intensity of the band related to the PF_6^- specie rises up as expected and the Raman intensities of the Li^+ solvating solvent modes δ $(C=O)_n$-Li^+ and o $(O\text{-}C\text{-}O)_n$-Li^+ increase with respect to the free solvent modes δ C=O and o O-C-O (Figure 4-7b and 7c).

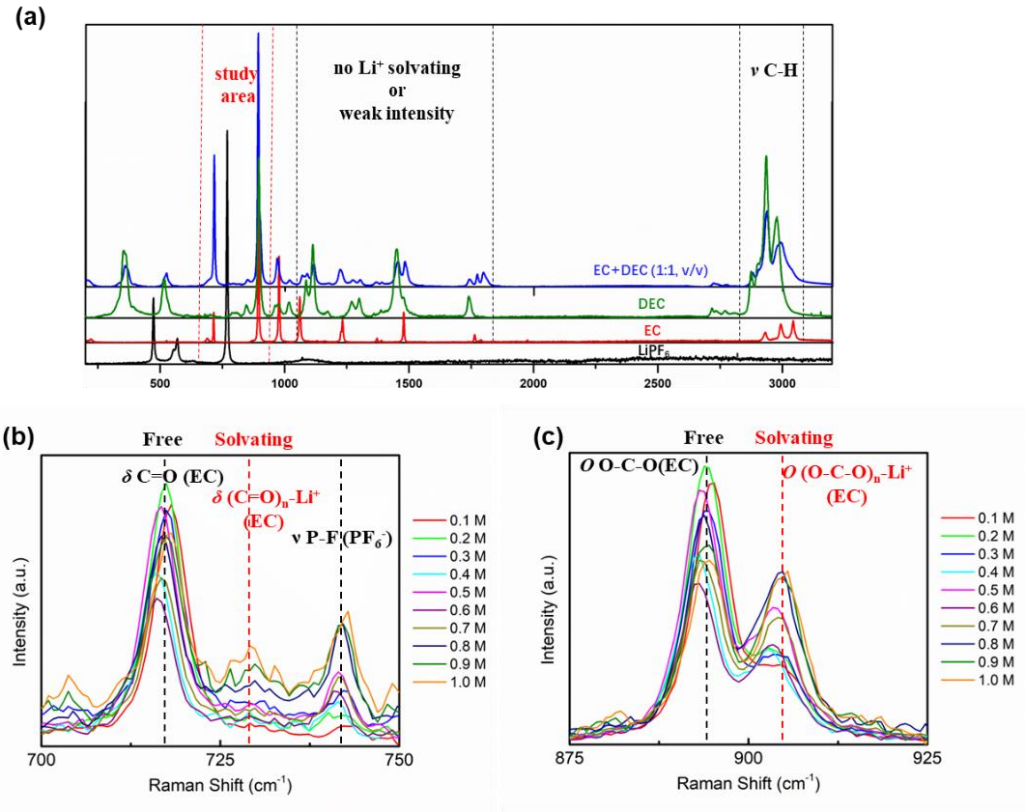


Figure 4-7. (a) Comparison of the whole Raman spectra of pure $LiPF_6$, EC, DEC and of the mixture of EC:DEC (1:1, v/v). (b,c) Evolution of the Raman spectrum of the electrolyte $LiPF_6$ in EC:DEC (1:1, v/v) with the salt concentration (details of the 700-750 cm^{-1} and 875-925 cm^{-1} spectral ranges, respectively).

Note that, since the binding between the Li^+ cation and solvent increases with the dielectric constant of the latter, the dielectric constant of EC (~95.3) being much higher

than that of DEC (~2.82), we assume here that the Li^+ solvation only involves EC species.

The spectral changes reported above, related to the salt amount in the electrolyte, allow to draw the plot calibration lines that will be used to measure the local Li^+ concentration during *in situ* Raman experiments. Figure 4-8a reports the evolution of the ratio between the intensity of the *o* $(O\text{-}C\text{-}O)_n\text{-}Li^+$ and *o* O-C-O (EC) spectral bands as a function of the salt concentration in the electrolyte: $S_{o\ (O\text{-}C\text{-}O)n\text{-}Li+} / S_{o\ O\text{-}C\text{-}O} = f(C)$ (R1). Figure 4-8b reports the evolution of the ratio between the intensity of the νPF_6^- and the δ C=O peaks: $S_{\nu PF6-} / S_{\delta\ C=O} = f(C)$ (R2). The R1 calibration line will be used preferentially because of the lower dispersion of the experimental values around the fit line and the larger slope implying larger sensibility.

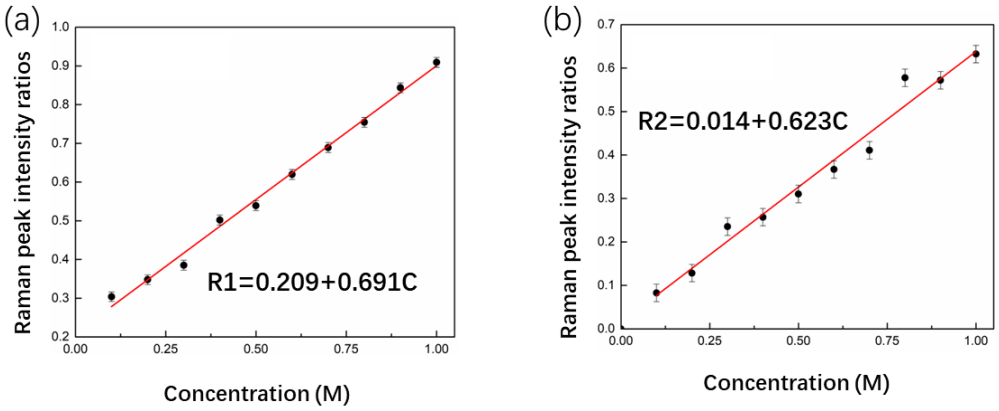


Figure 4-8. Calibration lines as obtained from the evolution of the Raman peak intensity ratios as a function of the $LiPF_6$ concentration in EC:DEC (1:1, v/v): (a) $S_{o\ (O\text{-}C\text{-}O)n\text{-}Li+} / S_{o\ O\text{-}C\text{-}O}$ and (b) $S_{\nu PF6-} / S_{\delta\ C=O}$ ratios.

Subsequently, we collected *in situ* Raman spectra of the electrolyte at 10, 50, and 100 µm from the surface of a non-coated Cu electrode during Li plating at 1 mA cm^{-2} (total capacity of 1mAh cm^{-2}, Figure 4-9a). Spectra were recorded after the generation of SEI film, every 0.1 mAh cm^{-2} (Figures 4-9b to 4-9d). It can be observed that both the intensity ratios $S_{o\ (O\text{-}C\text{-}O)n\text{-}Li+} / S_{o\ O\text{-}C\text{-}O}$ and $S_{\nu PF6-} / S_{\delta\ C=O}$ decrease with the increasing of the capacity i.e. as the reduction reaction carries on. This behavior, converted into local $[Li^+]$ by means of the calibration plot, leads to the concentration profiles reported in Figure 4-9e, representing the local $[Li^+]$ evolution during plating. Results attest the occurrence of Li^+ concentration gradients up to the noticeable distance of 100 µm and more from the electrode surface. The gradient appears to gradually increase and grow towards the electrolyte bulk as the plating reaction proceeds, without attaining stationary conditions during the time of the experiment.

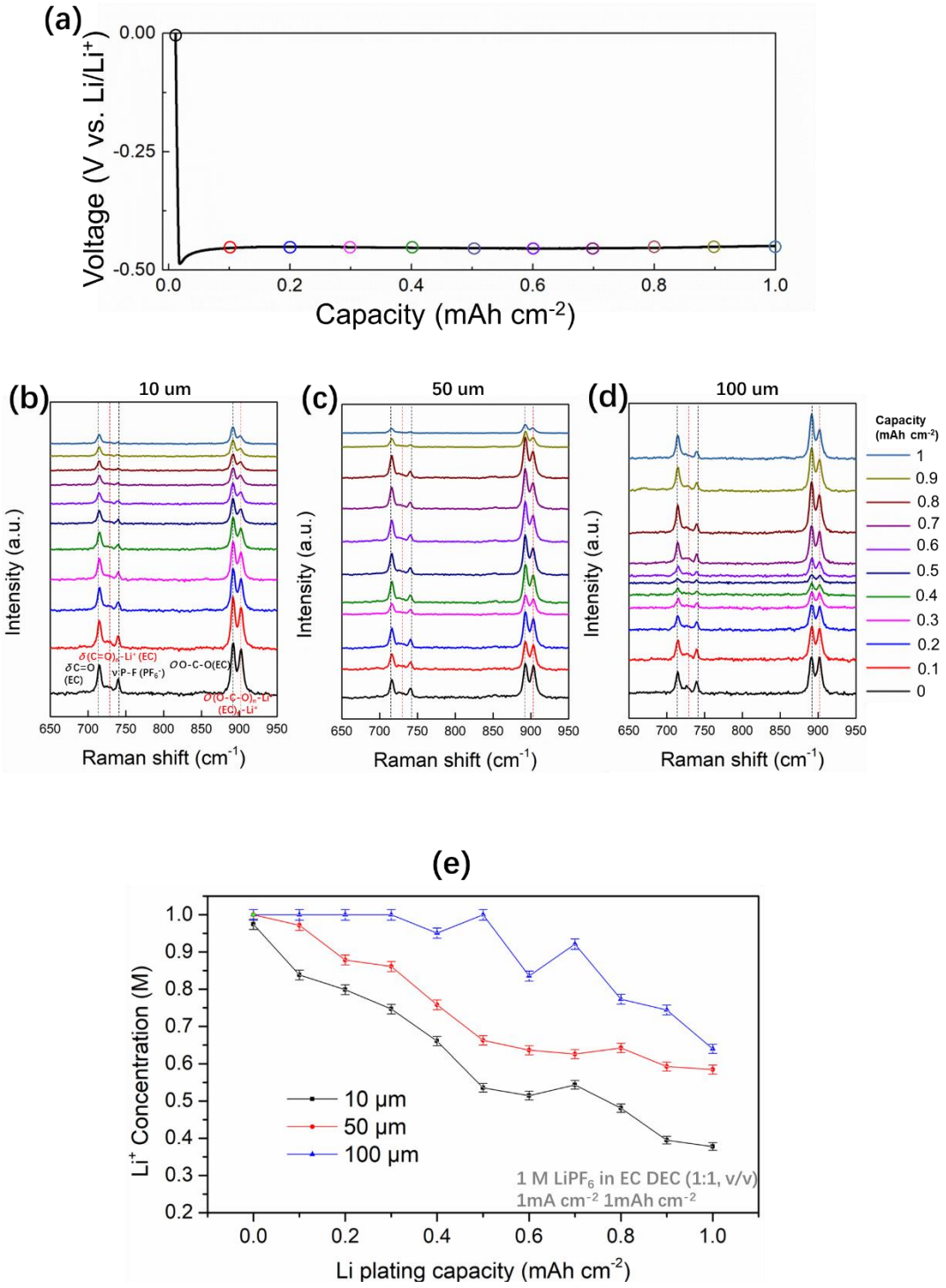


Figure 4-9. (a) Li plating carried out at 1 mA cm^{-2} (1mAh cm^{-2}) with the Li‖Cu cell filled with 1 M $LiPF_6$ in EC:DEC (1:1, v/v): (a) Voltage vs. Capacity curve, (b-d) corresponding *in situ* Raman spectra collected at different distances from the electrode surface and (e) resulting local [Li^+] evolution as the plating reaction progresses.

The SEM characterization of the Cu foil surface after plating confirms the heterogeneous, dendritic-like morphology of the Li deposit expected from this type of diluted electrolyte (Figure 4-10). As previously discussed, Li^+ mass transport in the

electrolyte phase occurs by the three mechanisms of diffusion, convection and migration. During electroreduction, the direction of cation diffusion aligns with their electromigration pathway. However, natural convection, unavoidable and unpredictable, interferes with this process and induces spatial heterogeneity of the Li^+ transfer rate. In other words, some cations will move faster or slower than others. In the case of diluted electrolytes, this phenomenon induces concentration gradients sensibly different at different areas of the electrode surface, with the apparition of separate Li deposition locations giving dendrites which propagate into the bulk electrolyte if the displacement of the Li^+ to the electrode surface is too slow to compensate consumption [1].

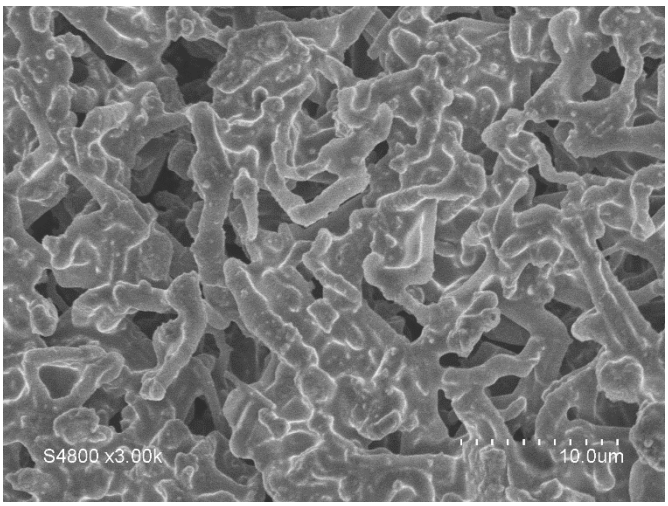


Figure 4-10. SEM image of dendritic Li deposition obtained with 1 M $LiPF_6$ in EC:DEC (1:1, v/v) at plating capacity of 1 mAh cm^{-2} and current density of 1 mA cm^{-2}.

This preliminary study of the diluted binary solvent electrolyte EC/DEC, widely investigated for perspective Li metal batteries, allowed us to attest the feasibility of *in situ* μ-Raman measurements to detect concentration gradients in the electrolyte of the working electrochemical cell. Unfortunately, the EC/DEC system could not be used to carry on our study with highly concentrated electrolytes (≥ 4M) because of the limited ability to dissolve $LiPF_6$. As shown in Figure S4-2 (see SI), a 2 M solution of $LiPF_6$ in EC:DEC (1:1, v/v) is turbid, and a 4 M solution presents consistent deposition of undissolved salt. Thus, in the following, the comparison between LCE, HCE and LHCE is carried out using another solvent, DMC, in which $LiPF_6$ is highly soluble.

4.3 *In situ* Raman measurements of the Li^+ concentration gradients occurring during plating: comparison between low-, high- and localized high-concentration electrolytes

This study has been carried out using the electrolytes already investigated in chapter 3, consisting in $LiPF_6$ either in DMC alone or in DMC:HFPM (7:3, v/v). Measurements have been done at different concentrations (1, 2 and 4M) and plating current densities (0.5, 1.0 and 2.0 mA cm^{-2}). The local [Li^+], probed at 10, 50 and 100 µm from the electrode surface, has been determined using the ratio between the intensities of the ν C-O modes of free and solvating DMC at 918 and 937 cm^{-1} respectively, i.e. $R_{sco} = S_{solvating\ C\text{-}O}/S_{free\ C\text{-}O}$ (see § 3.2, Figure 3-4). Actually, less accuracy was observed when using other ratios like $R_{soco} = S_{solvating\ O\text{-}C\text{-}O}/S_{free\ O\text{-}C\text{-}O}$, $R_{poco} = S_{PF6^-}/S_{free\ O\text{-}C\text{-}O}$ or $R_{pco} = S_{PF6^-}/S_{free\ C\text{-}O}$ because of (i) the overlapping between the Raman peaks related to the δ $(O\text{-}C\text{-}O)_n$-Li^+ mode and to the PF_6^- and HFPM species, inducing larger errors in the evaluation of the intensities by peak fitting, and (ii) the weakness of the PF_6^- vibration, becoming undetectable as the Li plating progresses (see Figure S4-3 in SI). Figure 4-11 reports the evolution of R_{sco} with the $LiPF_6$ concentration in DMC and the corresponding macroscopic and local concentrations in DMC:HFPM (7:3, v/v). As previously reported in chapter 3 (§ 3.2), R_{sco} first increases linearly with the $LiPF_6$ amount and, then, in a polynomial manner. So, the evolution of R_{sco} with [$LiPF_6$] in DMC is according to:

$$R_{sco} = 0.21C + 0.01 \ (0 \leq C \leq 1.2) \qquad \text{Equation 4-1}$$

$$R_{sco} = 0.61C^2 - 1.27C + 0.97 \ (1.2 < C \leq 5) \qquad \text{Equation 4-2}$$

The relation between R_{sco} and the macroscopic concentration of $LiPF_6$ in DMC:HFPM (7:3, v/v) is:

$$R_{sco} = 0.22C - 0.0045 \ (0 \leq C \leq 1.7) \qquad \text{Equation 4-3}$$

$$R_{sco} = 0.71C^2 - 1.94C + 1.69 \ (1.7 < C \leq 4) \qquad \text{Equation 4-4}$$

The evolution of R_{sco} as a function of the local concentration of $LiPF_6$ in DMC:HFPM (7:3, v/v) corresponds to:

$$R_{sco} = 0.15C - 0.0041 \ (0 \leq C \leq 2.43) \qquad \text{Equation 4-5}$$

$$R_{sco} = 0.35C^2 - 1.38C + 1.72 \ (2.43 < C \leq 5.71) \qquad \text{Equation 4-6}$$

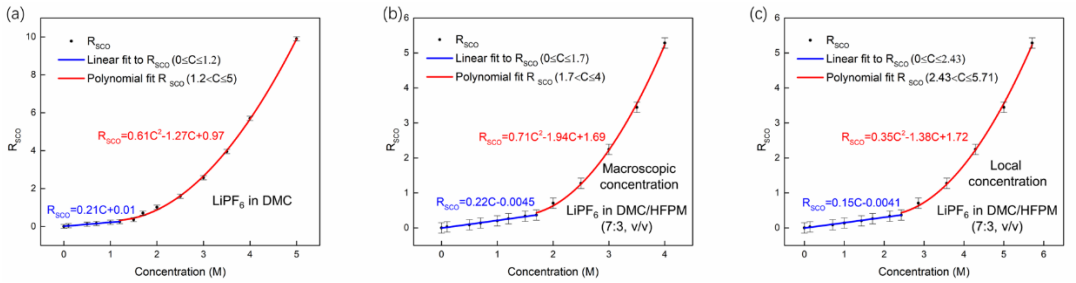


Figure 4-11. R_{sco} versus (a) the concentration of $LiPF_6$ in DMC, (b) the macroscopic and (c) local concentrations of $LiPF_6$ in DMC:HFPM (7:3, v/v).

Figure 4-12 compares the evolutions, during the Li deposition process, of the local Li^+ concentration in DMC and DMC:HFPM (7:3, v/v) solutions, obtained at different plating current densities and initial $LiPF_6$ concentrations. Note that, in the following, the same term "concentration" will correspond to "local concentration" when referred to $LiPF_6$ dissolved in the mixture DMC/HFPM, and to the usual macroscopic concentration when dealing with the $LiPF_6$ solution in DMC. Measurements have been carried out with the same experimental setup (Li‖Cu half-cell) than in the previous section (§ 4.2).

Some common features can be noticed for the measurements reported in Figure 4-12. As previously observed for 1 M $LiPF_6$ in EC:DEC (1:1, v/v) (Figure 4-9e), the local $[Li^+]$ decreases with the plating capacity (i.e. as the plating reaction progresses) and, on the whole, with the proximity of the probed position to the electrode surface. The last phenomenon becomes more and more enhanced with the increase of the plating current density and the initial electrolyte concentration. Differently, the $[Li^+]$ decreasing rate with the plating capacity observed for a given initial concentration, expressed by the slope of the concentration profile, appears almost unaffected by the probed position. Only at the largest current density, i.e. 2 mAh cm^{-2}, the $[Li^+]$ decreasing rate appears slightly larger for the more concentrated electrolytes. As a result of the different behaviors discussed above, the concentration profiles measured at a given position overlap at the lower concentrations and current densities, and then gradually separate as these parameters increase. This phenomenon, which corresponds to the occurring of progressively larger Li^+ concentration gradients across the electrolyte, appears slightly enhanced by the presence of the diluent LHCE (see also below).

As for the differences which can be observed between LCE (1M $LiPF_6$ in DMC), HCE (4 M $LiPF_6$ in DMC) and LHCE (4 M $LiPF_6$ in DMC/HFPM), they mainly concern the Li^+ depletion closer to the electrode surface and the occurrence of more or less enhanced

Li^+ concentration gradients. Figure 4-13 compares the Li^+ consumptions measured at 10 µm from the Cu electrode, calculated as the difference between the local [Li^+] measured at the beginning (0 mAh cm^{-2}) and at the end (1 mAh cm^{-2}) of the plating process at this position. The same data are reported in SI (Figure S4-4) as Li^+ consumption rates i.e. the ratio between the Li^+ consumption and the [Li^+] at the beginning of the plating process (at 0 mAh cm^{-2}).

As expected, Li^+ consumption increases with the plating current density, which obviously corresponds to the increasingly large difference between the rate of the Li^+ reduction reaction at the electrode surface and the rate of the Li^+ transport from the bulk

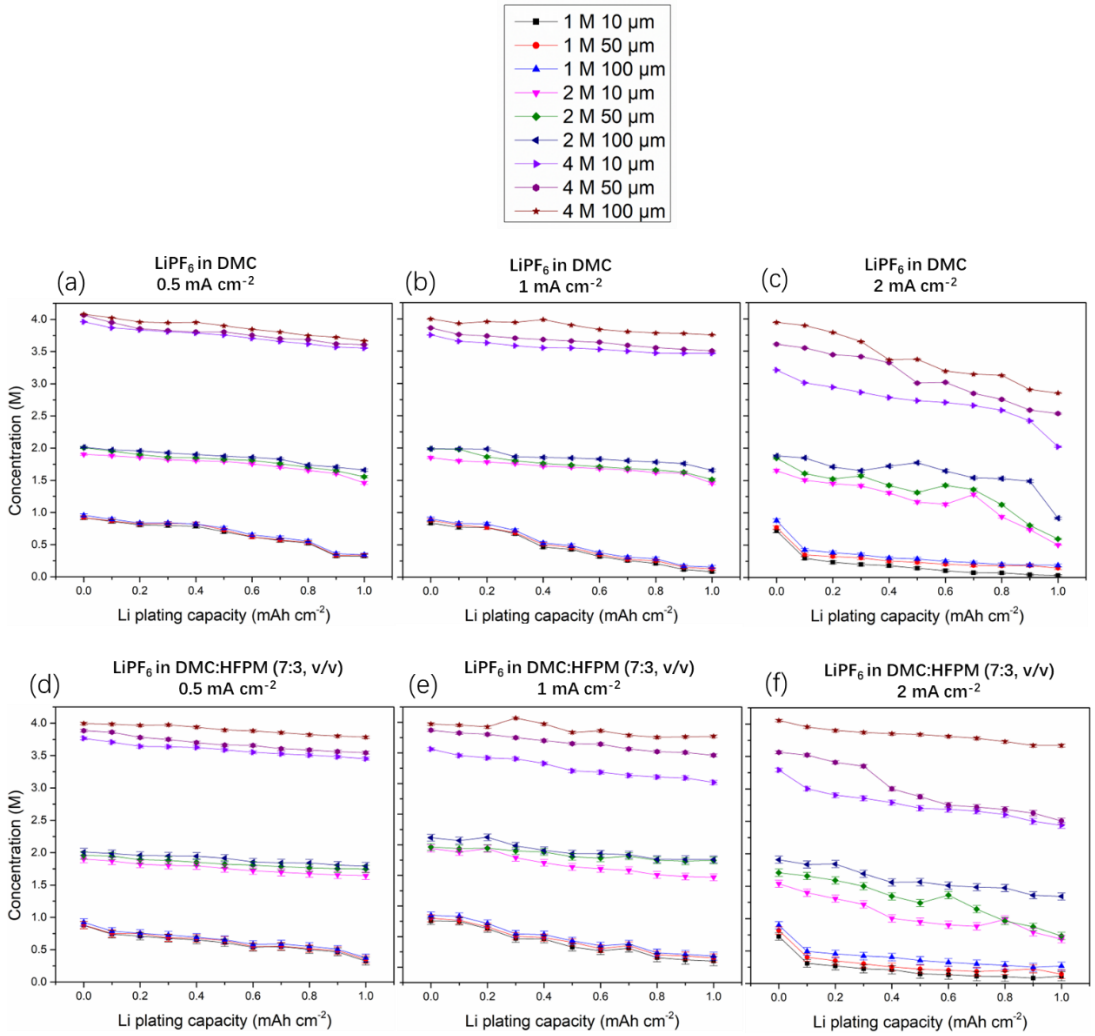


Figure 4-12. Evolution during the Li plating process (fixed capacity of 1 mAh cm^{-2}) of the local Li^+ concentration of the electrolytes consisting of $LiPF_6$ in (a-c) DMC and (d-f) DMC:HFPM (7:3, v/v), at different distances from the electrode surface, for different plating current densities and $LiPF_6$ initial (local) concentrations (indicated in the figure). Errors are within the symbol size when they are not visible.

electrolyte to the reaction site. Otherwise, no unique relationship can be observed between the Li^+ consumption and the electrolyte initial concentration. Consumption appears to decrease globally with concentration for plating carried out at 0.5 and 1 mA cm^{-2}, while the opposite is observed at 2 mA cm^{-2}. Anyway, insofar as the appearance of dendritic morphologies is related to the lack of Li^+ supply to the electrode surface, the most interesting to note here is that the addition of the solvent HFPM, to obtain LHCEs, decreases the Li^+ consumption rate compared to the LCEs and HCEs of same concentration and under the same current conditions (at least in the most of cases, the only exception being observed for the measurement carried out at 1 mA cm^{-2} with the 2 and 4 M electrolytes).

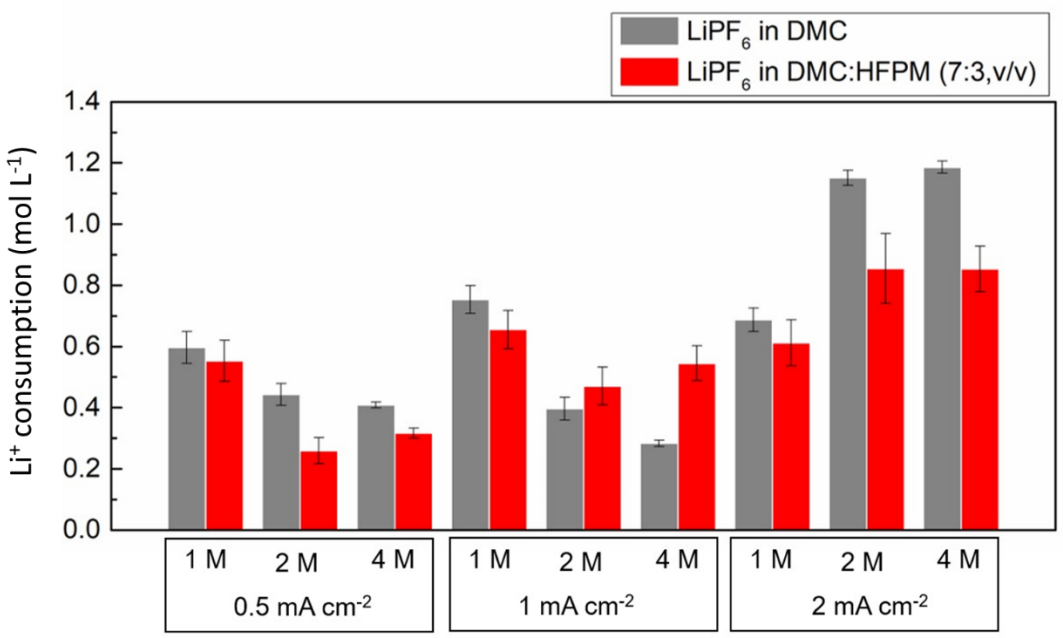


Figure 4-13. Li^+ consumption at 10 µm from the Cu electrode, for the different electrolytes of $LiPF_6$ in DMC and $LiPF_6$ in DMC:HFPM (7:3, v/v), at different salt concentrations and plating current densities.

In situ Raman measurements reported in Figures 4-12 allow to calculate approximate values of the Li^+ concentration gradient crossing the electrolyte during operation from the difference between the local [Li^+] probed at 10 and 100 µm from the electrode surface:

$$\text{Concentration gradient} = \frac{[Li^+]_{100\mu m} - [Li^+]_{10\mu m}}{100\mu m - 10\mu m} \qquad \text{Equation 4-7}$$

Figure 4-14 compare the rough concentration gradients as observed at the end of the plating process i.e. calculated from the local [Li^+] values measured at the plating

capacity of 1mAh cm^{-2}. It should be noted that the gradients obtained at other, previous, steps of the plating process are not significantly different, the only exception being the gradients measured at 0 mAh cm^{-2} which are slightly lower. This attests that, during plating, mass transport stationary conditions are already attained at the plating capacity of 0.1 mAh cm^{-2}. Concentration gradients increase with the plating current density (as expected) and the electrolyte concentration. Surprisingly, an even larger gradients increase is systematically observed when HFPM is added as diluent. Thus, the magnitude of the gradients follows the sequence: LCE < HCE < LHCE. This should correspond to the gradual decrease in the Li^+ transport rate according to the same order. Then, larger gradients should also correspond to larger Li^+ depletion at the electrode and, thus, to the formation of Li deposits with dendritic morphology. So, our results seem to contradict the usual observation of smooth homogeneous deposition obtained by LHCEs. But, at the same time, the comparison of data reported in Figures 4-13 and 4-14 suggest that gradients across the electrolyte and Li^+ depletion closer to the electrode surface may not be so directly related.

The parameter linking ionic transport rate and concentration gradients is the diffusion coefficient D [1,5]. We applied the method proposed by Yamanaka *et al.* [5] to roughly estimate D_{Li+}, according to:

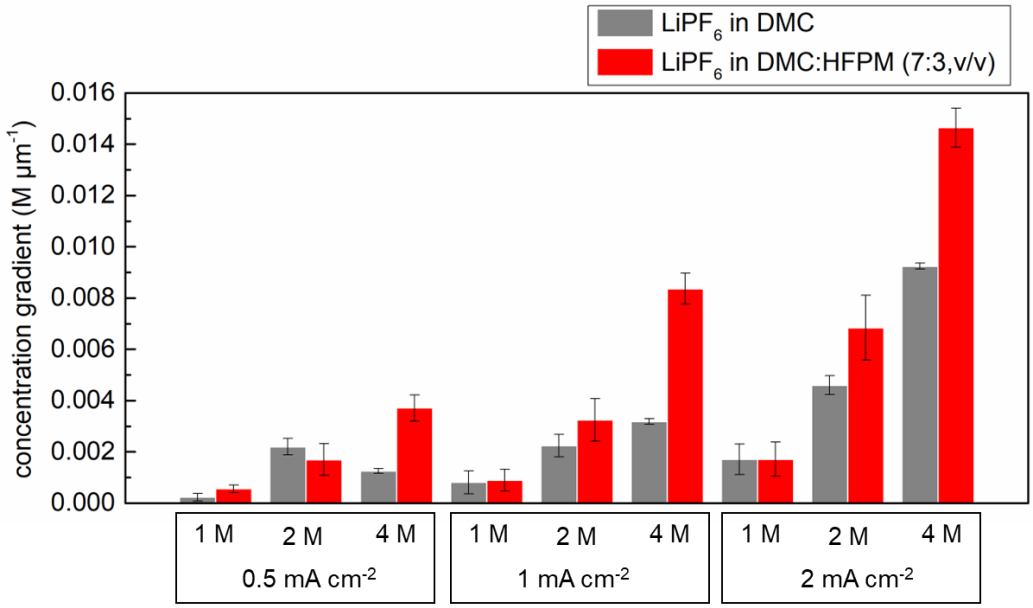


Figure 4-14. Concentration gradients observed with the different electrolytes: $LiPF_6$ in DMC and $LiPF_6$ in DMC:HFPM (7:3, v/v) at different concentrations and plating current densities.

$$N=\frac{J}{zF}=\frac{[Li^+]_{100\mu m}-[Li^+]_{10\mu m}}{100\mu m-10\mu m}D_{Li+} \qquad \text{Equation 4-8}$$

where N is diffusion flux, J the current density, F Faraday constant (96485 C mol^{-1}) and z the charge number of Li^+. Figure 4-15 reports the evolution of the Li^+ diffusion coefficients of the different electrolytes here investigated during the Li plating process. Figure 4-16 compares the average D_{Li+} values calculated at a given $LiPF_6$ concentration for each plating experiment. Values are of the same order of magnitude of those measured by Chen *et al.* [12] at ambient temperature by pulsed field gradient NMR and, similarly, decrease with the increase of the electrolyte concentration (a larger drop of the D_{Li+} value is observed between the 1 and 2 M solutions). Obviously, as for gradients (Figure 4-14), the electrolyte concentration appears again as the most affecting parameter. Otherwise, even if values reported in Figure 4-15 are sometime quite spread, it can nevertheless be concluded that D_{Li+} does not change significantly with the occurring of the Li plating and is not affected by the plating current density. Differently, the addition of the diluent HFPM to the salt/solvent mixture is observed to decrease sensibly the Li^+ diffusion. All the average D_{Li+} values calculated for the electrolyte $LiPF_6$ in DMC/HFPM are systematically lower than the corresponding coefficient calculated for $LiPF_6$ in DMC alone. Thus, the LCE constituted of 1 M $LiPF_6$ in pure DMC exhibits the highest D_{Li+} whereas the LHCE with the largest salt concentration (4 M) has the lower D_{Li+}. This further supports, in agreement with the ionic conductivities measurements reported by others (see for example Piao *et al.* [13] and Ren *et al.* [14]), that the addition of diluents like HFPM to form LHCEs, even if decreasing the electrolyte viscosity, hinders the Li^+ transport rate through the electrolyte, presumably because of the disaggregation of the ionic arrangement necessary for Li^+ transport by the hopping mechanism.

The salt concentration of the electrolyte remains the main parameter affecting D_{Li+}, which is observed to decrease with the increase of $[Li^+]$. This phenomenon has been previously observed for both binary and ternary solutions once their $[Li^+]$ exceeded ~1M [14,13]. To a first approximation, the D_{Li+} decrease with increasing $[Li^+]$ could be attributed to the inclusion of Li^+ into AGGs clusters, whose large size implies stronger friction with solvent molecules and, thus, slows down the cationic motion.

The comparison between Figures 4-13 and 4-16 shows that D_{Li+} and Li^+ consumption rates cannot be directly and systematically related to each other. Larger D_{Li+} should correspond to smaller Li^+ consumption (larger local concentration) at the proximity of

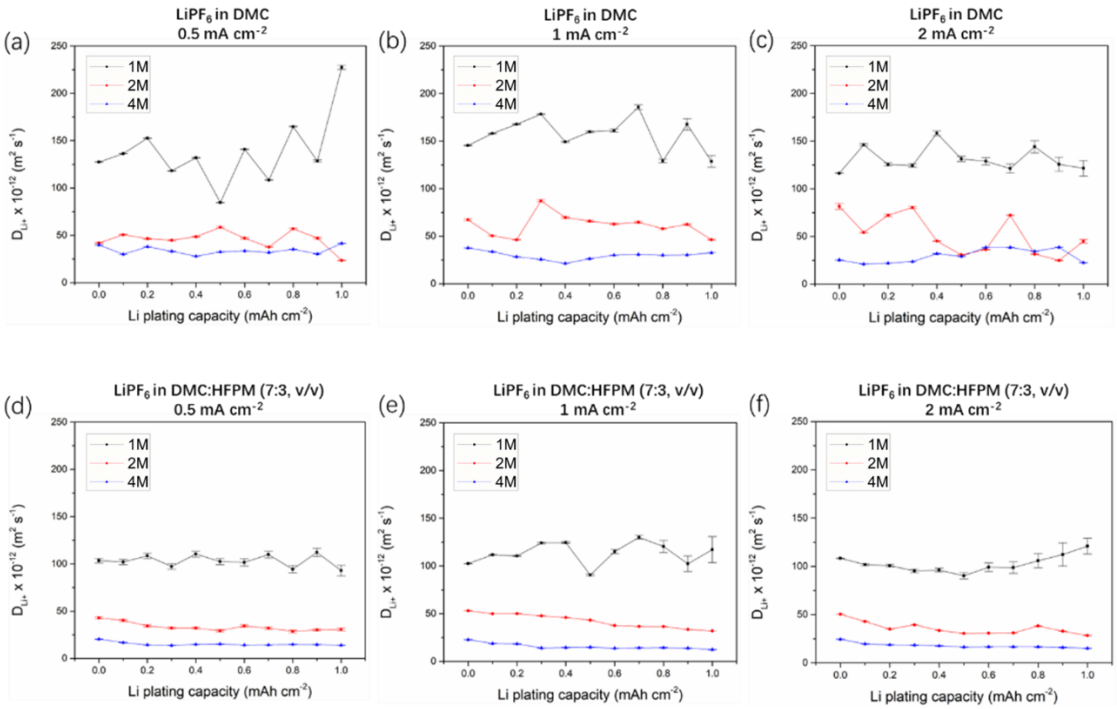


Figure 4-15. Evolution of D_{Li+} during the Li plating process at different current densities (indicated) and different concentrations of $LiPF_6$ in (a-c) DMC and (d-f) DMC:HFPM (7:3, v/v). Errors are within the symbol size when they are not visible.

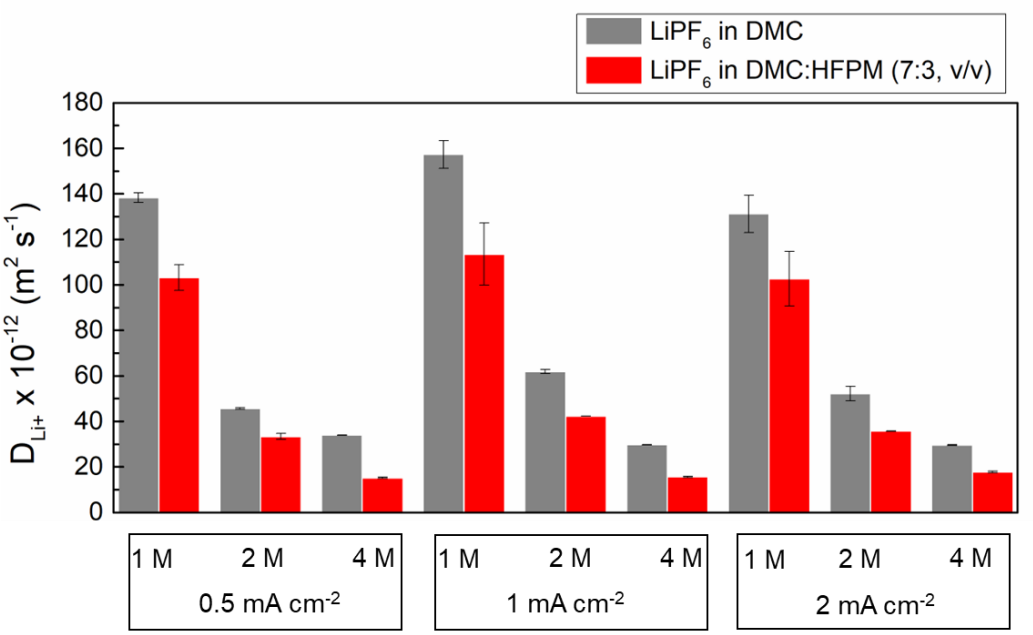


Figure 4-16. Average D_{Li+} values calculated for the different electrolytes and the different Li plating experiments.

10 µm from the Cu foil, if diffusion across the electrolyte solution were the only or the main mechanism regulating the charge transfer to the electrode.

But this is observed only at the lowest plating current density (0.5 mA cm^{-2}) whereas the opposite occurs at the largest (2 mA cm^{-2}) and no systematic correspondence

between data can be attested at the intermediate current. Characterization data reported in the following (§ 4.5) will suggest that the [Li^+] closest to the electrode surface is rather determined by the Li^+ transport ability of the SEI layer.

4.4 SEM characterization of the Li deposition morphology

SEM analysis attests the large variation of the Li deposit morphology with the electrolyte composition and concentration as well as with the Li plating current density (Figure 4-17). As far as the electrolyte consisting of $LiPF_6$ in pure DMC is concerned, typical long and twisty dendritic morphology is observed at the lower salt concentration and low (0.5 mA cm^{-2}) or intermediate current density (1 mA cm^{-2}, Figure 4-17a).[7] Increasing the electrolyte concentration decreases the amount of dendrites observed and induces a more bulk-like morphology to appear (Figure 4-17b) with the coexistence of dendrites and granular Li with similar sizes (Figure 4-17c). The addition of the diluent HFPM affects morphology even more. At the lower local concentration (1 M, Figure 4-17e), the Li deposit has the form of large "islands" or massive agglomerates with a diameter of several tens of μm. Increasing the electrolyte concentration initially decreases the islands' size (Figure 4-17f) and, then, induces uniform and smooth Li deposit (Figure 4-17g). Interestingly, the island-like outline can be still observed under the homogeneous deposit as if the Li plating occurred according to a 2-step process. The current density applied during plating also affects the deposit morphology but more or less strongly according to the electrolyte concentration. As far as the low concentration electrolyte based on pure DMC solvent is concerned, weak plating currents as 0.5 mA cm^{-2} mitigate the dendritic growth and promote a mainly granular deposit (Figure 4-18a) while larger currents increase dendritic morphology (Figure 4-18b). The increasing of the plating current density has less impact on the deposition morphologies of the concentrated electrolytes (Figure 4-17d and 17h). The same granular morphology observed for 4 M $LiPF_6$ in DMC at 1 mA cm^{-2} is essentially maintained at 2 mA cm^{-2}, even if the grain size appears to increase and a few dendrites arise again. The homogeneous, smooth deposit obtained with 4 M $LiPF_6$ in DMC:HFPM (7:3, v/v) at 1 mA cm^{-2} is also still observed at 2 mA cm^{-2}, even if a beginning of granular plating appears.

[7] Results obtained at 0.5 mA cm^{-2} are not reported since identical to those obtained at 1 mA cm^{-2}.

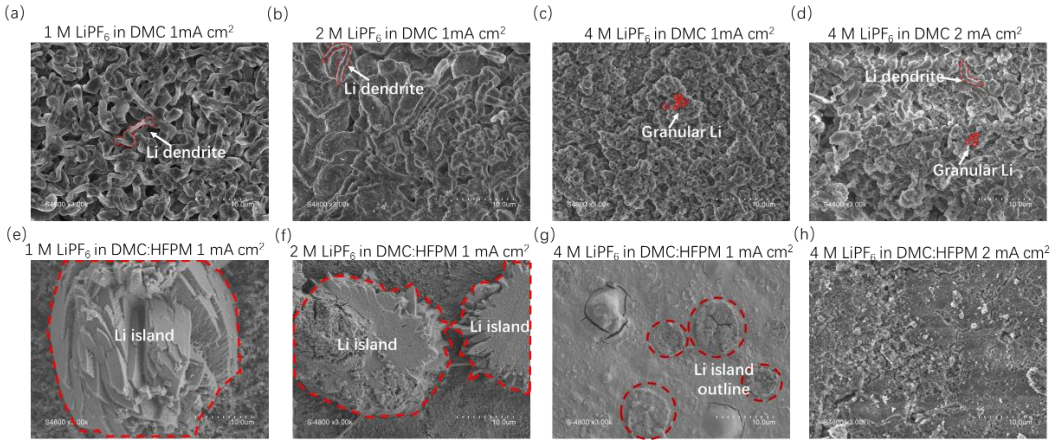


Figure 4-17. SEM images of metallic Li deposited from the solutions of $LiPF_6$ in (a-d) DMC and (e-h) DMC/HFPM, at different salt concentrations and plating current densities as indicated in the figure. The Li plating capacity was fixed at 1 mAh cm^{-2}.

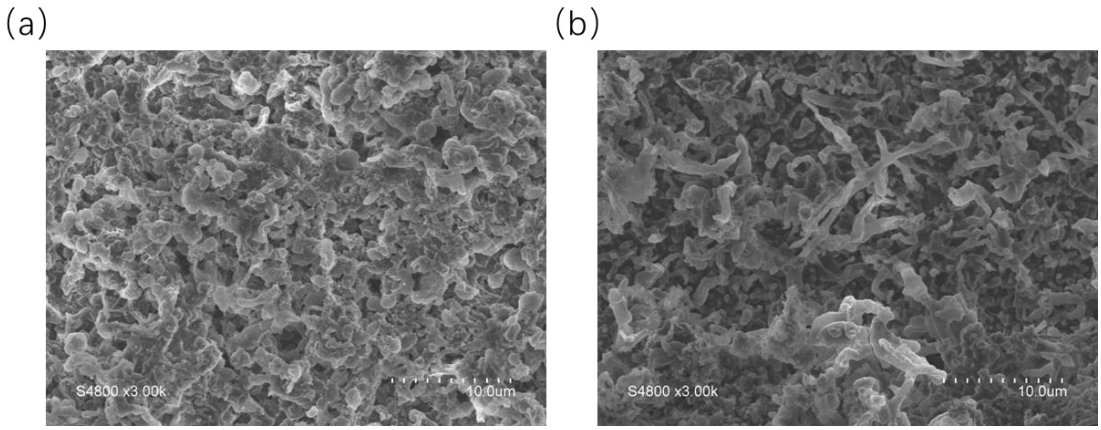


Figure 4-18. SEM images of metallic Li deposited from 1 M $LiPF_6$ in DMC at (a) 0.5 and (b) 2 mA cm^{-2}. The Li plating capacity was fixed at 1 mAh cm^{-2}.

Results reported above confirm that highly concentrated, and more particularly locally highly concentrated electrolytes reduce the dendritic generation, allowing granular Li deposits in the case of HCEs and smooth, homogeneous Li plating for LHCEs [12,15]. But the comparison with data from *in situ* μ-Raman show that this ability cannot be simply and directly related to a larger Li^+ diffusivity allowing less enhanced Li^+ concentration gradients at the electrode-electrolyte interface, as usually proposed (see [1] and references therein). Let's recall that heterogeneous Li electroplating is usually considered to appear when the lack of transport rate of Li^+ in the electrolyte does not allow the adequate renewal of the reactive specie of the reduction reaction at the electrode surface. This phenomenon is expected to be related to the occurrence of strong Li^+ concentration gradients at the electrolyte-electrode interface, with local concentration near the electrode surface approaching zero. The electroplated Li

therefore tends to grow preferentially towards the direction of the bulk electrolyte where more Li^+ is available, thus forming local protrusions i.e. dendrites. Then, we have to point out that the *in situ* spectroscopic results obtained in this work do not allow to confirm any direct relationship between the Li^+ concentration gradients experimentally observed (at least for the distance range investigated here i.e. between 10 and 100 μm from the electrode surface) and the D_{Li+} deduced from them on the one hand, and the Li^+ consumption rate observed closest to the electrode surface (i.e. 10 μm) and the Li deposit morphology on the other hand. Indeed, Li^+ concentration gradients increase approximately according to the sequence: 1M $LiPF_6$ in DMC < 1 M $LiPF_6$ in DMC/HFPM < 4 M $LiPF_6$ in DMC < 4 M $LiPF_6$ in DMC/HFPM, whereas the Li^+ consumption rate and D_{Li+} exhibit almost the opposite behavior. Thus, the more dendritic-like morphology is observed with the 1M $LiPF_6$ in DMC electrolyte, having the largest D_{Li+} (lowest [Li+] gradient) but also the largest Li^+ consumption, and the more homogeneously smooth deposit with 4 M $LiPF_6$ in DMC/HFPM, having the lowest D_{Li+} (largest [Li^+] gradient) but also the lowest Li^+ consumption. Increasing concentrations well correspond to decrease the heterogeneity of the Li plating but, at the same time, to the decreasing of the Li^+ diffusivity. On the whole, these data suggest that the Li deposit morphology is affected by the local Li^+ concentration closest to the electrode-electrolyte interface which, however, does not appear particularly related to the Li^+ transport rate across the electrolyte but rather, assuming by exclusion, to the transport properties of the SEI layer.

4.5 Characterization of the SEI film

The SEI layer characterization was carried out for the electrolytes showing the most different morphologies i.e. 1 M $LiPF_6$ in DMC, 4 M $LiPF_6$ in DMC and 4 M $LiPF_6$ in DMC:HFPM (7:3, v/v) (denoted respectively as #LCE, #HCE and #LHCE in the following). Indeed, deposits from #LCE always exhibit dendrites, at different amounts depending on the plating current density. The electrolyte #HCE produces deposits of mainly granular morphology and the #LHCE is the only to induce a smooth and homogeneous plating. Corresponding Li plating curves are reported in Figure 4-19a, together with the Li nucleation overpotentials (Figure 4-19b) and EIS spectra of the Li‖Cu half-cell at the end of the plating process (Figure 4-19c). EIS and XPS analyses have been carried out with the same instruments and experimental setup reported in chapter 3. Raman spectra collected *in situ* during the plating process are reported in SI

(Figure S4-5).

Plating curves obtained with #LCE and #HCE show voltage fluctuations, while this is not the case for #LHCE. Such fluctuations are usually observed when further electrolyte decomposition occurs due to the reformation of the SEI film once broken by the Li dendrites [16,17]. Therefore, this is the hint of a more severe electrolyte degradation for #HCE and #LCE than for #LHCE. Also, plating curves show that the Li nucleation over-potential increases according to: #LHCE < #HCE < #LCE, which attests the higher Li affinity for the SEI film of #LHCE or, speaking more generally, the lower hindering opposed by the SEI layer to the plating process.

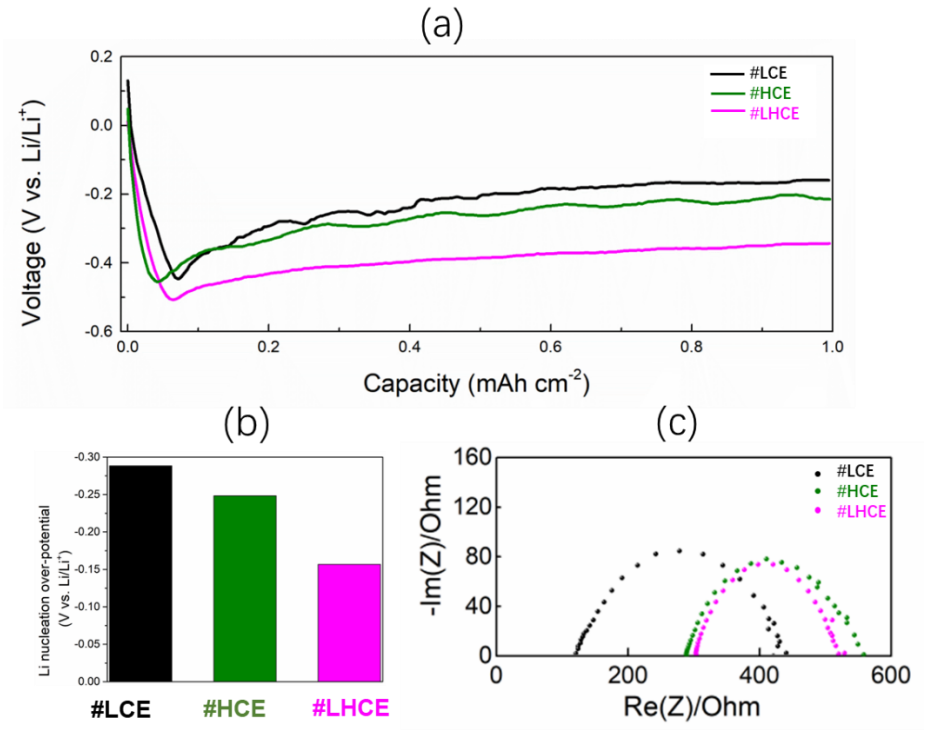


Figure 4-19. (a) Comparison of the Li plating curves of #LCE, #HCE and #LHCE carried out at 2 mA cm^{-2} (1mAh cm^{-2}) in the Li‖Cu cell, (b) corresponding Li nucleation over-potentials and (c) EIS spectra recorded at the end of the plating deposition experiment.

As mentioned in chapter 2 (§2.3.2), EIS spectra carried out at the end of the plating process allow to calculate the electrolyte ohmic resistivity, R_{ohm}, and the charge transfer resistance at the electrode-electrolyte interface, R_{ct}. Measurements reported in Figure 4-19c show that the charge transfer resistance decreases with the electrolyte concentration and the diluent addition: R_{ct} = 320, 268 and 225 Ω for #LCE, #HCE and #LHCE respectively. On the contrary, the electrolyte ohmic resistivity increases: R_{ohm} = 123, 290, and 305 Ω for #LCE, #HCE and #LHCE respectively. This corresponds

well to the decrease of the Li^+ diffusivity across the electrolyte attested by the Li^+ concentration gradients and the diffusion coefficients (Figure 4-14 and Figure 4-16). It should be noted that the electrolyte conductivity decreases observed when passing from the 1 to the 4 M solution could appear surprising since in contradiction with the increase of the number of charge carriers. Actually, conductivity drops at excessive salt concentration are often experimentally observed (see for example [18]) and can be attributed to the increase of the electrolyte viscosity and/or, as previously proposed in this chapter (§ 4.3), to the increase of friction forces between solvent and large AGGs clusters including Li^+. Differently, the conductivity decreases with the diluent addition, also previously observed [14,13], has to be ascribed to the disaggregation of the Li^+ conductivity path needed by the hopping mechanism (see also chapter 3, § 3.4).

The composition of the SEI films deposited on the Cu electrode during the plating process was analyzed by ATR-FTIR and XPS spectroscopy. As can be seen in Figure 4-20a, the SEI formed in the #LCE is the only showing peaks at 2850 and 2916 cm^{-1} related to the *v* C-H modes. The absence of these peaks on the spectra of #HCE and #LHCE indicates, by difference, the lower contents of organic species of their SEIs. As well, bands related to the species $ROCO_2Li$ (1640 cm^{-1}) and $(ROCO_2Li)_2$ (1700 cm^{-1}) [19], where R = CH_3, CH_2, etc. are observed for all the samples but with different intensities (Figure 4-20b). The area ratio $S_{(ROCO2Li)2}/S_{ROCO2Li}$ is larger for #LCE and decreases according to: #LCE > #LHCE > #HCE (Figure 4-20c). The different relative amounts of the dimer $(ROCO_2Li)_2$ reflect the different reactivity of the electrolytes towards the reduction degradation process. The larger $S_{(ROCO2Li)2}/S_{ROCO2Li}$ ratio observed for #LCE attests a degradation process mainly involving organic species, what agree with the largest amount of reactive free solvents molecules observed in this electrolyte (see chapter 3, § 3.3). Actually, the degradation mechanism proposed by Qian *et al.* [19] and explaining the formation of dimers, involves the generation of intermediate free radical anion species CH_3-$\dot{C}H$-CH_2-OCO_2^-:

$$CH_3CHCH_2CO_3 + e^- \rightarrow CH_3\text{-}\dot{C}H\text{-}CH_2\text{-}OCO_2^- \qquad \text{Equation 4-9}$$

$$CH_3\text{-}\dot{C}H\text{-}CH_2\text{-}OCO_2^- + CH_3CHCH_2CO_3 + 2Li^+ + e^- \rightarrow$$

$$CH_3CHCH_2 + CH_3\text{-}CH(OCO_2Li)\text{-}CH_2\text{-}OCO_2Li\downarrow \qquad \text{Equation 4-10}$$

Such a mechanism implies that less or no dimerization should occur if other species, more reactive than the organic radical anion, would compete. Conversely, the lower

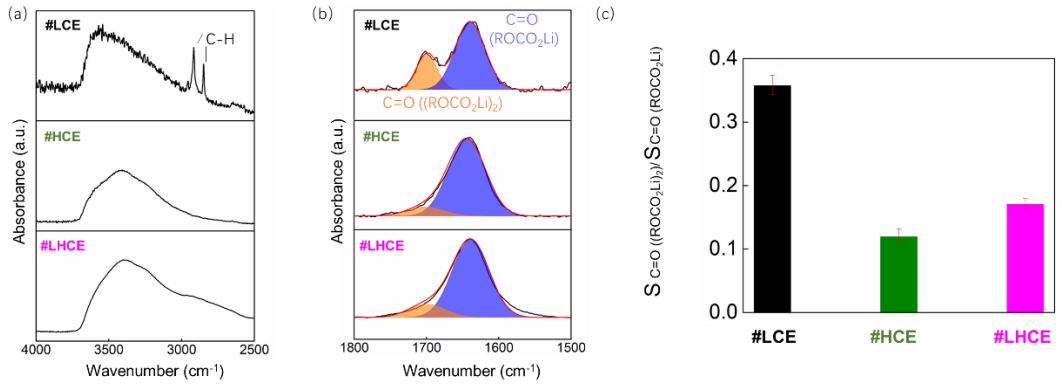


Figure 4-20. ATR-FTIR spectra of the SEI films obtained with #LCE, #HCE and #LHCE: (a) 4000-2500 cm^{-1} and (b) 1800-1500 cm^{-1} spectral ranges. (c) Ratio of the intensity of the peak related to the $(ROCO_2Li)_2$ specie to the intensity of the peak from $ROCO_2Li$ for the different SEI films.

$S_{(ROCO2Li)2}/S_{ROCO2Li}$ ratio observed for #LHCE and #HCE agrees with a degradation process more involving the PF_6^- anion decomposition and, thus, leading to SEI enriched with inorganic species.

ATR-FTIR results are fully confirmed by the XPS analysis (Figure 4-21). Obviously, all SEIs show the presence of organic degradation products (Figure 4-21a) but LiF containing layers are also observed for #HCE and #LHCE. No traces of this fluorinated species can be observed for #LCE (Figure 4-21b). $Li_xPF_yO_z$, an intermediate decomposition product of $LiPF_6$ [20], is also observed in the #HCE SEI (Figures 4-21a and 21b), suggesting the larger reactivity of the PF_6^- species compared to #LHCE, which presumably should correspond to larger degradation and, thus, thicker SEI film. Indeed, the SEI formed by #LHCE has an intermediate LiF content between those of #LCE and #HCE (Figure 4-20a), reflecting the particular solvation structure of LHCEs due to the diluent addition. XPS Li 1s spectra (Figure 4-21c) exhibit a plasmon-loss peak at 62-65 eV clearly noticeable for the SEI film formed by #LCE and much weaker for the degradation layer formed by #LHCE (absent for #HCE). The plasmon-loss peak is a typical feature of Li metal surfaces [21], whose detection confirms the larger thickness of the SEI film generated by #LCE, compared to #HCE and #LHCE.

In chapter 3, we have yet shown how the electrolyte concentration and, consequently, the solvation structure affect the physical-chemical properties of the SEI layer formed during plating. Here, we confirm these assumptions and support the finding that the properties of the SEI, whose formation is assumed to precede the Li plating [22], are key parameters for the Li deposit morphology, prevailing over others like the Li^+ transport rate across the bulk electrolyte.

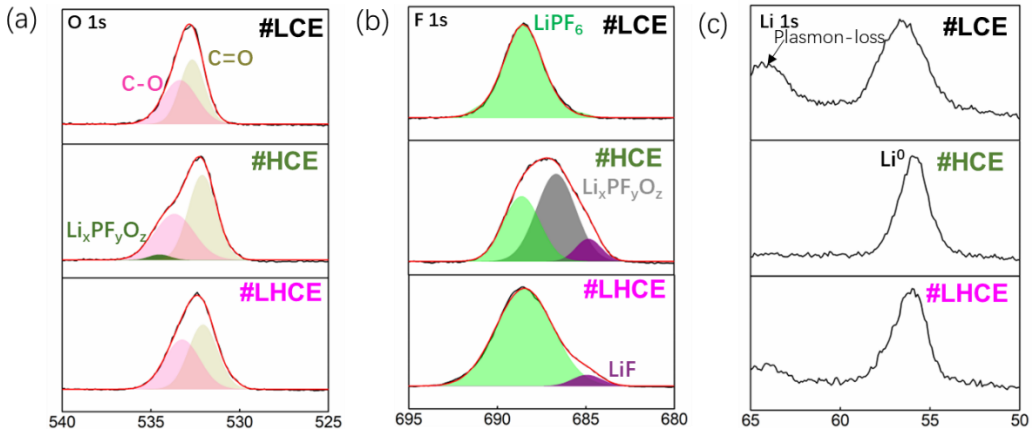


Figure 4-21. (a) O 1s (b) F 1s and (c) Li 1s XPS spectra of the SEI films formed by #LCE, #HCE and #LHCE.

The increasing of the electrolyte concentration induces stronger interaction between Li^+ and PF_6^- so as to lower the LUMO level of the anion which become more prone to reduction. SEI is then mainly derived from the PF_6^- anion decomposition [22]. Among the different degradation products, inorganic LiF confers higher conductivity to the SEI and, thus, decreases the contribution of the last to the interface charge transfer resistance R_{ct} [23,24]. The result is a more homogeneous Li deposit containing fewer dendrites. In more detail, the largest R_{ct} of #LCE, whose SEI is mostly organic, corresponds to the lower mobility of the charge carrier Li^+ across the layer inducing typical dendritic deposit (Figure 4-17a), whereas the lowest R_{ct} of #LHCE allows an almost uniform Li deposit at the same current density (1 mA cm^{-2}, Figure 4-17g). The intermediate R_{ct} of #HCE, due to excessive $LiPF_6$ decomposition producing a SEI film with similar composition but thicker than that of #LHCE, results in few dendrites growing from a predominantly granular morphology.

4.6 Conclusion

In this chapter, we carried out *in situ* Raman spectroscopy to compare the Li^+ ion concentration attenuation at different distances from the electrode surface during the Li deposition from low-, high- and localized high-concentration electrolytes. The so-obtained Li^+ concentration gradients and Li^+ consumption rates (as measured at 10 µm from the electrode surface) appear to depend on the plating current density, the presence or not of the diluent and the starting electrolyte concentration (the last being the most affecting parameter) but, sometimes, in opposite way. Li^+ concentration gradients are observed to increase with the initial concentration and the presence of the diluent, so

that the LCE here investigated (1 M $LiPF_6$ in DMC) exhibits the lowest value and the LHCE (4 M $LiPF_6$ in DMC:HFPM (7:3,v/v)) the largest. Corresponding diffusion coefficients obviously decrease according to the same sequence (LCE > HCE > LHCE) so that lower Li^+ transport rate is observed for more concentrated electrolytes, especially if containing the diluent. At the same time, results from the characterization of the Li deposit morphology are as expected: larger salt concentrations and the use of diluents allows to form LHCEs with smooth and homogeneous Li while the LCE studied here clearly generates dendritic-like deposit. Then, the comparison between *in situ* Raman and *ex situ* SEM results leads us to a few conclusions at the opposite to what is currently accepted, namely that the occurring of stronger Li^+ concentration gradients across the electrolyte during the plating process (or the related lower value of the Li^+ diffusion coefficient) cannot be roughly associated to a more heterogeneous morphology of the plated Li. Actually, if the phenomenon inducing Li dendrites is still considered the [Li^+] local heterogeneity, this has to be localized closer to the electrode surface, namely at the SEI layer. FTIR, XPS and EIS measurements suggest that the factor prevailing on the others (at least under the specific experimental conditions of our investigation) in determining the Li morphology are the composition and thickness of the SEI, insofar these two parameters affect the layer ability of transferring Li^+ charge carrier species from the electrolyte to the electrode. We should probably also include the porosity and stiffness as essential SEI properties determining the Li deposit morphology, but these aspects have not been particularly approached in our study. Thus, as resumed in Figure 4-21, mostly organic SEI films i.e. made by the degradation of solvent species as that obtained by LCE, have lower Li^+ ion conductivity and induce larger charge transfer resistance at the electrode-electrolyte interface. We can then suppose that the limited Li^+ diffusion across the layer generates larger local heterogeneity of the Li^+ distribution at the electrode active surface, resulting in dendritic morphology. HCE and LHCE exhibit much less protrusive morphology of the Li deposit because of the "doping" presence of LiF in SEI film, decreasing the charge transfer resistance. Besides LiF, the SEI film of the HCE here investigated also contains $Li_xPF_yO_z$, which is the hint of the more enhanced reactivity of the Li salt giving a conductive but thicker SEI film compared to the LHCE. This results in an intermediate morphology consisting of some Li dendrites growing from granular deposits. Finally, the thinner and conductive SEI formed by the LHCE allows smooth, homogeneous Li deposition.

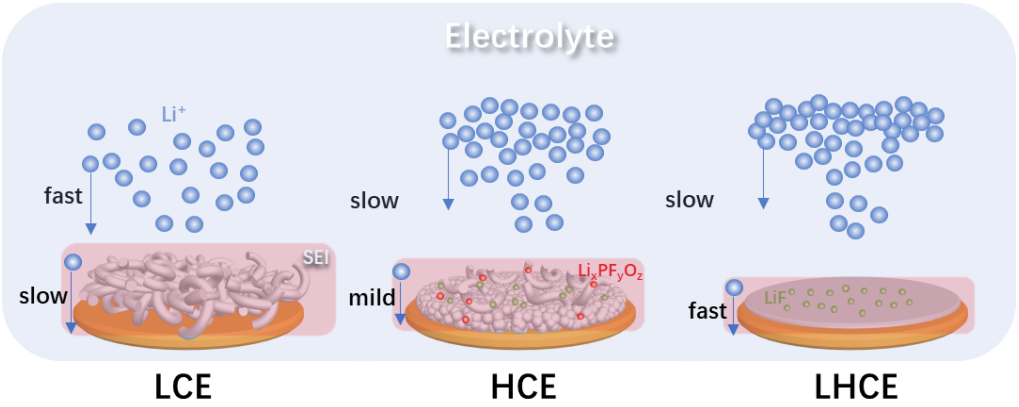


Figure 4-21. Schematic of Li plating in LCE, HCE, and LHCE at large current density, showing the different Li^+ transport rates across the electrolyte and the SEI layer.

Supplementary information

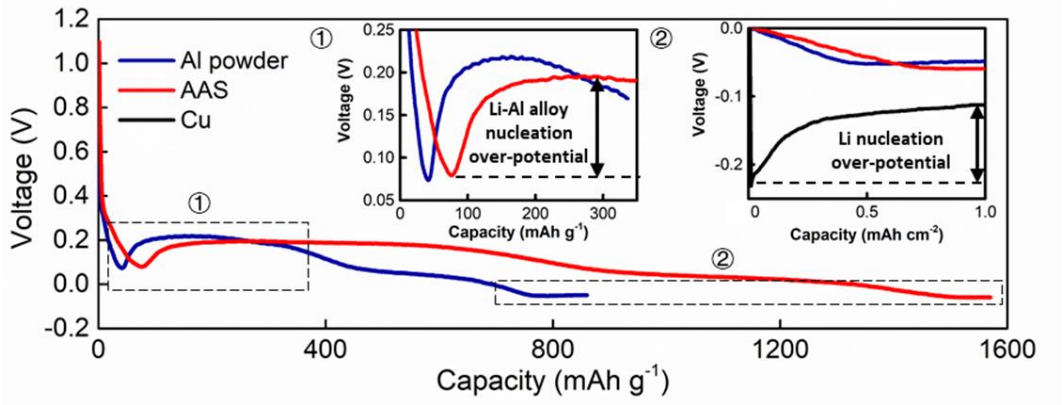


Figure S4-1. Comparison of the discharge curves obtained with AAS modified and Al powders coated Cu electrodes at the current density of 0.5 mA cm^{-2} (Li plating of 1 mAh cm^{-2}).

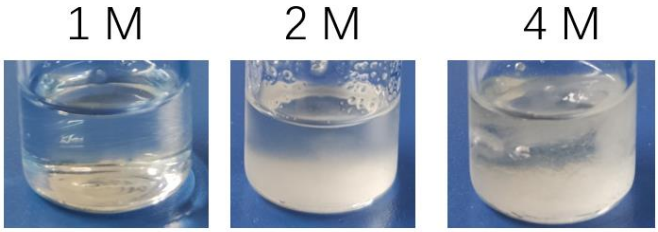


Figure S4-2. Images of 1, 2 and 4 M solutions of $LiPF_6$ in EC:DEC (1:1, v/v).

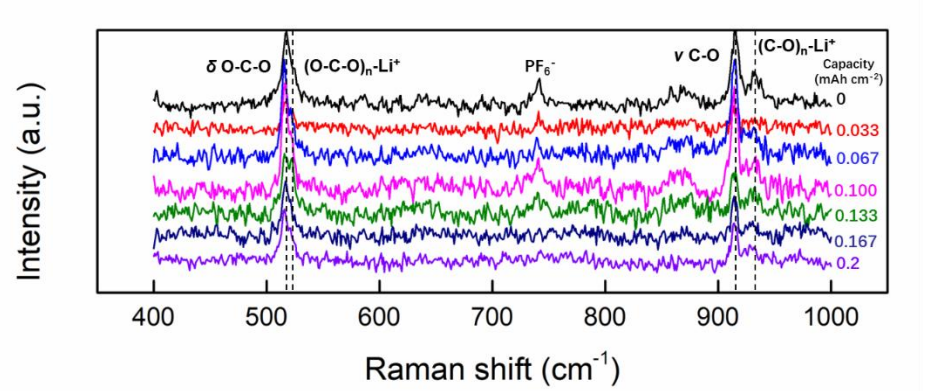


Figure S4-3. *In situ* Raman spectra of 1 M $LiPF_6$ in DMC collected during operation in the Li‖Cu half-cell at 1 mA cm^{-2}, at 10 µm from the Cu electrode surface.

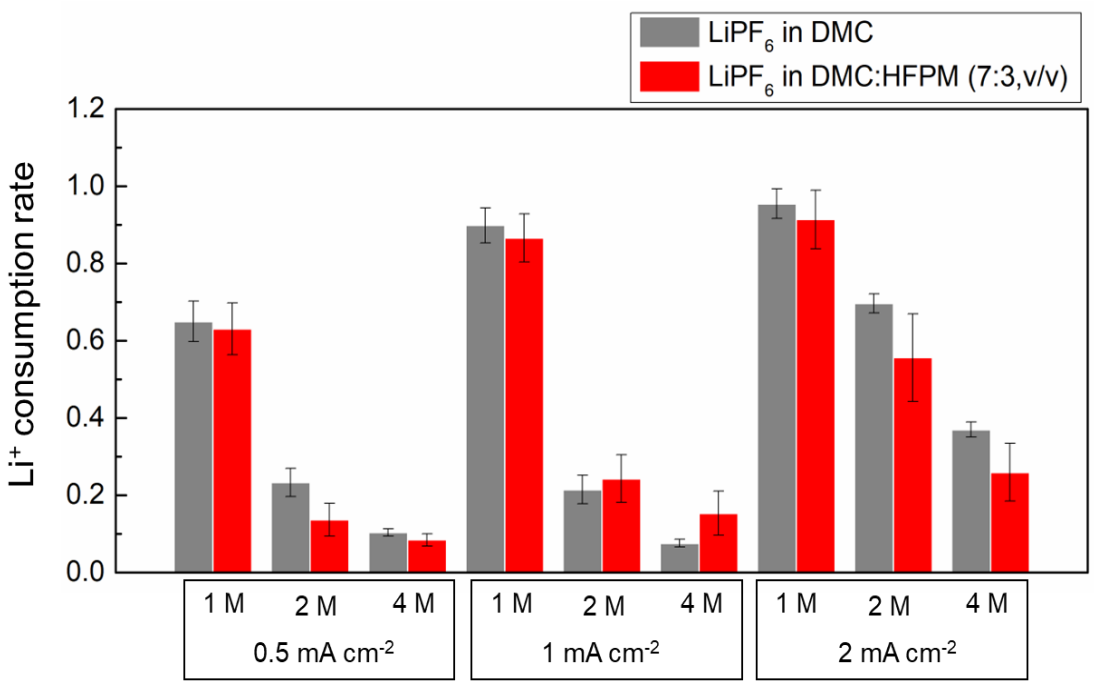


Figure S4-4. Li^+ consumption rates of the different electrolytes of $LiPF_6$ in DMC and $LiPF_6$ in DMC:HFPM (7:3, v/v), at the different salt concentrations and plating current densities.

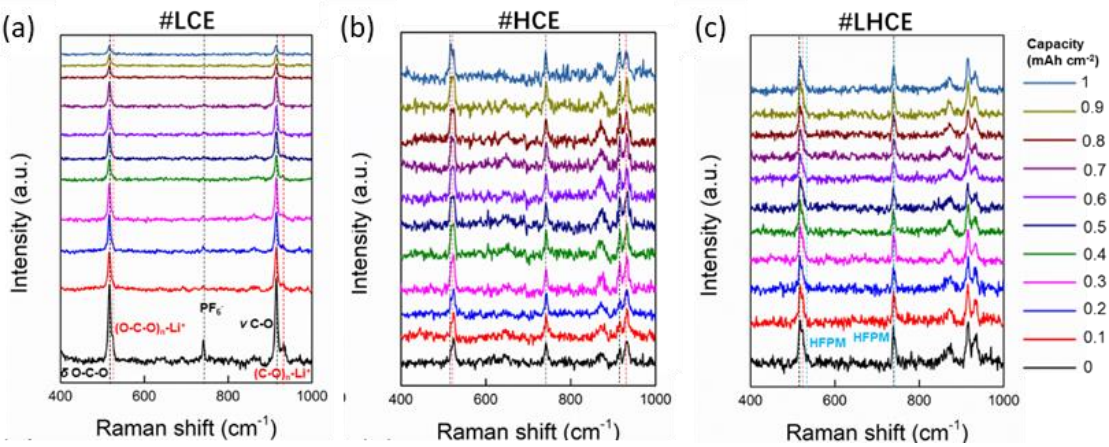


Figure S4-5. *In situ* Raman spectra collected at 10 µm from the Cu electrode surface during Li-plating carried out with the Li‖Cu half-cell at 2 mA cm^{-2} (1mAh cm^{-2}): (a) 1 M $LiPF_6$ in DMC (#LCE), (b) 4 M $LiPF_6$ in DMC (#HCE) and (c) 4 M $LiPF_6$ in DMC:HFPM (7:3, v/v) (#LHCE).

References

[1] J. Xiao, How lithium dendrites form in liquid batteries, Science 366 (2019) 426–427.

[2] W.A. Henderson, D.M. Seo, S.-D. Han, O. Borodin, Electrolyte solvation and ionic association. VII. Correlating Raman spectroscopic data with solvate species, Journal of the electrochemical society 167 (2020) 110551.

[3] G. Yang, I.N. Ivanov, R.E. Ruther, R.L. Sacci, V. Subjakova, D.T. Hallinan, J. Nanda, Electrolyte solvation structure at solid–liquid interface probed by nanogap surface-enhanced Raman spectroscopy, ACS nano 12 (2018) 10159–10170.

[4] D.M. Seo, O. Borodin, S.-D. Han, P.D. Boyle, W.A. Henderson, Electrolyte solvation and ionic association II. Acetonitrile-lithium salt mixtures. Highly dissociated salts, Journal of the electrochemical society 159 (2012) A1489.

[5] T. Yamanaka, H. Nakagawa, S. Tsubouchi, Y. Domi, T. Doi, T. Abe, Z. Ogumi, In situ Raman spectroscopic studies on concentration change of ions in the electrolyte solution in separator regions in a lithium ion battery by using multi-microprobes, Electrochemistry communications 77 (2017) 32–35.

[6] T. Yamanaka, H. Nakagawa, S. Tsubouchi, Y. Domi, T. Doi, T. Abe, Z. Ogumi, In situ Raman spectroscopic studies on concentration of electrolyte salt in lithium-ion batteries by using ultrafine multifiber probes, ChemSusChem 10 (2017) 855–861.

[7] J.D. Forster, S.J. Harris, J.J. Urban, Mapping Li^+ concentration and transport via in situ confocal Raman microscopy, The journal of physical chemistry letters 5 (2014) 2007–2011.

[8] F. Ren, Z. Li, Y. Zhu, P. Huguet, S. Deabate, D. Wang, Z. Peng, Artificial nucleation sites with stable SEI for Li metal anodes by aggressive Al pulverization, Nano energy 73 (2020) 104746.

[9] Y. Zhang, Y. Zhong, Z. Wu, B. Wang, S. Liang, H. Wang, Solvent molecule cooperation enhancing lithium metal battery performance at both electrodes, Angewandte chemie international edition 59 (2020) 7797–7802.

[10] B. Klassen, R. Aroca, M. Nazri, G.A. Nazri, Raman spectra and transport properties of lithium perchlorate in ethylene carbonate based binary solvent systems for lithium batteries, The journal of physical chemistry B 102 (1998) 4795–4801.

[11] G. Yang, I.N. Ivanov, R.E. Ruther, R.L. Sacci, V. Subjakova, D.T. Hallinan, J.

Nanda, Electrolyte solvation structure at solid–liquid interface probed by nanogap surface-enhanced Raman spectroscopy, ACS nano 12 (2018) 10159–10170.

[12] S. Chen, J. Zheng, D. Mei, K.S. Han, M.H. Engelhard, W. Zhao, W. Xu, J. Liu, J.-G. Zhang, High-voltage lithium-metal batteries enabled by localized high-concentration electrolytes, Advanced materials 30 (2018) 1706102.

[13] N. Piao, X. Ji, H. Xu, X. Fan, L. Chen, S. Liu, M.N. Garaga, S.G. Greenbaum, L. Wang, C. Wang, Countersolvent electrolytes for lithium-metal batteries, Advanced energy materials 10 (2020) 1903568.

[14] X. Ren, L. Zou, X. Cao, M.H. Engelhard, W. Liu, S.D. Burton, H. Lee, C. Niu, B.E. Matthews, Z. Zhu, Enabling high-voltage lithium-metal batteries under practical conditions, Joule 3 (2019) 1662–1676.

[15] Z. Peng, X. Cao, P. Gao, H. Jia, X. Ren, S. Roy, Z. Li, Y. Zhu, W. Xie, D. Liu, High-power lithium metal batteries enabled by high-concentration acetonitrile-based electrolytes with vinylene carbonate additive, Advanced functional materials 30 (2020) 2001285.

[16] J. Zeng, Q. Liu, D. Jia, R. Liu, S. Liu, B. Zheng, Y. Zhu, R. Fu, D. Wu, A polymer brush-based robust and flexible single-ion conducting artificial SEI film for fast charging lithium metal batteries, Energy storage materials 41 (2021) 697–702.

[17] X. Feng, H.-H. Wu, B. Gao, M. Świętosławski, X. He, Q. Zhang, Lithiophilic N-doped carbon bowls induced Li deposition in layered graphene film for advanced lithium metal batteries, Nano research 15 (2022) 352–360.

[18] E.R. Logan, E.M. Tonita, K.L. Gering, J. Li, X. Ma, L.Y. Beaulieu, Dahn, JR, A study of the physical properties of Li-ion battery electrolytes containing esters, Journal of the electrochemical society 165 (2018) A21.

[19] Q. Qian, Y. Yang, H. Shao, Solid electrolyte interphase formation by propylene carbonate reduction for lithium anode, Physical chemistry chemical physics 19 (2017) 28772–28780.

[20] R. Tatara, P. Karayaylali, Y. Yu, Y. Zhang, L. Giordano, F. Maglia, R. Jung, J.P. Schmidt, I. Lund, Y. Shao-Horn, The effect of electrode-electrolyte interface on the electrochemical impedance spectra for positive electrode in Li-ion battery, Journal of the electrochemical society 166 (2018) A5090.

[21] T. Doi, Y. Shimizu, M. Hashinokuchi, M. Inaba, Dilution of highly concentrated $LiBF_4$/propylene carbonate electrolyte solution with fluoroalkyl ethers for 5-V $LiNi_{0.5}Mn_{1.5}O_4$ positive electrodes, Journal of the electrochemical society 164

(2017) A6412.

[22] Y. Zhang, J. Qian, W. Xu, S.M. Russell, X. Chen, E. Nasybulin, P. Bhattacharya, M.H. Engelhard, D. Mei, R. Cao, Dendrite-free lithium deposition with self-aligned nanorod structure, Nano letters 14 (2014) 6889–6896.

[23] L. Fan, H.L. Zhuang, L. Gao, Y. Lu, L.A. Archer, Regulating Li deposition at artificial solid electrolyte interphases, Journal of materials chemistry A 5 (2017) 3483–3492.

[24] X.-Q. Zhang, X. Chen, R. Xu, X.-B. Cheng, H.-J. Peng, R. Zhang, J.-Q. Huang, Q. Zhang, Columnar lithium metal anodes, Angewandte chemie 129 (2017) 14395–14399.

Chapter 5. Recycling the Li electrolyte into catalyst for CO_2RR applications via laser irradiation

5.1 General introduction

Li-based batteries have been taking a crucial role in recent advancement and development of the modern life [1]. This implies that the amount of spent Li batteries entering the waste stream has strongly increased in recent years [2,3]. Effective recycling of end-of-life batteries then acquires primary importance to avoid environmental pollution and waste of resources. Recycling of Li batteries not only concerns the metal elements constituting the electrodes (Ni, Co, Mn, etc.), but also the electrolyte, which is often neglected [4–6]. It should then be pointed out that the current way of recycling the electrolyte, consisting in separating and regenerating the different Li salts and solvents by precipitation and distillation or extraction respectively, is complex and expensive [7,8]. Developing new methods to convert the wasted electrolyte into other useful materials could then represent an interesting, alternative solution for recycling.

During some of the experiments reported in chapters 4, namely when we accidently focused the laser on the edge of Cu electrode, we casually observed the local degradation of the carbonate-based electrolyte (namely, 1 M $LiPF_6$ in EC/DEC) into graphite-like carbon deposited on Cu_xO ($1 \leq x \leq 2$). As far as we know, this is the first time that such an observation is reported. Aware of the current application of Cu and Cu_xO compounds as catalysts for the electrochemical CO_2 reduction reaction (CO_2RR) [9], this phenomenon appeared to us a promising way to recycle wasted electrolytes into useful catalysts. Then, we decided to extend our investigation on the electrolytes for Li-metal batteries to the understanding of the conditions and mechanisms of their photochemical conversion at first, and then to the characterization of the electrocatalytic properties of the so-obtained materials.

5.2 Short introduction to the CO_2RR

Carbon dioxide is the most dangerous and prevalent greenhouse gas. Nowadays, the risks of excess CO_2 in the atmosphere are universally recognized. Electrocatalytic reduction of CO_2 to valuable chemicals then represents a sustainable technology to achieve a carbon-neutral energy cycle in the environment [10].

Electroreduction of carbon dioxide is a multielectron transfer process that results in

various chemical products, from C1 to C3, depending on the number and binding positions of electrons and protons in the reaction (Table 5-1) [11]. A main drawback is that, in aqueous electrolytes, CO_2RR competes with the H_2 evolution reaction which suppresses the CO_2 electrochemical conversions at low overpotentials. Anyhow, carbon dioxide has an extremely stable structure, so that large negative potentials are required to transform it into the reactive CO_2^- species. Catalysts are then needed to increase the reaction rate and selectivity of the electroreduction process. Research carried out so far suggests that copper is one of the best catalysts (in any case the most studied) for the electroreduction of CO_2 into hydrocarbons [12].

The catalytic properties of Cu as reaction pathway and selectivity depend (among others) on the parameters of the potential applied during the electroreduction, i.e. value and pulse conditions (shape and duration). Indeed, potential affects the surface structure and composition (i.e. oxidation state) of the catalyst and the so-obtained cupper oxides participate to the CO_2RR. The recent work of Timoshenko *et al.* [14] shows how one can steer the CO_2RR selectivity by controlling the type and amount of Cu_2O formed under pulsed conditions on Cu nano-cubes. As shown in Figure 5-1, longer cathodic

Table 5-1. Half-reactions of CO_2RR and their potentials (vs. Normal Hydrogen Electrode, N.H.E.) in aqueous electrolyte at conditions: pH=7, 25 °C, 1.0 atm [13].

Equation	Half-reactions of CO_2 reduction	E (V vs. N.H.E.)
1	$CO_2(g) + e^- \rightarrow CO_2^{\cdot -}$	-1.90
2	$CO_2(g) + 2H^+ + 2e^- \rightarrow HCOOH\ (l)$	-0.61
3	$CO_2(g) + 2H^+ + 2e^- \rightarrow CO(g) + H_2O(l)$	-0.52
4	$CO_2(g) + 4H^+ + 4e^- \rightarrow HCHO(l) + H_2O(l)$	-0.51
5	$CO_2(g) + 6H^+ + 6e^- \rightarrow CH_3OH(l) + H_2O(l)$	-0.38
6	$CO_2(g) + 8H^+ + 8e^- \rightarrow CH_4(g) + 2H_2O(l)$	-0.24
7	$2CO_2(g) + 12H^+ + 12e^- \rightarrow C_2H_4(g) + 4H_2O(l)$	-0.06
8	$2CO_2(g) + 12H^+ + 12e^- \rightarrow CH_3CH_2OH(l) + 3H_2O(l)$	0.08
9	$2H^+ + 2e^- \rightarrow H_2(g)$	-0.42

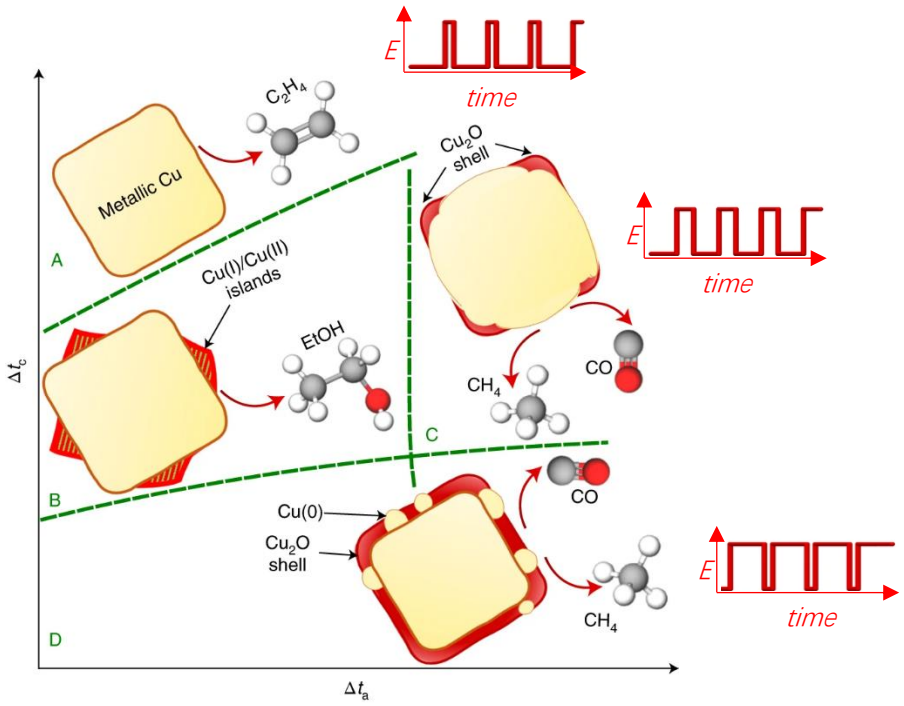


Figure 5-1. Schematic depiction of the evolution of the Cu derived catalyst structure, composition and selectivity as a function of the duration of the cathodic Δt_c and anodic Δt_a,pulses ($0s \leq \Delta t \leq 17s$) [14].

pulses Δt_c (region A) promote metallic Cu and the consequent selective conversion of CO_2 into C_2H_4, while longer anodic pulses Δt_a (regions C and D) generate Cu_2O which yields mainly C1 products like CO and CH_4. At intermediate conditions (region B), mixed Cu(I)/Cu(II) islands give EtOH preferentially.

Then, developing further effective ways, other than potential pulses, to modulate the Cu oxidation should help to improve the CO_2RR technology. In the following, we will also show a facile way to adjust the oxidation state of copper in the catalyst obtained by the irradiated electrolyte.

5.3 The photochemical conversion of the electrolyte in contact with Cu into graphitic carbon onto Cu_xO

5.3.1 First observations

After the initial incidental observation, we first confirmed the photochemical conversion phenomenon by dedicated experiments. As schematized in Figure 5-2a, 100 µL of 1 M $LiPF_6$ in EC:DEC (1:1, v/v) was dropped on 2 x 2 cm^2 Cu foil, sealed between two glasses and irradiated continuously by the red laser at λ = 659.55 nm. After a few

seconds, a black area could be observed. The Raman spectra collected at this location shows the presence of copper oxide and carbon (Figure 5-2b) i.e. the CuO A_g mode at 296 cm^{-1} [15] and the typical carbon bands at 1328 cm^{-1} and 1593 cm^{-1} corresponding to the so-called D and G modes respectively [15,16]. Accordingly, the occurring of the following reaction can be proposed:

$$\text{Cu + carbonates} \xrightarrow{\text{red laser, } LiPF_6} Cu_xO + C \qquad \text{Equation 5-1}$$

It should be noted that dark areas can also be observed at the surface of the pristine Cu foil, due to the spontaneous oxidation at ambient conditions and/or to the manufacturing process. But Raman spectra collected at the as-received Cu foil (Figure S5-1 in SI) attest solely the presence of Cu(I) (i.e. T_{2g} and T_{1u} modes at 520 and 625 cm^{-1} respectively, belonging to the Cu_2O specie [17]) while samples obtained by photochemical reaction always contain Cu_xO with $x > 1$ (depending on the exposition time to the air after irradiation; see XPS measurements reported in the following).

The spectrum of the material (dark area) obtained by irradiation (Figure 5-2b), besides main Raman bands related to CuO and carbon, also shows weak peaks in the ranges of 710-744 cm^{-1}, 880-916 cm^{-1} and 2860-3050 cm^{-1} due to the pristine electrolyte: δ C=O mode of EC at 716 cm^{-1}, C=O-Li^+ of EC at 730 cm^{-1}, ν P-F of PF_6^- at 741 cm^{-1}, ν C-O of EC at 893 cm^{-1}, C-O-Li^+ at 905 cm^{-1} and ν C-H of carbonates in the range 2860-3050 cm^{-1} [18,19]. As shown in Figure 5-2c, the intensity of these peaks decreases gradually when shifting the laser focus point from the liquid electrolyte side towards the Cu surface, until they cannot be detected anymore and only the bands from carbon and CuO can be observed. This observation allows to confirm that the electrolyte photochemical reaction occurs at the Cu surface.

Interestingly, *in situ* Raman carried out with the Li‖Cu cell (see Figure S5-2 in SI for the experimental setup) show the reversible, gradual appearance and disappearance of the D and G peaks of the carbon layer submitted to charge and discharge processes respectively (Figure 5-3 and Figure S5-3 in SI). This behavior, previously reported by Hardwick and co-workers [20], can be related to the modifications induced by the Li^+ intercalation into the graphitic structure and the consequent loss of intensity of the ν C-C modes. In short, these data show that the carbon formed by the photochemical conversion of the electrolyte is graphite-like and can participate reversibly to the electrochemical Li^+ intercalation/de-intercalation process.

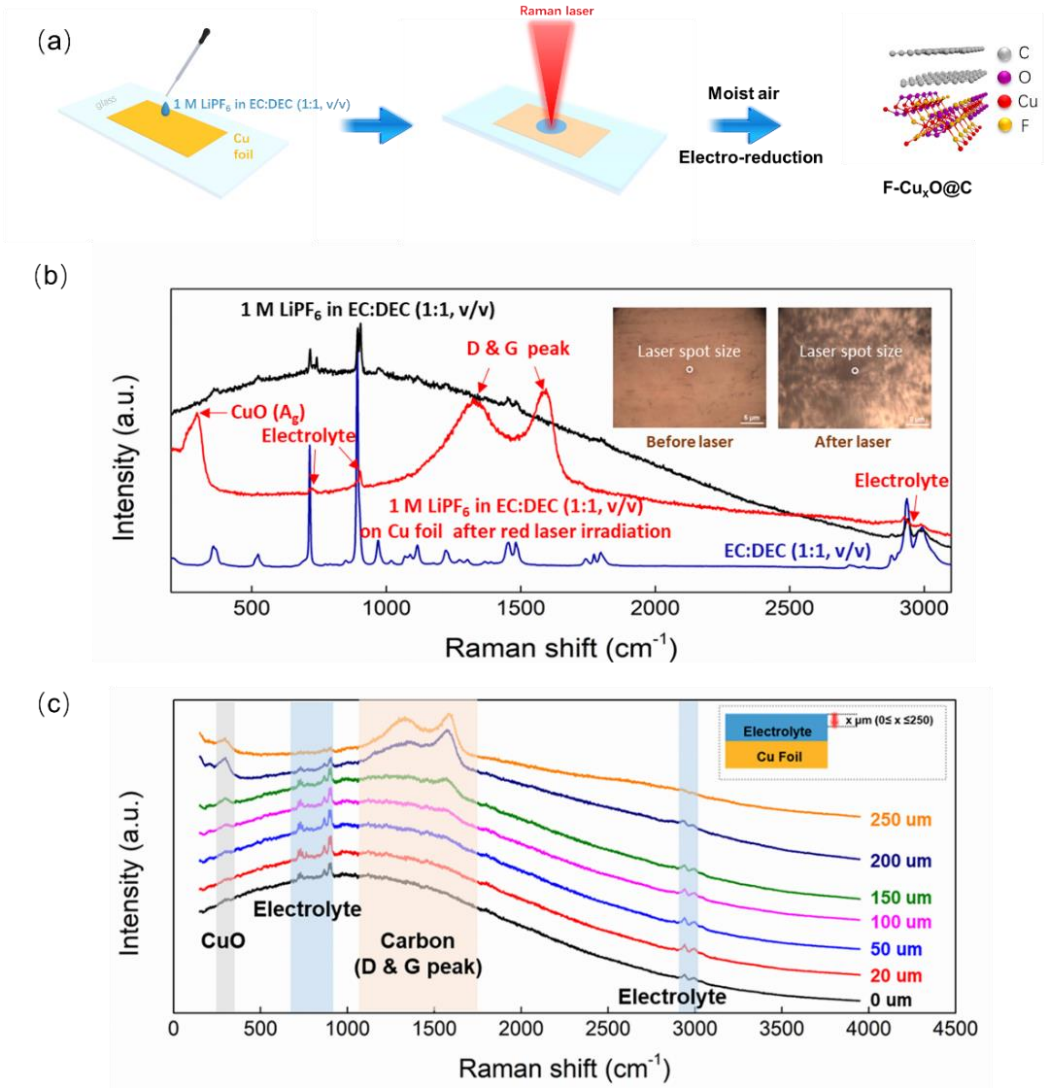


Figure 5-2. (a) Schematic illustration of the photochemical conversion of the electrolyte onto Cu foil. (b) Raman spectra of the conversion products from the electrolyte consisting of 1 M $LiPF_6$ in EC:DEC (1:1, v/v) irradiated at λ = 659.55 nm: comparison with spectra of the pristine electrolyte and solvent mixture alone (the insets are optical images of the Cu foil before and after irradiation). (c) Raman spectra collected at different distances from the Cu surface after the photochemical reaction: 0 µm corresponds to the starting position at the bulk electrolyte and the other values (reported in the legend) to the progressive moving of the laser focus point towards the Cu foil surface.

5.3.2 Conditions and mechanism of the photochemical reaction

To explore the conditions necessary for the photochemical reaction to occurs and, thus, progress in the understanding of the formation mechanism, we carried out several experiments according to a typical control variate method. Table 5-2 lists the different conditions we studied (involving metallic substrate, Li salt, electrolyte solvent and laser

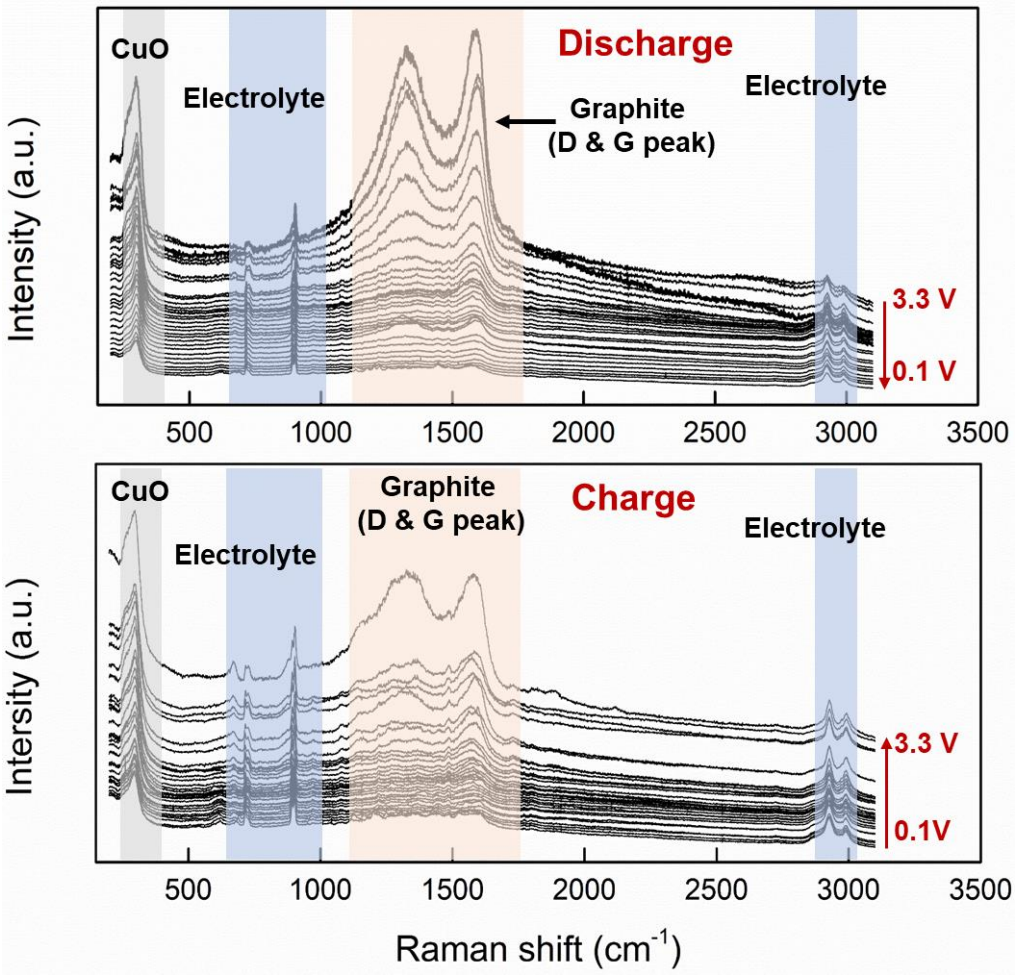


Figure 5-3. Evolution of the D and G Raman peaks of the carbon layer obtained by photochemical degradation during the Li^+ extraction/de-intercalation (charge) and insertion/intercalation (discharge) processes. The electrolyte is 1 M $LiPF_6$ in EC: DEC (1:1, v/v). Electrochemical cycling is carried out under potentiodynamic conditions i.e. by cyclic voltammetry within the range from 0.1 to 3.3 V (OCV) and with a scanning rate of 0.5 mV s^{-1}.

wavelength) and indicates if reaction occurs or not. Laser power density at the sample surface and exposure time were 150 mW and 5h respectively. As also indicated in the Table, the different Raman spectra recorded for each experiment are either those reported in Figure 5-2c (whose experiment has been arbitrarily chosen as that under default conditions) or gathered in the Figure 5-4. More details about materials used here (and for the catalytic experiments reported in the section 5.4) are given in SI (§ S.1.1). This study shows that the substrate, the laser wavelength and the presence of Li salt are main parameters for the occurring of the photochemical reaction. In fact, no reaction can be observed (i) on Al foil (Figure 5-4a), (ii) with pure solvents i.e. without any Li salt dissolved within (Figure 5-4g) or (iii) under irradiation by a green laser (Figure 5-

Table 5-2. Conditions investigated for the photochemical reaction.

Substrate	Salt	Solvent	Laser wavelength (nm)	Variate	Reaction	Figure
Cu	$LiPF_6$	EC+DEC	659.55	/	Yes	5-2c
Al	$LiPF_6$	EC+DEC	659.55	Substrate	No	5-4a
Cu	$LiPF_6$	EC+DEC	514.58	Laser wavelength	No	5-4b
Cu	$LiPF_6$	EC	659.55	Solvent	Yes	5-4c
Cu	$LiPF_6$	DEC	659.55	Solvent	Yes	5-4d
Cu	$LiPF_6$	DMC	659.55	Solvent	Yes	5-4e
Cu	$LiPF_6$	Diethyl ether	659.55	Solvent	Yes	5-4f
Cu	/	EC+DEC	659.55	Salt	No	5-4g
Cu	LiFSI	EC+DEC	659.55	Salt	Yes	5-4h
Cu	KPF_6	EC+DEC	659.55	Salt	Yes	5-4i

4b). The last observation attests that the conversion of the electrolyte solvent into carbon is photochemical, and not just a thermal degradation of organic species submitted to laser heating. As far as the lack of reactivity observed in the absence of Li salt is concerned, one can assume that the coordination of the solvating species to the Li^+ cation is necessary to change the energy of ground and excited states [21,22] so as to allow the solvating (coordinated) solvent molecules to have the suitable energy gap to undergo radiative excitement and generate intermediate reactive species necessary for the photochemical reaction (Figure 5-5).

All the different solvents studied (EC, DEC, DMC and diethyl ether), as well as their mixture, can be converted into carbon if the Li salt is dissolved within. Raman spectra collected at different depths in the experiments carried out with DMC and diethyl ether-based electrolytes suggest the presence of thicker carbon layers, i.e. a larger photochemical reaction rate, since weak D and G carbon peaks can be observed yet at the 0 nm position (Figures 5-4e and 5-4f). As far as the effect of the nature of the salt cation or anion is concerned, we compared the reference compound $LiPF_6$ to lithium bis(fluorosulfonyl)amide (LiFSI) and potassium hexafluorophosphate (KPF_6). Results show only a slight effect of FSI^- and K^+ specie on the photochemical reaction. Compared to $LiPF_6$, Raman spectra obtained with KPF_6 (Figures 5-4h and 5-4i

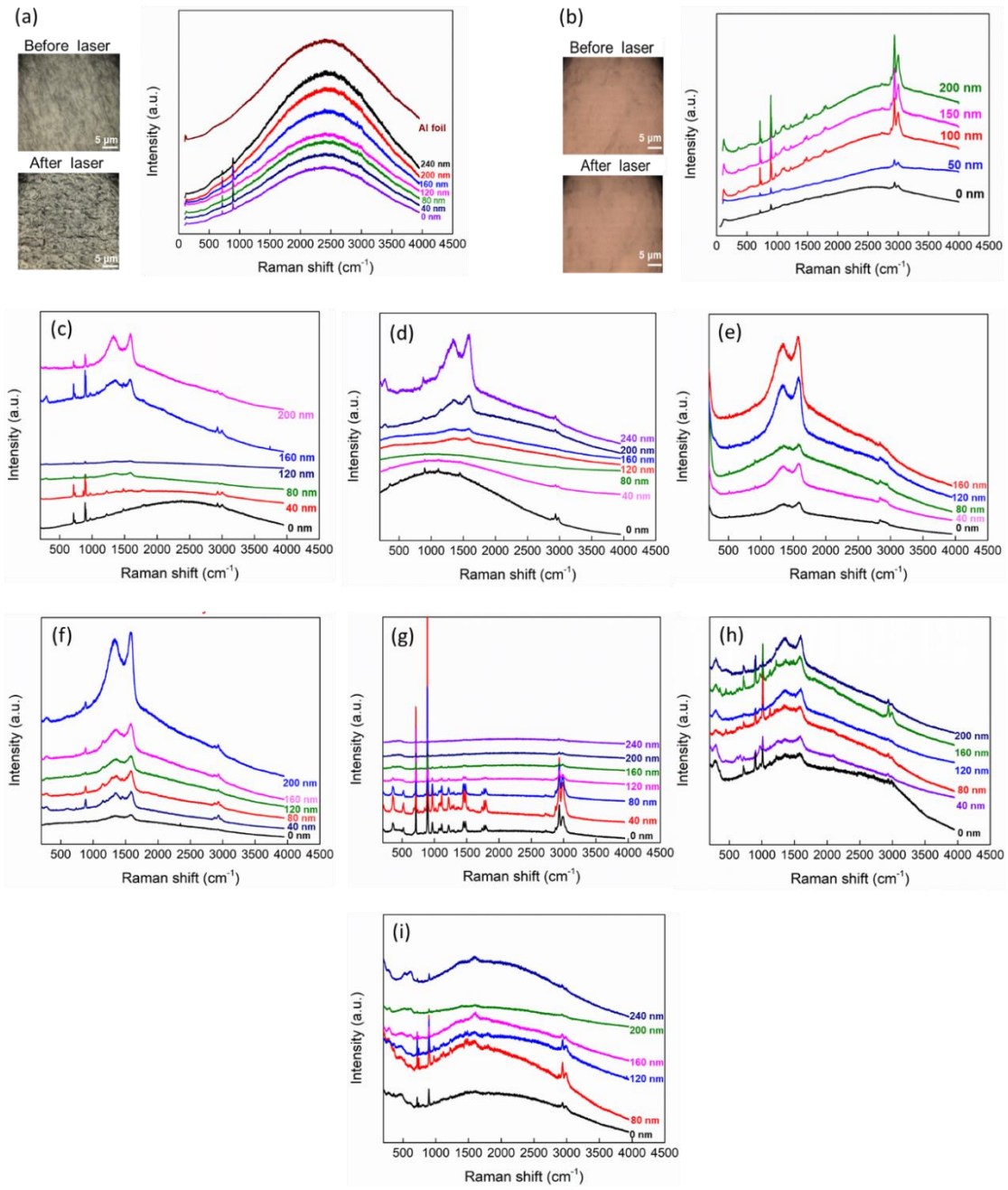


Figure 5-4. Raman spectra obtained at different distances from the metal substrate according to the different conditions reported in Table 5-2: (a) 1 M $LiPF_6$ in EC:DEC (1:1, v/v) on Al foil irradiated at λ = 659.55 nm (optical images of the metal substrate surface before and after irradiation are reported on the left side), (b) 1 M $LiPF_6$ in EC:DEC (1:1, v/v) on Cu foil irradiated at λ = 514.58 nm (optical images of the metal substrate surface before and after irradiation are reported on the left side), (c) 1 M $LiPF_6$ in EC on Cu foil irradiated at λ = 659.55 nm, (d) 1 M $LiPF_6$ in DEC on Cu foil irradiated at λ = 659.55 nm, (e) 1 M $LiPF_6$ in DMC on Cu foil irradiated at λ = 659.55 nm, (f) 1 M $LiPF_6$ in diethyl ether on Cu foil irradiated at λ = 659.55 nm, (g) EC:DEC (1:1, v/v) on Cu foil irradiated at λ = 659.55 nm, (h) 1 M LiFSI in EC:DEC (1:1, v/v) on Cu foil irradiated at λ = 659.55 nm, (i) 1 M KPF_6 in EC:DEC (1:1, v/v) on Cu foil irradiated at λ = 659.55 nm.

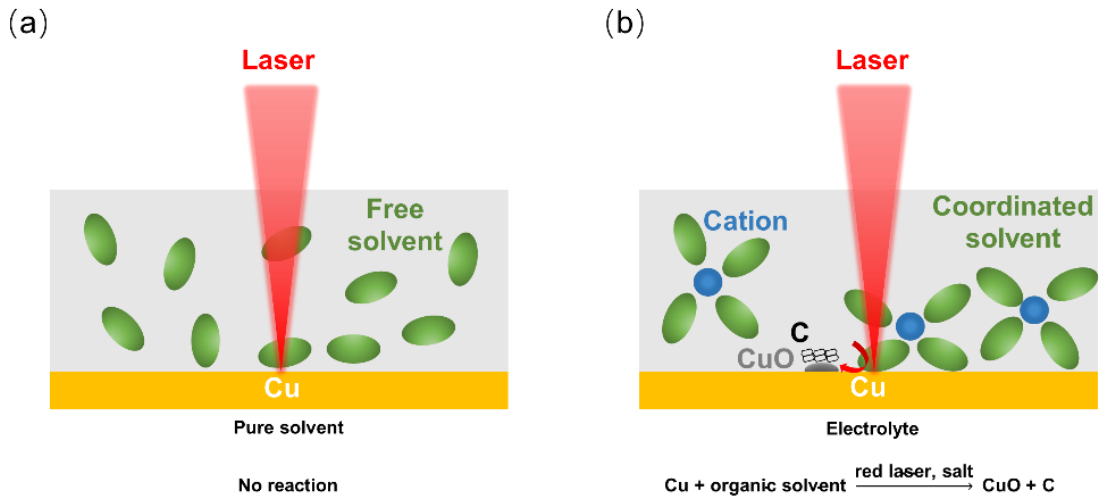


Figure 5-5. Schematic illustration of the different behavior of free and coordinated solvent molecules under red laser irradiation: (a) pure solvent (no reaction) and (b) electrolyte (photochemical reaction).

respectively) exhibit less strong D and G carbon peaks and the presence, together with the A_g mode of CuO, of the T_{2g} and T_{1u} modes of Cu_2O. This suggests a lower effectiveness of the photochemical reaction. The lower reactivity observed with KPF_6 could then be related to the larger ionic diameter of K^+ compared to Li^+, decreasing the number of solvent molecules coordinated around which are available for the radiative excitation.

5.3.3 Characterization of the photochemical reaction products

The composition and morphology of the layers photochemically obtained have been characterized before and after the electrocatalytic tests reported in the next section, by scanning electron microscopy (SEM), energy dispersive x-ray spectroscopy (EDS), x-ray photoelectron (XPS) spectroscopy and extended x-ray absorption fine structure (EXAFS). Detailed experimental conditions are reported in SI (§ S1.2). The characterization study has been focused on the material obtained from the electrolyte 1 M $LiPF_6$ in EC: DEC (1:1, v/v), the most used in commercial Li batteries. Dedicated samples have been prepared by irradiating larger surfaces of Cu (Figure 5-6), then exposed to air in a fuming cupboard to evaporate the remaining solvents, for three different time periods: 1, 35 and 60 days.

Figure 5-7, 5-8 and 5-9 gather respectively the results from the XPS analysis and the SEM characterization (coupled to EDS) of materials before their use in catalysis experiments. Cu 2p and Cu LMM spectra (Figures 5-7a and 5-7b respectively) show that the time spent in the fuming cupboard affects the oxidation state of the Cu substrate.

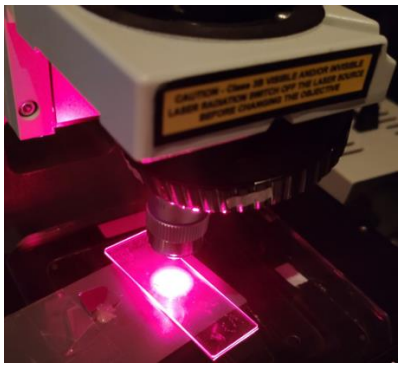


Figure 5-6. Image of operation to obtain large-scale reaction on Cu foil by adjusting the height of Raman objective. (The irradiated area has a diameter around 3.5 cm, the laser power density is 31.2 mW cm^{-2})

Three distinct copper species are identified, corresponding to metallic Cu (918 eV), Cu_2O (916 eV) and CuO (917.6 eV) [23]. The Cu/O atomic ratio calculated from the corresponding areas as obtained by deconvolution of the Cu LMM spectra allows to determine the global stoichiometry of the Cu oxide. The average Cu oxidation state is then observed to increase with the exposition time to the air in the fuming cupboard: the $Cu_{1.41}O$, $Cu_{1.22}O$ and CuO compositions are respectively obtained after 1, 35 and 60 days' periods. The larger intensity of the satellite peaks observed in the Cu 2p spectra of the irradiated samples, compared to that of the pristine Cu foil (Figure 5-7a), further attest the effectiveness of the photochemical treatment and exposure to the air in increasing the Cu oxidation state [24]. C 1s and F 1s spectra (Figures 5-7c and 5-7d respectively) show that the carbon phase deposited on the Cu_xO surface still contains traces of the pristine electrolyte. C 1s spectra result from the overlap of contributions from C=O (287.8 eV), C-O (286.2 eV) and C-C (284.4 eV) species [25], with the C=O signal slightly decreasing with the increasing of the exposure time to air in the fuming cupboard, while C-O and C-C increase. Traces of remaining PF_6^- (686.8 eV) as well as the reaction product with H_2O in the air, i.e. LiF, are also detected (684 eV) [26]. The amount of LiF increases with the time of exposition to the air, at the expense of PF_6^-. Results reported above are supported by the SEM and EDS analysis (Figures 5-8 and 5-9). The surface of the pristine Cu is largely flat (Figure 5-8a) while the appearance of some roughness in the material exposed to the air during 1 day confirms the apparition of CuO (Figure 5-8b) [28]. Then, increasing exposition times correspond to the formation of increasingly larger cubic particles typical of crystalline LiF (Figures 5-8c and 5-8d) [27]. The EDS mapping shows a relatively homogeneous distribution of the different elements analyzed for the material exposed 1 day to the air (Figures 5-9a) and

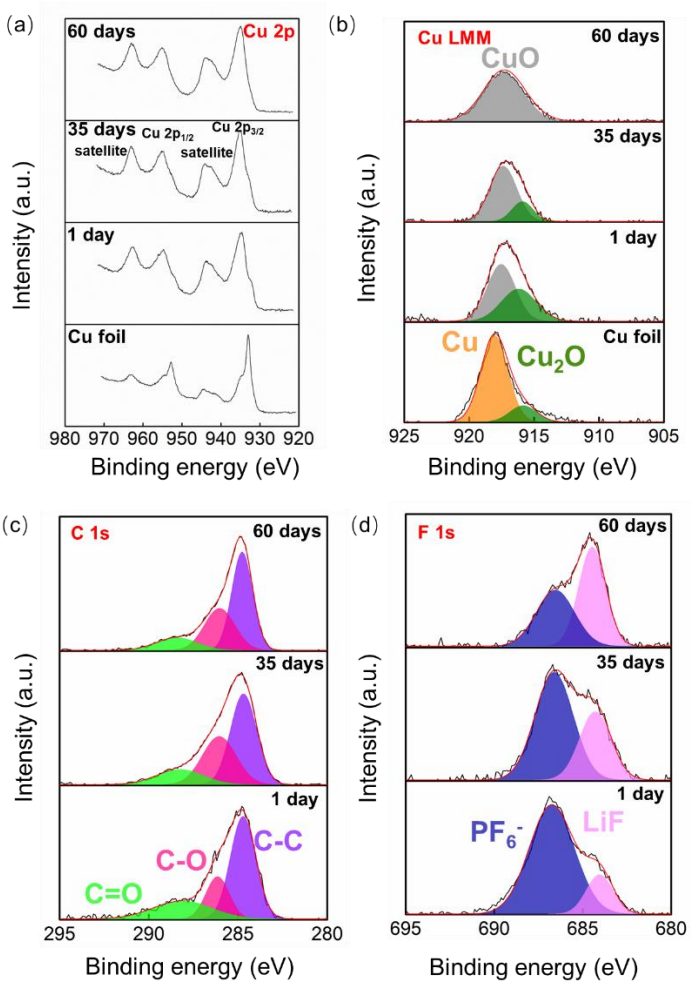


Figure 5-7. XPS analysis of the photochemical reaction products after different exposure times to air in the fuming cupboard: (a) Cu 2p, (b) Cu LMM, (c) C 1s and (d) F 1s spectra.

the progressive transition to a more uneven surface composition with the increasing of the exposure time, according to the morphological modifications revealed by SEM (Figures 5-9b and 5-9c). Some F and O rich areas seem to correspond.

Figure 5-10 reports results from the SEM, EDS, XPS and EXAFS characterization of the material obtained after 35 days' exposure to air, once used for the catalysis experiments (the last consisting in linear sweep voltammetry between 0 and -1 V vs. RHE in $CO_{2(g)}$ saturated KOH solution, see next section).

SEM (Figure 5-10a) attests the disappearance of the cubic morphology characteristic of crystalline LiF. At the same time, EDS analysis shows the redistribution of O, F and Cu elements according to a more uniform repartition (compare Figures 5-9c and 5-10a). XPS Cu 2p spectrum (Figure 5-10b) exhibits weak satellite peaks suggesting partial reduction of the $Cu_{1.22}O$ phase to Cu or/and Cu_2O. Cu LMM and F 1s spectra show new

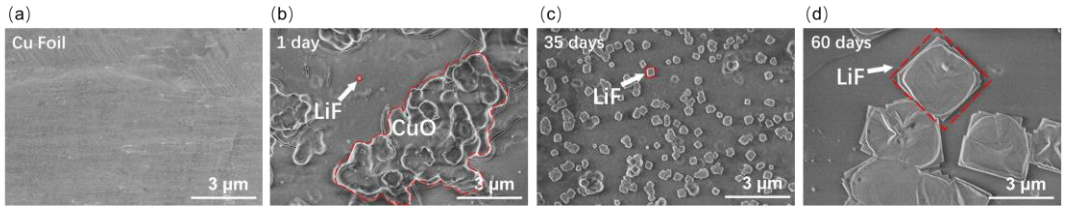


Figure 5-8. SEM images of the Cu foil surface before (pristine) (a) and after the photochemical reaction and the following exposure to air in the fuming cupboard during (b) 1, (c) 35 and (d) 60 days.

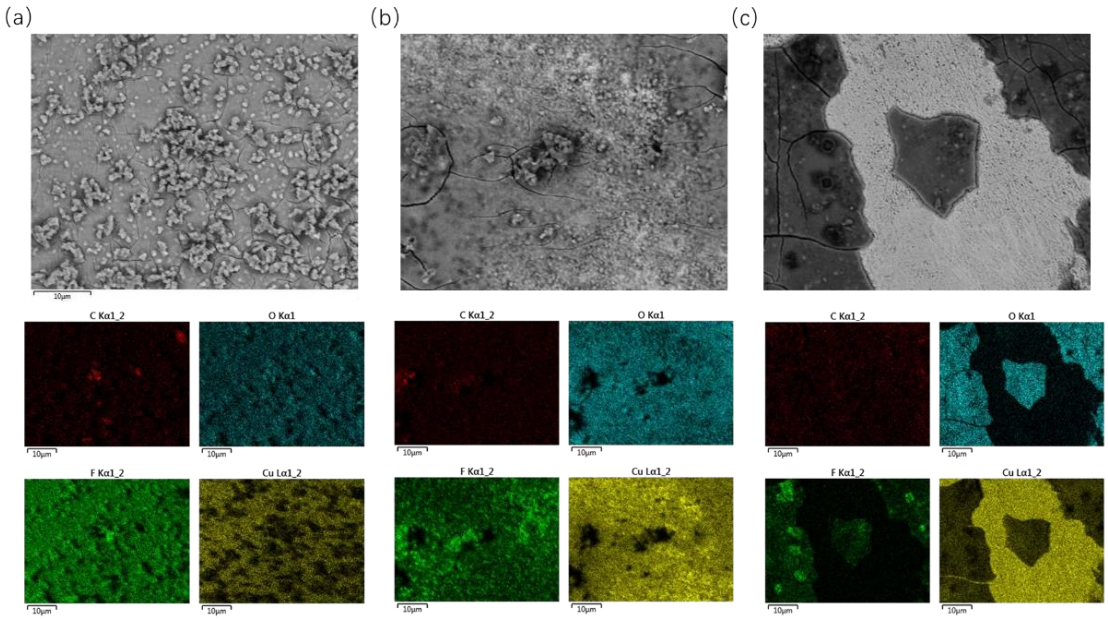


Figure 5-9. SEM images and corresponding EDS analysis of the Cu foil surface after the photochemical reaction and the following exposure to air in the fuming cupboard during (a) 1, (b) 35 and (c) 60 days.

peaks (at 913.5 and 684.2 eV respectively) which can be tentatively related to the presence of a new copper oxide compound incorporating some fluoride (indicated as F-Cu_xO in the figure). This is supported by the EXAFS wavelet transform 2D data (Figure 5-10c) showing that, if only Cu-Cu bonding can be observed in the pristine Cu foil (left side), both Cu-O and Cu-F can be detected in the catalyst after the electrochemical experiments (right side). Concerning C 1s XPS spectra, these show less amount of C=O species and corresponding larger proportion of C-O and C-C moieties, suggesting the continuation of the EC and DEC solvents decomposition during the CO_2RR experiment. Characterization results obtained after the catalytic experiment strongly suggest that the original material obtained by irradiation and exposure to the air is only the precursor of the actual catalyst: a F-Cu_xO/C composite (F-Cu_xO@C) which originates from the

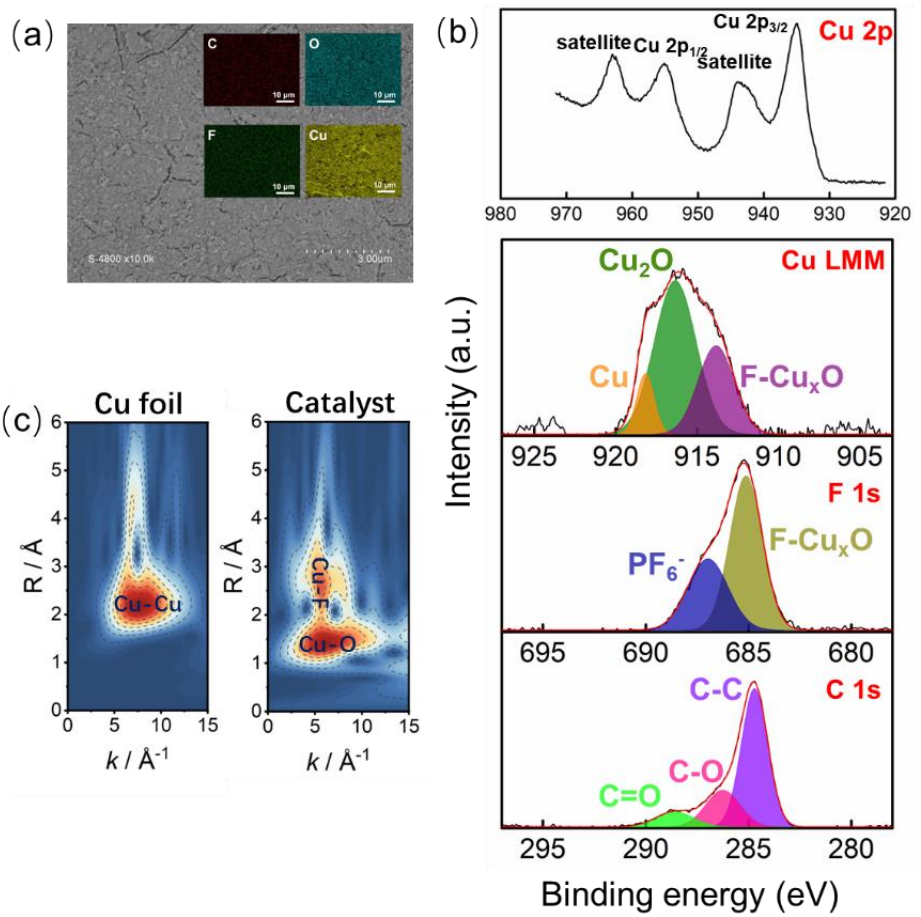


Figure 5-10. (a) SEM images (with the corresponding EDS mapping in the inlets), (b) XPS spectra and (c) EXAFS wavelet transform 2D plot of the photochemical reaction products exposed 35 days' to air, after the catalysis experiment. EXAFS results are compared to data obtained with the pristine Cu foil (on the left side).

insertion of F atoms into the Cu_xO structure to give a new phase. This process presumably occurs at the beginning of the electrocatalytic test i.e. at the onset of the potential sweep towards reduction potentials (see below).

5.4 Study of the catalytic properties

The different materials obtained after variable exposure to the air in the fuming cupboard have been investigated with the aim of attesting their perspective interest as catalysts for the CO_2RR. Electrocatalytic experiments have been carried out with the gastight two-compartment electrochemical cell reported in Figure 5-11, where the Cu foil supporting the F-Cu_xO@C layer represents the working electrode (WE). The electrolyte was a 0.5 M KOH solution saturated with CO_2 at the pH = 6.82 (equivalent to a 0.5 M $KHCO_3$ solution). The counter electrode (CE) was a 3 cm x 3cm platinum

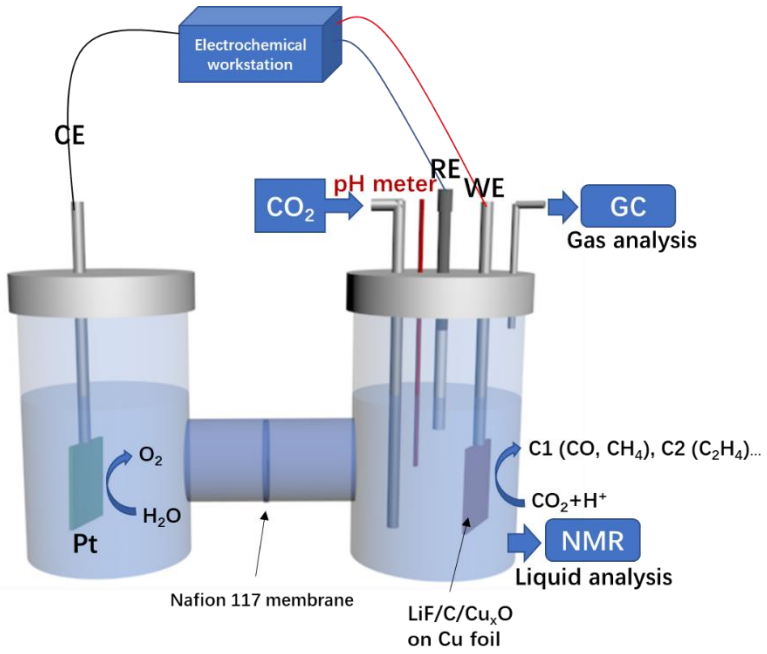


Figure 5-11. Experimental set-up for the CO_2RR electrochemical measurements.

foil and the Ag/AgCl electrode was used as reference (RE).[8]

To investigate the CO_2RR activity, linear sweep voltammetry was carried out from 0 to -1000 mV vs. RHE, at the 20 mV s^{-1} rate, at room temperature. A long-term stability test was also performed under chronoamperometric conditions, at a constant potential of -600 mV vs. RHE. CO_2RR gas products were collected continuously during the experiment and analysed every 15 min. Gas products were quantified by an online gas chromatograph while liquid products were collected in a cold trap and analysed by ^{1}H nuclear magnetic resonance (further details in sections S1.2.4 of SI). The Faradaic efficiency (FE) of the CO_2 electrocatalytic conversion into gas products was calculated as following:

$$FE_{gas}=g_i \times v \times \frac{z_i}{RT} FP_0 \times \frac{1}{I_{total}} \times 100\% \qquad \text{Equation 5-2}$$

where g_i is the volume fraction of gas product i, v the flow rate of CO_2 bubbling in the electrolyte, z_i the number of electrons required to produce one molecule of product i, I_{total} the total current, P_0 = 1.01 × 10^5 Pa, T = 273.15 K, F = 96,485 C mol^{-1} and R = 8.314 J mol^{-1} K^{-1}.

[8] All potentials here reported refers to the reversible hydrogen electrode (RHE), according to:

$$E_{RHE}=E_{Ag/AgCl}+0.059pH+0.197$$

The FE of the CO_2 conversion into liquid products was calculated as:

$$FE_{liquid} = l_i \times \frac{z_i}{Q_{total}} F \times 100\% \quad \text{Equation 5-3}$$

where l_i is the number of moles of liquid product i and Q_{total} is the charge passed while the liquid products are being collected.

The partial energy efficiency (EE) was also calculated for the catalytic process of the CO_2 conversion into CH_4:

$$EE(\%) = \frac{\Delta E_0}{\Delta E_{applied}} \times FE \quad \text{Equation 5-4}$$

where ΔE_0 is the equilibrium cell potential ($E_{CO2/CH4} - E_{water\ oxidation}$ = -0.11 V - 1.23 V = -1.34 V), $\Delta E_{applied}$ is the potential applied to the cell during the experiment ($E_{CO2/CH4\ (applied)} - E_{water\ oxidation}$ = -0.60 V - 1.23 V = -1.83 V) and FE is the Faradaic efficiency for the CO_2 conversion into CH_4 at -0.60 V vs. RHE.

Electrocatalytic experiments show that the materials obtained by irradiation of the carbonate electrolyte on Cu and then exposed to the air are able to convert CO_2 into CO, CH_4 and C_2H_4, while pristine Cu has almost no catalytic properties under the same experimental conditions. Figure 5-12a reports the FEs observed for the different CO_2RR products which can be obtained at -0.7 V (vs. RHE) as a function of the copper oxidation state in the catalyst precursor material. In the figure, the degrees of oxidation are given as O/Cu ratio. The value equal to 0 corresponds to a sample of Cu foil treated with concentrated HCl to eliminate any surface copper oxides previously formed by the spontaneous oxidation at ambient condition. The value of 0.14 corresponds to the pristine Cu foil as it and the values from 0.71 to 1.00 to the F-Cu_xO@C compounds obtained by irradiation (the value of 0.71 corresponding to the compound obtained after 1 day of exposure to the air and containing the oxide $Cu_{1.41}O$, the value of 1.00 being CuO obtained after 60 days' exposure). The Figure S5-4 in SI reports electrocatalytic measurements carried out with a sample of pure monoxide CuO obtained by treating the pristine Cu foil with H_2O_2. Electrocatalytic measurements then show that pure Cu and CuO are just able to convert a minority part of CO_2, and mainly into CO. Under the specific conditions of our experiments, the FE of pure Cu (O/Cu = 0) stays so low as 4.62 % (Figure 5-12a). The largest part of the FE measured with pure CuO (between the 70 and the 80 %, depending on the working potential) is due to the side reaction of $H_{2(g)}$ production. Differently, the catalytic activity of the F-Cu_xO@C compounds

obtained by irradiation are larger and increases with the O/Cu ratio (the copper oxidation degree) up to a maximum for the catalyst from the precursor containing $Cu_{1.22}O$ (O/Cu = 0.82), for which FE attains 66,81%. The main product of the electrocatalytic reaction is then CH_4 (46.72 %), followed by C_2H_4 (16.83 %) and CO (3.26 %). Worth of noting, when compared to other Cu based catalysts previously reported [29–31], this material not only exhibits comparable FEs but also a very high stability of the catalytic activity: data reported in Figure 5-12b show that the FE measured for the conversion of CO_2 into CH_4 stays constant around 46% during 100 h (with a constant current density at -55 mA cm^{-2}). Energy efficiencies calculated for the CH_4 production (Figure 5-12c) exhibit the same trend than FE i.e. increase continuously with the Cu oxidation degree from O/Cu = 0 to 0.82, so that the EE maximum value of 33.85 % is still attained with F-$Cu_{1.22}O$@C.

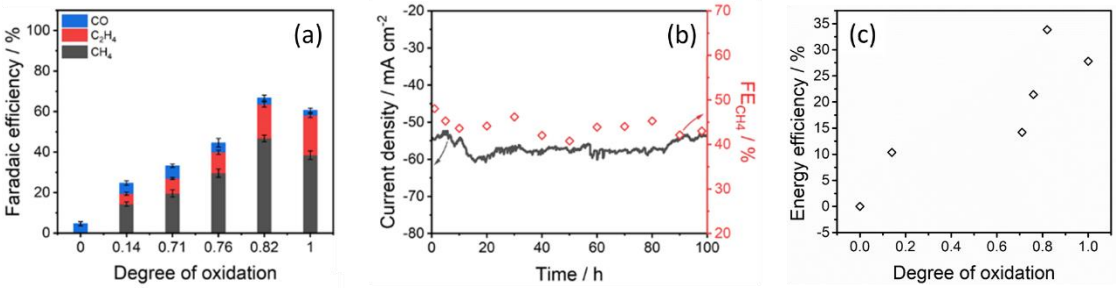


Figure 5-12. Results from the electrocatalytic measurements: (a) faradaic efficiencies as a function of the Cu oxidation degree, (b) long-term stability test of the catalytic activity of the F-$Cu_{1.22}O$@C compound for the CO_2 conversion to CH_4 (V = -600 mV vs. RHE) and (c) energy efficiency for the CO_2 conversion to CH_4 as a function of the Cu oxidation degree.

5.5 Conclusion

Recovering and reusing the electrolyte is a considerable topic for recycling Li-based batteries. The state-of-art technology of liquid electrolytes recycling focuses on the separation of Li salts and solvents, but it neglects the reutilization of the overall solution. Herein, we propose a novel photochemical reaction converting the carbonate electrolyte in contact with a Cu substrate into a layer consisting of LiF and graphitic carbon deposited on Cu_xO. This material represents then the precursor of an effective catalyst for CO_2RR, obtained *in situ* (by electrochemical reduction) under the experimental conditions required by the CO_2 electrocatalytic conversion and whose exact composition and structure remain to be defined. The experimental results taken as a whole suggest some key role of fluorine inserted in the Cu_xO structure for the activity

and selectivity of the catalyst, but this topic certainly requires further research in the next future. Worth of noting, the photochemical reaction producing the catalyst precursor, even if showing specificity for what concerns the metallic substrate and irradiation wavelength, appears extremely versatile as far as the electrolyte components, solvents and salts, are concerned. This broadens the range of potential applications up to alkalis batteries. Finally, the procedure we have developed for the synthesis of the catalyst precursor allows the modulation of the Cu substrate oxidation degree by simply controlling the exposure time to air of the irradiated sample, which represents the easiest way to tune the selectivity of the final catalyst. By this way, the FE has been improved greatly up to 66.81%, with an excellent stability of the catalytic activity of the CO_2 conversion into CH_4 (remaining around 46% during 100 h). Therefore, this work successfully provides a novel and useful way to recycle the electrolyte for Li batteries in catalyst for CO_2RR via laser irradiation.

Supporting Information

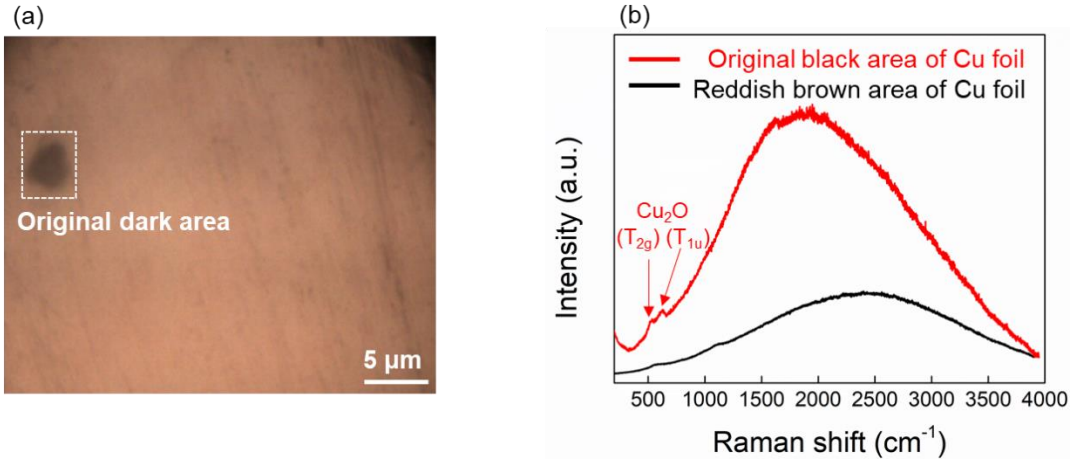


Figure S5-1. (a) optical image and (b) Raman spectra of pristine Cu foil as received.

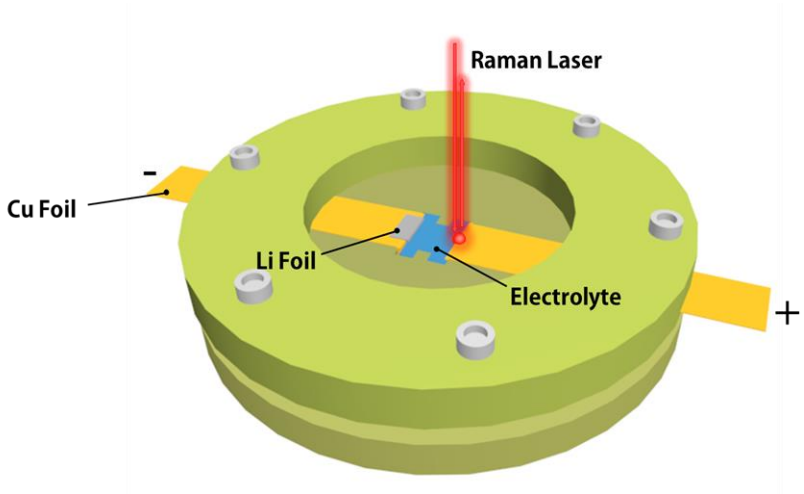


Figure S5-2. Experimental setup of *in situ* Raman measurements carried out in this chapter: laser focus at the edge of the Cu foil.

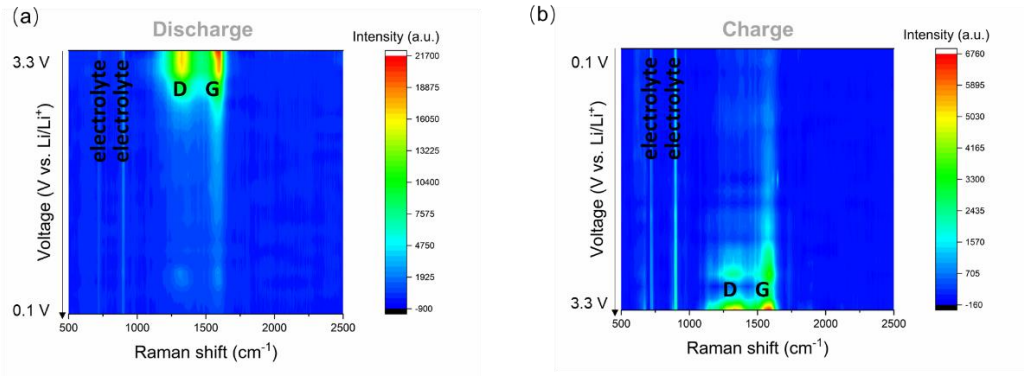


Figure S5-3. Raman intensity map (corresponding to spectra reported in Figure 5-3) reporting the evolution of the graphitic carbon signals during the (a) discharge and (b) charge of the Li||Cu half-cell filled with 1 M $LiPF_6$ in EC:DEC (1:1, v/v).

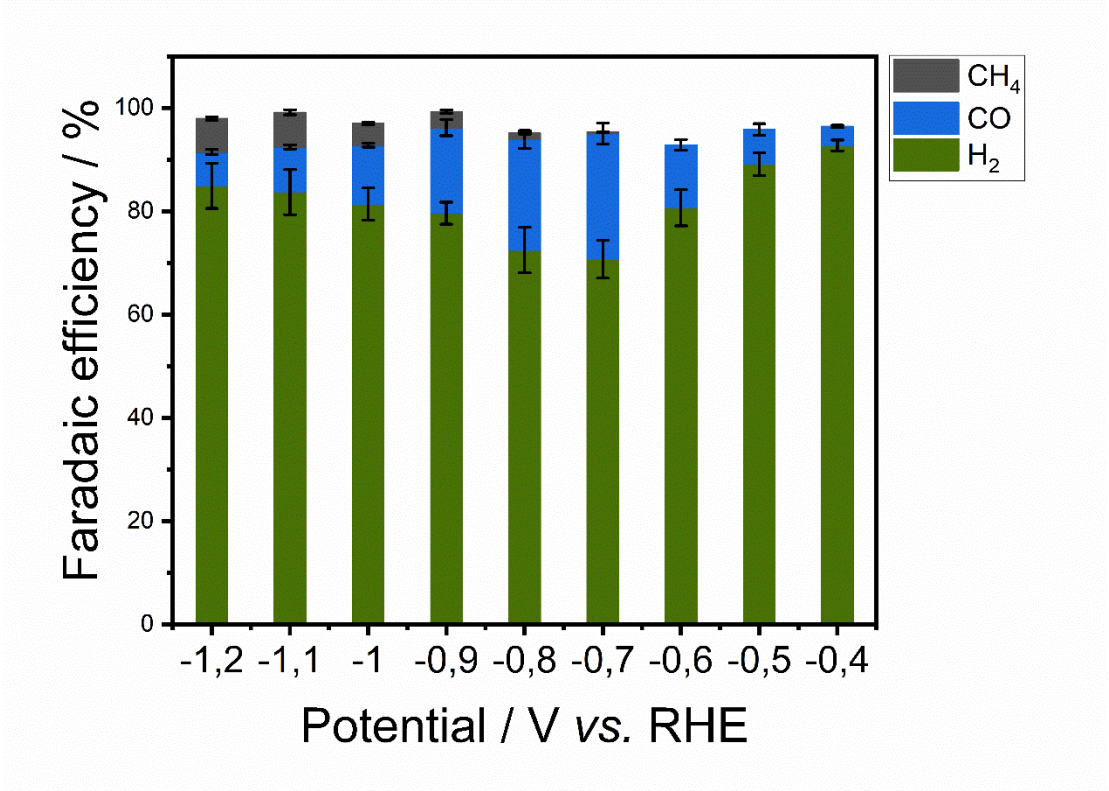


Figure S5-4. Faradaic efficiencies at different potentials of the CuO sample obtained by H_2O_2 treatment

References

[1] J.M. Tarascon, M. Armand, Issues and challenges facing rechargeable lithium batteries, Nature 414 (2001) 359–367.

[2] K.M. Winslow, S.J. Laux, T.G. Townsend, A review on the growing concern and potential management strategies of waste lithium-ion batteries, Resources conservation and recycling 129 (2018) 263–277.

[3] J. Ordonez, E.J. Gago, A. Girard, Processes and technologies for the recycling and recovery of spent lithium-ion batteries, Renewable & sustainable energy reviews 60 (2016) 195–205.

[4] V. Coman, B. Robotin, P. Ilea, Nickel recovery/removal from industrial wastes. A review, Resources conservation and recycling 73 (2013) 229–238.

[5] E.S. Fan, L. Li, Z.P. Wang, J. Lin, Y.X. Huang, Y. Yao, R.J. Chen, F. Wu, Sustainable recycling technology for Li-Ion batteries and beyond: Challenges and future prospects, Chemical reviews 120 (2020) 7020–7063.

[6] B. Huang, Z.F. Pan, X.Y. Su, L. An, Recycling of lithium-ion batteries. Recent advances and perspectives, Journal of power sources 399 (2018) 274–286.

[7] F. Arshad, L. Li, K. Amin, E. Fan, N. Manurkar, A. Ahmad, J. Yang, F. Wu, R. Chen, A comprehensive review of the advancement in recycling the anode and electrolyte from spent lithium ion batteries, ACS sustainable chemistry & engineering 8 (2020) 13527–13554.

[8] D.Y. Mu, Z. Liu, S. Jin, Y.L. Liu, S. Tian, C.S. Dai, The recovery and recycling of cathode materials and electrolyte from spent lithium ion batteries in full process, Progress in chemistry 32 (2020) 950–965.

[9] H. Xie, T. Wang, J. Liang, Q. Li, S. Sun, Cu-based nanocatalysts for electrochemical reduction of CO_2, Nano today 21 (2018) 41–54.

[10] Y. Zhao, L. Zheng, D. Jiang, W. Xia, X. Xu, Y. Yamauchi, J. Ge, J. Tang, Nanoengineering metal–organic framework-based materials for use in electrochemical CO_2 reduction reactions, Small 17 (2021) 2006590.

[11] M.B. Savitha, A. Jayarama, R. Pinto, Electrocatalytic reduction of CO_2 into useful chemicals-A brief review, SahyadriJournal of Research (2017).

[12] A. Saxena, W. Liyanage, J. Masud, S. Kapila, M. Nath, Selective electroreduction of CO_2 to carbon-rich products with a simple binary copper selenide electrocatalyst, Journal of materials chemistry A 9 (2021) 7150–7161.

[13] T. Ouyang, S. Huang, X.-T. Wang, Z.-Q. Liu, Nanostructures for electrocatalytic

CO_2 reduction, Chemistry–A European journal 26 (2020) 14024–14035.

[14] J. Timoshenko, A. Bergmann, C. Rettenmaier, A. Herzog, R.M. Arán-Ais, H.S. Jeon, F.T. Haase, U. Hejral, P. Grosse, S. Kühl, Steering the structure and selectivity of CO_2 electroreduction catalysts by potential pulses, Nature catalysis (2022) 1–9.

[15] J.F. Xu, W. Ji, Z.X. Shen, W.S. Li, S.H. Tang, X.R. Ye, D.Z. Jia, X.Q. Xin, Raman spectra of CuO nanocrystals, Journal of Raman spectroscopy 30 (1999) 413–415.

[16] R. Escribano, J.J. Sloan, N. Siddique, N. Sze, T. Dudev, Raman spectroscopy of carbon-containing particles, Vibrational spectroscopy 26 (2001) 179–186.

[17] F.A. Akgul, G. Akgul, N. Yildirim, H.E. Unalan, R. Turan, Influence of thermal annealing on microstructural, morphological, optical properties and surface electronic structure of copper oxide thin films, Materials chemistry and physics 147 (2014) 987–995.

[18] S. Hwang, D.-H. Kim, J.H. Shin, J.E. Jang, K.H. Ahn, C. Lee, H. Lee, Ionic conduction and solution structure in $LiPF_6$ and $LiBF_4$ propylene carbonate electrolytes, The journal of physical chemistry C 122 (2018) 19438–19446.

[19] Y. Zhang, Y. Zhong, Z. Wu, B. Wang, S. Liang, H. Wang, Solvent molecule cooperation enhancing lithium metal battery performance at both electrodes, Angewandte chemie international edition 59 (2020) 7797–7802.

[20] C. Sole, N.E. Drewett, L.J. Hardwick, In situ Raman study of lithium-ion intercalation into microcrystalline graphite, Faraday discussions 172 (2014) 223–237.

[21] B. Dietzek, W. Kiefer, G. Hermann, J. Popp, M. Schmitt, Solvent effects on the excited-state processes of protochlorophyllide. A femtosecond time-resolved absorption study, The journal of physical chemistry B 110 (2006) 4399–4406.

[22] A.M. Moran, C. Delbecque, A.M. Kelley, Solvent effects on ground and excited electronic state structures of the push-pull chromophore julolidinyl-n-N,N‘-diethylthiobarbituric acid, The journal of physical chemistry A 105 (2001) 10208–10219.

[23] M.M. Sung, Y.S. Kim, Self-assembled monolayers of alkanethiols on clean copper surfaces, Bulletin of the Korean chemical society 22 (2001) 748–752.

[24] Y. Wang, Y. Lü, W. Zhan, Z. Xie, Q. Kuang, L. Zheng, Synthesis of porous Cu_2O/CuO cages using Cu-based metal–organic frameworks as templates and their gas-sensing properties, Journal of Materials Chemistry A 3 (2015) 12796–12803.

[25] S. Xiao, P. Xu, Q. Peng, J. Chen, J. Huang, F. Wang, N. Noor, Layer-by-layer assembly of polyelectrolyte multilayer onto PET fabric for highly tunable dyeing with water soluble dyestuffs, Polymers 9 (2017).

[26] L. Zheng, H. Zhang, P. Cheng, Q. Ma, J. Liu, J. Nie, W. Feng, Z. Zhou, Li[(FSO_2)(n-$C_4F_9SO_2$)N] versus $LiPF_6$ for graphite/$LiCoO_2$ lithium-ion cells at both room and elevated temperatures. A comprehensive understanding with chemical, electrochemical and XPS analysis, Electrochimica acta 196 (2016) 169–188.

[27] M.A. Vallejo, E. Rivera, J.C. Azorín, J. Bernal, C. Camacho, R. Navarro, E.K. Encarnación, L.A. Díaz-Torres, M.A. Sosa, Effect of synthesis temperature on morphological and luminescent properties of lithium fluoride crystals, Journal of nanoscience and nanotechnology 17 (2017) 5612–5616.

[28] J. Luan, Q. Zhang, H. Yuan, D. Sun, Z. Peng, Y. Tang, X. Ji, H. Wang, Plasma-strengthened lithiophilicity of copper oxide nanosheet–decorated Cu foil for stable lithium metal anode, Advanced science 6 (2019) 1901433.

[29] S.Y. Lee, H. Jung, N.-K. Kim, H.-S. Oh, B.K. Min, Y.J. Hwang, Mixed copper states in anodized Cu electrocatalyst for stable and selective ethylene production from CO_2 reduction, Journal of the American chemical society 140 (2018) 8681–8689.

[30] H. Jung, S.Y. Lee, C.W. Lee, M.K. Cho, D.H. Won, C. Kim, H.-S. Oh, B.K. Min, Y.J. Hwang, Electrochemical fragmentation of Cu_2O nanoparticles enhancing selective C–C coupling from CO_2 reduction reaction, Journal of the American chemical society 141 (2019) 4624–4633.

[31] T.-C. Chou, C.-C. Chang, H.-L. Yu, W.-Y. Yu, C.-L. Dong, J.-J. Velasco-Vélez, C.-H. Chuang, L.-C. Chen, J.-F. Lee, J.-M. Chen, Controlling the oxidation state of the Cu electrode and reaction intermediates for electrochemical CO_2 reduction to ethylene, Journal of the American chemical society 142 (2020) 2857–2867.

General conclusion

The main goal of this thesis was the study and systematic comparison of low-, high- and localized high-concentration electrolytes for Li metal batteries. Raman micro-spectroscopy, implemented by other techniques like SEM and XPS, was extensively employed to (i) investigate the relationships between the electrolyte solvation structure, its physical properties as viscosity and ionic conductivity, and the electrochemical performances; (ii) characterize and correlate the Li^+ concentration gradients crossing the electrolyte during the Li plating process with the morphology of the Li deposit.
During Raman measurements, we accidentally observed the photochemical conversion of the electrolyte into a material which is the precursor of catalysts for the electrochemical CO_2 reduction reaction. We then devoted the last part of our work to the study of this phenomenon and to the development of the process that allows to obtain effective catalysts.

The following, main conclusions can be drawn from this thesis:
(1) The systematic *ex situ* Raman study and comparison of electrolytes consisting in $LiPF_6$ dissolved either in DMC or in DMC/HFPM at the same concentrations but different diluent contents showed, for the first time, the impact of the diluent nature and relative amount on the solvation sheath of the Li^+ cations. By increasing the diluent content, the number of free solvent molecules and the ratio of CIPs onto AGGs rise up simultaneously, showing that the diluent molecules not only create a nonsolvating medium, but also break the inner solvation structures via the dipole-dipole interactions between the diluent and solvent molecules. We then confirmed that this phenomenon occurs not only with $LiPF_6$ in DMC/HFPM but also with other salts (LiFSI), solvents (EC/DMC, DME) and diluents (TTE).
As a consequence of the diluent effect on the Li^+ solvation sheath, the diluent content affects (in opposite ways) the reductive stability of both the Li salt anion and solvent towards side degradation reactions and, thus, the SEI film composition and, finally, the electrochemical properties of the Li‖Cu cell. Excessive diluent content should be avoided since increasing the reactivity of solvent (by simultaneously enhancing the anion stability and the number of reactive free solvent species) and, thus, inducing organic rich SEI layers with worst mechanical and conductivity properties. The diluent amount has been also observed to affects the solvent degradation mechanism i.e. the

final DMC degradation products. Two different degradation routes have been proposed for dimethyl carbonate, depending on the abundance of free DMC species.

In the end, the increase of the diluent content in the LHCE corresponds well to the decrease of the electrolyte viscosity and the obtaining of smoother Li deposits but, at the same time, induces larger electrolyte resistivity and decrease the electrochemical performances in terms of cycling stability and average Li capacity exchange.

(2) Local Li^+ concentration in the electrolyte was measured by *in situ* Raman micro-spectroscopy during the Li plating process. Three different positions were probed: at 10, 50 and 100 mm from the electrode surface. This allowed to evaluate approximate [Li^+] gradients crossing the electrolyte and, thus, calculate Li^+ diffusion coefficients. D_{Li+} was observed to decrease with the increase of the Li^+ concentration and the diluent addition. Obviously, Li^+ concentration gradients exhibit the opposite behavior i.e. increase approximately according to the sequence: 1M $LiPF_6$ in DMC < 1 M $LiPF_6$ in DMC/HFPM < 4 M $LiPF_6$ in DMC < 4 M $LiPF_6$ in DMC/HFPM. At the same time, the SEM analysis of the electrode surface at the end of the plating process showed, as expected, that the Li deposit morphology is increasingly smoother as the electrolyte concentration increases and with the diluent addition. Typically, the LHCE electrolyte (4 M $LiPF_6$ in DMC/HFPM) has the smoothest Li deposition, maintained even at high current density (2 mA cm^{-2}). These results seem to contradict what is usually accepted, namely that the occurring of dendritic-like morphologies would be related to inadequate Li^+ transport rate from the bulk electrolyte to the electrode surface and should, thus, involve the presence of strong [Li^+] gradients crossing the electrolyte. It is indubitable that the apparition of Li protruded morphologies is due to the inadequate Li^+ supply to the reactive surface. Nevertheless, under the experimental conditions applied in our study, no direct relationships can be established between Li^+ concentration gradients and diffusion coefficients, on the one hand, and the Li deposit morphology on the other. Otherwise, results from the characterization of the layer deposited by the electrolyte reduction strongly suggest the Li^+ mobility across the SEI film to be a main parameter affecting the Li morphology. Larger salt concentration and diluent addition, even if limiting the Li^+ diffusion across the electrolyte, promote the reduction of PF_6^- over the solvent, which allows the formation of more conductive, LiF rich films. Indeed, the Li nucleation over-potential and the charge transfer resistance at the electrode-electrolyte interface decrease according to: 1M $LiPF_6$ in DMC (LCE) > 4 M $LiPF_6$ in DMC (HCE) > 4 M $LiPF_6$ in DMC/HFPM (LHCE). The over-potential and R_{ct} diminutions correspond

well to the progressive transition from a mainly dendritic (LCE) to a granular morphology (HCE), and finally to a flat homogeneous deposit (LHCE). The lower Li^+ transport ability observed for the HCE SEI compared to that from LHCE is due to the greater reactivity of PF_6^- anions, undergoing larger degradation and, thus, producing a SEI layer as good conductors as that from the LHCE but thicker.

(3) A novel photochemical reaction converting the electrolyte in contact with a Cu substrate into graphitic carbon and Cu_xO via laser irradiation has been studied as an effective way to recycle exhausted electrolytes in useful materials precursors of catalysts for the CO_2 electrochemical redaction reaction. Indeed, this materials, submitted to the potential sweeping of the electrocatalytic test, convert into fluorine containing F-Cu_xO@C layers with catalytic efficiencies and selectivities as good if not better than those of the state-of-art catalysts. The photochemical reaction has been observed to be specific as far as the metallic substrate (Cu), the laser wavelength (659.55 nm) and the presence of the Li salt are concerned, but occurred with all the different solvents (DMC, EC, DEC, diethyl ether) and salt ($LiPF_6$, KPF_6 or LiFSI) we tested. The fact that the addition of a salt is required for the photochemical reaction to take place shows that the coordination of the solvating species to the Li^+ cation is necessary to change the energy of their ground and excited states in order to have the suitable energy gap to undergo radiative excitement and generate intermediate reactive species.

We have developed a procedure for the synthesis of the catalyst precursor allowing the modulation of the Cu substrate oxidation degree by simply controlling the exposure time to air of the irradiated sample. This represents the easiest way to tune the selectivity of the final catalyst. The better catalytic properties have been measured for the $Cu_{1.22}O$ based catalyst, having a total faradaic efficiency of 66.81% (definitively larger of the 4.62 and 24.64 % obtained with pure CuO and the pristine Cu foil) and an excellent performance stability for the conversion of CO_2 to CH4, the related faradaic efficiency staying around 46% during 100 h.

To sum up, this thesis gives the following enlightenments: (i) the diluent content optimization is essential for designing improved LHCE for perspective, high-energy-density Li-metal batteries; (ii) again regarding the most effective criteria to develop advanced electrolytes, improving Li^+ transport properties of the SEI film appears definitively more important than increasing the Li^+ transport rate across the bulk

electrolyte; (iii) converting the electrolyte into effective catalyst for CO_2RR via laser irradiation provides a novel way for recycling this component in exhausted batteries.

In perspective, several aspects of the research presented above could be subject of further work. Among these: (i) the computational simulation of the solvation structure of LHCEs should certainly allow to progress in our understanding of these electrolytes and, namely, to verify any withdrawing effect caused by dipole-dipole interaction between diluent and solvent molecules hindering the formation of AGG structures; (ii) a lot of work remains to improve the *in situ* Raman micro-spectroscopy methodology, experimental setup and conditions so that to enhance both spatial and temporal resolutions together with sensitivity, as needed for mapping the establishment of concentration gradients under more representative conditions and closer to the electrode/electrolyte interface; (iii) our work concerning the recycling of exhausted electrolytes into CO_2RR catalysts is just beginning: the detailed composition of the catalyst is still to be determined, nothing is known of the fundamental mechanism of its specific catalytic reaction and the catalytic performances of materials obtained from salts other than $LiPF_6$ (e.g. LiFSI, $LiClO_4$, etc.) and solvents others than EC and DEC (e.g. DMC, DME, etc.) are currently unknown.

Annex

Annex 1: Basic principle of confocal Raman micro-spectroscopy [1]

The Raman effect

When a material is subjected to monochromatic radiation, four phenomena can occur [2]:

(1) part of the light is reflected by the first layer of atoms;

(2) a second is transmitted by the material (isotropic or anisotropic) according to conventional optical laws;

(3) a third is absorbed and transformed into heat;

(4) and finally, a fourth is scattered in all directions of space.

The Raman effect, discovered by C.V. Raman [3], is a component of the scattered light and consists in inelastic scattering. As for the absorption of infra-red radiation, this phenomenon is observed solely for material composed of covalent molecules.

Consider a molecule whose vibrational energy levels E_0 and E_1 are separated by the energy $h\nu_M$, where ν_M is the frequency of the molecular vibration. When incident light of energy $h\nu_L$, belonging to the visible spectrum, induces a transition at a higher energy level (called virtual level), the excited molecule has then three different ways to come back to the stable energy state E_0 by radiative emission (Figure A-1a). Elastic light scattering (Rayleigh scattering) occurs without energy transfer between the photon and the system. After the interaction, the system returns to the same energy as the initial state. Differently, for Raman scattering, there is an exchange of energy between the system and the photon. The system can gain or lose energy. If, after the interaction, the system is at an energy level higher than that of the initial state, scattering is called Stokes. Otherwise, the anti-Stokes scattering corresponds to the come back to an energy level lower than that of the initial state.

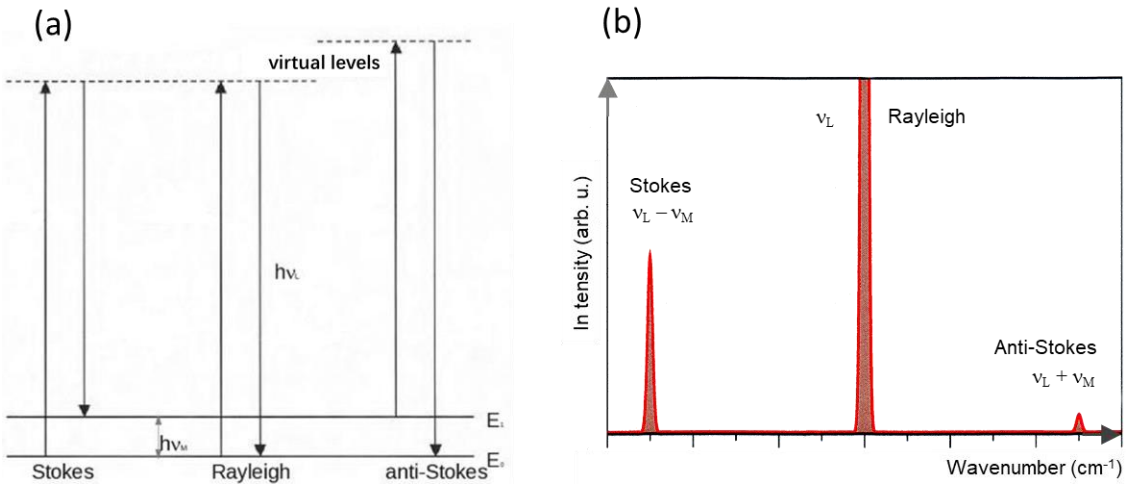


Figure A-1. Schematic representation of (a) the photon/system interaction and corresponding energy transitions, (b) the resulting Raman spectrum. Energy gain for the system: Stokes Raman scattering. Energy loss for the system: Anti-Stokes Raman scattering Elastic diffusion: Rayleigh.

For a system at the thermal equilibrium, the population of vibrational levels N_0, N_1, N_2, characterized by the energy levels E_0, E_1, E_2, follows the Boltzmann's law. The population ratio between two energy levels is then given by the Arrhenius equation (assuming that the two energy levels have the same degeneracy):

$$\frac{N_1}{N_0} = \exp\left(\frac{-\Delta E}{kT}\right) = \exp\left(\frac{-(E_1-E_2)}{kT}\right) \qquad \text{Equation A-1}$$

where k is the Boltzmann constant and T the absolute temperature. Thus, the intensity of anti-Stokes transitions, starting from less populated levels, is weaker than that observed for Stokes transitions (Figure A-1b). The Raman spectra reported in literature usually corresponds to the Stokes frequency domain.

Experimental considerations

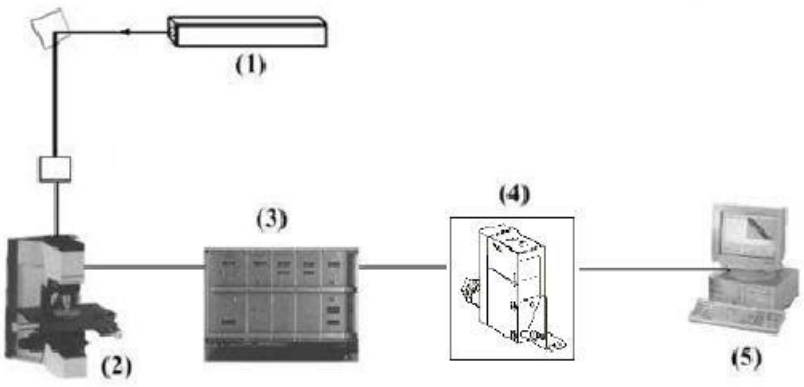


Figure A-2. Scheme of the main elements of a Raman micro-spectrometer.

In a Raman micro-spectrometer, the backscattering geometry is employed: a laser beam is focused on the sample through a microscope objective, and then the Raman light is collected by the same objective in the inverse direction of the incident light. Figure A-2 shows the schematic of the different elements of a Raman micro-spectrometer:

(1) A light source (laser) providing polarized monochromatic radiation for the sample exciting;

(2) A microscope, on which different objectives are usually available. They are chosen to have an optimal illumination of the sample, the most effective collection of the light scattered by Raman effect, and a transfer to the entrance of the spectrometer as efficient as possible. The sample is placed on the sample holder of the microscope which is equipped with an automatic micro-displacement device allowing the acquisition of 3D maps;

(3) The spectrometer, which performs the spectral analysis of the radiation. This includes either a pre-monochromator or a holographic filter (Notch or Edge) which cuts out reflected or scattered radiations at the laser wavelength. The pre-monochromator is followed by a dispersive spectrograph. There are then so-called “single-channel” and “multi-channel” spectrometers;

(4) The photoelectric detector, for which two different devices can be used. "Single-channel" spectrometers employ single photo-detector. The analysis of the various elements of the spectrum is then carried out sequentially, by rotation of the axes of a diffraction grating, so as to scroll the various radiations focused in the plane of a slot that isolates a narrow bandwidth. In the more efficient generation of “multi-channel spectrometer” instruments, the photoelectric detector consists of a charge coupled device (CCD) cooled by Pelletier effect.

(5) The last part of the instrument measures and processes the electrical signals from the detector. The development of digital processing techniques and the power of the microcomputer systems available nowadays have significantly increased the quality of spectroscopic measurements, ensuring at the same time the management of the various functions of the spectrometer.

The confocal arrangement.

Unlike the conventional microscope, where the entire field of view is uniformly illuminated and observed, the “confocal” arrangement takes benefit from the combined

effects of spatial filtering by optically conjugated pinhole diaphragms. Such a system isolates the light originating from a small region of the sample coincident with the illuminated spot, and efficiently eliminates the contributions from out-of-focus zones (Figure A-3). Lateral and axial spatial resolution of the microscope are improved so that sample volumes as small as a few μm^3 can be selectively probed,

The ability of the confocal setup to decrease contributions from the out-of-focus regions has several advantages:

(1) Contrast enhancement;

(2) Discrimination of a well-defined spatial region in a complex multiphase specimen;

(3) Strong rejection of the stray light;

(4) Strong rejection of the surrounding material when small inclusions embedded in a solid matrix or immersed in a liquid have to be analyzed.

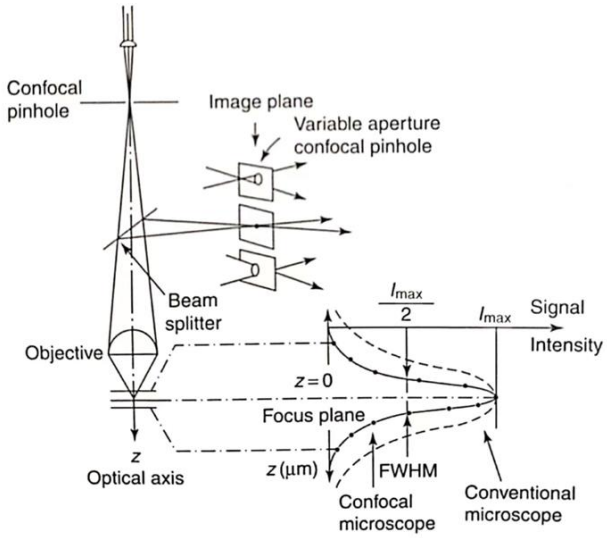


Figure A-3. Schematic description of the confocal microscopy arrangement [1].

Annex 2. Fourier transform infrared spectroscopy [4]

Basic principle.

Fourier transform infrared (FTIR) spectroscopy is based on the absorption or emission of infrared radiation by the material to analyze. As for Raman spectroscopy, FTIR allows the analysis of the chemical functions constituting a material *via* the detection of characteristic vibrations of chemical bonds. In the absorption IR spectroscopy technique, a sample is irradiated by a polychromatic beam, more usually in the mid-infrared range between 400 and 4000 cm^{-1}. Simplifying a lot, when the photon energy matches the energy difference between the ground and the excited states of a chemical group vibration, the radiation is absorbed and the decrease of the transmitted intensity of the incident beam is observed at the frequency of the vibration. In reality, other conditions must also be respected for the interaction between electromagnetic radiation and matter to occur, related the symmetry of the chemical group and the effect of the vibration on its permanent dipolar moment [4].

Compared to dispersive spectrometers, a FTIR spectrometer allow to simultaneously collect high-resolution spectral data over a wider spectral range with the aid of a Michaelson interferometer (Figure A-4). A Fourier transform (a mathematical process) is then carried out to convert the raw data into the actual spectrum. The light from the polychromatic infrared source is first collimated and directed to a beam splitter. Half of the light is refracted towards the fixed mirror and the rest is transmitted towards the moving mirror. Light is reflected from the two mirrors back to the beam splitter and some fraction of the original light passes into the sample compartment. There, the light is focused on the sample. On leaving the sample compartment the light is refocused on to the detector. The difference in optical path length between the two arms to the interferometer is known as the retardation or optical path difference. An interferogram is obtained by varying the retardation and recording the signal from the detector for various values of the retardation. The interferogram is then converted to a spectrum by Fourier transformation.

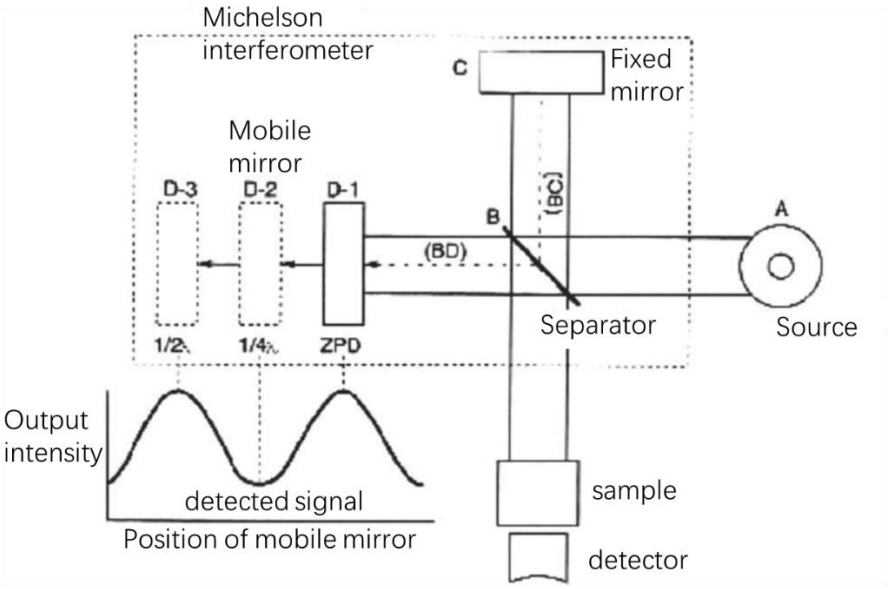


Figure A-4. Schematic diagram of a Michaelson interferometer configured for FTIR [5].

Attenuated total reflection IR spectroscopy (ATR-FTIR).

In ATR-FTIR spectroscopy, the infrared beam passes through an crystal on which the sample is placed, so as to be reflected at the interface with the material to be analyzed (Figure A-5). Different materials can be used as ATR crystals (ZnSe, TlBr, AgCl, diamond, etc.), whose main feature is to have a refractive index n_2 higher than that of the sample (n_1). In this case, an evanescent wave is formed at each reflection, extending into the adjacent medium and interacting with species at the sample surface and in the bulk so that absorption occurs (the total reflection is attenuated). The light penetration depth, d_p, into the sample is of the order of a few μm and depends on the wavelength, the refractive indexes and the incidence angle θ, according to:

$$d_p = \frac{\lambda}{2\pi n_1 (\sin^2\theta - (\frac{n_2}{n_1})^2)^{1/2}} \qquad \text{Equation A-2}$$

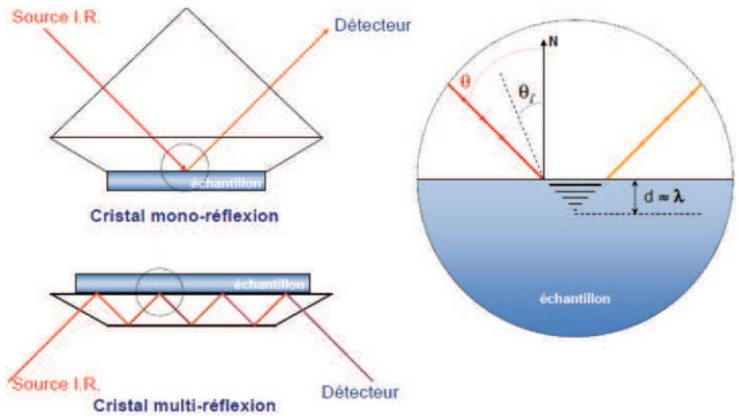


Figure A-5. Diagram of an ATR-FTIR principle [5].

The ATR technique is ideal for thick or very absorbent samples (liquids containing water for example) and for thin films for surface studies. Solids analyzed by this technique must be flat or flexible to best match the shape of the crystal.

Annex 3. Basic principle of scanning electron microscopy [6]

Scanning electron microscopy (SEM) produces detailed, magnified images of an object by scanning its surface with a focused beam of electrons. An electron gun fires this beam, which then accelerate down the column of the scanning electron microscope (Figure A-6a). During this action, the electron beams pass through a series of lenses and apertures, which act to focus it. This occurs under vacuum conditions, which prevents molecules or atoms already present in the microscope column from interacting with the electron beam. The electron beam scans the sample in a raster pattern, scanning the surface area in lines from side to side, top to bottom. The electrons interact with atoms on the surface of the sample (Figure A-6b). This interaction creates various types of signal, including secondary electrons, backscattered electrons, x- rays and light, that contain information about the surface topography and composition of the sample. Detectors in the microscope pick up these signals and create high-resolution images. Some SEMs can achieve resolutions better than 1 nanometer.

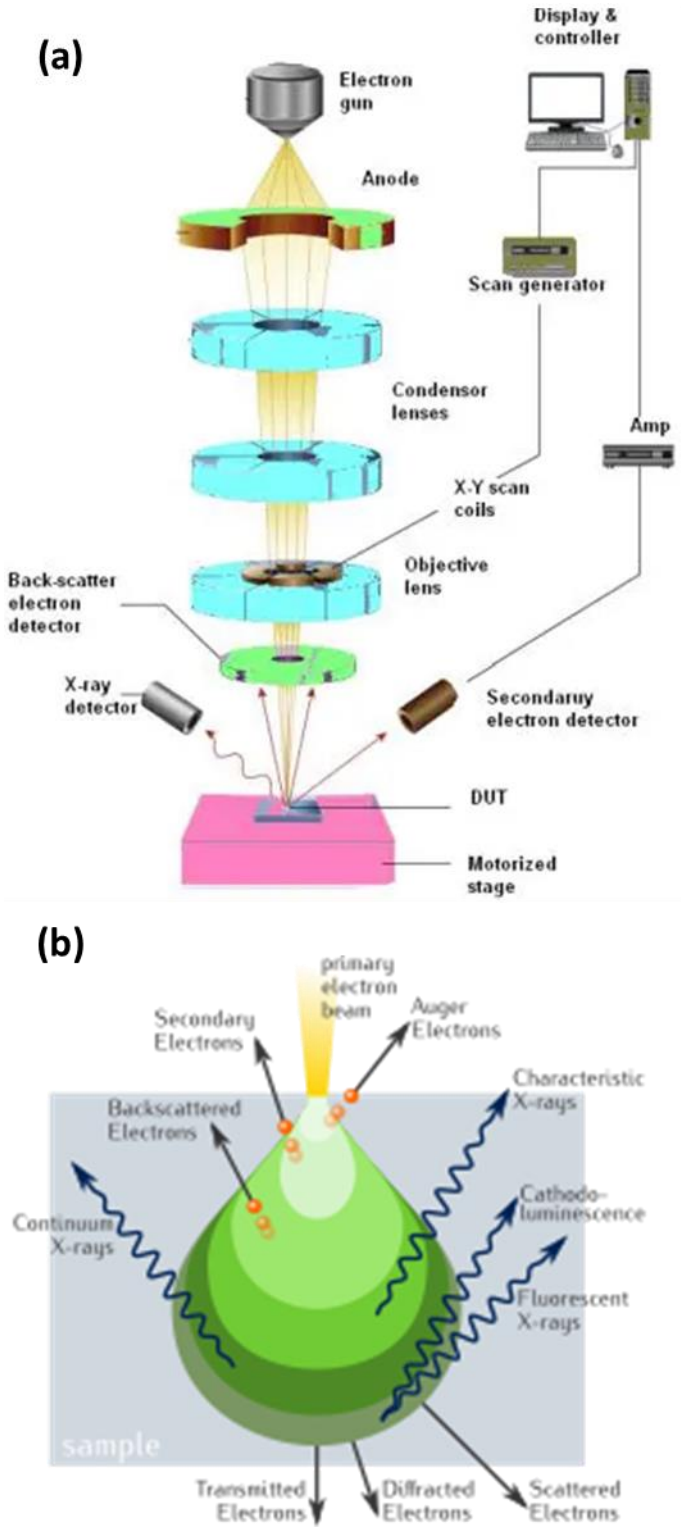


Figure A-6. (a) SEM schematic block diagram and (b) illustration of the electron–matter interaction volume and types of generated signal [6].

Annex 4. Basic principle of X-ray photoelectron spectroscopy [7]

X-ray photoelectron spectroscopy (XPS) is based on the photoelectric effect, discovered by Heinrich Hertz in 1887 [8], which allow to identify the elements of a material. The two main advantages of this technique are its surface sensitivity (~10nm)

and its ability to distinguish differences in chemical environment. XPS can detect all elements except hydrogen and helium with detection limits of approximately 0.1% - 1%, is quantitative without standards and is relatively nondestructive.

In XPS, the sample is irradiated with soft X-rays (energy lower than ~6 keV) and the kinetic energy of the emitted electrons is analyzed (Figure A-7a).

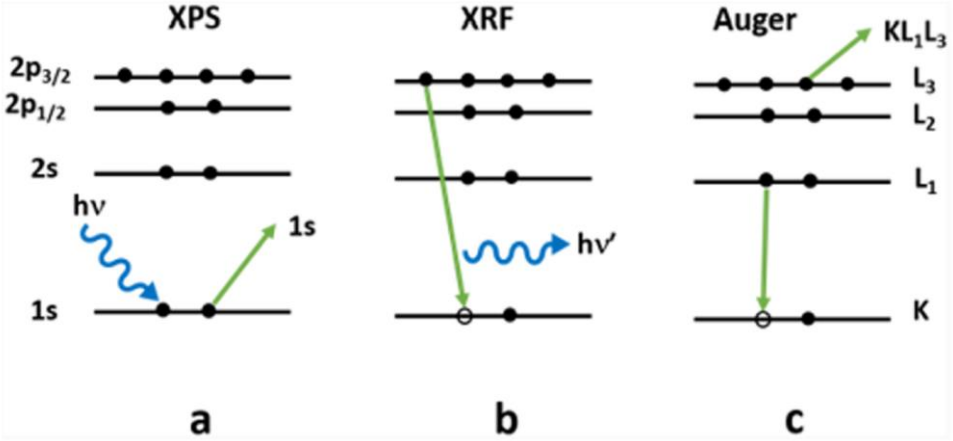


Figure A-7. Illustration of some of the phenomena resulting from the x-ray irradiation of a material: (a) emission of a photoelectron, (b) X-ray fluorescence and (c) emission of an Auger electron [7].

The emitted photoelectrons result from the full transfer of the X-ray energy to a core level electron, which can be expressed with the following equation:

$$h\nu = BE + KE + \Phi_{spec} \qquad \text{Equation A-3}$$

simply stating that the energy of the x-ray (hv) is equal to the binding energy (BE) of the electron (how tightly it is bound to the atom/orbital to which it is attached), plus the kinetic energy (KE) of the electron that is emitted, plus the spectrometer work function Φ_{spec}, a constant value. It follows that the binding energy of the electron, a material property independent of the x-ray source used to eject it, can be known by the measurement of the its kinetic energy once ejected:

$$BE = h\nu - KE - \Phi_{spec} \qquad \text{Equation A-4}$$

Photoelectron peaks are notated by the element and orbital from which they were ejected. For example, “O 1s” describes electrons emitted from the 1s orbital of an oxygen atom.

The loss of the XPS core electron results in a core “hole”. This excited ionized state

relaxes rapidly by filling the hole with an electron from a valence orbital. This relaxation process releases energy in one of the two competing processes: x-ray fluorescence or the emission of an Auger electron. X-ray fluorescence (Figure A-7b) is not detected in the electron spectrum and will not be considered further here. Auger electrons generated by the process described in Figure A-7c will be detected and are often used in XPS analysis. The notation of Auger peaks traditionally relies on the K, L, and M nomenclature for atomic orbitals. For example, the main oxygen Auger peak is denoted by KLL, which indicates that the first ejected electron came from a K orbital, the electron that filled the core hole came from an L orbital, and the final Auger electron ejected also came from an L orbital (subscripts are sometimes used to differentiate between specific L, M, and N orbitals as shown in Figure A-7c). The Auger process then involves three different electron transitions and the kinetic energy of the ejected Auger electron is:

$$KE_{Auger} \sim BE(K) - BE(L_1) - BE(L_3) \qquad \text{Equation A-5}$$

Annex 5. Extended X-ray Absorption Fine Structure (EXAFS) [9]

EXAFS and X-ray Absorption Near Edge Structure (XANES) are the two sub-parts of the same spectrum obtained by x-ray absorption. X-ray absorption techniques follow the Beer's Law. X-rays of a narrow energy resolution are directed to the sample, the incident and transmitted x-ray intensities are recorded as the incident x-ray energy is incremented and the X-ray absorption coefficient of the investigated material is obtained as a function of energy. When the incident x-ray energy matches the binding energy of an electron of an atom within the sample, the number of x-rays absorbed by the sample increases dramatically, causing an absorption edge (Figure A-9). Every element has a set of unique absorption edges corresponding to different binding energies of its electrons. Thus, EXAFS and XANES are highly sensitive techniques with elemental specificity. EXAFS corresponds to the portion of the x-ray absorption spectrum well above the absorption edge (between 15 and 50 eV above). The correct interpretation of the oscillatory structure in this energy domain allows EXAFS to be also a structural technique, while XANES gives information about the valence state of the absorbing atom, energy bandwidth and bond angles.

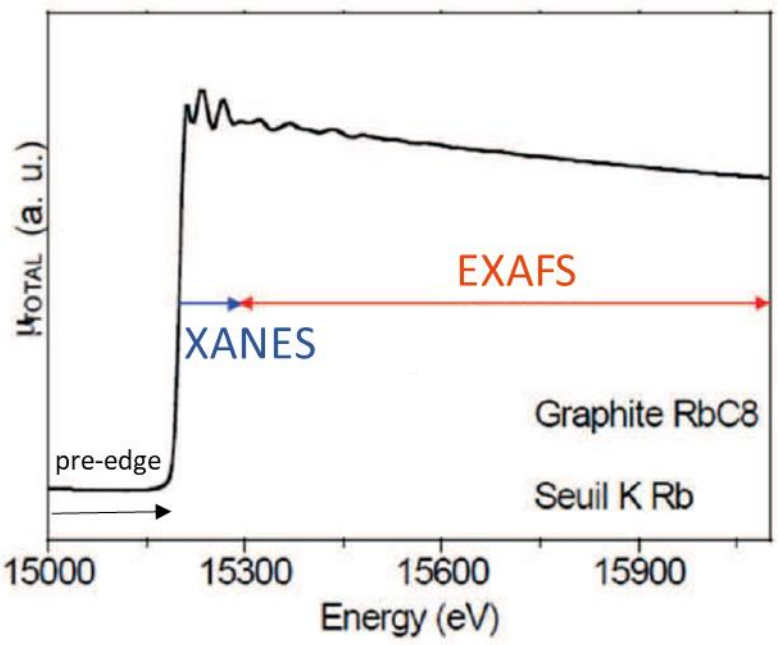


Figure A-9. Example of x-ray absorption spectrum (obtained at the K threshold of Rb, carried out on a sample of graphite RbC8 [5]).

EXAFS can be interpreted as due to scattering of the photoelectron ejected from the absorbing atom by the photoelectric effect. The photoelectron will scatter from surrounding atoms and a portion of it will return to the absorbing atom still in its excited state (before the hole in the core electron level has been refilled). The photoelectron can be modelled as a spherical wave of wavenumber $k=2\pi/\lambda$. The interference between the outgoing wave corresponding to the ejected electron and the waves scattered by neighbors constitutes the EXAFS oscillations (Figure A-10). This phenomenon allows to deduce the number and the distance of the backscattering atoms for an absorbing atom, equivalent to an average coordination number. Thus, EXAFS is a technique complementary to x-ray diffraction but which does not require long-range structural order and can, then, be applied also to liquid and gaseous samples and to amorphous solids.

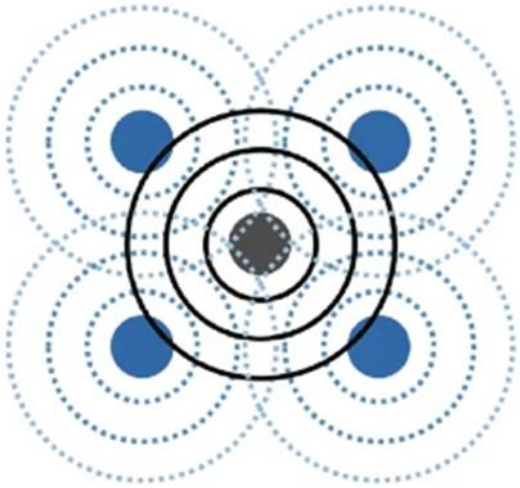


Figure A-10. Schematic of interference pattern created by the outgoing (solid black lines) and reflected (dashed blue lines) photoelectron waves between absorbing atom (gray) and its nearest atoms (blue) [5].

References

[1] J.M. Chalmers, P.R. Griffiths, Handbook of vibrational spectroscopy, Wiley (2002).

[2] S. Perkowitz, Optical characterization of semiconductors: Infrared, Raman, and photoluminescence spectroscopy, Academic press, London, San Diego (1993).

[3] C.V. Raman, K.S. Krishnan, A new type of secondary radiation, Nature 121 (1928) 501–502.

[4] A. Dutta, Fourier transform infrared spectroscopy, Spectroscopic methods for nanomaterials characterization (2017) 73–93.

[5] C. Marino, Optimisation de nouvelles électrodes négatives énergétiques pour batteries lithium-ion: Caractérisation des interfaces électrode/électrolyte, 2012.

[6] K. Akhtar, S.A. Khan, S.B. Khan, A.M. Asiri, Scanning electron microscopy. Principle and applications in nanomaterials characterization, in: Handbook of materials characterization, Springer, (2018) 113–145.

[7] F.A. Stevie, C.L. Donley, Introduction to x-ray photoelectron spectroscopy, Journal of vacuum science & technology A: Vacuum, surfaces, and films 38 (2020) 63204.

[8] H.-L. Lee, N.T. Flynn, X-ray photoelectron spectroscopy, in: Handbook of applied solid state spectroscopy, Springer, (2006)485–507.

[9] B.-K. Teo, Extended x-ray absorption fine structure (EXAFS) spectroscopy: Techniques and applications, in: EXAFS spectroscopy, Springer, (1981) 13–58.

Full list of publications

[1] **F. Ren**, Z. Li, J. Chen, P. Huguet, Z. Peng, S. Deabate, Solvent–diluent interaction-mediated solvation structure of localized high-concentration electrolytes, ACS applied materials & interfaces 14 (2022) 4211–4219.

[2] **F. Ren**, Z. Li, L. Huai, Z. Ren, M. Wang, J. Liu, H. Lin, Z. Peng, D. Wang, High-loading lateral Li deposition realized by a scalable fluorocarbon bonded laminates, Carbon 171 (2021) 894–906.

[3] **F. Ren**, Z. Li, Y. Zhu, P. Huguet, S. Deabate, D. Wang, Z. Peng, Artificial nucleation sites with stable SEI for Li metal anodes by aggressive Al pulverization, Nano energy 73 (2020) 104746.

[4] Z. Zhang, Z. Li, H. Lin, M. Wang, Z. Luo, **F. Ren**, Z. Liu, C. Zhou, Z. Peng, D. Wang, Transplantable carbonaceous Li^+ filtrating membrane for lithium metal protection, ACS applied materials & interfaces 12 (2020) 30494–30502.

[5] **F. Ren**, Z. Peng, M. Wang, Y. Xie, Z. Li, H. Wan, H. Lin, D. Wang, Over-potential induced Li/Na filtrated depositions using stacked graphene coating on copper scaffold, Energy storage materials 16 (2019) 364–373.

[6] Z. Peng[1], **F. Ren**[1], S. Yang, M. Wang, J. Sun, D. Wang, W. Xu, J.-G. Zhang, A highly stable host for lithium metal anode enabled by Li_9Al_4-Li_3N-AlN structure, Nano energy 59 (2019) 110–119.

[7] M. Wang, Z. Peng, W. Luo, **F. Ren**, Z. Li, Q. Zhang, H. He, C. Ouyang, D. Wang, Tailoring lithium deposition via an SEI-functionalized membrane derived from LiF decorated layered carbon structure, Advanced energy materials 9 (2019) 1802912.

[8] Y. Zhu, F. Meng, N. Sun, L. Huai, M. Wang, **F. Ren**, Z. Li, Z. Peng, F. Huang, H. Gu, Suppressing sponge-like Li deposition via AlN-modified substrate for stable Li metal anode, ACS applied materials & interfaces 11 (2019) 42261–42270.

[9] **F. Ren**, Z. Lu, H. Zhang, L. Huai, X. Chen, S. Wu, Z. Peng, D. Wang, J. Ye, Pseudocapacitance induced uniform plating/stripping of Li metal anode in vertical graphene nanowalls, Advanced functional materials 28 (2018) 1805638.

[10] M. Wang, L. Huai, G. Hu, S. Yang, **F. Ren**, S. Wang, Z. Zhang, Z. Chen, Z. Peng, C. Shen, Effect of LiFSI concentrations to form thickness-and modulus-controlled SEI layers on lithium metal anodes, The journal of physical chemistry C 122 (2018) 9825–9834.

[11] Z. Lu, Z. Zhang, X. Chen, Q. Chen, **F. Ren**, M. Wang, S. Wu, Z. Peng, D. Wang, J. Ye, Improving Li anode performance by a porous 3D carbon paper host with plasma assisted sponge carbon coating, Energy storage materials 11 (2018) 47–56.

[12] Z. Peng, Z. Zhang, M. Wang, **F. Ren**, D. Wang, Extending lifespan of lithium metal electrodes via surface structure regulation strategies, ECS meeting abstracts, MA2018-01 (2018) 457.

Résumé: Les batteries Li-métal sont des candidats idéaux pour les dispositifs de stockage à haute densité d'énergie de nouvelle génération, grâce à l'anode en lithium métallique ayant une capacité ultra-élevée (3860 mAh g^{-1}) et le potentiel redox le plus bas (-3,04 V par rapport à S.H.E.). Cependant, leur large commercialisation est actuellement entravée par le problème bien connu de la génération de dendrites de lithium. Pour surmonter cette difficulté majeure, les premiers électrolytes à faible concentration (LCE) ont été remplacés par des électrolytes à haute concentration (HCE). Ces derniers limitent en fait la génération de Li dendritique mais impliquent au même temps de nouveaux défauts tels qu'une mauvaise conductivité ionique, une viscosité élevée et un prix accru. Ces inconvénients sont alors résolus à leur tour en ajoutant un diluant pour obtenir ainsi des électrolytes à haute concentration localisée (LHCE). Néanmoins, les performances électrochimiques de l'anode Li métal restent toujours insuffisantes.

Ce travail est consacré à la comparaison détaillée et systématique entre les structures et les propriétés des électrolytes à faible concentration, haute concentration et haute concentration localisée constitués des mêmes sels et solvants, le but étant de proposer de nouveaux critères pour le développement d'électrolytes améliorés. Nous utilisons la micro-spectroscopie Raman afin d'établir des relations strictes entre la structure locale de solvatation de l'électrolyte, sa réactivité vis-à-vis de l'anode Li métal qui conduit à la formation du film d'électrolyte solide d'interface (SEI) et, au final, les propriétés électrochimiques. Nous montrons que l'augmentation de la quantité de diluant dans le LHCE affecte la réactivité de l'électrolyte en augmentant le nombre de molécules de solvants libres et les structures locales du type « pair d'ions de contact » (CIP), au détriment des clusters AGG. Il ressort pour la première fois de cette étude que, du fait des conséquences qu'un ajout excessif de diluant a sur la réactivité de l'électrolyte et in fine sur la durée de vie de l'anode Li métal, l'ajustement de la teneur en diluant est un paramètre clé pour la conception de LHCEs améliorés pour futures batteries à haute densité d'énergie.

La consomption des espèces Li+ à la surface de l'électrode est généralement considéré comme le phénomène sous-jacent à l'apparition et à la croissance des dendrites. Par conséquence, dans la suite de cette étude, nous utilisons la spectroscopie Raman in situ pour étudier les gradients de concentration de Li+ traversant l'électrolyte pendant l'opération électrochimique et, de cette manière, calculer le coefficient de diffusion de Li+ aux différentes conditions expérimentales de courant, concentration, etc.. La comparaison entre LCEs, HCEs et LHCEs montre que la diffusion du Li+ à travers l'électrolyte diminue avec l'ajout de solvant et l'augmentation de la concentration de l'électrolyte. Mais cela n'empêche pas d'obtenir le dépôt de Li métallique homogène et lisse attendu avec le LCHE. En effet, la caractérisation de l'interface électrode/électrolyte montre que le principal paramètre affectant la morphologie du dépôt métallique est la mobilité du Li+ à travers le film SEI, dont la conductivité est améliorée par la présence de LiF dans le cas des électrolytes HCE et LHCE.

La dernière partie de ce travail est consacrée à l'étude plus approfondie d'un phénomène que nous avons initialement observé par hasard lors des expériences Raman : la conversion photochimique (c'est-à-dire par l'irradiation du laser) de l'électrolyte en carbone graphitique déposé sur un substrat d'oxyde de cuivre, CuxO contenant du fluor. Nous montrons alors que ce matériau est le précurseur d'un catalyseur efficace pour la réaction de réduction du CO2, ce qui représente une voie des plus intéressantes pour recycler les électrolytes épuisés des batteries Li.

Mots-clés: Batterie Li métal, spectroscopie Raman, électrolyte à haute concentration localisée, CO_2RR

Abstract: Li-metal batteries are ideal candidates for next-generation high-energy density storage devices, thanks to the Li metal anode having ultrahigh capacity (3860 mAh g^{-1}) and the lowest redox potential (-3.04 V vs. S.H.E.). However, their wide commercial deployment is currently hindered by the notorious Li dendrites generation. To overcome this main issue, the early low-concentration electrolytes (LCEs) have been replaced with high-concentration electrolytes (HCEs). The latter limit actually the generation of dendritic Li but involve new shortcomings such as poor ionic conductivity, high viscosity and increased price. These drawbacks are solved in turn by adding a diluent to obtain localized high-concentration electrolytes (LHCEs). Nevertheless, the electrochemical performances of the Li metal anode still remain inadequate.

This work is devoted to the detailed and systematic comparison between the structure and properties of low-, high- and localized high-concentration electrolytes consisting of the same salt and solvents, the purpose implied being to propose new criteria for the development of improved electrolytes. In order to establish more rigorous relationships between the electrolyte local solvation structure, its reactivity towards the Li metal anode leading to the formation of the solid electrolyte interface (SEI) film and, finally, the electrochemical properties, we use Raman micro-spectroscopy to probe the Li^+ inner solvation sheath. We show that the increase of the diluent amount in the LHCE affects the electrolyte reactivity by increasing the number of free solvent species and contact ion pairs (CIPs) to the detriment of AGG clusters. Then, due to the consequences that an excessive diluent addition has on the reactivity of the electrolyte and, ultimately, on the Li metal anode lifespan, tuning the diluent content appears for the first time as a key parameter for the designing of improved LHCEs for high-energy-density batteries.

The depletion of Li^+ species at the electrode surface is usually considered the phenomenon underlying the dendrite appearance and growth. Then, we also use *in situ* Raman spectroscopy to study the Li^+ concentration gradients occurring across the electrolyte during the electrochemical operation and, by this way, calculate approximate Li^+ diffusion coefficients. The comparison between LCEs, HCEs and LHCEs show that the Li^+ diffusion across the electrolyte decreases with the solvent addition and the increase of the electrolyte concentration. But this does not prevent the homogeneous and smooth Li deposition expected with LCHE from being obtained. Indeed, the characterization of the electrode/electrolyte interface shows that the main parameter affecting the Li deposit morphology is the Li^+ mobility across the SEI film, enhanced by the presence of LiF in the case of HCEs and LHCEs.

The last part of this work is devoted to the more in-depth study of a phenomenon that we initially observed by chance during the Raman experiments: the photochemical conversion (i.e. by the laser irradiation) of the electrolyte into graphitic carbon onto a fluorine containing Cu_xO substrate. We show that this material is the precursor of an effective catalyst for the CO_2 reduction reaction, which can represent a most interesting way to recycle exhausted Li battery electrolytes.

Keywords: Li metal battery, Raman spectroscopy, localized high-concentration electrolyte, CO_2RR